

Optimal delineation of agricultural parcels from satellite imagery using the  
multiresolution segmentation algorithm

**Dissertation**  
**zur Erlangung des**  
**Doktorgrades der Naturwissenschaften (Dr. rer. nat.)**

der

Naturwissenschaftlichen Fakultät III  
Agrar- und Ernährungswissenschaften,  
Geowissenschaften und Informatik

der Martin-Luther-Universität Halle-Wittenberg

vorgelegt von

Herrn Gideon Okpoti Tetteh  
Geb. am 19.11.1984 in Accra

Gutachter:

1. Prof. Dr. Christopher Conrad
2. Prof. Dr. Birgit Kleinschmit

Datum der Verteidigung: 30. März 2022

## **Acknowledgment**

This thesis was initiated as a result of the cooperation between the Thünen Earth Observation (ThEO) working group of the Thünen Institute and the Geocology working group of the Martin Luther University of Halle-Wittenberg. This scientific research was funded by the Thünen Institute and carried out at the Thünen Institute of Farm Economics, Braunschweig, Germany. My foremost appreciation goes to Prof. Dr. Christopher Conrad for accepting to be my first supervisor and giving me all the necessary scientific guidance. I am deeply grateful to my second supervisor, Dr. Alexander Gocht, whose meticulousness and hands-on approach to the supervision were very instrumental in shaping me as a scientific researcher.

I am thankful for the scientific support of my current work colleagues in the ThEO working group especially Dr. Stefan Erasmi and Dr. Marcel Schwieder, who were also co-authors of my second and third papers. Their in-depth comments were key to the successful publication of those papers. I am also grateful to two former colleagues (Antonia Ortmann and Ann-Kathrin Holtgrave) of the ThEO working group, with whom I shared the same office and had intriguing conversations during the formative years of the Ph.D.

My last vote of thanks goes to my siblings (Isaac Laryea Tetteh and Eugene Mensah Tetteh), my dad (Ebenezer Anum Tetteh), and most importantly my late mom (Evelyn Adotsoo Prempeh). I could not have done this without your fervent prayers, support, and encouragement. This thesis is dedicated to all of you.

## Summary

Meeting the food demands of the growing world population through the conversion of natural habitats to arable lands and the intensification of existing arable lands have negative effects on the environment including the destruction of biodiversity and an increase in greenhouse gas (GHG) emissions. Formulating policies to tackle the adverse environmental impacts of agriculture requires the development of an agricultural monitoring system. The building block of such a monitoring system is the spatial location of agricultural parcels. Agricultural parcels are useful for subsequent processes like agricultural land-use monitoring, GHG modeling, biodiversity monitoring, and the control of subsidy payments to farmers. Traditionally, agricultural parcels have been delineated through the manual digitization of orthoimages or direct field measurements. Due to the costly and inefficient nature of those approaches, alternative methods like the automated segmentation of agricultural parcels from satellite imagery are increasingly being used.

This thesis, which comprises three published papers, presents a framework for the optimal delineation of agricultural parcels from Sentinel-1 (S1) and Sentinel-2 (S2) images using the multiresolution segmentation (MRS) algorithm. The quality of the segmentation results generated with the MRS algorithm depends on the prior knowledge of which parameter (scale, shape, compactness) combination to use. With each of those three parameters taking a varying range of input values, an automated approach for determining the optimal parameter combination without evaluating all possible combinations was developed in this thesis. Further, the optimal input feature set derived from S1 and S2 images for effectively segmenting agricultural parcels was identified. For segmentation evaluation, agricultural parcels declared by farmers as part of the European Common Agricultural Policy (CAP) framework were used as reference parcels. The federal state of Lower Saxony, Germany was used as the study area in this thesis.

In the first paper (Chapter 3), a supervised approach was used to identify the optimal MRS parameters. To efficiently determine the optimal parameters, Lower Saxony was divided into tiles. The visible (red, green, blue) and near-infrared bands were extracted from S2 and then clipped to those tiles. Before segmenting those tiled images, all non-agricultural areas were masked out. To identify the optimal parameters for each tile, Bayesian optimization was combined with an area-weighted Jaccard index. Jaccard index, which is popularly known as Intersection over Union (IoU), was used in measuring the geometric similarity between the segmented objects and the reference parcels.

Due to the difficulties and costs often associated with obtaining reference data over large geographical areas, an unsupervised optimization approach that does not require reference parcels was developed in the second paper (Chapter 4) to identify the optimal parameters from the S2 images. An unsupervised evaluation metric for measuring the quality of segmentation was proposed and combined with the Bayesian optimization

approach developed in Chapter 3. This unsupervised optimization approach was tested on some selected tiles in Lower Saxony. The segmentation outcome of this unsupervised optimization approach was compared to the supervised results obtained in Chapter 3.

The third paper (Chapter 5) focused on identifying the optimal feature set derived from the S1 and S2 images for optimally segmenting the agricultural parcels. In contrast to Chapters 3 and 4, here, monthly mean composites (MMCs) of S1 and S2 were used. Various band indices were computed from the MMCs. Based on the MMCs and the band indices, different feature sets were generated. To efficiently identify the optimal feature set, some test tiles were selected and the supervised Bayesian optimization approach that was developed in Chapter 3 was accordingly applied.

Unlike most existing studies that focused on optimizing only the scale parameter, the results obtained in Chapters 3 and 4 proved that to optimally segment agricultural parcels, all three MRS parameters must be optimized. Although unsupervised optimization is often used in the literature, the outcome of Chapter 4 showed that supervised optimization yields higher segmentation accuracies. Beyond the optimization approaches, Chapter 5 highlighted the importance of optimizing the input data to optimally segment the agricultural parcels. The best segmentation results were achieved through the synergistic use of multitemporal S1 and S2 band indices. Using this dataset, all agricultural parcels in Lower Saxony were segmented. A further analysis of the segmented agricultural parcels revealed the following segmentation accuracies: 27.02% for very small parcels (< 0.5 ha), 57.65% for small parcels (0.5 – 1.5 ha), 75.71% for medium parcels (1.5 ha – 15 ha), and 68.31% for large parcels (> 15 ha).

Two potential uses of the segmented agricultural parcels were highlighted in this thesis. First, the role that image segmentation could play in the monitoring of CAP was shown in the results of Chapter 3. For farmers in the European Union (EU) to access the subsidies provided within the CAP framework, they have to make annual declarations including the boundaries of their agricultural parcels. To ensure the correct distribution of the subsidies, the declarations of the farmers are verified by the National Control and Paying Agencies (NCPAs) of the EU countries. The results of this thesis showed that image segmentation could help in this verification process by flagging potentially non-compliant geometry declarations of the farmers. Second, the use of the segmentation results for generating an object-based crop-type map was demonstrated in Chapter 5, where the segmented agricultural parcels of Lower Saxony were spatially overlaid on an existing pixel-based crop-type map and then majority filtering was applied. The creation of this object-based crop-type map led to an improvement in the classification accuracy by 3.4 percentage points. Based on McNemar's test, the difference between the pixel-based map and the object-based map was found to be statistically significant ( $p$ -value < 0.01). Overall, this thesis shows how to optimally delineate agricultural parcels from satellite images, which will be useful for developing or improving agricultural monitoring systems.

## **Zusammenfassung**

Die Deckung des Nahrungsmittelbedarfs der wachsenden Weltbevölkerung durch die Umwandlung natürlicher Lebensräume in Ackerland und die Intensivierung der Nutzung von bestehenden Ackerflächen hat negative Auswirkungen auf die Umwelt, einschließlich der Zerstörung der biologischen Vielfalt und eines Anstiegs der Treibhausgasemissionen (THG). Die Formulierung von Maßnahmen zur Bekämpfung der negativen Umweltauswirkungen der Landwirtschaft erfordert die Entwicklung eines landwirtschaftlichen Monitoringsystems. Der Grundbaustein eines solchen Monitoringsystems ist die räumliche Lage der landwirtschaftlichen Parzellen. Landwirtschaftliche Parzellen sind nützlich für nachfolgende Prozesse wie die Kartierung der landwirtschaftlichen Flächennutzung, die Modellierung von Treibhausgasemissionen, die Beobachtung der biologischen Vielfalt und die Kontrolle von Subventionszahlungen an Landwirte. Traditionell wurden landwirtschaftliche Parzellen durch die manuelle Digitalisierung von Orthobildern oder direkte Feldmessungen abgegrenzt. Da diese Verfahren kostspielig und ineffizient sind, werden zunehmend alternative Methoden wie die automatische Segmentierung landwirtschaftlicher Parzellen aus Satellitenbildern eingesetzt.

In dieser Dissertation, die drei wissenschaftliche Veröffentlichungen umfasst, wird ein Rahmen für die optimale Abgrenzung landwirtschaftlicher Parzellen aus Sentinel-1- (S1) und Sentinel-2- (S2) Daten unter Verwendung des Multiresolution Segmentation (MRS) Algorithmus vorgestellt. Die Qualität der mit dem MRS-Algorithmus erzielten Segmentierungsergebnisse hängt von einer optimierten Kombination der Parameter „Scale“, „Shape“ und „Compactness“ ab. Da jeder dieser drei Parameter einen unterschiedlichen Bereich von Eingabewerten annehmen kann, wurde in dieser Dissertation ein automatisierter Ansatz zur Bestimmung der optimalen Parameterkombination entwickelt, bei dem nicht alle möglichen Parameterkombinationen evaluiert werden müssen. Außerdem wurde der optimale Inputdatensatz aus S1- und S2-Bildern für eine effektive Segmentierung landwirtschaftlicher Parzellen ermittelt. Für die Bewertung der Segmentierung wurden die von den Landwirten im Rahmen der Gemeinsamen Europäischen Agrarpolitik (GAP) angemeldeten landwirtschaftlichen Parzellen als Referenzparzellen verwendet. Als Untersuchungsgebiet wurde in dieser Dissertation das Bundesland Niedersachsen in Deutschland gewählt.

In der ersten Veröffentlichung (Kapitel 3) wurde ein überwachter Ansatz verwendet, um die optimalen MRS-Parameter zu ermitteln. Um die optimalen Parameter effizient zu bestimmen, wurde Niedersachsen in einzelne Kacheln unterteilt. Die sichtbaren (rot, grün, blau) sowie die Nahinfrarot-Bänder wurden aus S2 extrahiert und dann auf diese Kacheln beschnitten. Vor der Segmentierung dieser Kachelbilder wurden alle nicht landwirtschaftlich genutzten Flächen ausmaskiert. Um die optimalen Parameter für jede Kachel zu ermitteln, wurde die Bayessche Optimierung mit einem flächengewichteten Jaccard-Index kombiniert. Der Jaccard-Index, der allgemein als Intersection over Union (IoU) bekannt ist, wurde zur Messung der geometrischen Ähnlichkeit zwischen den segmentierten Objekten und den Referenzparzellen verwendet.

Aufgrund der Schwierigkeiten und Kosten, die häufig mit der Beschaffung von Referenzdaten über große geografische Gebiete verbunden sind, wurde in der zweiten Veröffentlichung (Kapitel 4) ein unüberwachter Optimierungsansatz entwickelt, der keine Referenzparzellen benötigt, um die optimalen Parameter anhand der S2-Bilder zu ermitteln. Es wurde eine unüberwachte Bewertungsmetrik zur Messung der Segmentierungsqualität entwickelt und mit dem entwickelten Bayesschen Optimierungsansatz aus Kapitel 3 kombiniert. Dieser unüberwachte Optimierungsansatz wurde an einigen ausgewählten Kacheln in Niedersachsen getestet. Das Segmentierungsergebnis dieses unüberwachten Optimierungsansatzes wurde mit den überwachten Ergebnissen aus Kapitel 3 verglichen.

Die dritte Veröffentlichung (Kapitel 5) konzentrierte sich auf die Ermittlung des optimalen Inputdatensatzes aus den S1- und S2-Bildern, um die landwirtschaftlichen Parzellen optimal zu segmentieren. Im Gegensatz zu den Kapiteln 3 und 4 wurden hier Monatsmittelwerte (MMCs) von S1 und S2 verwendet. Aus den MMCs wurden verschiedene Band-Indizes errechnet. Aus diesen MMCs und Bandindizes wurden verschiedene Inputdatensätze erstellt. Zur effizienten Ermittlung des optimalen Inputdatensatzes wurden einige Testkacheln ausgewählt und der in Kapitel 3 entwickelte überwachte Bayessche Optimierungsansatz entsprechend angewandt.

Im Gegensatz zu den meisten bisherigen Studien, die sich hauptsächlich auf die Optimierung des „Scale“-Parameters konzentrierten, haben die in den Kapiteln 3 und 4 erzielten Ergebnisse gezeigt, dass für eine optimale Segmentierung landwirtschaftlicher Parzellen alle drei MRS-Parameter optimiert werden müssen. Obwohl in der Literatur häufig die unüberwachte Optimierung verwendet wird, zeigten die Ergebnisse aus Kapitel 4, dass die überwachte Optimierung zu einer höheren Segmentierungsgenauigkeit führt. Neben den Optimierungsansätzen wurde in Kapitel 5 die Bedeutung der Eingabedaten für eine optimale Segmentierung der landwirtschaftlichen Parzellen hervorgehoben. Die besten Segmentierungsergebnisse wurden durch die synergetische Verwendung von multitemporalen S1- und S2-Bandindizes erzielt. Anhand dieses Datensatzes wurden alle landwirtschaftlichen Parzellen in Niedersachsen segmentiert. Eine weitere Analyse der segmentierten landwirtschaftlichen Parzellen ergab die folgenden Segmentierungsgenauigkeiten: 27,02 % für sehr kleine Parzellen (< 0,5 ha), 57,65 % für kleine Parzellen (0,5 – 1,5 ha), 75,71 % für mittlere Parzellen (1,5 ha – 15 ha) und 68,31 % für große Parzellen (> 15 ha).

In dieser Dissertation wurden zwei potenzielle Verwendungsmöglichkeiten der segmentierten landwirtschaftlichen Parzellen hervorgehoben. Erstens wurde mit den Ergebnissen aus Kapitel 3 gezeigt, welche Rolle die Bildsegmentierung bei der Überwachung der GAP spielen könnte. Damit die Landwirte in der Europäischen Union (EU) die im Rahmen der GAP bereitgestellten Subventionen in Anspruch nehmen können, müssen sie jährliche Erklärungen abgeben, in denen sie die Grenzen ihrer landwirtschaftlichen Parzellen angeben. Um die korrekte Verteilung der Subventionen zu gewährleisten, werden die Erklärungen der Landwirte von den

Nationalen Kontroll- und Zahlstellen (NCPAs) der EU-Länder überprüft. Die Ergebnisse dieser Dissertation haben gezeigt, dass die Bildsegmentierung bei diesem Überprüfungsprozess helfen kann, indem sie potenziell nicht konforme Geometrieangaben der Landwirte kennzeichnet. Zweitens wurde in Kapitel 5 die Nutzung der Segmentierungsergebnisse zur Erstellung einer objektbasierten Ackerkulturkarte demonstriert, indem die segmentierten landwirtschaftlichen Parzellen Niedersachsens räumlich mit einer bestehenden pixelbasierten Ackerkulturkarte überlagert und anschließend eine Mehrheitsfilterung vorgenommen wurde. Die Erstellung dieser objektbasierten Ackerkulturkarte führte zu einer Verbesserung der Klassifikationsgenauigkeit um 3,4 Prozentpunkte. Anhand des McNemar-Tests konnte festgestellt werden, dass der Unterschied zwischen der pixelbasierten Karte und der objektbasierten Karte statistisch signifikant ist ( $p$ -Wert  $< 0,01$ ). Insgesamt zeigt diese Dissertation, wie landwirtschaftliche Parzellen anhand von Satellitenbildern optimal abgegrenzt werden können, was für die Entwicklung oder Verbesserung landwirtschaftlicher Monitoringsysteme von Nutzen sein wird.

## Table of contents

Acknowledgment.....	I
Summary .....	II
Zusammenfassung .....	IV
Table of contents .....	VII
List of Abbreviations.....	VIII
1 Introduction .....	1
1.1 Motivation .....	1
1.2 Algorithms for segmenting agricultural fields.....	2
1.3 Multiresolution segmentation (MRS).....	5
1.3.1 Algorithm description.....	5
1.3.2 Parameter optimization.....	7
1.4 Impact of input data on image segmentation.....	8
1.5 Research goals and objectives .....	9
1.6 Structure of the thesis .....	9
2 Overview of methodology.....	10
3 Optimal parameters for delineating agricultural parcels from satellite images based on supervised Bayesian optimization .....	12
4 Unsupervised parameterization for optimal segmentation of agricultural parcels from satellite images in different agricultural landscapes.....	28
5 Evaluation of Sentinel-1 and Sentinel-2 feature sets for delineating agricultural fields in heterogeneous landscapes.....	56
6 Discussion .....	75
6.1 Optimization of the data preparation .....	75
6.2 Optimization of the MRS algorithm.....	76
6.3 Optimization of the input data.....	77
6.4 Spatial distribution of the optimal parameters.....	78
6.5 Application of identified optimal parameters.....	83
6.6 Potential usage of the segmentation results .....	84
6.6.1 Object-based crop-type mapping.....	84
6.6.2 Verification of the GSAA parcels .....	85
6.6.3 Essential agricultural variables.....	86
6.7 Limitations of this thesis .....	87
7 Conclusions .....	88
References .....	89
Curriculum vitae.....	97
List of publications.....	98
Eidesstattliche Erklärung / Declaration under Oath .....	99

## List of Abbreviations

AD	Absolute difference
ARD	Analysis-ready data
ARD (Chapter 3)	Automatic relevance determination
ATKIS	German Official Topographic Cartographic Information System
BKG	German Federal Agency for Cartography and Geodesy
BOA	Bottom-Of-Atmosphere
BRDF	Bidirectional reflectance distribution function
BS	Backscatter
CAP	Common Agricultural Policy
CARD	Copernicus Analysis Ready Data
CbM	Checks by monitoring
CLAHE	Contrast limited adaptive histogram equalization
CLI	Command-line interface
CNN	Convolutional neural network
CR	Cross Ratio
DEM	Digital Elevation Model
DLM	Digital Landscape Model
DNN	Deep neural network
DTW	Dynamic time warping
DWT	Dyadic wavelet transformation
EAV	Essential agricultural variable
EC	European Commission
ED	Euclidean Distance
EFA	Ecological focus area
EI	Expected improvement
EPSG	European Petroleum Survey Group
ESA	European Space Agency
ESP	Estimation of Scale Parameters
ETM	Enhanced Thematic Mapper
EU	European Union
EV	Essential variable
FCIS	Fully Convolutional Instance-aware Semantic Segmentation
FCN	Fully convolutional neural network
FORCE	Framework for Operational Radiometric Correction for Environmental monitoring

## List of Abbreviations

GCOS	Global Climate Observing System
GEO BON	Group on Earth Observations Biodiversity Observation Network
GEOGLAM	Group on Earth Observations Global Agricultural Monitoring Initiative
GHG	Greenhouse gas
GP	Gaussian Process
GRD	Ground Range Detected
GS	Global score
GSAA	Geospatial Aid Application
GVI	Green Vegetation Index
IACS	Integrated Administration and Control System
ISODATA	Iterative Self-Organizing Data Analysis Technique
IW	Interferometric Wide Swath
JRC	Joint Research Centre
L-BFGS	Limited Broyden–Fletcher–Goldfarb–Shanno
LC	Land-cover
LOESS	Locally estimated scatterplot smoothing
LPIS	Land Parcel Identification System
LU	Land-use
LV	Local variance
MBR	Minimum bounding rectangle
MI	Moran's I
MMC	Monthly mean composite
MRS	Multiresolution segmentation
NCPA	National Control and Paying Agency
NDRE	Normalized Difference Red Edge Index
NDSVI	Normalized Differential Senescent Vegetation Index
NDTI	Normalized Difference Tillage Index
NDVI	Normalized difference vegetation index
NDWI	Normalized Difference Water Index
NIR	Near-infrared
OBIA	Object-based image analysis
OLI	Operational Land Imager
OR	Over-segmentation
OSM	Open Street Map
OSQ	Overall segmentation quality
OSS	Open-source software

## List of Abbreviations

OTSC	On-the-spot check
PCA	Principal component analysis
QR	Quality rate
RBF	Radial basis function
RF	Random Forest
RMS	Root mean square
RS	Remote sensing
RVI	Radar Vegetation Index
S1	Sentinel-1
S2	Sentinel-2
SAA	Segmentation accuracy assessment
SCG	Single-scale Combinatorial Grouping
SDG	Sustainable Development Goal
SF	Shape factor
SLIC	Simple Linear Iterative Clustering
SMBO	Sequential model-based optimization
SNAP	Sentinel Application Platform
SNIC	Simple Non-Iterative Clustering
SPOT	Satellite for observation of Earth
SSE	Supervised segmentation evaluation
SSO	Supervised segmentation optimization
SWIR	Short-wave infrared
TCT	Tasseled cap transformation
TM	Thematic Mapper
TT	Test tile
UR	Under-segmentation
USE	Unsupervised segmentation evaluation
UTM	Universal Transverse Mercator
VNIR	Visible (red, green, blue) and near-infrared
VRGAC	Variational region-based geometric active contour
WV	Weighted variance

# 1 Introduction

## 1.1 Motivation

Meeting the food demands of the growing world population while minimizing the negative impact of agricultural production on the environment requires the use of sustainable agricultural practices (Adams and Eswaran, 2000; Dudley and Alexander, 2017; Foley et al., 2011). Within the European Union (EU), the most prominent policy framework targeted at ensuring sustainable agriculture is the Common Agricultural Policy (CAP). Among others, CAP aims at increasing agricultural productivity within the EU through the use of sustainable agricultural practices while ensuring a decent standard of living for farmers (European Commission, 2021a). A substantial part of the CAP budget goes into the direct payment of subsidies to farmers (European Commission, 2021a). To receive the CAP subsidies, farmers within the EU have to make annual declarations including the geometry (boundary) of their agricultural parcels and the land-use (LU) type per parcel. Before the subsidies are paid to the farmers, their declarations are first verified by the National Control and Paying Agencies (NCPAs) of the EU countries. To check the declarations, each NCPA is required to set up and operate an Integrated Administration and Control System (IACS) (European Commission, 2013). Three key components of the IACS are the Land Parcel Identification System (LPIS), Geospatial Aid Application (GSAA), and on-the-spot checks (OTSCs). LPIS is a reference system for geolocating and identifying all agricultural parcels eligible for subsidy payment. Based on the LPIS and very high-resolution orthoimages with a spatial resolution of at least 1 m, the farmers digitize the actual boundaries of their agricultural parcels and then indicate the existing LU type (e.g., mowing pasture, meadow, maize, winter wheat, etc.) through the GSAA. Out of all the declarations, 5% are randomly selected and then checked by the NCPAs using OTSCs via computer-aided photo-interpretation of very high-resolution images or direct on-site measurements.

Due to the cumbersome nature of the OTSCs, the European Commission (EC) introduced checks by monitoring (CbM) in 2018 to substitute OTSCs (European Union, 2018). With CbM, the datasets of the European Copernicus program like Sentinel-1 (S1) and Sentinel-2 (S2) could be used to verify the declarations of all farmers. The introduction of CbM has triggered numerous studies (Campos-Taberner et al., 2019; d'Andriamont et al., 2018; López-Andreu et al., 2021; Lozano-Tello et al., 2021; Rousi et al., 2021; Sarvia et al., 2021; Sitokonstantinou et al., 2018) that have largely focused on the classification of S1 and/or S2 images as a means of verifying the LU types declared by the farmers. The potential of S1 and S2 for verifying the geometry declarations of the farmers is yet to be explored. While the spatial resolutions of S1 (20 m) and S2 (10 m) do not allow for the direct verification of the geometries of the declared agricultural parcels, they can still be used in flagging instances where the geometry of a declared agricultural parcel does not represent the real situation existing on the ground. For example, a farmer may own an agricultural field composed of several agricultural parcels with different LU types. One agricultural parcel can be used to cultivate maize and an

adjacent parcel may contain grass. During the declaration process, the farmer may inadvertently declare the agricultural field instead of the individual agricultural parcels within the field representing the different LU types. The S1 and S2 images can be used to flag the disparities between the declared agricultural parcel and the real-world situation. Image segmentation, which is the process of partitioning an image into homogeneous and distinct objects (Blaschke, 2010), can be used to automatically delineate the boundaries of agricultural parcels representing single LU types from S1 and S2 images. Those extracted segments can then be compared to the declared agricultural parcels to identify any disparities.

From here onwards, an agricultural field and an agricultural parcel will be interchangeably used to mean any agricultural land with a single LU type worked by a single farmer. Beyond their critical role within CAP, agricultural fields are also essential agricultural variables (Whitcraft et al., 2019) that can be used for object-based crop classification. The quality of agricultural fields delineated from satellite images through image segmentation and subsequently used for object-based crop classification can have a significant impact on the accuracy of the classification results. It was proved in numerous studies (Akçay et al., 2018; Gao et al., 2011; Georganos et al., 2018b, 2018a; Liu and Xia, 2010) that the quality of the image segmentation results directly impacts the classification accuracy. Therefore, there is value in pursuing the optimal segmentation of agricultural fields from S1 and S2 images. This thesis takes a novel and holistic approach to the optimal segmentation of agricultural fields by looking at both the parameter optimization of the segmentation algorithm and the optimization of the input data given to the segmentation algorithm.

### **1.2 Algorithms for segmenting agricultural fields**

Traditionally, agricultural fields have been delineated through the manual digitization of hardcopy maps (aerial images, topographic maps, etc.) (Ji, 1996) or direct field measurements. A more efficient and cost-effective approach is the automated delineation of the fields from remote sensing (RS) images. Through RS, spatially explicit and timely information about agricultural fields over wide geographical areas like regions, countries, and continents could be efficiently obtained. One method that can be used to obtain this information from RS images is image segmentation. Different image segmentation algorithms have been proposed in the literature for extracting agricultural fields from RS images. The algorithms can be categorized into four main groups.

The first category is based on edge detection. In an image, edges serve as transitions between different objects (Ji, 1996; Martin et al., 2004). The edge-based methods first apply edge filtering to an image to identify edges and then apply post-processing to connect the edges to create complete boundaries. Ji (1996) used dyadic wavelet transformation (DWT) (Mallat and Zhong, 1992) to extract edges of agricultural fields from Landsat Thematic Mapper (TM) images acquired in the Guangdong Province of southeast China. The DWT was separately applied to the near-infrared (NIR) band, normalized difference vegetation index (NDVI), and the wetness index of the tasseled cap transformation (TCT). The edges extracted from the three DWT

transformations were then consolidated to generate the final map. The consolidation resulted in closed polygons but there were some instances of isolated edges. To deal with those cases, the authors suggested the use of manual digitization. To delineate sub-fields within already identified agricultural fields, Turker and Kok (2013) applied the Canny edge detector (Canny, 1987) to first identify edges from SPOT images observed in the Marmara region of Turkey. The detected edges were then linked to create complete polygons through perceptual grouping. Based on multitemporal Landsat images acquired in an area south of the Amazon River and north of Patagonia in South America, Graesser and Ramankutty (2017) proposed a field delineation approach that consisted of edge extraction with pre-defined convolution filters, contrast limited adaptive histogram equalization (CLAHE), adaptive thresholding, and morphological cleaning. To delineate agricultural fields in the Mid-Canterbury plains of New Zealand, North et al. (2019) initially used a circular window filter with a diameter of five pixels to calculate the local standard deviation at each pixel location in the red, NIR, and short-wave infrared (SWIR) bands of seven dates of SPOT images. The standard deviation images were combined to create an edge map. Directional convolution filters were then applied to this edge map to obtain linear features (field boundaries). In a more recent study, Wagner and Oppelt (2020) used the Sobel operator to detect edges from S2 images in Schleswig-Holstein, Germany. To extract the agricultural fields from the extracted edges, they applied a modified version of the active contour model (Kass et al., 1988).

The second category comprises the region-based methods. This category can further be classified into region growing, and region splitting and merging (Hossain and Chen, 2019; Kotaridis and Lazaridou, 2021). For region growing, pixels are used as seed points and in subsequent steps, similar nearby objects are merged based on a homogeneity criterion. With region splitting and merging, the image is first partitioned into arbitrary objects and in iterative steps, objects are split or merged to create more homogenous objects. In RS, the region growing methods are more commonly used than the region splitting and merging methods for extracting agricultural fields. Evans et al. (2002) combined morphological filtering and local canonical transformation to identify seed points for seeded region growing (Adams and Bischof, 1994) to generate agricultural fields from Landsat TM images near Esperance in Western Australia. A supervised approach was employed by García-Pedrero et al. (2017) to delineate agricultural fields from a WorldView-2 image acquired in the Chilean central valley. The Simple Linear Iterative Clustering (SLIC) (Achanta et al., 2012) algorithm was first applied to generate over-segmented fields. To identify which neighboring fields to merge, a supervised classifier named RUSBoost (Seiffert et al., 2010) was used. Agricultural fields extracted with the mean shift algorithm (Fukunaga and Hostetler, 1975) from NDVI temporal profiles generated from S2 images were used by Nasrallah et al. (2018) to classify wheat areas in the Bekaa plain of Lebanon. Csillik et al. (2019) used the multiresolution segmentation (MRS) (Batz and Schäpe, 2000) algorithm to segment agricultural fields from multitemporal S2 images at two test areas in Southern California and Northwestern Texas. The segments were used as an input to a dynamic time warping (DTW) classification routine. Using an improved version of SLIC named Simple Non-Iterative Clustering (SNIC) (Achanta and Susstrunk, 2017), Luo et al. (2021)

segmented agricultural areas from a time-series of S1 images in Heilongjiang Province, China, and later performed crop-type classification using Random Forest (RF).

The third category is a hybrid approach. The output of an edge detection algorithm is passed as an input to a region-based method to create the objects. A gradient edge detector was combined with the Iterative Self-Organizing Data Analysis Technique (ISODATA) clustering (Ball and Hall, 1965) algorithm by Rydberg and Borgefors (2001) to delineate agricultural fields from Landsat TM and SPOT images acquired in an area in Västra Götaland, Sweden. Based on multidimensional dilation and erosion (Plaza et al., 2002), Li and Xiao (2007) extracted a gradient magnitude image from a SPOT image of an agricultural area in Hengshui, China, and subsequently applied a watershed transformation to delineate the fields. To segment crop fields in Texas, California, and South Dakota, Yan and Roy (2014) extracted a crop probability map and a crop field edge probability map from a five-year time-series of Landsat 7 Enhanced Thematic Mapper Plus (ETM+) images and passed them to a variational region-based geometric active contour (VRGAC) (Chan and Vese, 2001) method to create a candidate field map. A watershed algorithm was then applied to decompose connected segments in the candidate field map to create distinct crop fields. Based on a Canny edge detector and an implementation of the watershed algorithm in eCognition (Trimble Germany GmbH, 2019), agricultural fields were delineated from multitemporal S2 images in South Africa (Watkins and van Niekerk, 2019a, 2019b).

The last category is based on Deep Neural Networks (DNNs). This category is based on supervised learning. Hence, reference data is required. Within this category, two approaches are distinguishable. The first approach involves the use of a fully convolutional neural network (FCN) for semantic segmentation (Long et al., 2015), followed by post-processing to generate the final segments. To segment agricultural fields in small-holder farms from WorldView-2 and -3 images captured in Mali and Nigeria, Persello et al. (2019) treated the task as a binary classification problem to distinguish between boundary pixels and non-boundary pixels. The output generated after applying SegNet (Badrinarayanan et al., 2017) to the images produced fragmented contours. The oriented watershed transform and agglomerative clustering procedure of Arbeláez et al. (2011) and Single-scale Combinatorial Grouping (SCG) (Pont-Tuset et al., 2017) were then employed to generate the final segmentation output. Instead of two classes, García-Pedrero et al. (2019) created three classes: background, agricultural plots, and buffered boundaries of the agricultural plots. They then trained a U-Net (Ronneberger et al., 2015) model using orthorectified aerial images and LPIS of the Chartered Community of Navarre, Spain to predict those three classes in new images. As their main post-processing strategy, instead of just applying the trained model to an input image, eight different transformations were first applied to the input image before the prediction was done with the trained model. The final segmentation was obtained as the arg max of the sum of predicted probabilities. The authors noted that there were several instances where incomplete fields were created. Just like Persello et al. (2019), Yang et al. (2020) also treated the field

delineation as a binary classification problem but no post-processing was used. They simply evaluated U-Net, SegNet, and DenseNet (Huang et al., 2017) for detecting the agricultural field boundaries from a WorldView-3 image in the Patuakhali district of Bangladesh. Their results showed that DenseNet outperformed the other models. Waldner and Diakogiannis (2020) applied ResUNet-a (Diakogiannis et al., 2020) to S2 images covering test sites in South Africa, Argentina, Australia, Canada, Russia, and Ukraine to generate these outputs: an extent mask, boundary probability mask, and distance mask. They subsequently tested two post-processing methods to retrieve the agricultural fields. The first method creates two binary masks by thresholding the extent mask and boundary probability mask and then computes the symmetric difference between the two binary masks to generate closed fields. The second method applies thresholding to the extent, boundary probability, and distance masks before using them as inputs to watershed segmentation. The second approach within this last category is based on instance segmentation, which is a combination of semantic segmentation and object recognition. Without any post-processing, the algorithms belonging to this second approach directly yield objects. Based on S2 images and the LPIS dataset of test sites in central Denmark, Rieke (2017) trained the Fully Convolutional Instance-aware Semantic Segmentation (FCIS) architecture proposed by Li et al. (2016) to directly segment agricultural fields. A combination of orthophotos, Landsat 8 images, and ground truth data was used by Lv et al. (2020) to train Mask R-CNN (He et al., 2017) to segment agricultural plots in the smallholder agricultural areas in Da'an City, Jilin Province, China.

Amongst the four categories presented above, the region-based methods are the most popular primarily due to the frequent use of the MRS algorithm in eCognition (Kotaridis and Lazaridou, 2021). Kotaridis and Lazaridou (2021) observed that 65% of the 122 research papers they reviewed used eCognition, while Ma et al. (2017) observed that number to be 80.9% of the 254 studies they reviewed. The frequent use of the MRS algorithm can be attributed to its superiority over other algorithms as was demonstrated in several studies (Kavzoglu and Tonbul, 2018, 2017; Marpu et al., 2010; Neubert et al., 2008). In the study of Reis et al. (2015), it was observed that the implementation of the MRS algorithm in eCognition achieved better results than the implementation of the same algorithm in an open-source software named InterIMAGE (InterImage, 2014). Therefore, in this thesis, the MRS algorithm in eCognition was used for image segmentation. The description of the MRS algorithm is explained in the next section.

### **1.3 Multiresolution segmentation (MRS)**

#### **1.3.1 Algorithm description**

The description of the MRS algorithm presented here is based on the summarized explanations of Benz et al. (2004) and Huang et al. (2020). The MRS algorithm starts with well-distributed pixels in an image as seed objects. In numerous steps, the algorithm identifies and merges object pairs that result in the lowest change in heterogeneity. The definition of heterogeneity is very critical to the MRS algorithm just like any other region growing or merging algorithm (Hossain and Chen, 2019). For the MRS algorithm, the heterogeneity

of each object is computed as a linear combination of the shape and color heterogeneity of that object (Eq. 1);

$$h = w_1 h_{shape} + w_2 h_{color} \quad (1)$$

where  $h_{shape}$  is the shape heterogeneity,  $h_{color}$  is the color heterogeneity, and  $w_1$  and  $w_2$  are the corresponding weights. The weights sum up to 1. The shape heterogeneity is computed as a function of the compactness and smoothness of the object (Eq. 2);

$$h_{shape} = w_3 \frac{l}{\sqrt{n}} + w_4 \frac{l}{b} \quad (2)$$

where  $l$  is the perimeter of the object,  $b$  is the perimeter of the object's bounding box, and  $n$  is the number of pixels in that object. The compactness and smoothness of the object are respectively represented by  $l/\sqrt{n}$  and  $l/b$ , with  $w_3$  and  $w_4$  being their corresponding weights. Here as well, the weights sum up to 1. The computation of the color heterogeneity is shown in Eq. 3;

$$h_{color} = \sum_{i=1}^x n(c_i \sigma_i) \quad (3)$$

where  $x$  is the number of bands in the image,  $n$  is the number of pixels per object,  $c_i$  is the weight of the  $i$ th band, and  $\sigma_i$  is the standard deviation within the object for the  $i$ th band. The change in heterogeneity between two objects is then computed by Eq. 4;

$$\Delta h = (n_1 + n_2)h_m - (n_1 h_1 + n_2 h_2) \quad (4)$$

where  $h_1$  and  $h_2$  are the computed heterogeneity values for two neighboring objects,  $h_m$  is the heterogeneity value of their combined geometries, and  $n_1$  and  $n_2$  represent the respective number of pixels in the two objects. The neighboring object pair that minimizes the change in heterogeneity (Eq. 4) are considered to be optimal and subsequently merged into one.

The outcome of the MRS algorithm is dictated by the user-given weights ( $w_1, w_2, w_3, w_4, c_i$ ) and scale parameters. In eCognition, amongst the weights, the user can only input shape ( $w_1$ ) and compactness ( $w_3$ ). The color weight ( $w_2$ ) is automatically calculated as  $(1 - w_1)$ , while the smoothness weight ( $w_4$ ) is computed as  $(1 - w_3)$ . The scale parameter is used by the MRS algorithm as the stopping criterion. The segmentation process stops as soon as the change in heterogeneity between two objects exceeds the user-given scale value.

Therefore, the scale parameter determines the average size of the objects. Determining the optimal scale, shape, and compactness values is a prerequisite to obtaining the best segmentation results using the MRS algorithm. Different parameter optimization approaches are explained in the next section.

### 1.3.2 Parameter optimization

Given a user-defined objective function and a parameter space, parameter optimization is the identification of the parameter combination that minimizes or maximizes that objective function. The conventional approach to parameter optimization is grid search. Using a set of input values per parameter, grid search generates a list of all possible combinations and then returns the evaluation score of the objective function for each combination. The combination with the minimum or maximum evaluation score is considered optimal. To optimize the MRS algorithm, grid search has been used in several studies (Conrad et al., 2010; Forkuor et al., 2014; Watkins and van Niekerk, 2019b). As the number of parameters and number of elements in each parameter space increases, grid search suffers from the *curse of dimensionality* (Bergstra and Bengio, 2012) and becomes inefficient. To overcome this limitation, random search was introduced by Bergstra and Bengio (2012). In their study, Bergstra and Bengio (2012) indicated that within a small fraction of computation time, the random search was capable of obtaining similar or better results over the same parameter space used for the grid search. However, from the studies reviewed in this thesis, random search was not used by any researcher to optimize the MRS algorithm. One flaw with grid search and random search relates to how samples are selected for evaluation with the objective function. They do not consider previous evaluations of the objective function to make an informed decision on which new parameter combinations to sample with the highest probability of optimizing the objective function. Overcoming such a flaw requires the use of sequential model-based optimization (SMBO) (Bergstra et al., 2011) methods like Bayesian optimization. Bayesian optimization is designed for globally optimizing objective functions with unknown derivatives (Frazier, 2018) and it outperforms grid search and random search (Bergstra et al., 2011; Snoek et al., 2012). Using some initially given samples, Bayesian optimization obtains the posterior probability distribution of the objective function and then uses this as the basis for choosing new samples with the highest likelihood of optimizing the objective function. Newly selected samples are sequentially used to update the posterior probability distribution. The benefits of Bayesian optimization are yet to be explored within the context of optimizing the MRS algorithm. Therefore, Bayesian optimization was adopted in this thesis to optimize the parameters of the MRS algorithm, which is novel.

To optimize any objective function, for any given parameter combination, the function must return an evaluation score as a scalar value. For image segmentation optimization, the definition of this score can be done through supervised or unsupervised segmentation evaluation. In supervised segmentation evaluation (SSE), the segmentation output of each parameter combination is compared to a reference dataset (ground truth) to compute the evaluation score, which represents the level of similarity between the segmentation result and

the reference dataset (Zhang et al., 2008). In RS, the most common SSE metrics include the quality rate (Weidner, 2008), over-segmentation (Clinton et al., 2010), under-segmentation (Clinton et al., 2010), root mean square (Weidner, 2008), and area fit index (Lucieer and Stein, 2002). Amongst those metrics, the quality rate is the most used. It is based on the Jaccard index (Jaccard, 1901), which is popularly known in computer vision as Intersection over Union (IoU). IoU is used in measuring the geometric similarity between a reference object and a target object. It was selected as the supervised evaluation score in this thesis. For unsupervised segmentation evaluation (USE), the evaluation score for each segmentation output is computed using the spectral values of the input image. This unsupervised score is indicative of the level of intra-segment uniformity and/or inter-segment dissimilarity within the segmentation output (Chabrier et al., 2006). Intra-segment uniformity can typically be measured through the variance of spectral values within each segment and inter-segment dissimilarity can be measured through spatial autocorrelation. For example, local variance values (Woodcock and Strahler, 1987) were the basis of the estimation of scale parameter (ESP) (Drăguț et al., 2014; Drăguț et al., 2010) tool, while area-weighted variance and Moran's I (MI) (Moran, 1950) were used by Espindola et al. (2006). In RS, the ESP tool and the approach of Espindola et al. (2006) are the most popular USE methods. A comparative analysis by Grybas et al. (2017) highlighted the superiority of the method of Espindola et al. (2006) to the ESP tool. Various variations of the method of Espindola et al. (2006) exist in the literature (Böck et al., 2017; Chen et al., 2014; Georganos et al., 2018a; Johnson and Xie, 2011; Johnson et al., 2015; Kim et al., 2008; Martha et al., 2011; Yang et al., 2019). In this thesis, the global score of Espindola et al. (2006) was modified and used as the unsupervised evaluation score.

#### **1.4 Impact of input data on image segmentation**

To segment agricultural fields from satellite images, most authors use existing segmentation algorithms, some propose new segmentation algorithms, and others propose new segmentation parameter optimization approaches. A lot of attention has not been given to the determination of the optimal feature set for segmenting agricultural fields. In experimenting with a WorldView-2 image, Mesner and Oštir (2014) observed that the feature set used as input to the image segmentation algorithm influences the accuracy of the segmentation result. To segment agricultural fields from S1, the VV and VH bands are mostly used as was done in these studies (Clauss et al., 2018; Luo et al., 2021). For S2, most authors (Belgiu and Csillik, 2018; Csillik et al., 2019; Vogels et al., 2019; Waldner and Diakogiannis, 2020; Watkins and van Niekerk, 2019a, 2019b) used only the visible (red, green, blue) and near-infrared (NIR) bands. The creation of different S1 and S2 feature sets and the evaluation of the impact of those feature sets on the segmentation accuracy of agricultural fields are yet to be comprehensively explored. The S1 and S2 sensors have different bands. Additionally, new features like band indices can be calculated from those bands. Therefore, it is worth exploring the impact of different S1 and S2 feature combinations on the segmentation accuracy of agricultural fields.

## 1.5 Research goals and objectives

The ultimate goal of this thesis is the optimal segmentation of agricultural fields from S1 and S2 images for all the federal states of Germany using the MRS algorithm. For experimentation purposes, the focus of this thesis was placed on the federal state of Lower Saxony as the study area. To optimally segment the agricultural fields, both the MRS parameters and input feature dataset passed to the MRS algorithm ought to be optimized. Therefore, the main objectives of this thesis are:

1. to develop a supervised approach for determining the optimal MRS parameters for segmenting agricultural fields,
2. to develop an unsupervised approach for determining the optimal MRS parameters for segmenting agricultural fields,
3. to identify the optimal input feature set for segmenting agricultural fields.

## 1.6 Structure of the thesis

This thesis is based on three peer-reviewed research papers. Chapter 1 gives an introduction to the thesis including the motivation behind the research, the state-of-the-art regarding the automated delineation of agricultural fields from satellite images, and the research goals and objectives. Chapter 2 gives a general overview of the methodologies used in this thesis. The first published paper is captured by Chapter 3. This paper deals with the first objective of this thesis. Bayesian optimization was introduced in this paper, its mathematical foundation was explained, and then together with the GSAA, a supervised approach for optimizing the MRS parameter was proposed. The supervised approach developed in the first paper requires reference data (here the GSAA) for segmentation optimization. Given that the GSAA datasets are not publicly available in all the federal states of Germany, the second paper (Chapter 4) proposed an unsupervised metric and combined it with Bayesian optimization for segmentation optimization. The second paper deals with the second objective of this thesis. The third paper, which deals with the third objective, can be found in Chapter 5. In this paper, the supervised Bayesian optimization approach developed in the first paper was applied to different feature sets generated from the S1 and S2 images to identify the feature set that generates the most accurate agricultural fields. Chapter 6 is a synthesis of the methodologies and results presented in this thesis. The chapter discusses the most significant results achieved, compares and contrasts the three research papers, highlights some potential usage of the overall outcomes of the thesis, and then points out some limitations associated with the thesis. Based on the main findings of the three papers, some conclusions are accordingly drawn in Chapter 7 and some ideas for future research are given as well.

## 2 Overview of methodology

Figure 2-1 is an integrated workflow that summarizes the methodologies used in this thesis.

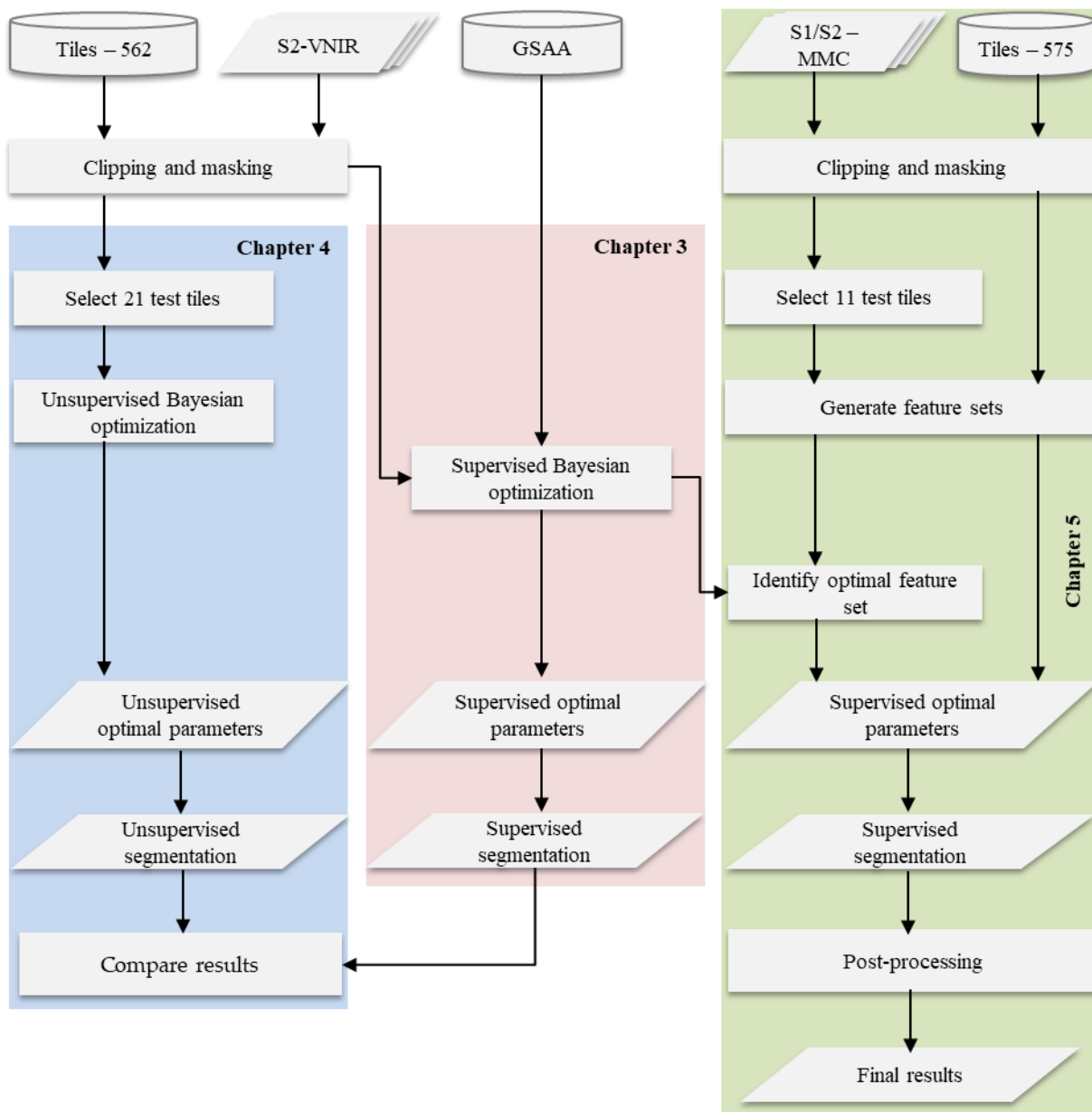


Figure 2-1. The workflow used in this thesis. VNIR stands for the visible (red, green, blue) and near-infrared (NIR) bands. MMC stands for monthly mean composite and GSAA refers to the Geospatial Aid Application.

In Chapter 3, to efficiently segment the agricultural fields, Lower Saxony was divided into 562 tiles with each tile being 10 km by 10 km. Only the visible (red, green, blue) and near-infrared (NIR) bands of S2, hereby named S2-VNIR, were used for segmentation. The S2-VNIR images of May in 2018 were first clipped to the tiles and subsequently all non-agricultural areas were masked out. To optimize the segmentation of each tiled image, Bayesian optimization was combined with an area-weighted IoU, which is calculated by geometrically

comparing extracted segments to their corresponding parcels in a reference dataset. The reference dataset used in this study was the GSAA parcels. In this thesis, LPIS and GSAA are interchangeably used to mean the reference dataset containing the agricultural parcels declared by the farmers.

In Chapter 4, 21 tiles that were representative of the other tiles in terms of landscape composition were selected as test tiles and were used as the basis to define a new USE metric. This USE metric was combined with Bayesian optimization to segment agricultural fields at the 21 tiles. The unsupervised segmentation results at those 21 tiles were compared to the supervised results achieved in Chapter 3 at those same tiles.

In Chapter 5, a new tiling system containing 575 tiles with variable sizes was created. The average size per tile is 11 km by 11 km. Here, monthly mean composites (MMCs) of S1 and S2 in 2018 were used. The MMCs were also clipped and non-agricultural areas were removed. Various band indices were calculated using the MMCs. Different feature combinations were done with the MMCs and the band indices to create different feature sets. To efficiently identify the optimal feature set, eleven test tiles were selected and the supervised optimization approach developed in Chapter 3 was applied. After identifying the optimal feature set, the segmentation optimization process was extended to the other 564 tiles in Lower Saxony. The optimal segments from the tiles were merged. The final segmentation result of 2018 for Lower Saxony was obtained by post-processing the merged segmentation result. The post-processing involved the removal of duplicate polygons and the simplification of the geometries of the polygons.

3 Optimal parameters for delineating agricultural parcels from satellite images based on supervised Bayesian optimization

### **3 Optimal parameters for delineating agricultural parcels from satellite images based on supervised Bayesian optimization**

Full bibliographic entry of paper:

Tetteh, G.O., Gocht, A., Conrad, C., 2020. Optimal parameters for delineating agricultural parcels from satellite images based on supervised Bayesian optimization. *Computers and Electronics in Agriculture* 178, 105696. <https://doi.org/10.1016/j.compag.2020.105696>



# Optimal parameters for delineating agricultural parcels from satellite images based on supervised Bayesian optimization

Gideon Okpoti Tetteh<sup>a,\*</sup>, Alexander Gocht<sup>a</sup>, Christopher Conrad<sup>b</sup>

<sup>a</sup> Thünen Institute of Farm Economics, Bundesallee 63, 38116 Braunschweig, Germany

<sup>b</sup> Martin-Luther-University Halle-Wittenberg, Institute of Geosciences and Geography, 06099 Halle, Germany

## ARTICLE INFO

### Keywords:

Agricultural parcel delineation  
Multiresolution segmentation  
Bayesian optimization  
Land parcel identification system  
Empirical segmentation evaluation

## ABSTRACT

Accurate spatial information of agricultural parcels is fundamental to any system used in monitoring greenhouse gas emissions, biodiversity developments, and nutrient loading in agriculture. The inefficiency of the traditional methods used in obtaining this information is increasingly paving the way for Remote Sensing (RS). The Multiresolution Segmentation (MRS) algorithm is a well-known method for segmenting objects from images. The quality of segmentation depends on the *a priori* knowledge of which scale, shape and compactness values to use. With each parameter taking a varied range of input values, this research developed an automated approach for identifying the optimal parameter set without testing all possible combinations. At the core of our approach is Bayesian optimization, which is a sequential model-based optimization (SMBO) method for maximizing or minimizing an objective function. We maximized the Jaccard index, which is a measure that indicates the similarity between segmented agricultural objects and their corresponding reference parcels. As the optimal parameter combination varies between different agricultural landscapes, they were determined at a grid resolution of 10 km. Mono-temporal Sentinel-2 images covering Lower Saxony in Germany were tiled to these grids and the optimal parameters were subsequently identified for each tiled grid. The optimal parameter combinations identified over the grids varied considerably, which indicated that a single parameter combination would have failed to achieve optimal segmentation. We found that the quality of segmentation correlated with the size of agricultural parcels. Under-segmentation was largely minimized but in areas with a predominant agricultural land-use, it was unavoidable. In agricultural parcels composed of heterogeneous pixels, over-segmentation was prevalent. Our approach outperformed other segmentation optimization methods existing in the literature.

## 1. Introduction

The increasing world population places enormous pressure on agricultural lands due to the growing demand for food. To meet this demand, natural habitats are being converted to farmlands, while existing farmlands are being intensively utilized (Dudley and Alexander, 2017). These conversions often lead to the destruction of biodiversity, high nutrient surpluses, and greenhouse gas emissions (Dudley and Alexander, 2017). The challenge then is to increase food production through sustainable agricultural management practices that leave minimal impact on the environment (Foley et al., 2011).

The foundation of any effective agricultural management scheme is accurate spatial information of all agricultural parcels. The most prominent agricultural parcel information system within the European Union (EU) is the Land Parcel Identification System (LPIS), which is a

spatial record of agricultural parcels declared by farmers (Taşdemir and Wirnhardt, 2012). It was established as part of the Common Agricultural Policy (CAP) framework to ensure that subsidies are correctly paid to farmers (Schmedtmann and Campagnolo, 2015). There have been suggestions by land managers to use LPIS as the foundation for developing sustainable agricultural schemes (Zielinski et al., 2008). Unfortunately, the LPIS has some drawbacks, which limits its use in an effective agricultural management scheme. Firstly, the LPIS does not record all agricultural parcels especially those with large grassland shares used for purposes like nature conservation and horse farming. This makes it difficult to monitor those parcels. Secondly, even though the LPIS is increasingly becoming available as open data in some EU countries, there is still restricted access in many countries including Germany. Thirdly, LPIS comes with a time lag, which makes in-season monitoring of parcels infeasible. In-season monitoring is critical to

\* Corresponding author.

E-mail address: [gideon.tetteh@thuenen.de](mailto:gideon.tetteh@thuenen.de) (G.O. Tetteh).

<https://doi.org/10.1016/j.compag.2020.105696>

Received 9 April 2020; Received in revised form 30 July 2020; Accepted 3 August 2020

0168-1699/© 2020 The Authors. Published by Elsevier B.V. This is an open access article under the CC BY-NC-ND license (<http://creativecommons.org/licenses/by-nc-nd/4.0/>).

understanding any emerging threats to biodiversity on agricultural lands in near real-time so that timely action can be taken to deal with those threats. Additionally, using LPIS requires a lot of pre-processing effort due to different technical implementations between different regions and countries within the EU. These drawbacks inhibit various agricultural bodies including public institutions from making use of the LPIS as source data for developing real-world agronomic and environmental applications.

An automated system for generating a spatial database of all agricultural parcels could provide a solution to these drawbacks. With satellite data becoming more accessible, Remote Sensing (RS) presents the best means of obtaining cost-effective, accurate and up-to-date information of agricultural parcels due to its ability to obtain information over large areas with a high repetition rate (Atzberger, 2013). The launch and subsequent provision of free data by the Sentinel-2 satellites provide us a unique opportunity to obtain spatial information on agricultural parcels at a high spatial resolution over large geographical areas. The use of Sentinel-2 data for obtaining information on agricultural parcels is an active area of research as depicted by these studies (Belgiu and Csillik, 2018; Immitzer et al., 2016; Nasrallah et al., 2018; Watkins and Van Niekerk, 2019). The main limitation of those studies is that their respective methodologies were applied to small test areas and not geographic regions. One commonality amongst them is the use of object-based image analysis (OBIA), where spectrally similar pixels are grouped into homogenous objects through image segmentation and then the land-use type of each object is determined through object classification. A successful image segmentation process is the most critical step in this OBIA paradigm (Baatz and Schäpe, 2000; Benz et al., 2004).

Various algorithms have been developed to segment agricultural parcels from satellite images. The first category of algorithms is based on edge detection. They involve the extraction of edges and the subsequent linking of those edges to form boundaries. Turker and Kok (2013) and Ji (1996) applied edge-based methods to extract agricultural fields from SPOT and Landsat images respectively. The edge-based methods generate incomplete objects and often fail in landscapes where agricultural fields are small and boundaries are indistinct (Persello et al., 2019). Due to this limitation, region-based methods are more favored. Their underlying principle is that neighboring pixels with similar spectral values are merged into objects. Image clustering is one of the most simple and popular region-based methods. The Simple Linear Iterative Clustering (SLIC) algorithm developed by Achanta et al. (2012) was combined with supervised classification to segment agricultural fields from a WorldView-2 image by García-Pedrero et al. (2017). Nasrallah et al. (2018) used the mean shift clustering (Fukunaga and Hostetler, 1975) algorithm to delineate wheat fields from Sentinel-2 images. The main problem with clustering-based methods is that they often create very big objects, which do not follow the natural boundaries of image features. To deal with this problem, the third category of algorithms, a hybrid approach, is sometimes used. This approach involves the use of an edge extraction algorithm to produce an edge map, which is then given as an input to a region-growing algorithm. Using this approach, Li and Xiao (2007) and Yan and Roy (2014) respectively segmented crop fields from SPOT and Landsat images. The last category of algorithms, which is gaining traction in the RS world, is the use of Deep Neural Networks (DNN). A Fully Convolutional Network (FCN) called SegNet was employed by Persello et al. (2019) to identify initial agricultural boundaries from WorldView-3 images, which were later post-processed through a watershed transform and combinatorial grouping to obtain complete agricultural fields. Rieke (2017) adopted the Fully Convolutional Instance-aware Semantic Segmentation (FCIS) architecture of Li et al. (2016) for the segmentation of agricultural fields from a Sentinel-2 image. The computationally complex nature of DNNs puts them at a disadvantage for use in RS because they take a lot of time for model training and optimization (Kamilaris and Prenafeta-Boldú, 2018).

Therefore, they are mostly applied to small test areas as was done by Persello et al. (2019) and Rieke (2017).

Even though there are many segmentation algorithms of choice, the Multiresolution Segmentation (MRS) algorithm proposed by Baatz and Schäpe (2000) and implemented in eCognition Developer (Trimble Germany GmbH, 2019) is the most widely used segmentation algorithm as evidenced by Marpu et al. (2010) and Neubert et al. (2008). Many researchers (Belgiu and Csillik, 2018; Conrad et al., 2010; Lebourgeois et al., 2017; Peña-Barragán et al., 2011; Vogels et al., 2019) have applied the MRS algorithm for the delineation of agricultural parcels. MRS is a bottom-up region merging algorithm that starts with one-pixel objects and then subsequently merges neighboring objects into bigger objects where the change in the combined spectral and spatial heterogeneity is minimal (Benz et al., 2004). In the implementation in eCognition Developer, the three main parameters that control the output of the MRS algorithm are scale, shape, and compactness. Each of these parameters takes a varied range of input values, thereby yielding an infinite number of parameter combinations. Therefore, determining the optimal parameter combination is critical to achieving optimal segmentation results.

This research aims to develop an efficient approach to identify the optimal parameters needed to segment agricultural parcels using the MRS algorithm. The traditional approach to parameter optimization is the grid search method. Given any domain space of parameters, this method evaluates all possible parameter combinations using a given model and then returns the combination with the highest or lowest evaluation score as the optimal. As the number of parameters and elements in each parameter space increases, the computational time exponentially increases. This limitation was dealt with through the random search (Bergstra and Bengio, 2012) method. Using a smaller number of model evaluations within a shorter time frame, the random search method outperformed grid search (Bergstra and Bengio, 2012). However, these two methods are very inefficient in the process of identifying the optimal parameter because they do not consider the results of previous model evaluations before sampling new combinations, thereby wasting time on needless model evaluations. Overcoming these limitations requires the use of sequential model-based optimization (SMBO) (Bergstra et al., 2011). SMBO intuitively makes an informed prediction of which new combinations to test based on results from the previous model evaluations.

SMBO is a succinct formalism of Bayesian optimization (Dewancker et al., 2016). Bayesian optimization is used in globally optimizing black-box functions (Mockus, 2012) with unknown derivatives that take a long time to evaluate (Frazier, 2018). It outperforms the grid and random search methods (Bergstra et al., 2011; Snoek et al., 2012). Instead of directly solving a computationally expensive objective function, Bayesian optimization first constructs a surrogate model with prior information of the objective function. The surrogate model is initiated with some samples drawn from the domain space to obtain posterior information of the objective function. A new sample is automatically identified by maximizing an acquisition function over the posterior surrogate model. This new sample is evaluated with the objective function, and then the posterior surrogate model is updated with the result. This process is repeated until the maximum number of iterations or time allocation given by a user is reached (Dewancker et al., 2016; Shahriari et al., 2016). The sample from all the tests that minimized or maximized the surrogate model is returned as the optimal. The usage of Bayesian optimization for parameter optimization has become an active research area (Eggenesperger et al., 2013). It has been used in solving optimization problems (Brochu et al., 2010; Shahriari et al., 2016) in various areas such as robotics (Lizotte, 2007), environmental monitoring (Marchant and Ramos, 2012), sensor networks (Osborne et al., 2010), and machine learning (Snoek et al., 2012; Thornton et al., 2013). To the best of our knowledge, there has not been any research geared towards the use of Bayesian optimization to optimize the parameters needed for segmenting satellite images, hence our

research is novel.

To apply Bayesian optimization, the objective function must take a parameter combination from any domain space as an input and then return an evaluation score. We derived this score by making use of empirical segmentation evaluation (Zhang, 1996), where the similarity between segmented agricultural parcels and their corresponding reference objects was numerically assessed through the Jaccard index. The combination with the highest Jaccard index is returned by the Bayesian optimization method as the optimal. We tested our approach on mono-temporal Sentinel-2 images covering Lower Saxony, which is a federal state in Germany. The result achieved was compared with other optimization methods based on the MRS algorithm.

The rest of the paper is structured as follows: the study area and the data are first described. Afterward, we explain the overall methodology including data preparation, development of our optimization approach, and its application to images in Lower Saxony. The results achieved are then discussed. We finish the paper by drawing some conclusions and pointing out further research directions.

## 2. Study area and data

We selected Lower Saxony (Fig. 1) as the study area because the Ministry of Food, Agriculture and Consumer Protection of Lower Saxony permitted us to use the LPIS as reference data. The coordinates of the map in Fig. 1 and all other maps in this paper are in UTM Zone 32 N (EPSG:32632). Most of its landmass is located in the temperate climate zone of Europe. The southeastern part is located in the continental climate zone. Apart from the southeastern part, where one can

locate the Harz mountain range, the terrain is relatively flat, making it suitable for farming. Various agricultural land-use types cover about 62% of its total land area of about 4,770,041 ha. The LPIS data is made up of 907,564 agricultural parcels. Based on this data, the most dominant agricultural land-use types, in order of percentage coverage, are grasslands (40%), summer cereals (23%), winter cereals (17%), potatoes (3%), winter rapeseed (3%), and sugar beet (2%). The size of the agricultural parcels ranges from as low as 0.1 ha to as high as 155 ha. The average parcel size is 3 ha. Even though the agricultural landscape is composed of heterogeneous parcel sizes, the minimum parcel size is large enough to be detected by the Sentinel-2 satellite. To ensure that the optimal segmentation parameters are representative of the wide range of parcel sizes, a square tile grid system made up of 10 km × 10 km tiles covering Lower Saxony was created. The total number of tiles came up to 562. Neighboring tiles have an overlap of 1 km. These tiles served as the basic unit for which the optimal MRS parameter combination had to be determined.

The Sentinel-2 images provided by the European Space Agency (ESA) were used for this research. Sentinel-2 is an optical satellite with thirteen spectral bands in the visible, near-infrared, and short-wave infrared regions of the electromagnetic spectrum. The spatial resolution ranges from 10 m to 60 m. The Level 1C images with a maximum cloud cover of 20% in May of 2018 were downloaded from the data repository of ESA. In May, winter crops are nearly at peak growth, while summer crops are just about shooting up. This makes it easier to differentiate and segment agricultural parcels, hence the choice of images in May. Fourteen Sentinel-2 images were downloaded to cover every part of Lower Saxony. For each tile, the first image that is cloud-free and non-

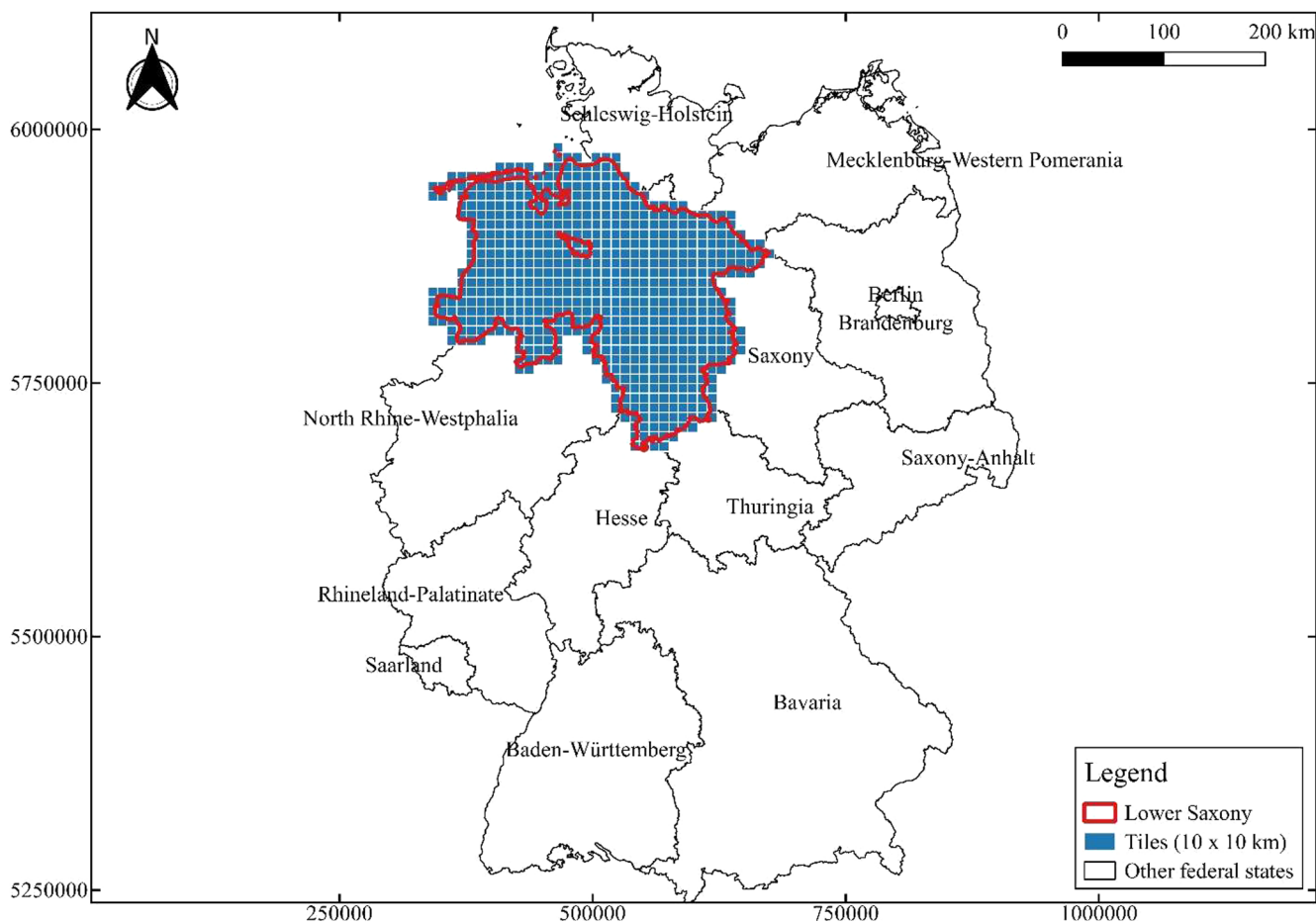


Fig. 1. The study area is Lower Saxony, Germany. This federal state was divided by a tile grid system made up of 10 km × 10 km tiles (blue polygons) numbering 562. For each tile, a Sentinel-2 image was extracted and used as input for segmentation. (For interpretation of the references to colour in this figure legend, the reader is referred to the web version of this article.)

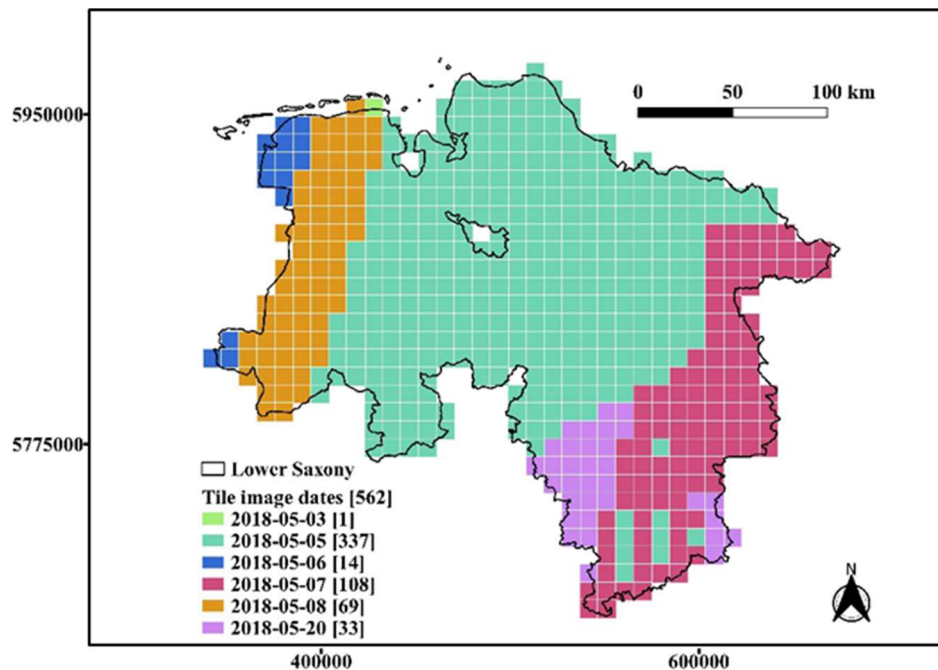


Fig. 2. A total of six cloud-free Sentinel-2 images covering Lower Saxony were used. The total number of tiles for each image acquisition date is shown as well. The majority of the tiles were captured by images from 5 May to 8 May 2018. The 5 May image covered most tiles.

defective was identified via visual inspection. The final image acquisition dates used in this research came up to six (Fig. 2).

Three auxiliary datasets were used to mask out non-agricultural areas from the Sentinel-2 images. The first dataset was the German Official Topographic Cartographic Information System (ATKIS) provided by the German Federal Agency for Cartography and Geodesy. ATKIS is a geographic database that captures the topography of Germany. The agricultural and non-agricultural vector layers covering Lower Saxony were extracted from this database. Out of the total agricultural land-cover area of about 2,936,292 ha, 65% are farmlands, 33% are grasslands, and the rest is composed of fruit plantations, tree nurseries, horticultural lands, and orchard meadows. The second one was the hydrological network dataset provided by the German Federal Institute of Hydrology, which contains all watercourses in Germany. Finally, linear features representing roads in Lower Saxony were downloaded from Open Street Map (OSM). The total length of roads is about 268,529 km. According to the OSM feature classification, there are 22 different types of roads in Lower Saxony. Majority of them are tracks (38%), followed by residential roads (16%), minor roads that link villages and hamlets (9%), service roads (7%), cycleways (6%), tertiary roads (6%), paths (5%), and the others.

### 3. Methodology

This section describes the development of our optimization approach and its application to image tiles in Lower Saxony, Germany. Our approach is a framework for identifying the optimal parameters needed for the segmentation of agricultural parcels and the actual delineation of those parcels from satellite images. Fig. 3 shows the general workflow.

#### 3.1. Data preparation

Using the Sen2Cor (Main-Knorn et al., 2017) plugin in the Sentinel Application Platform (SNAP) of ESA, the Sentinel-2 Level 1C images were atmospherically and terrain corrected to obtain Bottom-Of-Atmosphere (BOA) Level 2A images. For each Level 2A image, only the visible (red, green, blue) and near-infrared bands were used. These four

bands have a spatial resolution of 10 m, unlike the other bands that have a lower spatial resolution ( $\geq 20$  m). A higher spatial resolution leads to a higher segmentation quality (Mesner and Oštir, 2014). We stacked the four bands together into an image. Therefore, this image, which is henceforth named S2-VNIR, has a spatial resolution of 10 m.

The LPIS and ATKIS datasets sometimes contain sliver polygons. Those polygons were deleted based on their perimeter-to-area ratio. This deletion was more significant in the LPIS as the total number of parcels reduced to 853,892. The motorway line features in the OSM were buffered by 10 m, while the other line features like tracks and residential roads were buffered by 5 m to obtain polygon features. A buffer distance of 10 m was applied to all the watercourse line features. All the buffer distances were empirically determined by overlaying the line features on different images and testing various buffer distances such that the area of any resultant polygon was large enough to contain at least one pixel. Out of the various buffer distances we tested, the aforementioned buffer distances we used in this study were identified as optimal because they resulted in polygons with minimal encroachment on the boundaries of neighboring agricultural parcels. A no-data mask layer was created by merging the non-agricultural vector layer with the OSM and watercourse polygons. All pixels in each S2-VNIR data that intersected the no-data mask layer were masked out. Finally, each S2-VNIR data was clipped to the tile grid it spatially covered. These clipped S2-VNIR datasets were used for further processing. Fig. 4a shows one S2-VNIR image containing both agricultural and non-agricultural areas, while Fig. 4b shows the same image with all non-agricultural areas removed using the no-data mask layer.

#### 3.2. Optimization design and application

At the heart of our optimization approach are image segmentation, supervised evaluation of segmentation quality, and Bayesian optimization.

##### 3.2.1. Image segmentation

The Multiresolution Segmentation (MRS) algorithm as implemented in eCognition Developer 9.5.0 was used for image segmentation. MRS is a pair-wise merging process that starts with single-pixel objects well

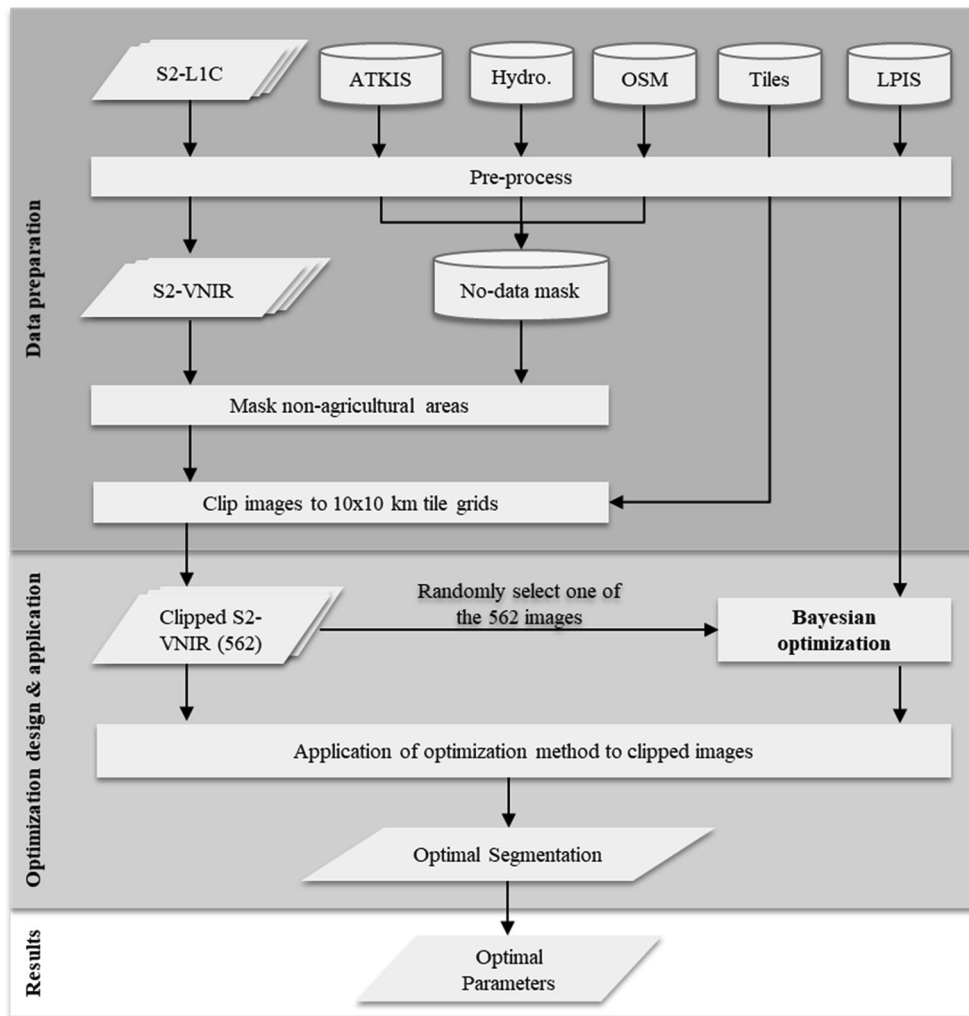


Fig. 3. The general workflow that was followed to determine the optimal parameter combinations for Lower Saxony.

distributed over an image. For each pixel object, a neighboring pixel object is found such that the change in heterogeneity between them is minimal. The heterogeneity of each object is computed as a function of the color and shape of that object. Where the change in heterogeneity is

minimal, the two objects are merged into a bigger object. Each object is handled once per loop cycle. This merging process stops as soon as the number of pixels in any object exceeds a user-given threshold value.

The three parameters that influence the segmentation outcome are

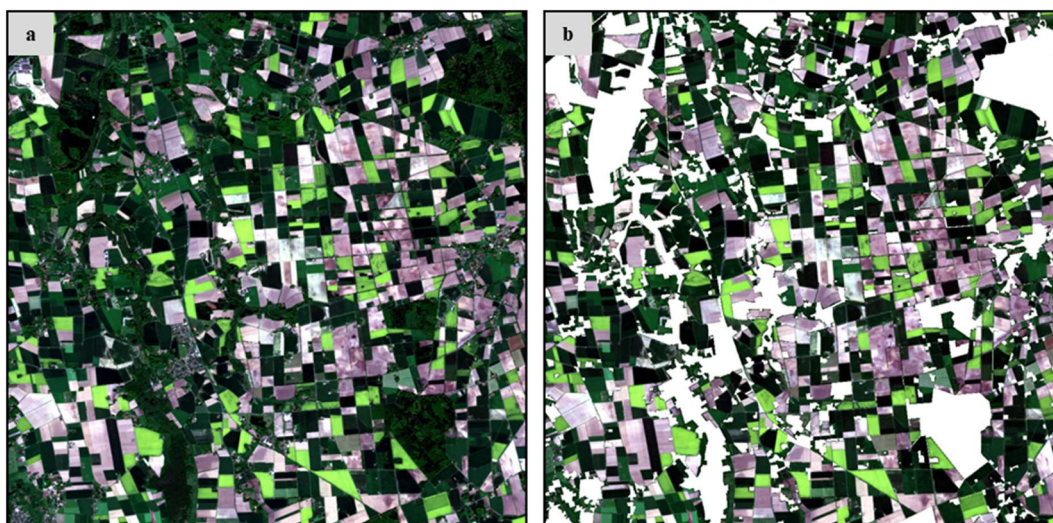


Fig. 4. (a) A non-masked S2-VNIR image. (b) The same image with non-agricultural areas, watercourses, and streets removed.

scale, shape, and compactness. Scale refers to the minimum object size, which is used as the stopping criteria for the algorithm. It is not bounded but mathematically, it cannot be lesser than one or greater than the size of the input image. The shape indicates the weight to put on the form of objects during the segmentation process as compared to color (spectral) information. Any change made to shape inversely affects color. The sum of the shape and color weights is equal to 1. Color is always required during the segmentation process, hence shape ranges from 0 to 0.9. The compactness weight defines the influence of the squareness of objects as opposed to their smoothness. The compactness and smoothness weights also add up to 1. Compactness ranges from 0 to 1. For a more detailed mathematical explanation of the MRS algorithm, readers are referred to the relevant literature (Baatz and Schäpe, 2000; Benz et al., 2004; Trimble Germany GmbH, 2019).

### 3.2.2. Evaluation of segmentation quality

Empirical segmentation evaluation (Zhang, 1996) was adopted for this research. It involves the computation of the geometric discrepancy or similarity between the LPIS and each segmentation layer. For each segmentation layer, the first step is to identify the segment that corresponds to a reference parcel in the LPIS. This was done using the two-sided overlap criteria (Clinton et al., 2010). A segment was considered to be a corresponding segment if the area of the intersection between that segment and a reference parcel was either more than half of the area of the segment or the reference parcel. A modification was made such that if a segment has more than one reference parcel with the same land-use type, those parcels are merged as a single reference parcel for that segment (Fig. 5). This was done to minimize under-segmentation.

The similarity between the reference parcel and the corresponding segment was computed via the Jaccard index (Jaccard, 1901), which is popularly known as Intersection over Union (IoU). It is a statistic widely used in computer vision tasks to measure the accuracy at which objects in an image or a video are detected by an algorithm. Its mathematical formulation is shown in Eq. (1);

$$IoU(Y) = \frac{Area(X \cap Y)}{Area(X \cup Y)} \quad (1)$$

where  $X$  is the reference parcel,  $Y$  is the corresponding segment,  $X \cap Y$  is the spatial intersection between the two objects and  $X \cup Y$  represents the spatial union of the two objects. It is bounded between 0 (no spatial similarity) and 1 (complete spatial match). The overall segmentation quality (OSQ) of each segmentation layer was finally computed as a weighted average of IoU over all segments using Eq. (2);

$$OSQ = \frac{\sum_{i=1}^n Area(Y_i) * IoU(Y_i)}{\sum_{i=1}^n Area(Y_i)} \quad (2)$$

where  $Y$  represents a segment and  $n$  is the total number of segments in

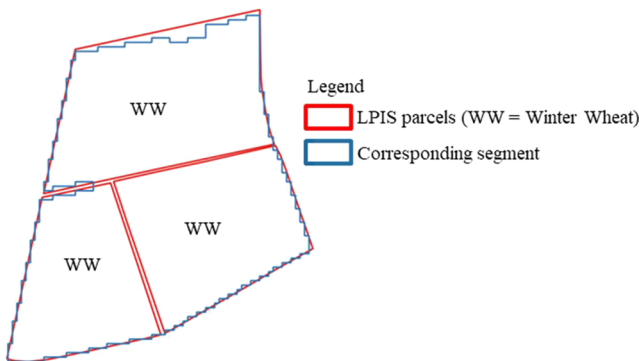


Fig. 5. The merger of reference parcels based on their land-use type. The segment corresponds to three reference parcels based on the two-sided overlap criteria. The three parcels were merged into one because winter wheat is grown on all of them.

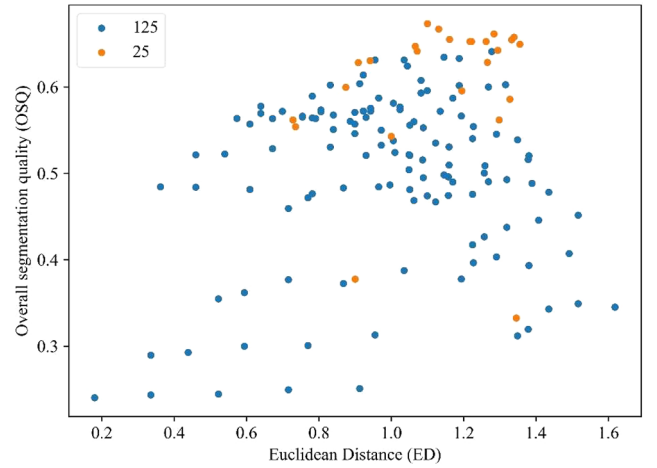


Fig. 6. The scatterplot showing the non-inverted OSQ computed for each segmentation layer of the test image. Each dot represents a data point of scale, shape, and compactness with its corresponding non-inverted OSQ. The blue dots (125) represent the initial parameter combinations and the red dots (25) represent the actual Bayesian iterations. (For interpretation of the references to colour in this figure legend, the reader is referred to the web version of this article.)

each segmentation layer. The segments along the spatial boundary of each segmentation layer were eliminated from the computation of the OSQ since they are artifacts created as a result of clipping the S2-VNIR images to the tiles.

### 3.2.3. Bayesian optimization

The essential components of our Bayesian optimization approach are:

- Domain space: this refers to the parameter space of each MRS parameter, of which the Bayesian optimization routine has to identify the optimal parameter combination. Scale ranged from 20 to 200, shape from 0 to 0.9, and compactness from 0 to 1.
- An objective function to minimize: our objective function,  $f(x)$ , takes a parameter combination,  $x$ , from the domain space, generates a segmentation vector layer, uploads the vector layer into a PostgreSQL database, computes the OSQ, and then returns an inverted OSQ as  $1 - OSQ$ .
- A surrogate model: it is a predictive probability model that captures the prior probability distribution,  $p(y)$ , of the objective function and is iteratively updated to capture the objective function's posterior probability distribution,  $p(y|x)$ , where  $y$  is the inverted OSQ. The surrogate model is a realization of the Bayes' rule (Eq. (3));

$$p(y|x) = \frac{p(x|y) * p(y)}{p(x)} \quad (3)$$

where  $p(x|y)$  is a likelihood distribution and is a marginal probability. To build the posterior probability distribution, we need to define two things: the prior distribution function and the initial parameter combinations with their corresponding inverted OSQ. Two of the most used prior distribution functions are Gaussian Process (GP) (Rasmussen and Williams, 2006) and Random Forest (RF) (Breiman, 2001). However, GP has become a standard prior (Brochu et al., 2010; Dewancker et al., 2016) in Bayesian optimization. GP is parametrized by a mean function,  $\mu$ , and covariance or kernel function,  $k$ . For convenience,  $\mu$  is set as a zero function, leaving the user with the more interesting  $k$ , which defines the quality of the surrogate model (Brochu et al., 2010). The default choice of  $k$  for GP regression is the automatic relevance determination (ARD) squared exponential kernel (Brochu et al., 2010; Snoek et al., 2012). However, Snoek et al. (2012) recommended the

**Table 1**

The impact of different initial parameter combinations on the results of Bayesian optimization. The number of initial combinations for TS1 was 64 and TS2 was 27. The number of Bayesian iterations for TS1 was 86 and for TS2 123.

Test	Scale		Shape		Comp.		Optimal Parameters			OSQ	Time
	Range	Interval	Range	Interval	Range	Interval	Scale	Shape	Comp.		
TS1	20–200	60	0.0–0.9	0.3	0.0–0.9	0.3	60	0.884	0.919	66.82%	36 min
TS2	30–190	80	0.0–0.8	0.4	0.0–0.8	0.4	56	0.9	0.677	67.54%	49 min

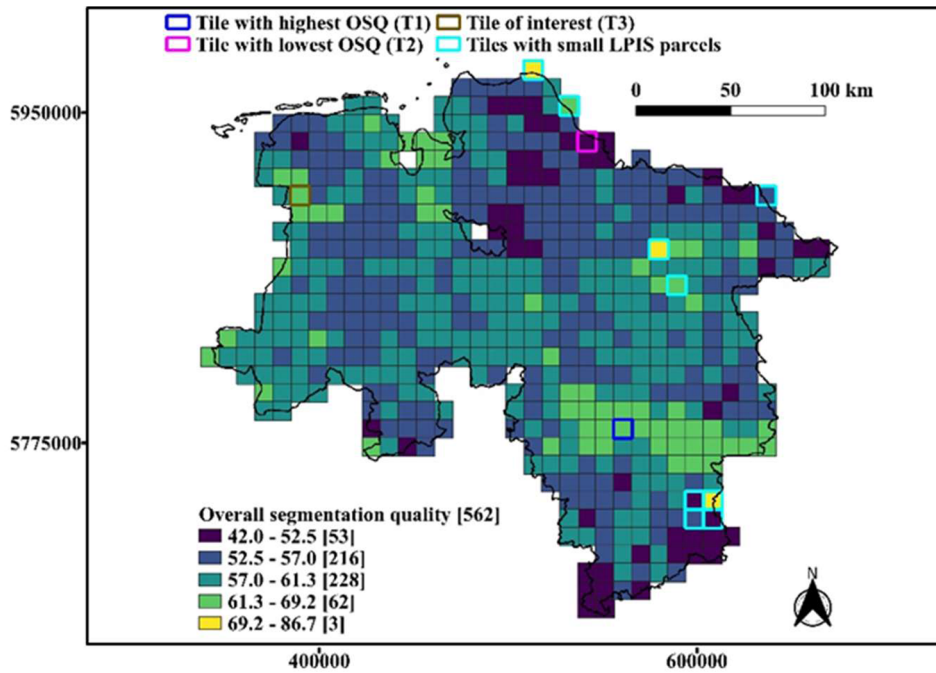


**Fig. 7.** The highest OSQ computed for each tile in Lower Saxony.

use of the ARD Matérn kernel (Stein, 1999) as captured by Eq. (4) because the squared exponential kernel is unrealistically smooth for practical optimization problems;

$$k(x_i, x_j) = \frac{1}{\Gamma(\nu)2^{\nu-1}} \left( \frac{\sqrt{2\nu}}{l} d(x_i, x_j) \right)^\nu K_\nu \left( \frac{\sqrt{2\nu}}{l} d(x_i, x_j) \right) \quad (4)$$

where  $\nu$  and  $l$  are non-negative parameters,  $d(x_i, x_j)$  is the distance between two parameter combinations  $x_i$  and  $x_j$ ,  $\Gamma$  is the gamma function, and  $K_\nu$  is the modified Bessel function (Rasmussen and Williams, 2006). We tested the first and second-order Matérn kernels recommended by Rasmussen and Williams (2006) for machine learning, and the first order proved superior, so we kept that. For first-order,  $\nu$  is 1.5 and for the second-order, it is 2.5. The next step is to initialize the GP prior model with actual data. This is usually done by randomly sampling a user-given number of parameter combinations from the domain space and then the inverted OSQs are computed with  $f(x)$ . This randomness would prevent reproducibility, so we opted for systematic sampling. To obtain the initial samples,  $D$ , we always sampled 125 parameter combinations covering the low, middle and high ends of each parameter range. The values for scale are [40, 80, 120, 160, 200], and for both shape and compactness [0.1, 0.3, 0.5, 0.7, 0.9]. We used two parallel processes for segmenting and calculating the inverted OSQ of each parameter combination in  $D$ .

- (d) An acquisition function: it is used to propose new  $x$  combinations in the domain space to evaluate with  $f(x)$  by making use of the GP posterior probability distribution,  $p(y|x)$ . Even though there are many acquisition functions, expected improvement (EI) (Jones et al., 1998) is the most commonly used (Frazier, 2018). The

possible improvement on the current optimal parameter combination,  $x^o$ , at any new parameter combination,  $x$ , is given by Eq. (5);

$$I(x) = \max \{ f(x^o) - f(x), 0 \} \quad (5)$$

where  $f(x^o)$  is the inverted OSQ value at  $x^o$ . Given that  $f(x)$  is computationally expensive to evaluate, the approach to identifying which  $x$  to evaluate next is rather to compute the expected value of  $I(x)$  using the GP posterior,  $p(y|x)$ , which is faster to compute. Computing this expected value involves several partial integrations of  $I(x)$  to obtain a closed form (Jones et al., 1998) as shown by Eq. (6);

$$EI(x) = (y^o - \hat{y}) \Phi \left( \frac{y^o - \hat{y}}{s} \right) + s \phi \left( \frac{y^o - \hat{y}}{s} \right) \quad (6)$$

where  $y^o$  is the inverted OSQ value at  $x^o$ ,  $\hat{y}$  is the GP posterior  $p(y|x)$ ,  $\phi$  and  $\Phi$  are the standard normal density and distribution functions, and  $s$  is the standard error of the GP posterior at  $x$ . Normally, many parameter combinations are randomly sampled from the given domain space, and the combination with the highest expected improvement is selected as a candidate and passed to  $f(x)$  as the next point to evaluate. We used 10,000 random parameter combinations from our domain space as defined in (a). Alternatively, the  $x$  candidate can be identified using the Limited Broyden–Fletcher–Goldfarb–Shanno (L-BFGS) (Liu and Nocedal, 1989) algorithm. From the 10,000 random combinations, we identified the first five combinations with the highest expected improvement. Using these combinations as initialization points, L-BFGS is iteratively able to find the local minima of EI, of which the optimal is then selected as the best candidate. We chose L-BFGS simply because it is more intuitive and ensures some level of reproducibility. This  $x$  candidate is then given to  $f(x)$  to compute the inverted OSQ. The  $x$

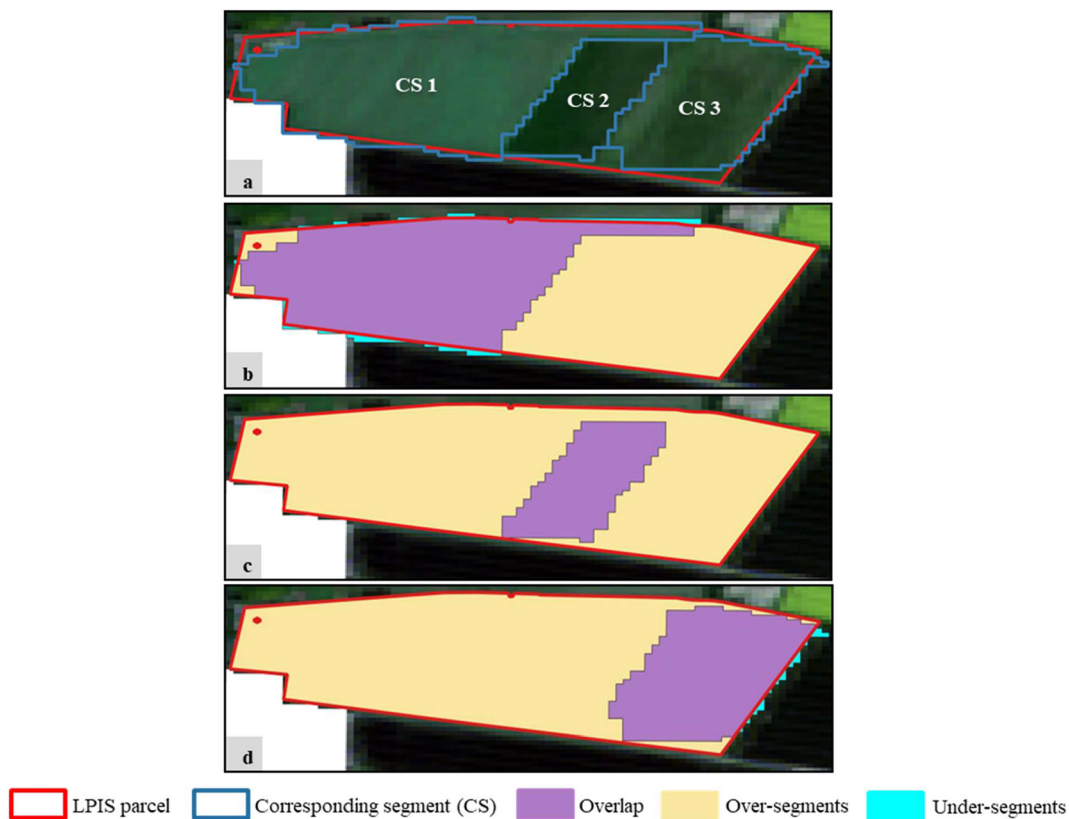


**Fig. 8.** Some of the contributing factors preventing the segmentation quality from reaching 100%. (a) A parcel in LPIS with three corresponding segments (CSs) overlaid on a Sentinel-2 image. The overlapping area, over-segments, and under-segments between each CS and the LPIS parcel are shown in (b), (c) and (d) respectively.

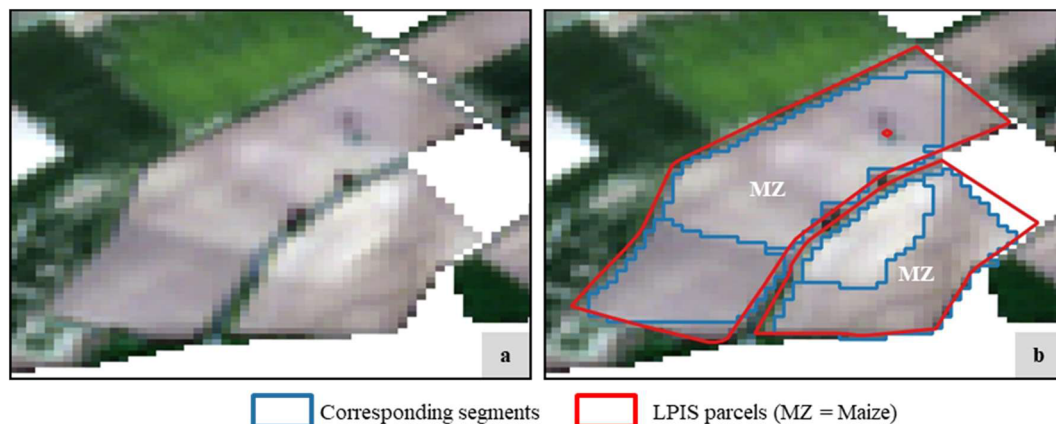


**Fig. 9.** The prevalent instances of over-segmentation. (a) A sentinel 2 image. (b) LPIS parcels and their corresponding segments overlaid on the Sentinel-2 image. Two corresponding segments were respectively created for each reference parcel due to the heterogeneity of the soil pixels in both parcels.

candidate and its inverted OSQ are then appended to  $D$ . The process is repeated from (c) to (d) with the current  $p(y|x)$  replacing  $p(y)$  to continuously update the posterior probability distribution. The repetition is done until a user-given number of iterations is completed. We allowed 150 function calls to  $f(x)$  including the 125 initial samples, meaning the actual number of Bayesian iterations was 25.

For the complete mathematical foundation of Bayesian optimization, readers are referred to Brochu et al. (2010), Frazier (2018) and Shahriari et al. (2016). For automation purposes, we used eCognition Server 9.5.0 and its command-line interface (CLI) for segmentation. We limited parallel execution of the MRS segmentation to two because we have two eCognition Server licenses. The Python programming language was used to chain everything together. We used the Bayesian

optimization implementation of *Scikit-optimize* in Python. It is important to mention that, the computed OSQ was inverted because *Scikit-optimize* is programmed for function minimization.

We randomly selected one of the 562 tiled images to test the effectiveness of our Bayesian optimization approach in identifying the optimal MRS parameters. To visualize the parameter combinations sampled by the Bayesian optimization routine alongside the corresponding non-inverted OSQs in two-dimensions, we first conflated each parameter combination of scale, shape, and compactness into a single value using Euclidean Distance (ED). Each scale value was normalized between zero and one before being used in the calculation of the ED. We then plotted each ED against its corresponding non-inverted OSQ (Fig. 6). Our Bayesian optimization approach was very efficient as it

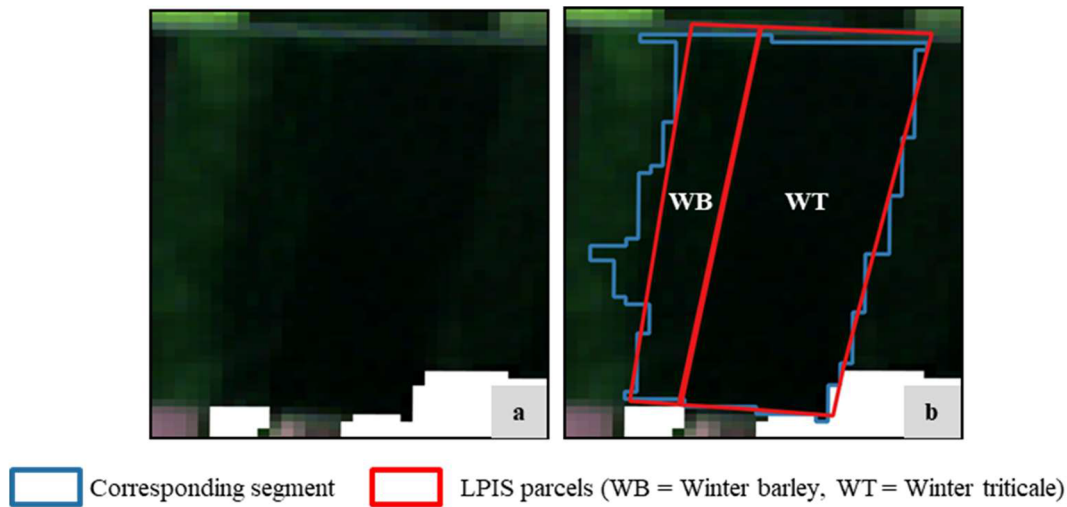


Fig. 10. Under-segmentation caused by adjacent parcels with similar spectral behavior. (a) A Sentinel-2 image. (b) Two LPIS parcels and their corresponding segment overlaid on the Sentinel-2 image. One corresponding segment was created due to the spectral similarity of winter barley and winter triticale.

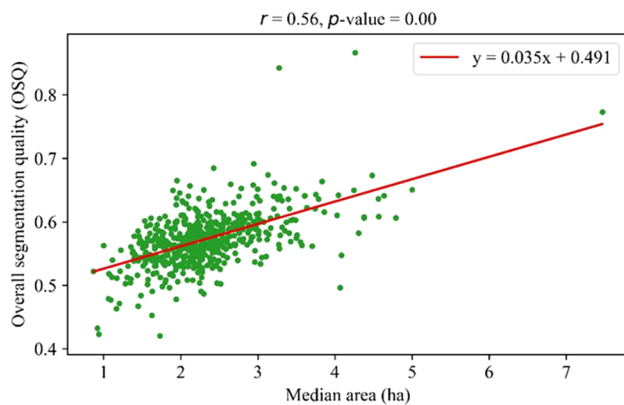


Fig. 11. Correlation between the highest OSQ and the median area of agricultural parcels for all tiles.

mostly exploited parameter combinations that yielded high OSQs. Out of the 25 combinations it sampled, 16 of them yielded OSQs above 60%. Using a total execution time of 16 min, the highest OSQ of 67.33% (ED = 1.1) was achieved with the parameter combination of 55 for scale, 0.9 for shape, and 0.602 for compactness.

Additional information discernable from Fig. 6 is that the distribution of the initial parameter combinations can play a role in identifying the optimal combination. Therefore, before applying our approach to the 562 tiles, we also tested it to see how the variation of the initial parameter combinations could affect the OSQ. Table 1 shows two tests labeled TS1 and TS2 that were done using different initial parameter combinations. It also captures the optimal parameter combination, OSQ, and execution time per test. The number of initial combinations for TS1 was 64 and for TS2 27. For all tests, the number of iterations was kept at 150, meaning 86 and 123 Bayesian iterations were run for TS1 and TS2 respectively.

From Table 1, the differences in OSQ between each test and the approach we adopted, which yielded an OSQ of 67.33%, was very marginal. Therefore, we concluded that the initial parameter combinations do not significantly affect the Bayesian optimization results as long as they are well distributed over the domain space and the number of Bayesian iterations is increased accordingly. Due to the increased number of Bayesian iterations, the execution time per test drastically increased. It is imperative to mention here that the actual optimal parameter combination needed for segmentation based on the MRS algorithm is unknown. This is true especially for shape and

compactness because they take floating-point numbers as input unlike scale, which accepts only integers, hence more deterministic. Additionally, different methods under different time constraints will most likely yield different results, an example of which is shown in Table 1. Therefore, a method that can approximate this unknown optimal combination in a time-efficient manner is the goal of any segmentation optimization approach. Our approach of using 125 initial combinations was more viable than the other two tests (TS1 and TS2) in terms of approximating the optimal MRS parameter combination within a shorter execution time. Therefore, we applied our approach to the 562 tiles in Lower Saxony to approximate the optimal segmentation parameters and delineate agricultural parcels. The execution was completed in seven days.

### 3.3. Other optimization methods

Two existing segmentation optimization methods based on the MRS algorithm in eCognition Developer were compared with our approach. The first one is the segmentation accuracy assessment (SAA) method (Anders et al., 2011). The SAA, just like our approach, is a supervised method. It creates segments at different scale levels, computes the discrepancy between reference objects and their corresponding segments at each level, and then identifies the level with the least discrepancy as optimal. To calculate the discrepancy measure for any segmentation layer, it first generates a frequency distribution from the spectral values of pixels that fall within each reference object and its corresponding segment, respectively. The two frequency distributions are then normalized with the respective number of pixels in each distribution. The segmentation error between the reference object and its corresponding segment is then calculated as the sum of absolute error between the two normalized frequency distributions. The discrepancy measure is finally computed as the average sum of absolute error over all segments (Eq. (7));

$$AAE = \frac{1}{n} \sum_{i=1}^n \left( \sum \left| \frac{H_x}{a_x} - \frac{H_y}{b_y} \right| \right)_i \quad (7)$$

where  $n$  is the total number of segments in the segmentation layer,  $H_x$  is the frequency distribution of pixels in the reference object,  $H_y$  is the frequency distribution of pixels in the corresponding segment, and  $a_x$  and  $b_y$  are the number of pixels within the reference object and the corresponding segment, respectively. The segmentation layer with the lowest AAE value is the optimal. The default values of 0.1 for shape and 0.5 for compactness were used. The scale ranged from 20 to 200 with

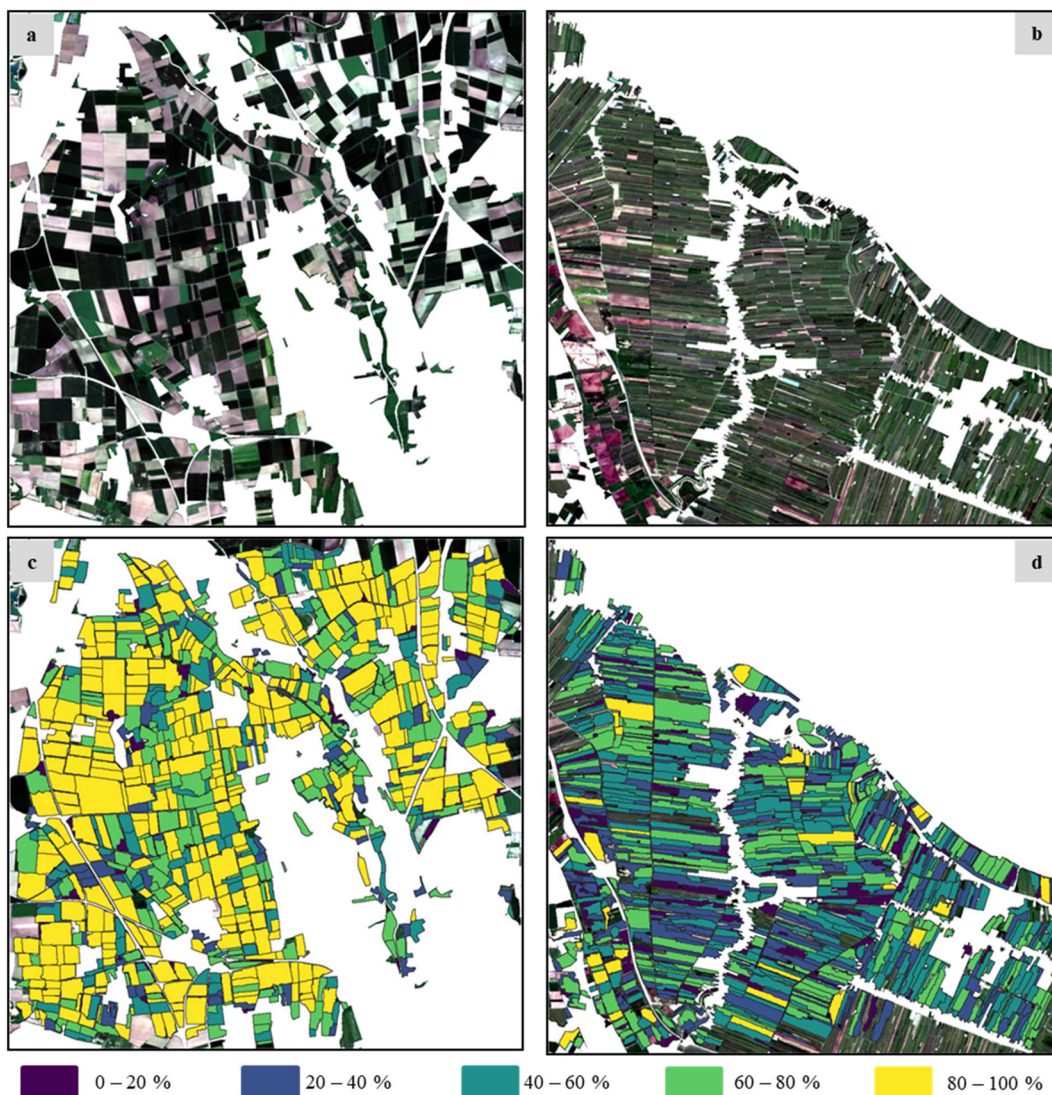


**Fig. 12.** Segmentation evaluation at the segment level for T1 (highest OSQ) and T2 (lowest OSQ). (a) and (b) show the Sentinel-2 images used for segmenting the T1 and T2 tiles respectively. The created segments have been colored according to the IoU computed for each of them and subsequently overlaid on each image respectively at (c) and (d). (For interpretation of the references to colour in this figure legend, the reader is referred to the web version of this article.)

increments of 5.

The second optimization method is the estimation of scale parameter (ESP-2) tool (Drăguț et al., 2014), which is an improvement of the original version (Drăguț et al., 2010). Unlike the SAA and our approach, the ESP-2 tool is an unsupervised method, which is purely driven by the image content and does not use any reference data. Additionally, it is fully automated and applicable to images with multiple bands. Due to those characteristics, it is very popular in the world of MRS. It is underpinned on the concept of local variance (LV) (Woodcock and Strahler, 1987). It creates segments in a stepwise manner using incremental scale values. For each segmentation layer, the standard deviation of pixels in each segment is computed for each image band. The LV per band is calculated as the average standard deviation over all segments. The LV is finally averaged over all bands to obtain one LV per segmentation layer (Eq. (8));

$$ALV = \frac{1}{b} \sum_{j=1}^b \left( \frac{1}{n} \sum_{i=1}^n \sigma_i \right)_j \quad (8)$$

where  $b$  is the total number of bands in an image,  $n$  is the total number of segments in a segmentation layer, and  $\sigma_i$  is the standard deviation of pixels per segment.  $ALV$  is a measure indicating the level of

homogeneity within a segmentation layer. When the  $ALV$  of the current scale level is equal to or lower than the previous  $ALV$ , the iteration stops, and the segments created at the previous scale level are maintained. Here again, the default values of 0.1 for shape and 0.5 for compactness were kept and the scale was automatically determined by the ESP-2 tool.

## 4. Results and discussion

### 4.1. Analysis of segmentation quality

The highest OSQ identified for each tile is shown in Fig. 7. Most of the values ranged from 42.0% to 69.2%. The three tiles with values above 69.2% are highly dominated by non-agricultural land-use such that only a few reference parcels were used for segmentation evaluation. The lower the number of reference parcels, the higher the probability of obtaining high OSQ values. This relationship was also observed by Novelli et al., (2017), who emphasized the importance of using a high number of reference objects in supervised segmentation evaluation after establishing a positive correlation between segmentation accuracy and the amount of reference data used for evaluation.

It is important to state that a 100% OSQ is not achievable for a

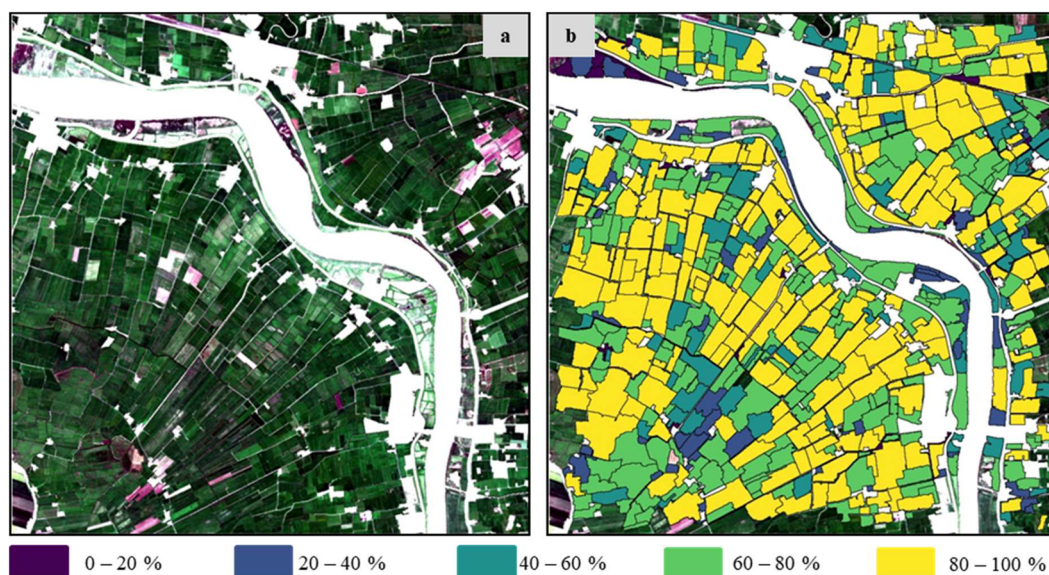


**Fig. 13.** Visual inspection of tile T3 with a relatively high OSQ of 68.46%. (a) The Sentinel-2 image of T3. (b) The evaluated corresponding segments colored by their respective IoU and draped over the Sentinel-2 image. (For interpretation of the references to colour in this figure legend, the reader is referred to the web version of this article.)

couple of reasons. The LPIS parcels are polygons with straight edges representing a single land-use digitized from orthophotos. Conversely, the segments automatically extracted from the Sentinel-2 images have pixelated edges. Additionally, the orthophotos have a higher spatial resolution ( $\leq 1$  m) than the Sentinel-2 images. These differences culminate in the segments and the LPIS parcels being misaligned especially at the borders (Fig. 8a). Simplifying the segments did not eliminate this problem.

Over-segmentation was the main contributing factor that negatively affected the OSQ. It mostly occurred due to the heterogeneity of pixels within a parcel. In Fig. 8a, the LPIS indicates that there is one parcel on which three types of clover are grown. Due to the different growth stages, the MRS algorithm created three different segments (CS1, CS2, and CS3) as captured by Fig. 8a. This led to over-segmentation (Fig. 8b–d). Even though this type of over-segmentation is acceptable within the context of biodiversity monitoring and structural change analysis of agricultural parcels, it reduces the OSQ. The IoU computed respectively for CS1, CS2, and CS3 are 49.27%, 16.48% and 26.59%. Using those three segments, the OSQ amounted to 37.39%. When all the segments are first merged into a single polygon before computing the OSQ, the OSQ increased to 90.51%. This underscores the negative impact of over-segmentation on the OSQ. Even though this instance of over-segmentation led to a lower OSQ, it is entirely acceptable given that the segmentation algorithm correctly delineated the different parcels present in that area as visible from the satellite image. The inability of LPIS to correctly capture the different agricultural parcels present in that area was the negative driving force behind the low OSQ. Therefore, the low OSQ can largely be attributed to the error in LPIS and not the segmentation.

Fig. 9 captures another instance of over-segmentation. In Fig. 9b, both LPIS parcels are used to grow maize. When the Sentinel-2 image (Fig. 9a) was taken on 5 May 2018, the parcels were bare consisting of soil patches with different colors, which led to the creation of small fragments within those parcels (Fig. 9b). Such instances of over-segmentation were more prevalent. As over-segmentation increases, the OSQ decreases. In general, the best possible way to deal with over-segmentation will be to merge neighboring segments with the same land-use type after classifying the segments.

Under-segmentation, which mostly occurred when the same crop types are grown on adjacent parcels, was highly minimized due to the

modification made at the segmentation evaluation stage. In adjacent parcels with different crop types but similar spectral properties, under-segmentation was unavoidable. In Fig. 10b, even though the LPIS indicates that two distinct parcels are present, one big segment was created because winter barley and winter triticale have similar spectral properties as shown in Fig. 10a.

Another factor that influenced the segmentation quality was the size of agricultural parcels. Fig. 11 shows the linear relationship between the OSQ and the median area of agricultural parcels per tile. The Pearson correlation coefficient ( $r$ ) of 0.56 indicated that at tiles with larger agricultural parcels, the OSQ was higher as opposed to tiles with smaller agricultural parcels. Tiles with similar median areas have similar OSQ values, thereby naturally clustering together as visible in Fig. 7.

To further demonstrate the impact of the area of agricultural parcels on the segmentation quality, two tiles with contrasting agricultural parcel structures were selected for analysis at the segment level. Fig. 12a captures the Sentinel-2 image of tile T1 with the highest OSQ (69.17%), while Fig. 12b shows that of tile T2 with the lowest OSQ of 42.04%. The median area of agricultural parcels in T1 and T2 is 4.12 ha and 1.73 ha respectively. The segments created for each tile are shown in Fig. 12c and d respectively. Each segment is colored by the geometric match, here the IoU, between that segment and its corresponding LPIS parcel. In Fig. 12a, the agricultural parcels are big and compact. Different agricultural land-use types like sugar beets and winter wheat exist there. This made it easier to delineate the parcels, which led to most parcels having high IoU values. Fig. 12b, on the other hand, shows that the parcels are small and elongated. Almost all of them are used to grow pome fruits with virtually no boundaries between them discernable from the Sentinel-2 image. This led to the creation of segments way bigger than the LPIS parcels, which led to most of the segments having very low IoU values. This consequently led to a low OSQ for that tile.

The fidelity of the OSQ was checked by visually inspecting tile T3, which has a relatively high OSQ of 68.46%. The Sentinel-2 image and the generated segments are shown in Fig. 13. About 86% of this tile is made up of pasture lands. With our segmentation evaluation process mostly focused on minimizing under-segmentation, it culminated in the creation of big segments, which were not representative of real-world agricultural parcels. Therefore, the OSQ should not be used alone but supported with visual inspection to make full deductions on

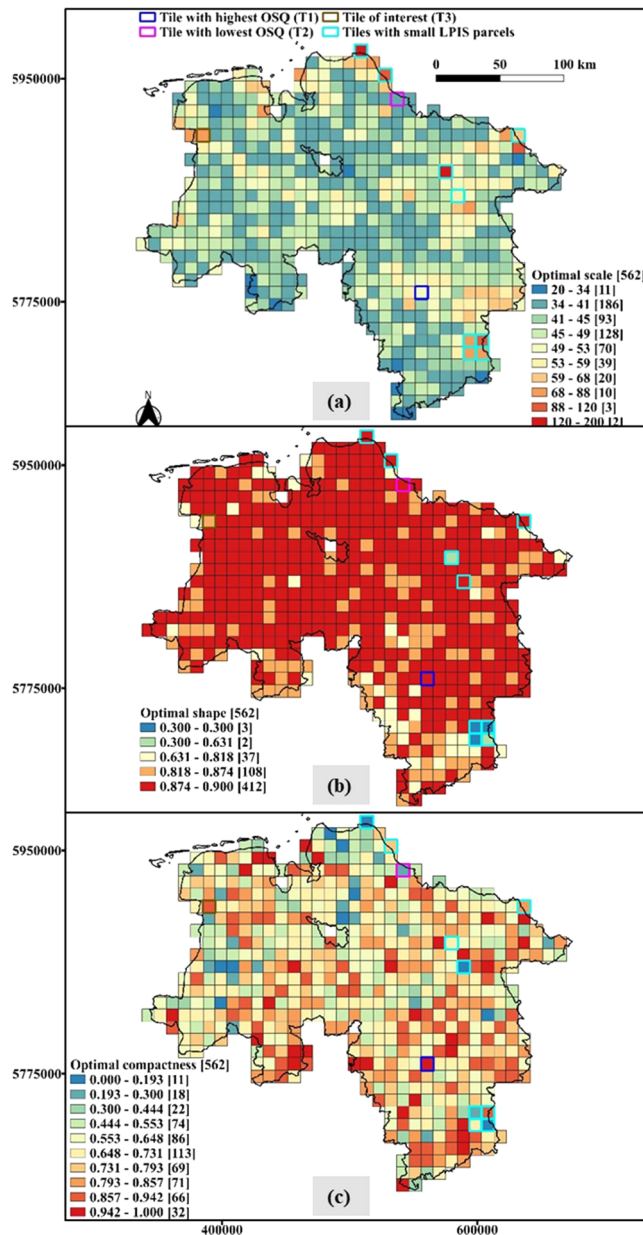


Fig. 14. The optimal parameter values identified for each tile in Lower Saxony.

segmentation quality.

#### 4.2. Optimal parameter combination per tile

The scale, shape, and compactness values that resulted in the highest OSQ for each tile are presented here. Fig. 14a shows the optimal scale values. Most of the scale values were from 34 to 53, with the modal value being 40. Scale values above 77 correspond to the tiles with a very small number of LPIS parcels for evaluation. The optimal shape value identified for each tile is depicted in Fig. 14b. The shape values did not show a lot of variability over its possible range. Most of the values were above 0.8 and often reached the maximum of 0.9, which signifies the dominance of the shape of the agricultural parcels as compared to their spectral information during the segmentation evaluation process. Fig. 14c shows the optimal compactness values for the tiles. Unlike shape, the compactness values were so variable that visible clusters were not established. Even though the values stretched over the possible compactness range, most of them were above 0.5, with 0.7 being very dominant. This stands to reason given that the optimal shape

Table 2

The optimal parameters and corresponding OSQ values obtained by the two optimization methods and our approach.

Tile	Method	Shape	Compactness	Scale	OSQ
T1	SAA	0.1	0.5	85	55.65%
	ESP-2	0.1	0.5	73	50.81%
	Our approach	0.9	0.966	51	69.17%
T2	SAA	0.1	0.5	45	30.24%
	ESP-2	0.1	0.5	147	33.23%
	Our approach	0.9	0.3	40	42.04%
T3	SAA	0.1	0.5	65	48.59%
	ESP-2	0.1	0.5	83	52.52%
	Our approach	0.842	0.906	77	68.46%

values were relatively high. Additionally, in Germany most agricultural farms have square or rectangular shapes, hence very compact.

#### 4.3. Comparison with other optimization methods

The SAA and ESP-2 methods were applied to the T1, T2, and T3 images. Table 2 captures the optimal parameters and corresponding OSQ values obtained by the two optimization methods and ours. As a reminder, the other two methods only optimized scale, while shape and compactness were kept at their default. At all tiles, SAA and ESP-2 obtained different scale and OSQ values, which is contrary to the results of Belgiu and Drăguț (2014). Belgiu and Drăguț (2014) evaluated the SAA and ESP-2 methods for optimal extraction of buildings from very high-resolution satellite images. In the test areas with big buildings, both methods achieved very similar results. In general, buildings are very compact and have very homogeneous surfaces making it easier to delineate them compared to agricultural parcels. This could have contributed to the differences in the results alongside the different satellite images used.

At all three tiles, the OSQs of SAA and ESP-2 were significantly lower than our approach (Table 2). The optimal shape and compactness values identified by our approach gave a better indication of the structural composition of parcels in each tile. Further, the visual assessment of the IoU computed at the segment level showed that there were more segments with higher qualities based on our optimization approach (Fig. 15a–c) than the SAA (Fig. 15d–f) and the ESP-2 (Fig. 15g–i) methods.

The outcome of the two methods using the optimal shape and compactness values identified with our optimization approach is shown in Table 3. This time around, their OSQs improved significantly and got closer to those of our approach. This underscores the importance of determining the optimal values not only for scale as is done by the SAA and ESP-2 but also for the other MRS parameters. This is what differentiates our approach from the other two, making ours demonstrably more accurate. At T2, the segmentation challenge remained. Both methods, as well as our approach, performed poorly due to the overwhelming presence of small and elongated agricultural parcels. This is more of a data issue than the segmentation optimization method. The likely solution to this problem is the use of an image with a higher spatial resolution than Sentinel-2 such that distinct boundaries between the agricultural parcels can be identified, thereby making it easier to delineate the parcels while minimizing under-segmentation.

## 5. Conclusions

Accurate and up-to-date information on agricultural parcels is pivotal to any agricultural management system. The most prominent spatial database of agricultural parcels within the European Union (EU) called the Land Parcel Identification System (LPIS) suffers certain drawbacks such as the inadequate coverage of all agricultural parcels, restricted access to the data, the time lag that comes with the data, and

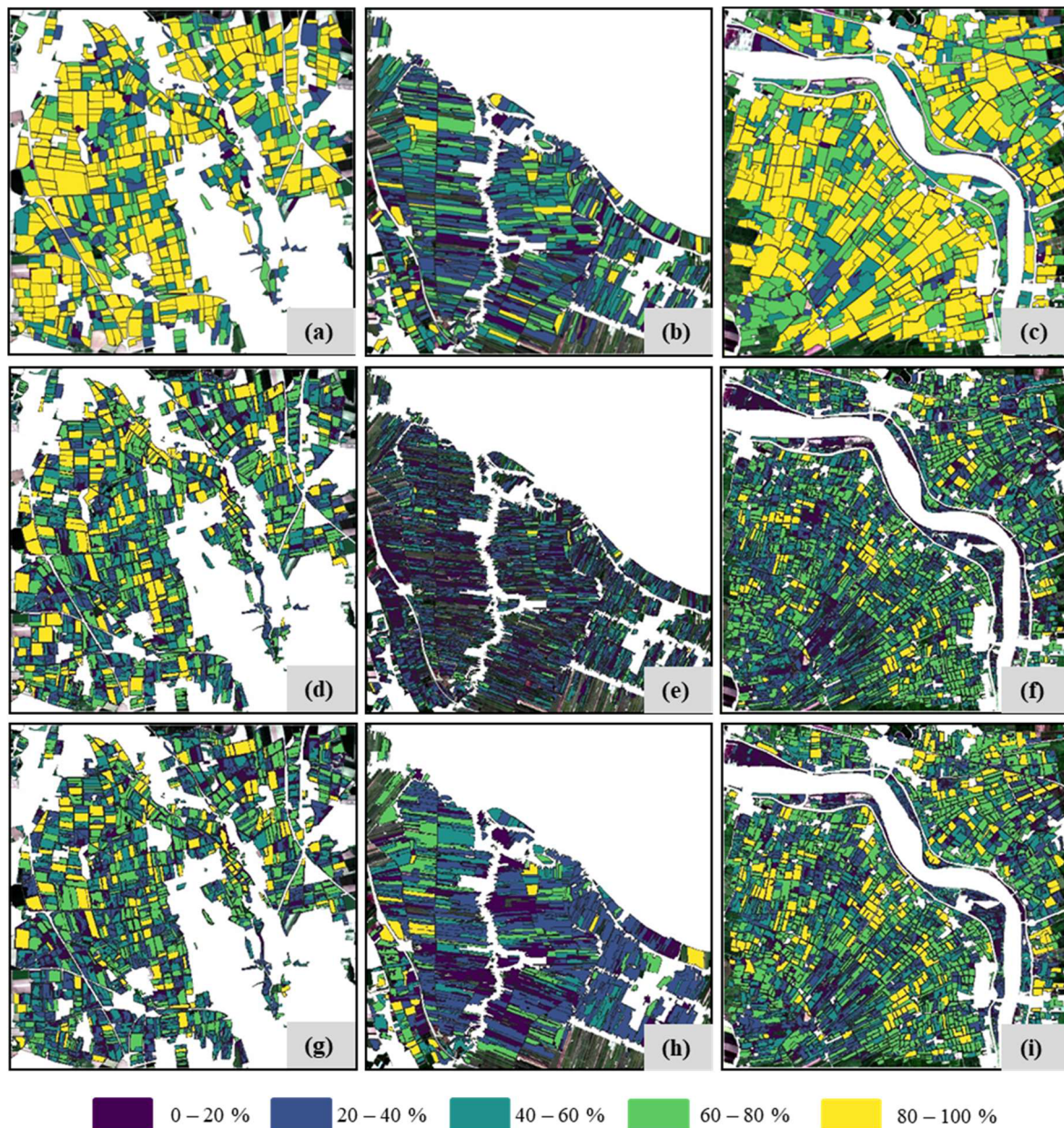


Fig. 15. Segmentation evaluation at the segment level for the different optimization approaches at T1 (a, d, g), T2 (b, e, h), and T3 (c, f, i). Each segment is symbolized by its IoU and draped over their respective images. (a)–(c) are the segments based on our optimization approach, (d)–(f) are based on the SAA method, and (g)–(i) are those of the ESP-2 method.

Table 3

The optimal scale and corresponding OSQ values obtained by the other optimization methods using the shape and compactness values identified with our approach.

Tile	Shape	Compactness	Scale		OSQ	
			SAA	ESP-2	SAA	ESP-2
T1	0.9	0.966	35	45	63.91%	68.75%
T2	0.9	0.3	30	54	42.00%	39.30%
T3	0.842	0.906	35	64	58.50%	67.48%

the different implementation methods used by the different EU countries to generate the data leading to different sources of error. To deal with those drawbacks, a supervised and automated Bayesian optimization framework was developed to identify the optimal parameters of the Multiresolution Segmentation (MRS) algorithm for segmenting

agricultural parcels in the federal state of Lower Saxony in Germany based on mono-temporal Sentinel-2 images.

To determine the optimal parameters, an area-weighted Jaccard index was used as a proxy for segmentation quality. The parameter combination with the highest weighted Jaccard index was adjudged the optimal for each  $10 \text{ km} \times 10 \text{ km}$  tile grid in Lower Saxony. The established optimal parameters were variable especially the compactness and scale, which indicated that a single parameter combination could not have guaranteed optimal segmentation for Lower Saxony. This reinforces the significance of our approach to determine the optimal parameters for different parts of Lower Saxony using tile grids. Given that the sizes of agricultural parcels in Germany do not drastically change from one year to another, the MRS parameters established for one year can potentially be used to segment agricultural parcels from images acquired within the same time window (month) from another year. We came to this preliminary conclusion after doing two tests. In

the first test, we used the MRS parameters established for tiles in May of 2018 to segment cloud-free images of those same tiles in May of 2019 and then used the LPIS data of 2019 to calculate the overall segmentation quality (OSQ) per tile. For the second test, we applied our Bayesian optimization approach to optimally segment those cloud-free images in May of 2019 using the LPIS data of 2019 as a reference and subsequently identified the OSQ of the optimal parameter combination per tile. The average difference in OSQ between those two tests over all the tiles was below 2%. Therefore, in the absence of LPIS for a particular year, the optimal MRS parameters established from a previous year can be used to segment images acquired within the same month of the current year. The developed approach can also be used to segment images taken at different times of the year to do in-season monitoring of the structural changes on agricultural parcels. Our approach outperformed the scale optimization method of the SAA and ESP-2 in all test areas. Those methods only focus on scale optimization, neglecting the other MRS parameters like shape and compactness. Given that different agricultural landscapes may have different structural compositions, our approach proved the importance of optimizing all three MRS parameters to achieve optimal segmentation. Our approach is independent of the input data, hence can be applied to any satellite image and reference data to optimize segmentation.

The research showed that the structural composition of agricultural parcels in a particular area influences the segmentation quality. The bigger the sizes of agricultural parcels are, the higher the segmentation quality. Over-segmentation was another factor that influenced the segmentation quality. It showed up when crops on a parcel are at substantially different stages of growth or when pixels within a parcel are very heterogeneous, thereby leading to the creation of small objects within a parcel. Under-segmentation, on the other hand, was largely dealt with in this research by merging LPIS parcels of the same land-use type during the segmentation evaluation process. This research also revealed that discrepancy measures alone do not give a complete picture of segmentation quality. Therefore, they should not be used in isolation but supported by visual inspection to make final decisions.

It is imperative to finally mention here that as we used LPIS as reference data to optimize the segmentation process, we did not achieve better geometric results than the LPIS as we saw in the best obtained OSQ being 69.17% at T1. LPIS is generated based on very high-resolution orthoimages with the spatial resolution being at least 1 m. We used Sentinel-2, which has a lower spatial resolution. With very high-resolution orthoimages like those used to create the LPIS, our Bayesian optimization approach can potentially be used to generate segments with similar geometric accuracy as the LPIS.

## 6. Future outlook

Going into the future, we will focus on the tiles with low segmentation quality to develop new methods of improving the segmentation quality. In this research, we applied our optimization approach to mono-temporal images. Therefore, multi-temporal Sentinel-2 images would be tested. Other auxiliary datasets like a Digital Elevation Model (DEM) and soil map would be used to augment the satellite images during the segmentation process to check if they can improve the segmentation quality. Instead of segmenting all agricultural areas in an image at once, segmentation would be done by separating arable and grassland areas. Initial tests based on mono-temporal images show promising results when this separation is done. In areas dominated by a single land-use, the merger of reference parcels with the same land-use would be turned off during the segmentation evaluation stage. This can potentially lead to the creation of smaller segments. Finally, another area of possible improvement could be the creation of tile grids based on similar structural compositions of agricultural parcels.

## CRediT authorship contribution statement

**Gideon Okpoti Tetteh:** Conceptualization, Methodology, Software, Formal analysis, Visualization, Writing - original draft. **Alexander Gocht:** Conceptualization, Supervision, Writing - review & editing. **Christopher Conrad:** Conceptualization, Supervision, Writing - review & editing.

## Declaration of Competing Interest

The authors declare that they have no known competing financial interests or personal relationships that could have appeared to influence the work reported in this paper.

## Acknowledgments

The authors thank the Ministry of Food, Agriculture and Consumer Protection of Lower Saxony for providing the LPIS reference layer, the German Federal Agency for Cartography and Geodesy (BKG) for providing the ATKIS dataset, and the European Space Agency (ESA) for the Sentinel-2 images. The authors are grateful to the Thünen Institute of Farm Economics for providing the computing resources and working environment for this research. We are also grateful to Stefan Erasmi for proofreading the article.

## Appendix A. Supplementary material

Supplementary data to this article can be found online at <https://doi.org/10.1016/j.compag.2020.105696>.

## References

- Achanta, R., Shaji, A., Smith, K., Lucchi, A., Fua, P., Süsstrunk, S., 2012. SLIC superpixels compared to state-of-the-art superpixel methods. *IEEE Trans. Pattern Anal. Mach. Intell.* 34, 2274–2282. <https://doi.org/10.1109/TPAMI.2012.120>.
- Anders, N.S., Seijmonsbergen, A.C., Bouten, W., 2011. Segmentation optimization and stratified object-based analysis for semi-automated geomorphological mapping. *Remote Sens. Environ.* 115, 2976–2985. <https://doi.org/10.1016/j.rse.2011.05.007>.
- Atzberger, C., 2013. Advances in remote sensing of agriculture: context description, existing operational monitoring systems and major information needs. *Remote Sens.* 5, 949–981. <https://doi.org/10.3390/rs5020949>.
- Baatz, M., Schäpe, A., 2000. Multiresolution Segmentation: an optimization approach for high quality multi-scale image segmentation. In: Strobl, J., Blaschke, T., Griesebner, G. (Eds.), *Angewandte Geographische Informations-Verarbeitung XII*. Wichmann Verlag, Karlsruhe, pp. 12–23.
- Belgiu, M., Csillik, O., 2018. Sentinel-2 cropland mapping using pixel-based and object-based time-weighted dynamic time warping analysis. *Remote Sens. Environ.* 204, 509–523. <https://doi.org/10.1016/j.rse.2017.10.005>.
- Belgiu, M., Drăguț, L., 2014. Comparing supervised and unsupervised multiresolution segmentation approaches for extracting buildings from very high resolution imagery. *ISPRS J. Photogramm. Remote Sens.* 96, 67–75. <https://doi.org/10.1016/j.isprsjprs.2014.07.002>.
- Benz, U.C., Hofmann, P., Willhauck, G., Lingenfelder, I., Heynen, M., 2004. Multi-resolution, object-oriented fuzzy analysis of remote sensing data for GIS-ready information. *ISPRS J. Photogramm. Remote Sens.* 58, 239–258. <https://doi.org/10.1016/j.isprsjprs.2003.10.002>.
- Bergstra, J., Bengio, Y., 2012. Random search for hyper-parameter optimization. *J. Mach. Learn. Res.* 13, 280–305.
- Bergstra, J.S., Bardenet, R., Bengio, Y., Kégl, B., 2011. Algorithms for hyper-parameter optimization. In: Shawe-Taylor, J., Zemel, R.S., Bartlett, P.L., Pereira, F., Weinberger, K.Q. (Eds.), *Advances in Neural Information Processing Systems 24*. Curran Associates Inc, pp. 2546–2554.
- Breiman, L., 2001. Random forests. *Mach. Learn.* 45, 5–32. <https://doi.org/10.1023/A:1010933404324>.
- Brochu, E., Cora, V.M., de Freitas, N., 2010. A Tutorial on Bayesian Optimization of Expensive Cost Functions, with Application to Active User Modeling and Hierarchical Reinforcement Learning. *ArXiv10122599 Cs*.
- Clinton, N., Holt, A., Scarborough, J., Yan, L., Gong, P., 2010. Accuracy assessment measures for object-based image segmentation goodness. *Photogramm. Eng. Remote Sens.* 76, 289–299. <https://doi.org/10.14358/PERS.76.3.289>.
- Conrad, C., Fritsch, S., Zeidler, J., Rücker, G., Dech, S., 2010. Per-field irrigated crop classification in arid Central Asia using SPOT and ASTER data. *Remote Sens.* 2, 1035–1056. <https://doi.org/10.3390/rs2041035>.
- Dewancker, I., McCourt, M., Clark, S., 2016. Bayesian Optimization Primer [WWW Document]. *Bayesian Optim. Primer*. URL <https://app.sigopt.com/static/pdf/SigOpt>.

- Bayesian Optimization Primer.pdf (accessed 3.4.20).
- Drăguț, L., Csillik, O., Eisank, C., Tiede, D., 2014. Automated parameterisation for multi-scale image segmentation on multiple layers. *ISPRS J. Photogramm. Remote Sens.* 88, 119–127. <https://doi.org/10.1016/j.isprsjprs.2013.11.018>.
- Drăguț, L., Tiede, D., Levick, S.R., 2010. ESP: a tool to estimate scale parameter for multiresolution image segmentation of remotely sensed data. *Int. J. Geogr. Inf. Sci.* 24, 859–871. <https://doi.org/10.1080/13658810903174803>.
- Dudley, N., Alexander, S., 2017. Agriculture and biodiversity: a review. *Biodiversity* 18, 45–49. <https://doi.org/10.1080/14888386.2017.1351892>.
- Eggensperger, K., Feurer, M., Hutter, F., Bergstra, J., Snoek, J., Hoos, H.H., Leyton-Brown, K., 2013. Towards an Empirical Foundation for Assessing Bayesian Optimization of Hyperparameters [WWW Document]. *Empir. Found. Assess. Bayesian Optim. Hyperparameters*. URL [https://ml.informatik.uni-freiburg.de/papers/13-BayesOpt\\_EmpiricalFoundation.pdf](https://ml.informatik.uni-freiburg.de/papers/13-BayesOpt_EmpiricalFoundation.pdf) (accessed 3.22.20).
- Foley, J.A., Ramankutty, N., Brauman, K.A., Cassidy, E.S., Gerber, J.S., Johnston, M., Mueller, N.D., O'Connell, C., Ray, D.K., West, P.C., Balzer, C., Bennett, E.M., Carpenter, S.R., Hill, J., Monfreda, C., Polasky, S., Rockström, J., Sheehan, J., Siebert, S., Tilman, D., Zaks, D.P.M., 2011. Solutions for a cultivated planet. *Nature* 478, 337–342. <https://doi.org/10.1038/nature10452>.
- Frazier, P.I., 2018. A Tutorial on Bayesian Optimization. ArXiv180702811 Cs Math Stat.
- Fukunaga, K., Hostetler, L., 1975. The estimation of the gradient of a density function, with applications in pattern recognition. *IEEE Trans. Inf. Theory* 21, 32–40. <https://doi.org/10.1109/TIT.1975.1055330>.
- García-Pedrero, A., Gonzalo-Martín, C., Lillo-Saavedra, M., 2017. A machine learning approach for agricultural parcel delineation through agglomerative segmentation. *Int. J. Remote Sens.* 38, 1809–1819. <https://doi.org/10.1080/01431161.2016.1278312>.
- Immitzer, M., Vuolo, F., Atzberger, C., 2016. First experience with sentinel-2 data for crop and tree species classifications in Central Europe. *Remote Sens.* 8, 166. <https://doi.org/10.3390/rs8030166>.
- Jaccard, P., 1901. Etude comparative de la distribution florale dans une portion des Alpes et du Jura. *Impr. Corbaz*.
- Ji, C.Y., 1996. Delineating agricultural field boundaries from TM imagery using dyadic wavelet transforms. *ISPRS J. Photogramm. Remote Sens.* 51, 268–283. [https://doi.org/10.1016/0924-2716\(95\)00017-8](https://doi.org/10.1016/0924-2716(95)00017-8).
- Jones, D.R., Schonlau, M., Welch, W.J., 1998. Efficient global optimization of expensive black-box functions. *J. Glob. Optim.* 13, 455–492. <https://doi.org/10.1023/A:1008306431147>.
- Kamilaris, A., Prenafeta-Boldú, F.X., 2018. Deep learning in agriculture: a survey. *Comput. Electron. Agric.* 147, 70–90. <https://doi.org/10.1016/j.compag.2018.02.016>.
- Lebourgeois, V., Dupuy, S., Vintrou, É., Ameline, M., Butler, S., Bégué, A., 2017. A combined random forest and OBIA classification scheme for mapping smallholder agriculture at different nomenclature levels using multisource data (simulated sentinel-2 time series, VHRS and DEM). *Remote Sens.* 9, 259. <https://doi.org/10.3390/rs9030259>.
- Li, P., Xiao, X., 2007. Multispectral image segmentation by a multichannel watershed-based approach. *Int. J. Remote Sens.* 28, 4429–4452. <https://doi.org/10.1080/01431160601034910>.
- Li, Y., Qi, H., Dai, J., Ji, X., Wei, Y., 2016. Fully Convolutional Instance-aware Semantic Segmentation. ArXiv161107709 Cs.
- Liu, D.C., Nocedal, J., 1989. On the limited memory BFGS method for large scale optimization. *Math. Program.* 45, 503–528. <https://doi.org/10.1007/BF01589116>.
- Lizotte, D., 2007. Automatic gait optimization with Gaussian process regression. *Proc. IJCAI* 944–949.
- Main-Knorn, M., Pflug, B., Louis, J., Debaecker, V., Müller-Wilm, U., Gascon, F., 2017. Sen2Cor for Sentinel-2. In: Bruzzone, L., Bovolo, F., Benediktsson, J.A. (Eds.), *Image and Signal Processing for Remote Sensing XXIII*. Presented at the Image and Signal Processing for Remote Sensing, SPIE, Warsaw, Poland, p. 3. <https://doi.org/10.1117/12.2278218>.
- Marchant, R., Ramos, F., 2012. Bayesian optimisation for Intelligent Environmental Monitoring. In: 2012 IEEE/RSJ International Conference on Intelligent Robots and Systems. Presented at the 2012 IEEE/RSJ International Conference on Intelligent Robots and Systems (IROS 2012). IEEE, Vilamoura-Algarve, Portugal, pp. 2242–2249. <https://doi.org/10.1109/IROS.2012.6385653>.
- Marpu, P.R., Neubert, M., Herold, H., Niemeyer, I., 2010. Enhanced evaluation of image segmentation results. *J. Spat. Sci.* 55, 55–68. <https://doi.org/10.1080/14498596.2010.487850>.
- Mesner, N., Oštir, K., 2014. Investigating the impact of spatial and spectral resolution of satellite images on segmentation quality. *J. Appl. Remote Sens.* 8, 083696. <https://doi.org/10.1117/1.JRS.8.083696>.
- Mockus, J., 2012. *Bayesian Approach to Global Optimization: Theory and Applications*. Springer Science & Business Media.
- Nasrallah, A., Baghdadi, N., Mhaweji, M., Faour, G., Darwish, T., Belhouchette, H., Darwich, S., 2018. A novel approach for mapping wheat areas using high resolution sentinel-2 images. *Sensors* 18, 2089. <https://doi.org/10.3390/s18072089>.
- Neubert, M., Herold, H., Meinel, G., 2008. Assessing image segmentation quality – concepts, methods and application. In: Blaschke, T., Lang, S., Hay, G.J. (Eds.), *Object-based Image Analysis: Spatial Concepts for Knowledge-Driven Remote Sensing Applications*, Lecture Notes in Geoinformation and Cartography. Springer, Berlin, Heidelberg, pp. 769–784. [https://doi.org/10.1007/978-3-540-77058-9\\_42](https://doi.org/10.1007/978-3-540-77058-9_42).
- Novelli, A., Aguilar, M., Aguilar, F., Nemmaoui, A., Tarantino, E., 2017. AssesSeg—a command line tool to quantify image segmentation quality: a test carried out in Southern Spain from satellite imagery. *Remote Sens.* 9, 40. <https://doi.org/10.3390/rs9010040>.
- Osborne, M.A., Garnett, R., Roberts, S.J., 2010. Active Data Selection for Sensor Networks with Faults and Change-points. In: 2010 24th IEEE International Conference on Advanced Information Networking and Applications. Presented at the 2010 24th IEEE International Conference on Advanced Information Networking and Applications. IEEE, Perth, Australia, pp. 533–540. <https://doi.org/10.1109/AINA.2010.36>.
- Peña-Barragán, J.M., Ngugi, M.K., Plant, R.E., Six, J., 2011. Object-based crop identification using multiple vegetation indices, textural features and crop phenology. *Remote Sens. Environ.* 115, 1301–1316. <https://doi.org/10.1016/j.rse.2011.01.009>.
- Persello, C., Tolpekin, V.A., Bergado, J.R., de By, R.A., 2019. Delineation of agricultural fields in smallholder farms from satellite images using fully convolutional networks and combinatorial grouping. *Remote Sens. Environ.* 231, 111253. <https://doi.org/10.1016/j.rse.2019.111253>.
- Rasmussen, C.E., Williams, C.K.I., 2006. *Gaussian Processes for Machine Learning, Adaptive Computation and Machine Learning*. MIT Press, Cambridge, Mass.
- Rieke, C., 2017. *Deep Learning for Instance Segmentation of Agricultural Fields* (Master's thesis dissertation). Friedrich-Schiller-University Jena, Thuringia, Germany.
- Schmedtmann, J., Campagnolo, M., 2015. Reliable crop identification with satellite imagery in the context of common agriculture policy subsidy control. *Remote Sens.* 7, 9325–9346. <https://doi.org/10.3390/rs70709325>.
- Shahriari, B., Swersky, K., Wang, Z., Adams, R.P., de Freitas, N., 2016. Taking the human out of the loop: a review of Bayesian optimization. *Proc. IEEE* 104, 148–175. <https://doi.org/10.1109/JPROC.2015.2494218>.
- Snoek, J., Larochelle, H., Adams, R.P., 2012. Practical Bayesian Optimization of machine learning algorithms. In: Pereira, F., Burges, C.J.C., Bottou, L., Weinberger, K.Q. (Eds.), *Advances in Neural Information Processing Systems 25*. Curran Associates, Inc., pp. 2951–2959.
- Stein, M.L., 1999. *Interpolation of Spatial Data: Some Theory for Kriging*, Springer Series in Statistics. Springer-Verlag, New York. <https://doi.org/10.1007/978-1-4612-1494-6>.
- Taşdemir, K., Wirthardt, C., 2012. Neural network-based clustering for agriculture management. *EURASIP J. Adv. Signal Process.* 2012. <https://doi.org/10.1186/1687-6180-2012-200>.
- Thornton, C., Hutter, F., Hoos, H.H., Leyton-Brown, K., 2013. Auto-WEKA: combined selection and hyperparameter optimization of classification algorithms. In: *Proceedings of the 19th ACM SIGKDD International Conference on Knowledge Discovery and Data Mining - KDD '13*. Presented at the the 19th ACM SIGKDD international conference. ACM Press, Chicago, Illinois, USA, p. 847. 10.1145/2487575.2487629.
- Trimble Germany GmbH, 2019. eCognition Developer 9.5.0 Reference Book. Trimble Germany GmbH, Germany.
- Turker, M., Kok, E.H., 2013. Field-based sub-boundary extraction from remote sensing imagery using perceptual grouping. *ISPRS J. Photogramm. Remote Sens.* 79, 106–121. <https://doi.org/10.1016/j.isprsjprs.2013.02.009>.
- Vogels, M.F.A., de Jong, S.M., Sterk, G., Douma, H., Addink, E.A., 2019. Spatio-temporal patterns of smallholder irrigated agriculture in the horn of Africa using GEOBIA and sentinel-2 imagery. *Remote Sens.* 11, 143. <https://doi.org/10.3390/rs11020143>.
- Watkins, B., Van Niekerk, A., 2019. Automating field boundary delineation with multi-temporal Sentinel-2 imagery. *Comput. Electron. Agric.* 167, 105078. <https://doi.org/10.1016/j.compag.2019.105078>.
- Woodcock, C.E., Strahler, A.H., 1987. The factor of scale in remote sensing. *Remote Sens. Environ.* 21, 311–332. [https://doi.org/10.1016/0034-4257\(87\)90015-0](https://doi.org/10.1016/0034-4257(87)90015-0).
- Yan, L., Roy, D.P., 2014. Automated crop field extraction from multi-temporal Web Enabled Landsat Data. *Remote Sens. Environ.* 144, 42–64. <https://doi.org/10.1016/j.rse.2014.01.006>.
- Zhang, Y.-J., 1996. A survey on evaluation methods for image segmentation. *Pattern Recognit.* 29, 1335–1346.
- Zielinski, R., Grandgirard, D., European Commission, Joint Research Centre, Institute for the Protection and the Security of the Citizen, 2008. Land Parcel Identification System (LPIs) anomalies' sampling and spatial pattern towards convergence of ecological methodologies and GIS technologies. Publications Office, Luxembourg.

4 Unsupervised parameterization for optimal segmentation of agricultural parcels from satellite images in different agricultural landscapes

#### **4 Unsupervised parameterization for optimal segmentation of agricultural parcels from satellite images in different agricultural landscapes**

Full bibliographic entry of paper:

Tetteh, G.O., Gocht, A., Schwieder, M., Erasmi, S., Conrad, C., 2020. Unsupervised Parameterization for Optimal Segmentation of Agricultural Parcels from Satellite Images in Different Agricultural Landscapes. Remote Sensing 12, 3096. <https://doi.org/10.3390/rs12183096>

Article

# Unsupervised Parameterization for Optimal Segmentation of Agricultural Parcels from Satellite Images in Different Agricultural Landscapes

Gideon Okpoti Tetteh <sup>1,\*</sup>, Alexander Gocht <sup>1</sup>, Marcel Schwieder <sup>1,2</sup>, Stefan Erasmi <sup>1</sup>  
and Christopher Conrad <sup>3</sup>

<sup>1</sup> Thünen Institute of Farm Economics, Bundesallee 63, 38116 Braunschweig, Germany;

alexander.gocht@thuenen.de (A.G.); marcel.schwieder@thuenen.de (M.S.); stefan.erasmi@thuenen.de (S.E.)

<sup>2</sup> Geography Department, Humboldt-Universität zu Berlin, Unter den Linden 6, D-10099 Berlin, Germany

<sup>3</sup> Institute of Geosciences and Geography, Martin-Luther-University Halle-Wittenberg, 06099 Halle, Germany; christopher.conrad@geo.uni-halle.de

\* Correspondence: gideon.tetteh@thuenen.de

Received: 27 July 2020; Accepted: 18 September 2020; Published: 21 September 2020



**Abstract:** Image segmentation is a cost-effective way to obtain information about the sizes and structural composition of agricultural parcels in an area. To accurately obtain such information, the parameters of the segmentation algorithm ought to be optimized using supervised or unsupervised methods. The difficulty in obtaining reference data makes unsupervised methods indispensable. In this study, we evaluated an existing unsupervised evaluation metric that minimizes a global score (GS), which is computed by summing up the intra-segment uniformity and inter-segment dissimilarity within a segmentation output. We modified this metric and proposed a new metric that uses absolute difference to compute the GS. We compared this proposed metric with the existing metric in two optimization approaches based on the Multiresolution Segmentation (MRS) algorithm to optimally delineate agricultural parcels from Sentinel-2 images in Lower Saxony, Germany. The first approach searches for optimal scale while keeping shape and compactness constant, while the second approach uses Bayesian optimization to optimize the three main parameters of the MRS algorithm. Based on a reference data of agricultural parcels, the optimal segmentation result of each optimization approach was evaluated by calculating the quality rate, over-segmentation, and under-segmentation. For both approaches, our proposed metric outperformed the existing metric in different agricultural landscapes. The proposed metric identified optimal segmentations that were less under-segmented compared to the existing metric. A comparison of the optimal segmentation results obtained in this study to existing benchmark results generated via supervised optimization showed that the unsupervised Bayesian optimization approach based on our proposed metric can potentially be used as an alternative to supervised optimization, particularly in geographic regions where reference data is unavailable or an automated evaluation system is sought.

**Keywords:** agricultural parcels; OBIA; multiresolution segmentation; unsupervised segmentation evaluation; spatial autocorrelation; weighted variance; bayesian optimization; optimal segmentation

## 1. Introduction

Agriculture is the single largest land use (LU) covering the Earth's land surface [1]. The increasing global population and the accompanying increase in food consumption are placing unparalleled demands on agricultural lands [2]. Some of the negative impacts of these demands include the loss of biodiversity [1], the degradation and destruction of natural ecosystems [3], and an increase in greenhouse gas (GHG) emission [4]. Ensuring food security while minimizing the negative impact of

agriculture on the environment requires the use of sustainable agricultural practices [2,5]. Formulating agricultural and environmental policies that ensure sustainable agriculture requires the development of an agricultural monitoring system. The foundation of such a system is accurate and up-to-date agricultural LU maps [6,7]. Agricultural LU maps are essential input data for various processes such as the estimation of biomass and yield [7], monitoring of the phenology of different agricultural LU types [7], modeling of GHG variability [8], estimation of the area of agricultural lands [9], and control of area-based subsidies paid to farmers [9].

The generation and continuous update of agricultural LU maps using traditional methods such as field surveys are inefficient and expensive [8]. Remote Sensing (RS) provides a better alternative due to the frequency at which data can be acquired over large geographical areas [10,11]. The availability of high-resolution satellite images has increased the popularity of Object-Based Image Analysis (OBIA) over traditional pixel-based image analysis [12]. Unlike pixels, which carry only spectral information, image objects additionally carry contextual and spatial information [12], thereby making them more useful for subsequent processes such as classification. The advantages of OBIA over pixel analysis for generating agricultural LU maps have been reported by these authors [10,13,14].

Image segmentation, which is the process of clustering image pixels into homogeneous objects, is a critical step in OBIA [15]. Various authors [16–20] have proved that the quality of segmentation has a direct impact on classification accuracy. One of the most popular segmentation algorithms is the Multiresolution Segmentation (MRS) algorithm proposed by Baatz et al. [21]. MRS is a bottom-up region merging algorithm that starts with one-pixel objects and then in a pairwise manner merges smaller objects into bigger ones until a user-given scale threshold is met [22]. In a recent review article by Ma et al. [23], the MRS algorithm as implemented in the eCognition software [24] accounted for 80.9% of 254 case studies the authors reviewed. This overwhelming popularity hinges on the fact that some exhaustive evaluation studies [25–27] have had eCognition coming up tops. In eCognition, the three main parameters that influence the quality of the MRS segmentation are scale, shape, and compactness. To obtain optimal segmentation results, it is imperative to optimize these parameters.

To optimize any segmentation algorithm, the quality of the segmentation output of that algorithm for different parameter combinations ought to be evaluated. This can be done through visual inspection, supervised segmentation evaluation, or unsupervised segmentation evaluation [28,29]. Visual inspection is subjective and inherently limits the number of segmentation evaluations that can be done due to its laborious nature [29]. The supervised evaluation methods assess a segmentation result by comparing it to a reference data and computing a global score (*GS*) that represents the degree of similarity between the segmentation result and the reference data [29]. The main limitation of supervised segmentation evaluation is that the acquisition of reference data is expensive and time-consuming [29]. This makes unsupervised segmentation evaluation indispensable, as it does not rely on reference data but purely on the content of an image to evaluate the segmentation result [29]. For the unsupervised evaluation methods, the *GS* is a statistical measure that indicates the level of intra-region uniformity and/or inter-region dissimilarity within the segmentation result [30]. In RS, two of the most used methods are the estimation of scale parameter (ESP) [31,32] tool and the objective function [33]. The ESP tool only addresses the intra-region uniformity of segments by making use of local variance graphs [34]. The objective function of Espindola et al. [33] is a combined measure that addresses intra-region uniformity through average area-weighted variance (*WV*) and inter-region dissimilarity through spatial autocorrelation using the global Moran's *I* (*MI*) [35]. A comparative analysis by Grybas et al. [36] showed that the objective function outperformed the ESP tool. Various variations [19,37–42] of the objective function have been used in the literature.

To compute the *GS* for each input image band, Espindola et al. [33] separately normalized the *WV* and *MI* between zero and one before summing them up. Böck et al. [43] identified a weakness with this normalization step, pointing out that the selection of which segmentation is optimal was dependent on the user-defined scale parameter range. They subsequently proposed the use of fixed ranges to normalize the *WV* and *MI*. This produced stable results regardless of the input range of the scale

parameter. In the remainder of the paper, we call this modification of Böck et al. [43] the Böck metric. Georganos et al. [16] identified some limitations with the normalization approach of the Böck metric, which triggered them to propose a different approach. The problem with their approach is that it adds some level of subjectivity to the evaluation process, because it requires some initial empirical tests. This makes their proposal unusable within our context of having a metric that can be used for automated segmentation evaluation without any human intervention.

In this study, we aimed at proposing a new unsupervised evaluation metric for assessing the segmentation output of any segmentation algorithm. To do so, we modified the Böck metric and proposed absolute difference (AD) as a means of computing the *GS*. We compared the Böck and AD metrics by separately using each of them in two unsupervised optimization approaches to optimize the parameters of the MRS algorithm to delineate agricultural parcels from 21 Sentinel-2 images of  $10 \times 10$  km sizes in Lower Saxony, Germany. In the first optimization approach, as is mostly done in the literature [20,31,37–39,43–45], we optimized scale while keeping the shape and compactness parameters constant at their default values. In the second optimization approach, we employed Bayesian optimization to optimize all three MRS parameters. The optimal segmentation results identified by each metric were evaluated with parcels from the Land Parcel Identification System (LPIS), which is a spatial database of agricultural parcels and their land-use types as declared by farmers within the European Union (EU) [46,47]. The optimal segmentation results of the Böck and AD metrics were compared to each other per each optimization approach. Further, we compared the optimal segmentation results of the unsupervised Bayesian optimization approaches based on the Böck and AD metrics to the benchmark segmentation results of Tetteh et al. [47], where they used supervised Bayesian optimization.

## 2. Study Area and Data

In this study, we used cloud-free Sentinel-2 images downloaded from the Copernicus Open Access Hub (<https://scihub.copernicus.eu>) covering the German federal state of Lower Saxony. The images were pre-processed in the previous study of Tetteh et al. [47] using the standard procedure of converting the top-of-atmosphere Level-1C images to the bottom-of-atmosphere Level-2A images with Sen2Cor [48] in the Sentinel Application Platform (SNAP) software. For each Level-2A image, the visible (red, green, blue) and near-infrared bands were extracted and composed into an image made up of four bands. This image is henceforth named VNIR. Each VNIR image has a spatial resolution of 10 m. To identify the optimal MRS parameters needed for segmenting agricultural parcels for every part of Lower Saxony, Tetteh et al. [47] clipped the VNIR images with  $10 \times 10$  km tile grids numbering 562 and additionally masked out all non-agricultural areas such as forests, built-up areas, water bodies, and roads. Out of these 562 images, we selected 21 tiles that spread across Lower Saxony as our study sites (Figure 1). These 21 tiles have diverse agricultural landscapes. The approach we used to select the 21 tiles can be found in the methodology section. Additional pieces of information such as the image acquisition date, percentage coverage of agricultural lands, and other descriptive statistics of the reference agricultural parcels in the LPIS per tile can be found in Appendix A (Table A1). The variation in the sizes of agricultural parcels per tile can also be found in Appendix A (Figure A1).

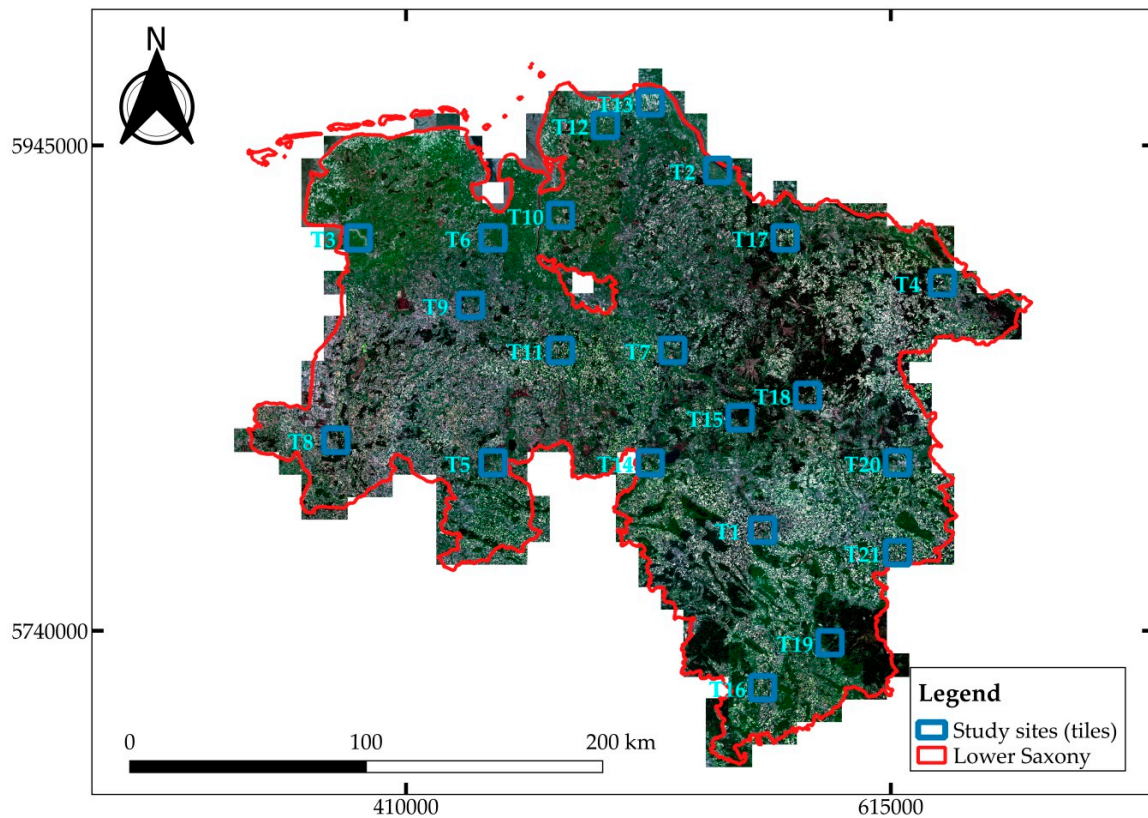


**Figure 1.** The study sites (tiles) overlaid on a mosaic of cloud-free and non-masked Sentinel-2 images captured in May 2018. The coordinates are in UTM Zone 32N (EPSG:32632).

### 3. Methodology

The simplified workflow we used to obtain the results is outlined in Figure 2. The core components of our workflow consist of image segmentation, modification of the existing unsupervised segmentation evaluation metric, unsupervised optimization of segmentation, and empirical evaluation of the segmentation results with reference parcels in the LPIS. These components will be fully covered in the proceeding subsections.

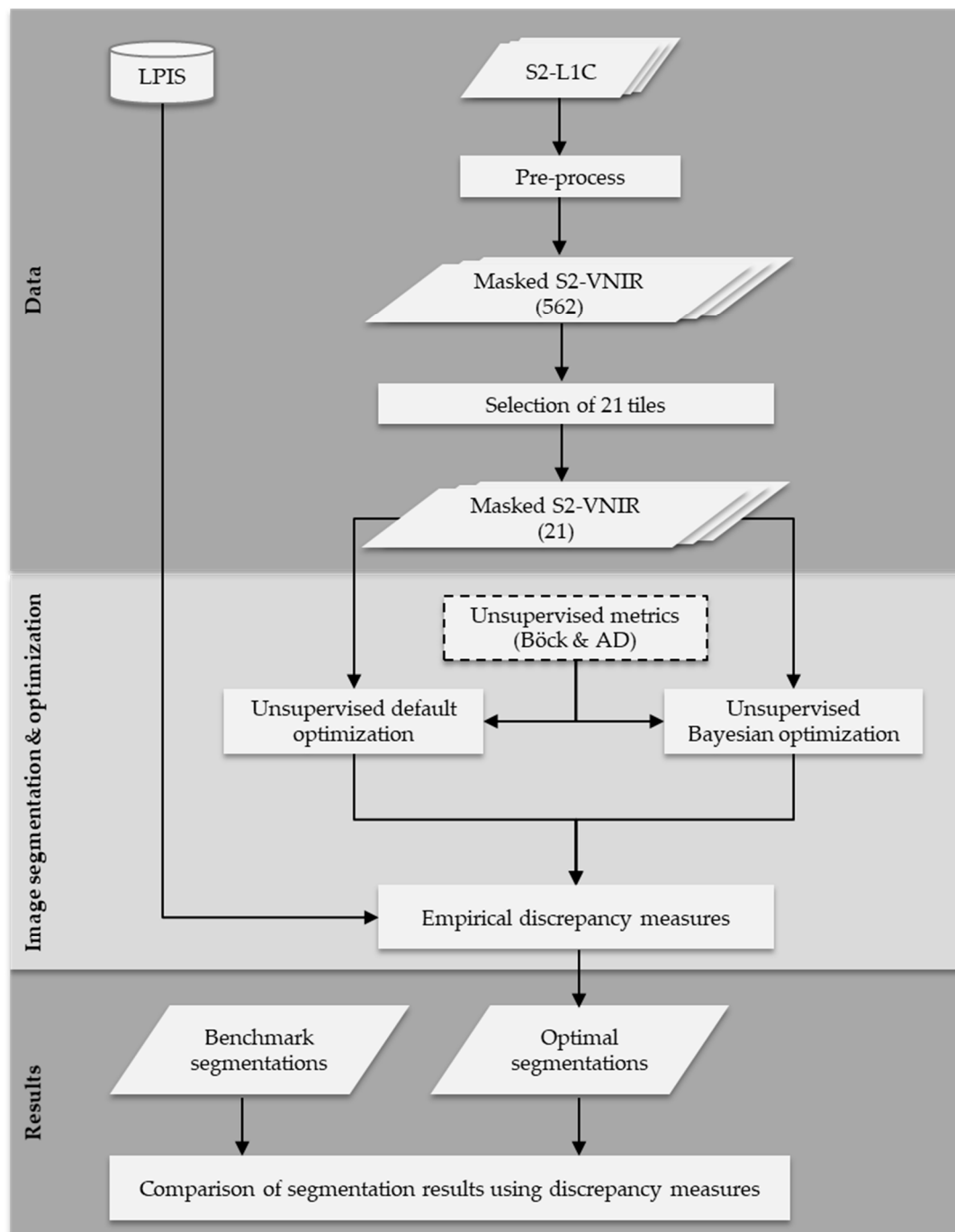


**Figure 2.** The simplified workflow we used in this study. Böck refers to the unsupervised segmentation evaluation metric proposed by Böck et al. [43], and absolute difference (AD) is the modified version we proposed in this study.

### 3.1. Selection of the 21 Tiles

The goal here is to reduce the number of tiles from 562 to a number that will lead to a reduction in the computational time needed for segmentation optimization. The 21 tiles were selected in a way that they were representative of the structural composition of the other tiles that were not used for further processing. The methodology we used to identify these 21 tiles is explained in this section.

For each reference parcel in the LPIS of the 562 tiles, we extracted the minimum bounding rectangle (MBR). The width and length of each MBR were calculated. Aspect was computed by dividing the width by the length. Then, we clustered the 562 tiles based on the average aspect per

tile using the k-means method. The determination of the appropriate number of clusters was done using the silhouette analysis [49]. This analysis is used to measure the internal consistency of clusters and the separability of those clusters. To perform the analysis, we clustered the average aspect of the 562 tiles using an incremental approach in which the number of clusters was initiated with two and increased by one in subsequent steps up to 21. For each cluster number, a silhouette coefficient was computed. The silhouette coefficients range from  $-1$  to  $1$ , with high values being more desirable, as it indicates the consistency within clusters and good separability among them. In our case, at cluster number 16, the silhouette coefficient was the highest (0.543), so we kept that. Then, we manually selected a tile from each of the 16 clusters and additionally included five more tiles to ensure a better spatial distribution over Lower Saxony, Germany.

### 3.2. Image Segmentation

In this study, image segmentation was done based on the implementation of the Multiresolution Segmentation (MRS) algorithm in eCognition Developer 9.5.0 [24]. Starting with one-pixel objects as seed points, in numerous subsequent steps, where the difference in heterogeneity between an object and any of its neighbors is minimal, the two objects are merged into a bigger one [22]. The heterogeneity of an object is calculated using the color and shape of that object [22,47]. The pairwise merging process is terminated when a user-given threshold is met [22]. In eCognition, three parameters (scale, shape, and compactness) influence the segmentation results of the MRS algorithm. Scale defines the minimum size of an object and is used as the threshold criterion to terminate the merging process. Shape refers to the weight placed on an object's form against its color information during the clustering process [47]. Shape and color add up to 1. In eCognition, one can only pass the shape weight, which then inversely modifies the color weight. Color is a requirement; hence, shape ranges from 0 to 0.9 [47]. Compactness defines the weight of an objects' squareness against its smoothness during the clustering process [47]. The compactness and smoothness weights also add up to 1. In eCognition, one passes the compactness weight, which inversely changes the smoothness weight. Extensive details about the MRS algorithm can be found in these pieces of literature [21,22,24]. Generating optimal segments requires the optimization of the MRS parameters [47].

### 3.3. Segmentation Optimization

To optimize any segmentation algorithm, one needs to be able to assess the quality of the segmentation results churned out by the algorithm for different parameter combinations. In this study, we used unsupervised segmentation evaluation metrics that measure the quality of the segmentation results purely based on the spectral values of the underlying image.

#### 3.3.1. Existing Unsupervised Segmentation Evaluation Metrics

To evaluate a segmentation result, Espindola et al. [33] used average area-weighted variance (*WV*) and Moran's I (*MI*) [35]. The *WV* measures intra-segment homogeneity [33]. Therefore, it shows the level of under-segmentation in a segmentation result. Lower *WV* values indicate lower under-segmentation [38]. It is derived by first calculating the variance of pixels within each segment per image band, weighting the variance by each segment's area, and then averaging over all segments to obtain one global value per band. Equation (1) shows the formulation of *WV*, where  $a_i$  represents the area of a segment,  $v_i$  is the variance of pixels within a segment, and  $n$  is the number of segments.

$$WV = \frac{\sum_{i=1}^n a_i * v_i}{\sum_{i=1}^n a_i} \quad (1)$$

*MI* measures the inter-segment heterogeneity [33] within the segmentation result, thereby being indicative of the level of over-segmentation. Lower *MI* values indicate lower over-segmentation [38]. Similar to the *WV*, it is also computed per image band. Its formulation is shown by Equation (2), where

$n$  is the number of segments,  $y_i$  and  $y_j$  are the respective mean values of an image band for segments  $i$  and  $j$ ,  $\bar{y}$  is the mean band value of the entire image, and  $w_{ij}$  is a weight matrix that measures the spatial contiguity [43] between a segment and its neighbors. The elements of the matrix are either zero or one. One indicates that segments  $i$  and  $j$  have a common boundary, and zero indicates they do not.

$$MI = \frac{n \sum_{i=1}^n \sum_{j=1}^n w_{ij} (y_i - \bar{y})(y_j - \bar{y})}{\left(\sum_{i=1}^n (y_i - \bar{y})^2\right) \left(\sum_{i=1}^n \sum_{j=1}^n w_{ij}\right)} \quad (2)$$

$MI$  ranges from  $-1$  (perfect dispersion of segments) to  $1$  (perfect clustering of segments). Lower  $MI$  values indicate that the mean spectral values of neighboring segments within a segmentation layer are more different from each other, thereby indicating lower over-segmentation. Higher  $MI$  values show that the mean spectral values of the neighboring segments are more similar, which means that there is more over-segmentation present in the segmentation layer.

To compute a single global score ( $GS$ ) per image band for a segmentation result, the  $WV$  and  $MI$  values are individually normalized using Equation (3) [37], where  $X$  is either the  $WV$  or  $MI$ . Then, the normalized  $WV$  ( $nWV$ ) and normalized  $MI$  ( $nMI$ ) are summed up to obtain the  $GS$  per image band [33]. Then, the final  $GS$  for the segmentation result is computed with Equation (4), where  $b$  represents the number of bands in the image, which is four in our case.

$$\frac{X - X_{min}}{X_{max} - X_{min}} \quad (3)$$

$$GS = \frac{1}{b} \sum_{i=1}^b (nWV_i + nMI_i) \quad (4)$$

The  $GS$  ranges from zero (best quality) to one (worst quality). Given a set of segmentation results generated with different segmentation parameters, the parameter combination that results in the lowest  $GS$  is deemed as optimal. Böck et al. [43] observed that the identification of the optimal  $GS$  based on the definition of Espindola et al. [33] is highly influenced by the range of the user-defined scale parameter. Different scale parameter ranges yield different optimal segmentation results for the same image. According to Böck et al. [43], this instability is due to the normalization process in Equation (3). To deal with this problem, Böck et al. [43] proposed fixed range normalization for  $WV$  and  $MI$  as respectively captured by Equation (5) and Equation (6) before computing the final  $GS$ , where  $\bar{V}$  is the variance of the entire image per band. To obtain Equation (6), Böck et al. [43] respectively replaced  $X_{min}$  and  $X_{max}$  in Equation (3) with  $-1$  and  $1$ , which are the theoretical extrema of  $MI$ .

$$nWV = \frac{WV}{\bar{V}} \quad (5)$$

$$nMI = \frac{MI + 1}{2} \quad (6)$$

The Böck metric also ranges from zero (best quality) to one (worst quality).

### 3.3.2. Metric Proposal Based on Absolute Difference (AD)

According to Georganos et al. [16], the fixed ranged normalization proposal put forward by Böck et al. [43] makes two problematic assumptions. The first one is that where there is complete under-segmentation, i.e., where one segment is created for the entire image, the  $WV$  becomes equal to the image variance; hence,  $nWV$  becomes 1. When this happens, the equivalent value of  $MI$  and by extension  $nMI$  becomes undefined, because a spatial network of more than one segment is required to compute  $MI$ . Secondly, in the case of complete over-segmentation, i.e., where each pixel in the image is a segment,  $MI$  is  $-1$  and  $nMI$  becomes 0, but the corresponding value of  $WV$  may be very low and

not necessarily zero. In RS, it is highly implausible to obtain complete over-segmentation; hence, an  $MI$  value of  $-1$  is hardly realized [16]. Furthermore, Georganos et al. [16] did some tests and observed that the Böck metric has the potential of selecting under-segmented objects as optimal. We tested this hypothesis using some simulated segmentation data captured by Figure 3. Figure 3a shows the reference data, while Figure 3b–d captures three different corresponding segmentation results. For each dataset in Figure 3, each row represents a segment; hence, there are four segments for each dataset. Figure 3b captures a situation where there is a lot of clustering with minimal under-segmentation, Figure 3c is a situation where there is a balance between clustering and dispersion with moderate under-segmentation, and Figure 3d represents a situation where there is a lot of dispersion with a high level of under-segmentation. The  $MI$ ,  $nMI$ ,  $nWV$ , and  $GS$  of the Böck metric computed for the simulated segmentation results (Figure 3b–d) are captured by Table 1. As postulated by Georganos et al. [16], the Böck metric selected the segmentation result with the highest level of under-segmentation as optimal, given that it had the lowest  $GS$  value.

(a)	(b)	(c)	(d)
1 1 1 1	1 1 1 1	1 1 1 1	1 2 1 2
1 1 1 1	1 1 1 2	1 1 2 2	2 1 2 1
2 2 2 2	1 2 2 2	1 2 1 2	1 2 1 1
2 2 2 2	2 2 2 2	2 2 2 1	2 1 2 2

**Figure 3.** Simulated reference and segmentation data. The reference dataset is represented by (a). Three different corresponding segmentation results are represented by (b–d), respectively. Each row in each dataset represents a segment; hence, there are four segments in all.

**Table 1.** The Moran’s  $I$  ( $MI$ ), normalized  $MI$  ( $nMI$ ), normalized weighted variance ( $nWV$ ), and global score ( $GS$ ) of the Böck metric computed for the simulated data at Figure 3. The bold-faced text within the body of the table is the optimal result.

Identifier	$MI$	$nMI$	$nWV$	$GS$ (Böck)
Figure 3b	0.400	0.700	0.375	1.075
Figure 3c	<b>-0.018</b>	<b>0.491</b>	<b>0.698</b>	<b>1.189</b>
Figure 3d	<b>-0.667</b>	<b>0.167</b>	<b>0.875</b>	<b>1.042</b>

The issues raised by Georganos et al. [16] point to the problem posed by Equation (6), where the theoretical extrema of  $MI$  are used to normalize the  $MI$ . As visible in Table 1, after normalizing the  $MI$ , the numerical difference between the  $nWV$  and  $MI$  increased in Figure 3b, where the  $MI$  was positive. However, for Figure 3c,d, the numerical differences diminished substantially. Therefore, in areas with more dispersion, the Böck metric has the potential of selecting under-segmented results as optimal, as it would be more biased toward  $nMI$  [16]. To overcome these issues, we used two steps. First, we did not normalize the  $MI$  given that by definition, it lies between  $-1$  and  $1$ . We maintained the  $nWV$ . Therefore, the minimum and maximum values of  $nWV$  will correspond to the minimum and maximum of  $MI$ . Second, to obtain the final  $GS$ , we computed the absolute difference between the  $MI$  and  $nWV$  per band and then averaged over all bands as shown by Equation (7), where the notations have the same meaning as Equation (4). This ensures that the  $MI$  and  $nWV$  have a fair chance of influencing the  $GS$  depending on their respective magnitudes. Similar to the Böck metric, low values mean good quality, and high values mean bad quality. The outcome of this modification, named the AD metric, for the simulated segmentation results (Figure 3b–d) is shown in Table 2. The AD metric correctly selected the least under-segmented result as optimal, followed by the moderately under-segmented. We tested another distance metric, specifically Euclidean Distance (ED), to combine the  $MI$  and  $nWV$  values at the 21 tiles, but the AD metric proved superior, so we maintained that as our proposal. The difficulty with using ED to compute the  $GS$  lies in the fact that given any two

numbers, here  $MI$  and  $nWV$ , it places more emphasis on the larger number than the smaller one, thereby accentuating the influence of the larger number on the overall outcome.

$$GS = \frac{1}{b} \sum_{i=1}^b |MI_i - nWV_i| \quad (7)$$

**Table 2.** The  $MI$ ,  $nWV$ , and  $GS$  of the AD metric computed for the simulated data in Figure 3. The bold-faced text within the body of the table is the optimal result.

Identifier	$MI$	$nWV$	$GS$ (AD)
Figure 3b	0.400	0.375	0.025
Figure 3c	-0.018	0.698	0.716
Figure 3d	-0.667	0.875	1.542

### 3.3.3. Unsupervised Segmentation Optimization

The point of optimization within the context of this study is to identify the MRS parameter combination that yields the lowest  $GS$  per metric. The segmentation output corresponding to this combination is the optimal result. We tested two optimization approaches in this study.

For the first approach, which we termed default optimization, we optimized the scale parameter while keeping the shape and compactness parameters constant at their default, as is mostly done in the literature [20,31,37–39,43–45]. Shape was kept at 0.1, and compactness was kept at 0.5. The scale ranged from 10 to 300 with intervals of 10. The segmentation output corresponding to the scale parameter with the lowest  $GS$  is the optimal output.

The second optimization approach is Bayesian optimization, which was used to optimize all three MRS parameters. We adopted the Bayesian optimization approach of Tetteh et al. [47] but used it within an unsupervised optimization framework. Applying Bayesian optimization requires four main definitions:

1. The domain space (minimum and maximum values) of each input parameter. The domain space of scale was defined as 20 and 200, for shape 0.0 and 0.9, and for compactness 0.0 and 1.0. These parameter ranges were also used by Tetteh et al. [47] in their approach.
2. An objective function to optimize. For our study, the objective function to optimize is  $f(x)$ , where  $x$  is a parameter combination of scale, shape, and compactness. The function takes the parameter combination, performs image segmentation, computes the  $GS$  of the segmentation output, and finally returns the  $GS$ .
3. A surrogate model for the objective function. To build the surrogate model, one has to first define a prior probability distribution that captures the prior behavior of the objective function. We chose Gaussian Processes (GP) [50] as the prior probability distribution. Then, some initial parameter combinations together with their corresponding  $GS$  are used to initialize the whole optimization process. We used 125 parameter combinations as initialization samples. These 125 parameter combinations were selected in a way to ensure uniform and representative distribution over each parameter space. For scale, the values were (40, 80, 120, 160, 200), and for both shape and compactness, the values were (0.1, 0.3, 0.5, 0.7, 0.9). The grid search method was used to calculate the corresponding  $GS$  for the 125 samples. These samples were used to update the GP to obtain posterior probability distribution over the objective function.
4. An acquisition function to be used in sampling new parameter combinations to be evaluated with the objective function. For the acquisition function, we used expected improvement (EI) [51]. EI is used to iteratively select new parameter combinations with the highest probability of optimizing the objection function. We sampled 50 new parameter combinations with the EI function in 50 iterations. At each iteration, out of 10,000 parameter combinations randomly

sampled from the domain space, the combination with the highest likelihood of improving upon the current optimal parameter combination is identified by the EI function using the current posterior probability distribution. Then, this identified parameter combination is evaluated with the objective function, and the corresponding *GS* is used to update the current posterior probability distribution. In all, 175 combinations were used within the Bayesian optimization approach to identify the optimal one.

A more detailed explanation of Bayesian optimization can be found here [52–55]. The Böck and AD metrics were separately used in the two optimization approaches to optimize the segmentation of agricultural parcels. The optimal segmentation identified by each metric was further evaluated through empirical discrepancy measures. Given the sheer number of segmentations that had to be done, we used eCognition Server 9.5.0 and the eCognition command-line interface (CLI) to automate the segmentation process [47]. For the initial 125 parameter combinations that were used to initialize the Bayesian optimization method, two parallel processes were executed, as our eCognition Server license was limited to two [47]. The Python programming language was used to glue everything together. The implementation of Bayesian optimization via Scikit-optimize in Python was used [47].

### 3.4. Empirical Discrepancy Measures

To identify which optimization approach and metric performed better per tile, we computed four empirical discrepancy measures (Table 3) by comparing the optimal segmentation results to the reference agricultural parcels in the LPIS. The quality rate (QR) [56] measures the level of geometric match between the segmentation result and the reference parcels. It is the only measure that takes into account both the amount of agreement and disagreement between the reference parcels and their corresponding segments [57]. Therefore, it can single-handedly be used to judge the quality of segmentation. When a reference parcel is larger than its corresponding segment, over-segmentation (OR) [57] occurs, and when the segment is larger, under-segmentation (UR) [57] occurs. The root mean square (RMS) [56] combines the OR and UR into a single measure. In the formulas in Table 3,  $X_i$  is a reference parcel and  $Y_i$  is its corresponding segment, and  $n$  is the total number of segments. The discrepancy measures are first computed per segment in a segmentation result. To obtain a single discrepancy measure for an entire segmentation result, an area-weighted average was used (Table 3).

**Table 3.** Empirical discrepancy measures used to evaluate the optimal segmentations.

Measure	Formula	Range	Source
Quality rate (QR)	$\frac{\sum_{i=1}^n \text{Area}(Y_i) * \frac{\text{Area}(X_i \cap Y_i)}{\text{Area}(X_i \cup Y_i)}}{\sum_{i=1}^n \text{Area}(Y_i)}$	0 (worst) to 1 (perfect) segmentation	[56]
Over-segmentation (OR)	$1 - \frac{\sum_{i=1}^n \text{Area}(Y_i) * \frac{\text{Area}(X_i \cap Y_i)}{\text{Area}(X_i)}}{\sum_{i=1}^n \text{Area}(Y_i)}$	0 (perfect) to 1 (worst) segmentation	[57]
Under-segmentation (UR)	$1 - \frac{\sum_{i=1}^n \text{Area}(Y_i) * \frac{\text{Area}(X_i \cap Y_i)}{\text{Area}(Y_i)}}{\sum_{i=1}^n \text{Area}(Y_i)}$	0 (perfect) to 1 (worst) segmentation	[57]
Root mean square (RMS)	$\sqrt{\frac{\text{OR}^2 + \text{UR}^2}{2}}$	0 (perfect) to 1 (worst) segmentation	[56]

## 4. Results

### 4.1. Optimal Segmentation Based on Default Optimization

For each tile, Figure 4 shows the QR for the optimal segmentations identified by the AD and Böck metrics using the default shape value of 0.1 and 0.5 for compactness. The other empirical evaluation measures (OR, UR, and RMS) are captured by Appendix A (Table A2). At T11, the two metrics obtained the same result. Except for T3 and T18, where the Böck metric was marginally better, the AD metric was remarkably better at the other tiles. The highest difference between the two metrics was recorded at T1, where the AD metric exceeded the Böck metric by 17%. The lowest differences were recorded at

T2 and T19, where the AD metric was about 1% better. The optimal segmentation results identified by our metric were the least under-segmented except for T2 and T19, where our metric was rather the least over-segmented. The RMS values of our metric were lower at all tiles except T19.

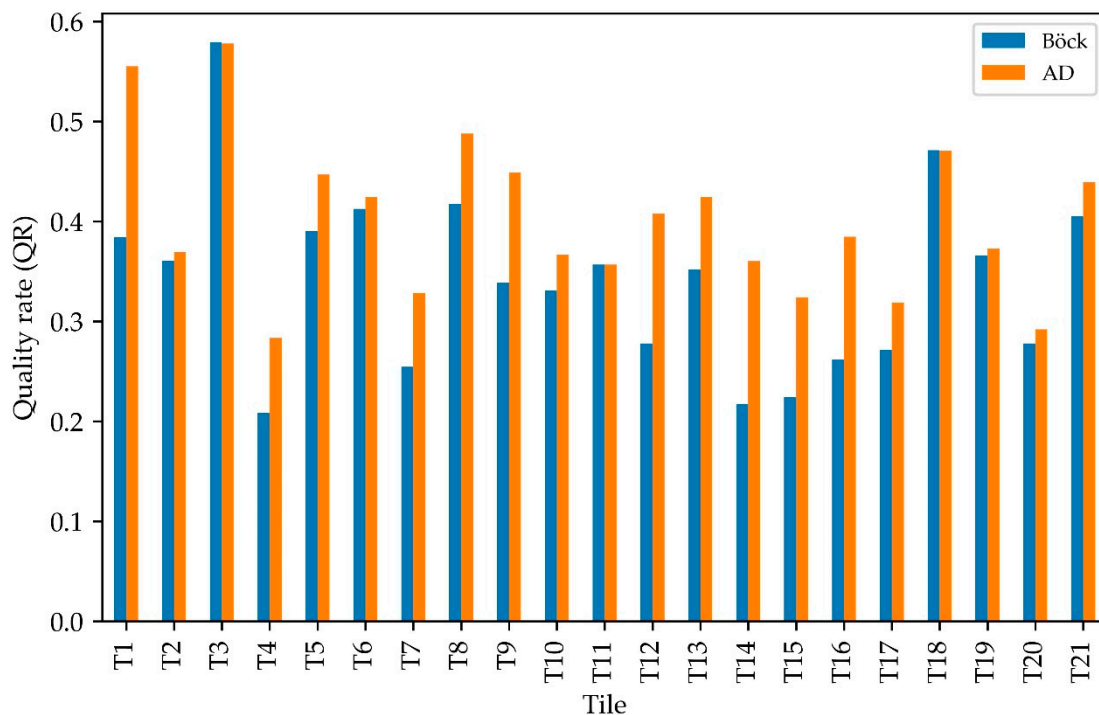


**Figure 4.** The quality rate (QR) measure computed for each optimal segmentation result identified by the AD and Böck metrics based on the default optimization (shape = 0.1, compactness = 0.5).

The Böck metric often selected higher scale values than the AD metric, even to the extent that at T1, it chose the highest scale value as the optimal. This led to massive under-segmentation, an example of which is shown in Figure 5a at T1. Four different LU types—namely, winter wheat, winter rapeseed, spring barley, and pastures—are present in this area. Due to the high scale value selected by the Böck metric, only one segment was created containing all the aforementioned LU types, leading to massive under-segmentation. The AD metric did a better job of separating the different LU types, hence reducing under-segmentation (Figure 5b). The segments generated based on the AD metric had a better geometric match to the LPIS reference parcels.

To understand the different behaviors of the Böck and AD metrics, we explored the  $nWV$ ,  $MI$ ,  $nMI$ , and the corresponding  $GS$  computed for each scale value at T1, where the AD metric was substantially better, and then T3, where the Böck metric was marginally better. For both metrics, the  $nWV$  increased with increasing scale as the pixels in each segment became more varied, while the  $MI$  and  $nMI$  exhibited an opposite behavior (Figures 6 and 7). Figure 6a shows that as the scale increased, the Böck metric decreased in response until it reached its minimum at scale 300. As a reminder, lower  $GS$  values of a metric correspond to more accurate segmentation results. Our metric, on the other hand, as captured by Figure 6b, exhibited a decreasing trend up to scale 190 and then started to increase in response to increasing  $nWV$  and decreasing  $MI$ . The  $GS$  was at its lowest at scale 190. At T3 (Figure 7), where the Böck metric was marginally better, the  $GS$  of both metrics had one commonality. After some initial decreasing behavior, they both started to continuously increase around the median of the scale range, which is 155. The optimal scale selected by the Böck metric was 150, and that of the AD metric was 140.

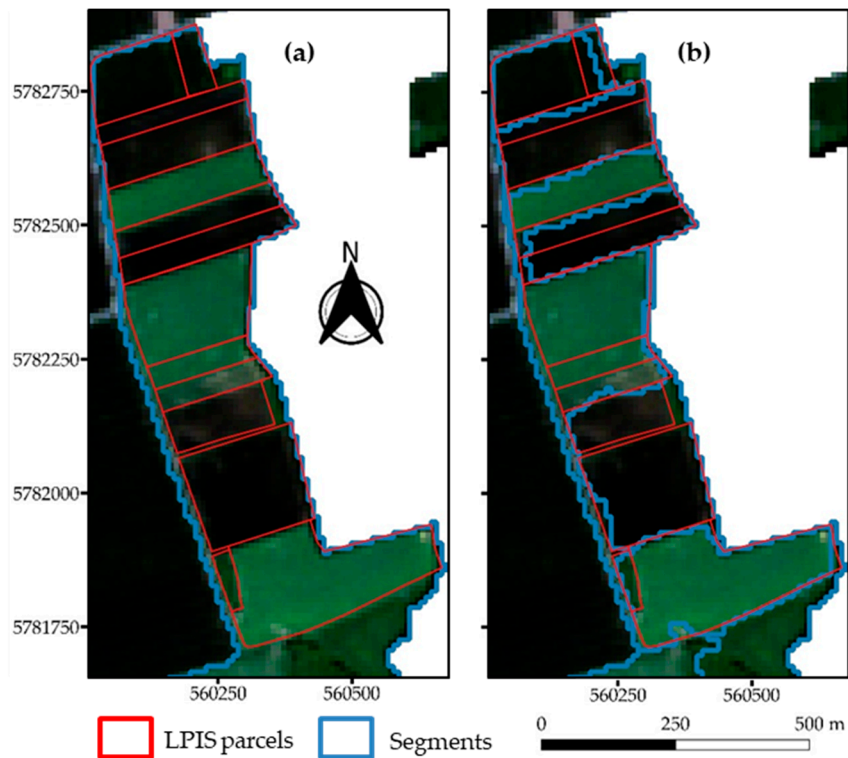


**Figure 5.** Examples of segments identified as optimal at T1 using the default shape and compactness parameters. (a) An example based on the optimal segmentation identified by the Böck metric showing massive under-segmentation and (b) based on the AD metric, which shows a better delineation of the agricultural parcels with lower under-segmentation compared to Böck. The coordinates are in UTM Zone 32N (EPSG:32632).

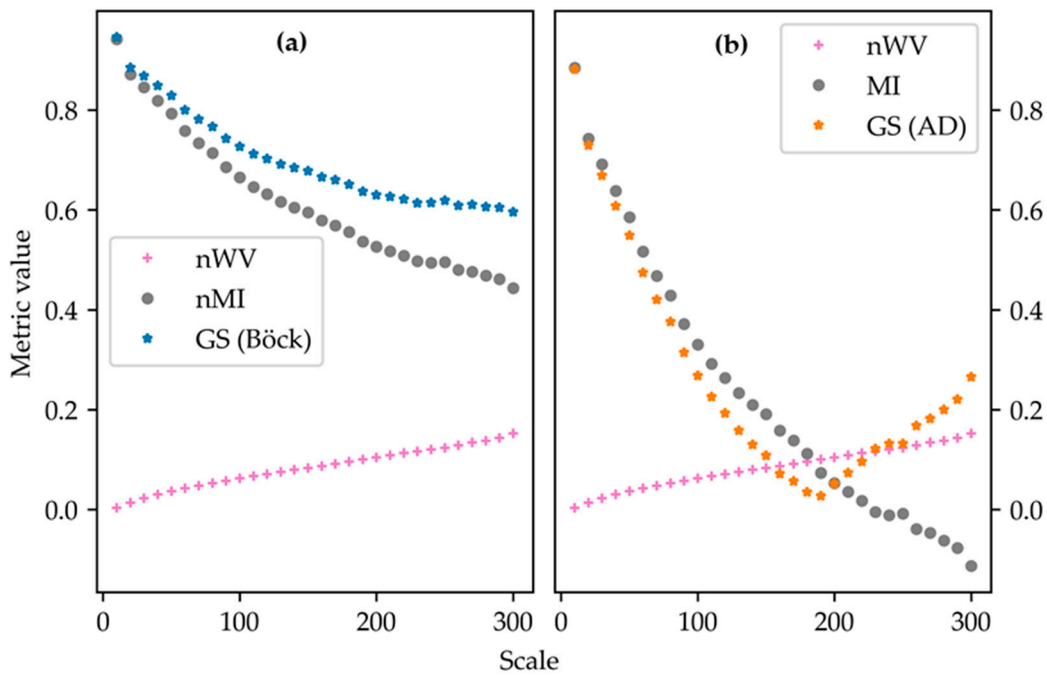


**Figure 6.** The normalized average area-weighted variance ( $nWV$ ), Moran’s I ( $MI$ ), normalized Moran’s I ( $nMI$ ), and global score ( $GS$ ) computed for each scale at T1 based on (a) the Böck metric and (b) the AD metric.

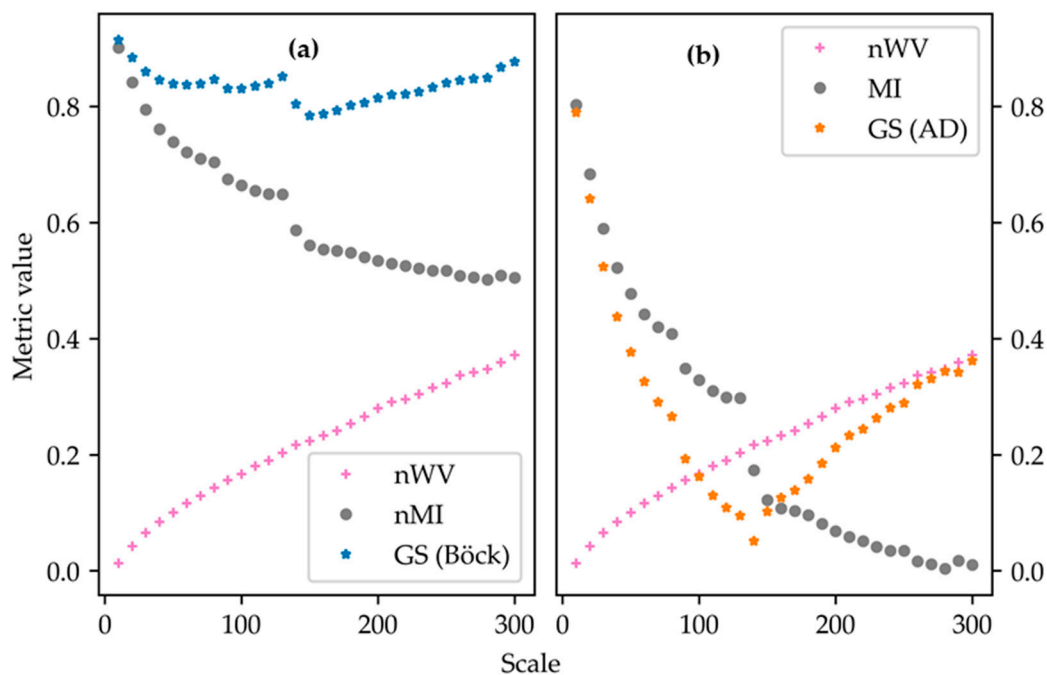


**Figure 7.** The normalized average area-weighted variance ( $nWV$ ), Moran's  $I$  ( $MI$ ), normalized Moran's  $I$  ( $nMI$ ), and global score ( $GS$ ) computed for each scale at T3 based on (a) the Böck metric and (b) the AD metric.

#### 4.2. Optimal Segmentation Based on Bayesian Optimization

We employed Bayesian optimization to respectively minimize the two unsupervised metrics (Böck and AD) at the 21 tiles to optimize the MRS parameters. To identify the optimal MRS parameters, Tetteh et al. [47] used their supervised Bayesian optimization approach to directly maximize the QR. We consider the results achieved by their approach as the benchmark results. For the analysis here, we compared the results achieved by the two unsupervised Bayesian optimization approaches to each other and in parallel compared both to the benchmark results. The QR measures of the optimal segmentations obtained by the supervised and the two unsupervised approaches for the 21 tiles used in this research are captured by Figure 8. The other empirical evaluation measures can be found in Appendix A (Table A3). The unsupervised Bayesian optimization approach based on the AD metric outperformed the Böck metric at all tiles. The approach based on the AD metric was over 22% better at T1 and T15, and it was about 1% better at T6 in comparison with the unsupervised Bayesian approach based on the Böck metric. The supervised approach was expectedly better than both unsupervised approaches at all tiles. At T7 and T17, the segmentation quality of the supervised approach was over 20% higher than the unsupervised AD approach. However, at T2 and T19, the supervised approach was just about 2% better. Regarding the Böck metric, the supervised approach was over 30% better at T1, T14, and T15, and it was about 5% better at T2. The segmentation results of the unsupervised approaches were generally more under-segmented but less over-segmented compared to the supervised approach. The RMS measure was in favor of the supervised approach at all tiles. The optimal segmentation results of the three Bayesian optimization approaches symbolized by the QR calculated per segment at T1, T2, and T17 are captured by Figures 9–11, respectively. For all three figures, panel (a) captures the Sentinel-2 image, panel (b) shows the Böck results, panel (c) shows the supervised Bayesian optimization results, and panel (d) captures the AD results. Figure 12 shows a specific case of segments within the optimal results of the three Bayesian optimization approaches at T1 for the same area shown in Figure 5.

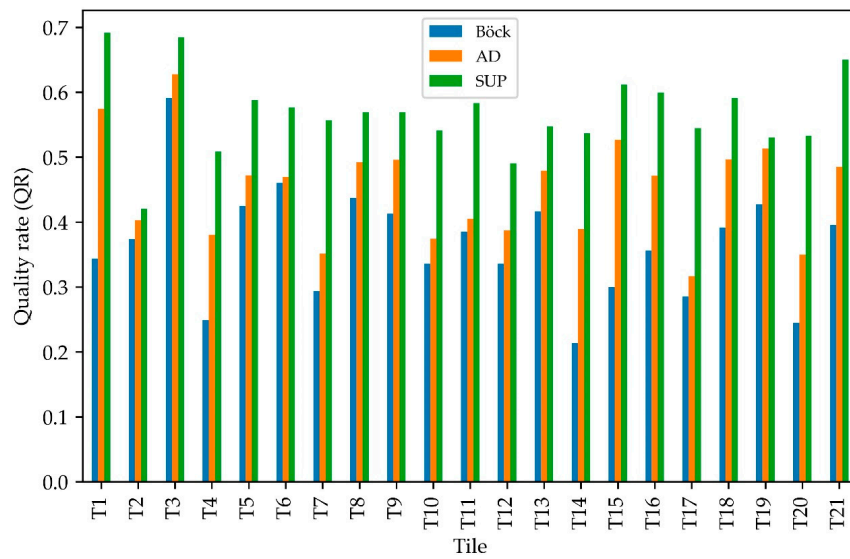


**Figure 8.** The quality rate (QR) measure computed for the unsupervised Bayesian optimization approaches based on the Böck and AD metrics, and the supervised Bayesian optimization (SUP) approach that was used to maximize the QR measure by Tetteh et al. [47].

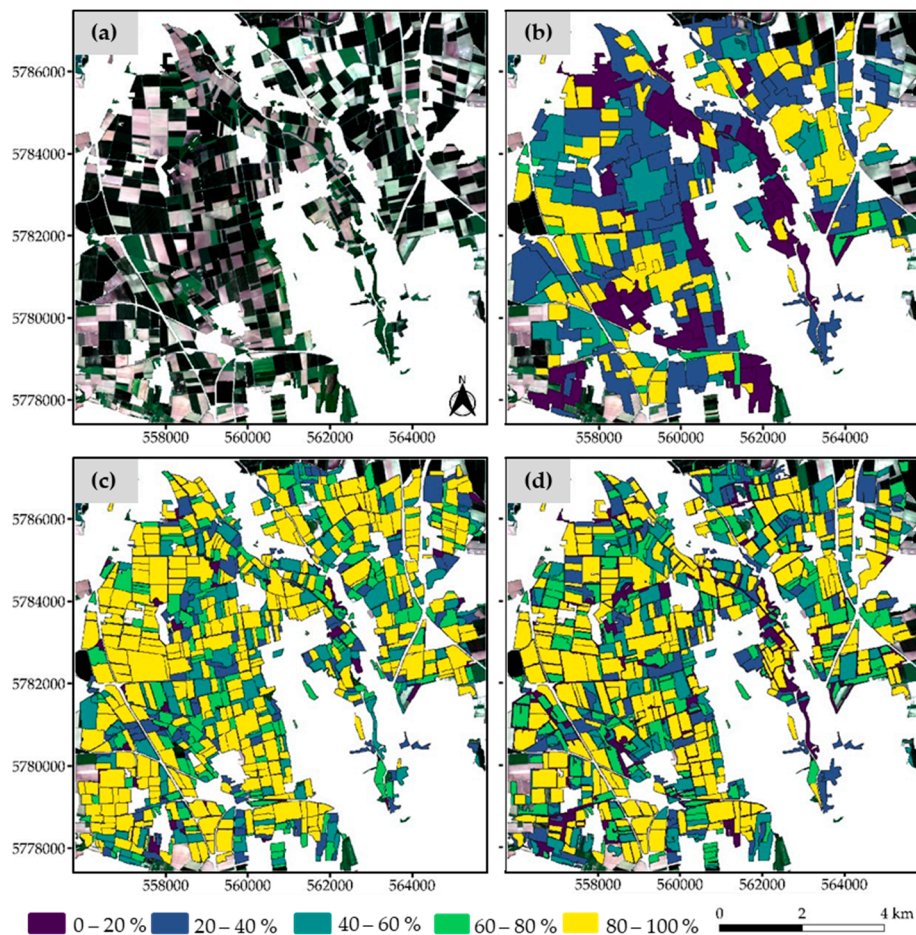


**Figure 9.** The outcome of the three Bayesian optimization approaches at T1. The Sentinel-2 image is shown by (a). The optimal segments as identified by (b) the Böck metric, (c) the supervised Bayesian optimization approach, and (d) the AD metric are symbolized by their respective QR measures. The coordinates are in UTM Zone 32N (EPSG:32632).

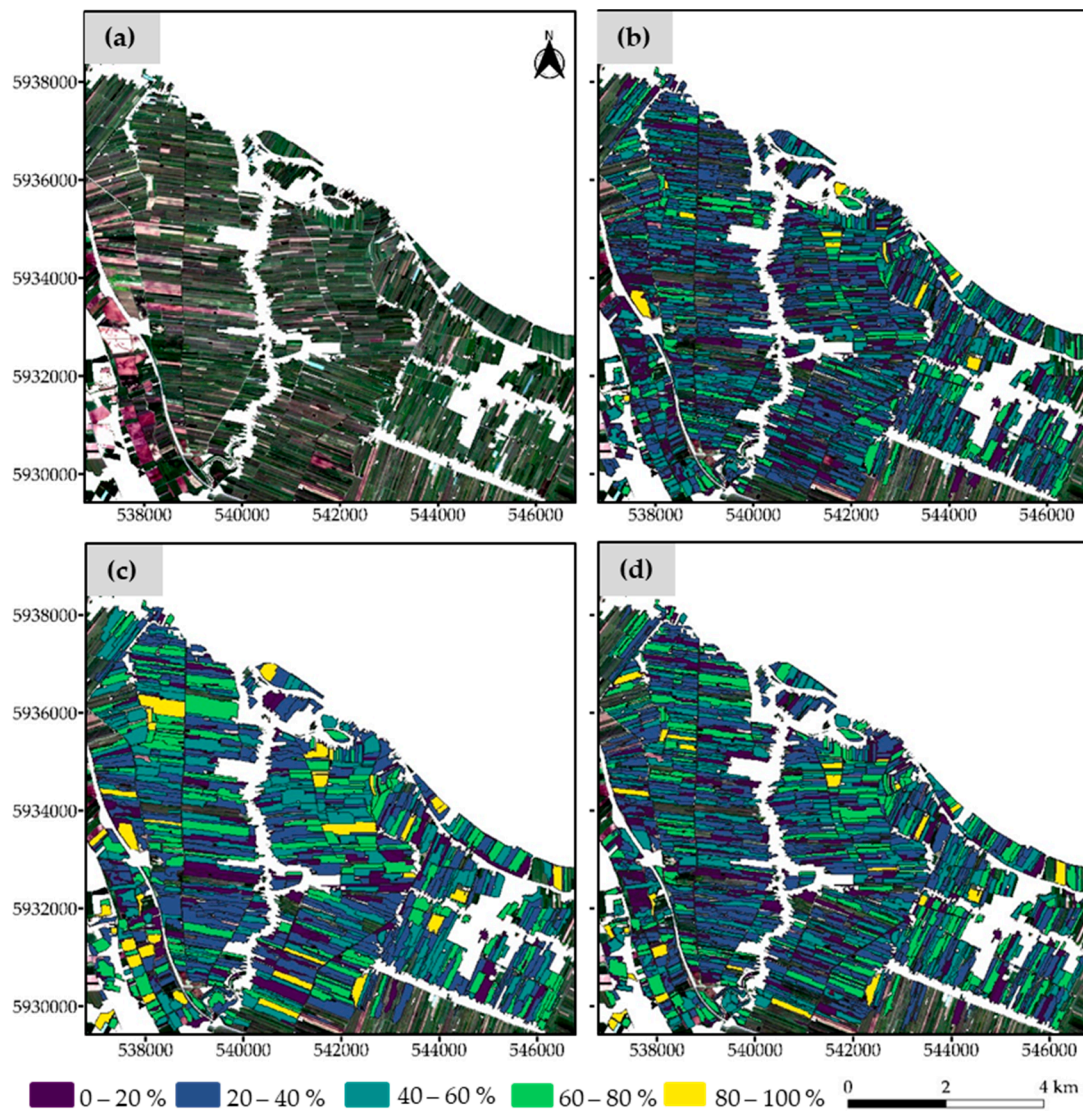


**Figure 10.** The outcome of the three Bayesian optimization approaches at T2. The Sentinel-2 image is shown by (a). The optimal segments as identified by (b) the Böck metric, (c) the supervised Bayesian optimization approach, and (d) the AD metric are symbolized by their respective QR measures. The coordinates are in UTM Zone 32N (EPSG:32632).

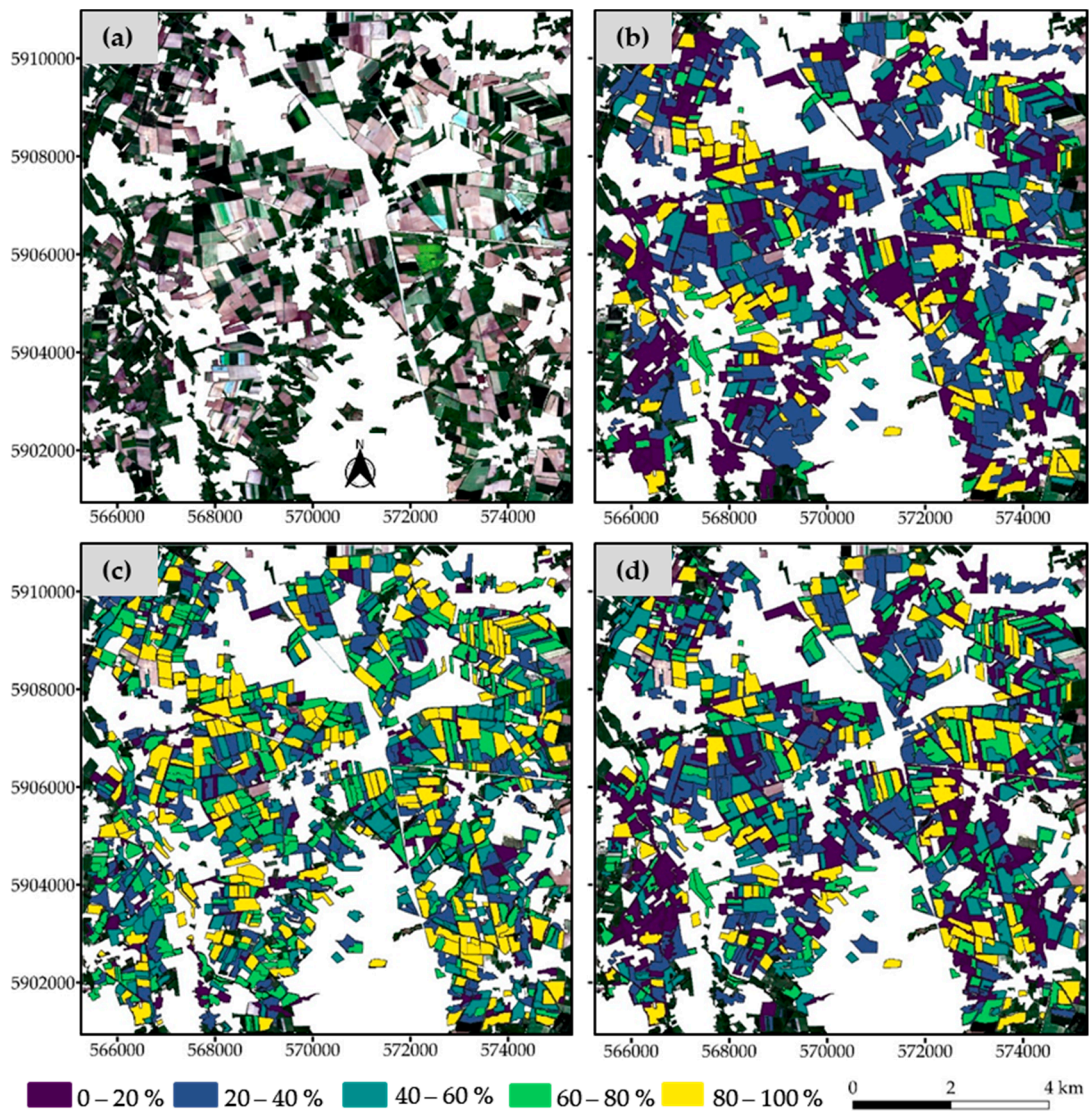


**Figure 11.** The outcome of the three Bayesian optimization approaches at T17. The Sentinel-2 image is shown by (a). The optimal segments as identified by (b) the Böck metric, (c) the supervised Bayesian optimization approach, and (d) the AD metric are symbolized by their respective QR measures. The coordinates are in UTM Zone 32N (EPSG:32632).

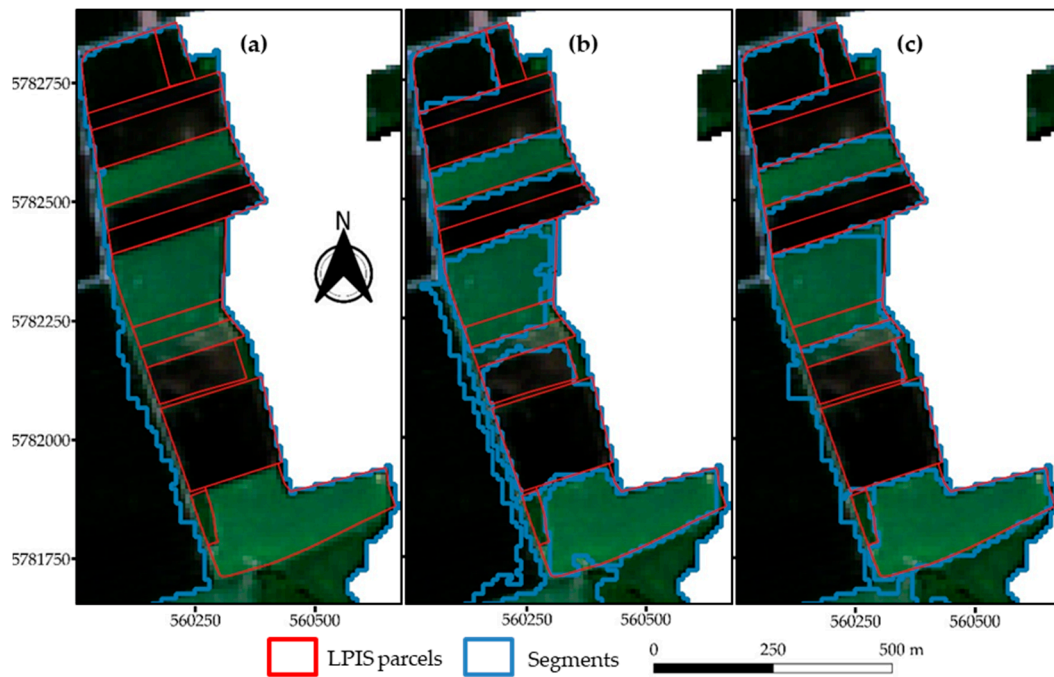


**Figure 12.** An example of segments created at T1 using the unsupervised Bayesian optimization approach based on (a) the Böck metric and (b) the AD metric. (c) Segments generated by the supervised Bayesian optimization approach (SUP) based on the QR metric. The coordinates are in UTM Zone 32N (EPSG:32632).

To understand the reason behind the differences in QR between the supervised optimization approach and the unsupervised Bayesian optimization approaches, we analyzed the linear relationship (Figure 13) between the differences in QR and the number of land-use types present at each tile. For each metric, the Pearson correlation coefficient ( $r$ ) was high, and the  $p$ -value was less than 0.05. Therefore, the relationship between the number of crop types and the differences in QR between the supervised approach and each unsupervised approach is significant.

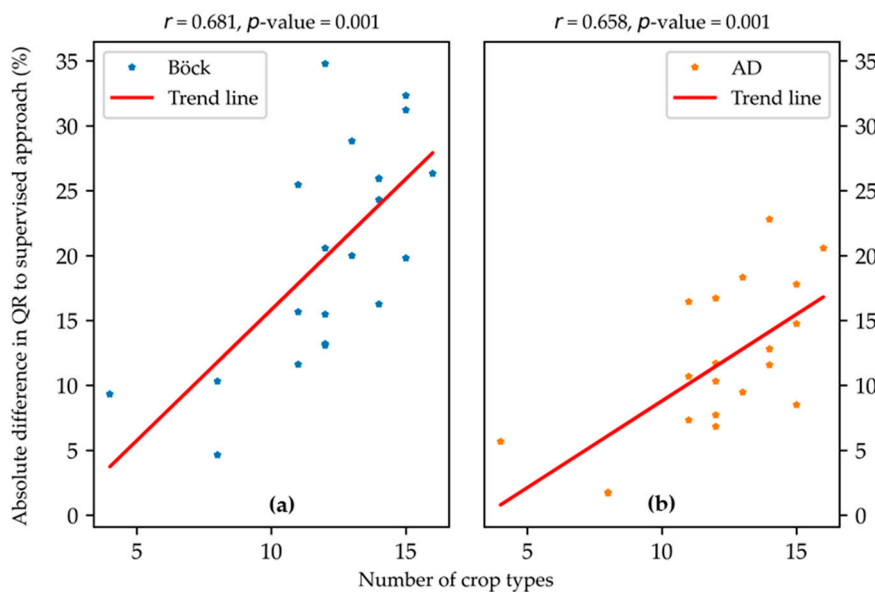


**Figure 13.** Correlation between the number of land use (LU) types and the difference in QR between the supervised benchmark results and the unsupervised Bayesian optimization approaches based on (a) the Böck metric and (b) the AD metric.

## 5. Discussion

The analysis of which metric was optimal for unsupervised segmentation evaluation within our experimental setup of using 21 tiles revealed that our metric (AD) was better than the Böck metric, whether one uses it within a default or Bayesian optimization approach. Visually and quantitatively, the segmentation results yielded by the AD metric were better than the Böck metric in different landscapes composed of diverse agricultural LU types.

For the default optimization approach, at tiles such as T3, where the Böck and AD metrics yielded very similar segmentation results, this is attributable to the fact that there was more clustering of objects as the scale was increased. This is captured by Figure 7b, where all the  $MI$  values were positive. Clustering normally occurs in areas where there are different LU types but with similar spectral behaviors sharing the same neighborhood or in areas highly dominated by a single LU type such as grasslands, as was the case of T3. Under those conditions, the  $GS$  values of the Böck and AD metrics exhibited a common behavior (Figure 7) and consequently selected similar scale values, leading to very similar segmentation results.

At other tiles such as T1, where there was an enormous disparity between the two metrics, the agricultural landscape is more diverse and interspersed with different LU types such as winter wheat, sugar beet, and maize. Consequently, they had more negative  $MI$  values with increasing scale (Figure 6b), which is indicative of the dispersion of objects. The Böck and AD metrics on such occasions differed in curve behavior and global minimum position (Figure 6). Based on the trajectory of the Böck metric in Figure 6a, one can safely conclude that the Böck metric would have further decreased if the scale value had further been increased. Our metric, on the other hand, as captured by Figure 6b, exhibited a decreasing trend up to scale 190 and then started to increase in response to increasing  $nWV$  and decreasing  $MI$ . The benefit of not normalizing the  $MI$  and using absolute difference to compute the  $GS$  became manifest on such occasions, where there was a greater dispersion of agricultural parcels. The AD metric was initially more influenced by the  $MI$ , but it was later more influenced by the  $nWV$  as the scale increased and more  $MI$  values became negative (Figure 6b). With the AD metric, the  $MI$  and  $nWV$  values have a fair chance of impacting the  $GS$  value depending on their respective magnitudes. The Böck metric, on the other hand, was continuously impacted by the  $nMI$  (Figure 6a). This can be attributed to the normalization approach applied to the  $MI$  by the Böck metric. As captured by Figure 6b, before normalization, all the originally negative  $MI$  values were numerically smaller than their corresponding  $nWV$  values. After normalizing the  $MI$  to obtain the  $nMI$  (Figure 6a), those negative  $MI$  values became numerically higher than their corresponding  $nWV$  values, thereby continuously influencing the  $GS$  of the Böck metric (Figure 6a).

The Böck metric is more impacted by the  $nMI$  than the  $nWV$  in all agricultural landscapes. This behavior of the Böck metric has the potential of selecting large-scale values as optimal, thereby leading to the identification of under-segmented objects as optimal. This observation was also made by Georganos et al. [16]. This particular behavior of the Böck metric becomes more problematic in areas with diverse LU types and a greater dispersion of objects, as previously shown in Figure 5a. The more diverse the LU types and the more spectrally similar they behave, the higher the probability of selecting under-segmented objects as optimal using any segmentation evaluation metric, especially a metric that is purely based on the image content. Therefore, a good unsupervised segmentation evaluation metric must reduce over-segmentation but more importantly under-segmentation as the AD metric proved to be able to do, at least in comparison with the Böck metric. For subsequent processes such as object classification, under-segmentation is preferable to over-segmentation [26,58,59]. In general, under-segmentation can largely be dealt with by using very high-resolution images in which visible boundaries between adjacent but spectrally similar parcels can be identified [47].

For the unsupervised Bayesian optimization approach, the approach based on the AD metric outperformed that of the Böck metric at all the tiles, especially at T1, which is composed of diverse LU types. Interestingly, at T3, the Bayesian optimization approach based on the AD metric became better than the Böck metric. This is opposite to the default optimization results at T3, where Böck was

marginally better than AD. Overall, in both optimization approaches, the AD metric consistently proved to be better suited for optimizing the segmentation of agricultural parcels in different landscapes. A look at the segmentation results for T1 (Figure 9) clearly shows that the Bayesian optimization approach based on the AD metric generated more segments (Figure 9d) with a higher segmentation quality than the results of the Bayesian approach based on the Böck metric (Figure 9b). There was a greater clustering of objects at T2 (Figure 10) and T17 (Figure 11) based on the computed *MI* values; hence, the Bayesian optimization approach based on the Böck (Figures 10b and 11b) and the AD (Figures 10d and 11d) metrics yielded very similar segmentation results.

As expected, the supervised Bayesian optimization approach performed better than all the unsupervised Bayesian optimization approaches at all the tiles used in our experiment. This is especially true for T1 (Figure 9c) and T17 (Figure 11c), where the landscape has diversified LU types. At T2, which is highly dominated by pome fruits, the segmentation quality was bad for all the optimization methods. Tetteh et al. [47] in using the supervised Bayesian optimization approach to delineate agricultural parcels made this observation as well for T2 and attributed it to the small size and elongation of agricultural parcels present at that tile. This also holds for the unsupervised Bayesian optimization approaches tested in this research. The high correlation between the number of LU types and the difference in QR between the supervised Bayesian optimization approach and the two unsupervised Bayesian optimization approaches as captured by Figure 13 indicated that at tiles with a smaller number of LU types, the unsupervised Bayesian approaches obtained results similar to the supervised approach. The supervised Bayesian approach was able to adapt more to diverse agricultural landscapes than the unsupervised Bayesian approaches. An example of this can be seen in Figure 12c, where the supervised approach generated segments with well-defined boundaries and a better geometric match to the LPIS parcels than the two unsupervised Bayesian approaches in Figure 12a,b, respectively. The adaptability of supervised segmentation optimization was also asserted by Yang et al. [39] after testing a supervised optimization approach based on the information gain ratio and an unsupervised optimization approach based on *MI* and *WV* as was proposed by Espindola et al. [33]. The major defect of any supervised optimization method is the reliance on reference data, which are tedious to obtain [29]. An unsupervised method such as the Bayesian optimization approach based on our proposed AD metric provides a good alternative to supervised segmentation optimization.

Unlike the proposition of Georganos et al. [16], our proposed metric is objective and fully automated. It does not require any human intervention to identify the optimal segmentation. The approach of Georganos et al. [16] requires the user to compute a certain number of initial segmentations with unknown step intervals, something the authors mentioned has a great impact on the results. Additionally, using locally estimated scatterplot smoothing (LOESS) requires a user to specify the order of the polynomial and a span, which controls the level of smoothing. Since the optimal values of those user inputs cannot be known beforehand, the user has to experiment to identify the optimal settings for normalization, which violates the principle behind unsupervised segmentation evaluation.

## 6. Conclusions

In this study, we modified an existing unsupervised segmentation evaluation metric based on global variance and spatial autocorrelation [43]. We proposed the use of absolute difference (AD) to combine the global variance and spatial autocorrelation. We tested the AD metric and the existing metric, named Böck, in identifying the optimal parameters for delineating agricultural parcels from Sentinel-2 images using the Multiresolution Segmentation (MRS) algorithm. We first tested both metrics at 21 tiles with different agricultural landscapes to optimize the scale parameter of the MRS algorithm through default optimization. In this default approach, we kept the shape and compactness parameters constant and increased the scale at equal intervals to determine the optimal one. The AD metric proved superior to the Böck metric in identifying the segmentation result with a better geometric match to reference agricultural parcels in the Land Parcel Identification System (LPIS). On average, the segmentation

quality of the AD metric was over 6% higher than the Böck metric in this default approach. Our metric often identified segmentations that were least under-segmented as optimal, unlike the Böck metric. We separately used each metric in a Bayesian optimization routine to optimize the three main parameters of the MRS algorithm at the same 21 tiles. The Bayesian optimization approach based on the AD metric performed better than that of the Böck metric at all tiles. In the Bayesian optimization approach, the quality of the segmentation result of the AD metric was on average about 9% better than the Böck metric. A comparison of the segmentation results in this study to existing benchmark results obtained via supervised Bayesian optimization showed that the unsupervised Bayesian optimization approach based on the AD metric can be a good alternative. In areas where the number of land-use (LU) types was small, supervised and unsupervised Bayesian optimization obtained similar segmentation results. Supervised segmentation optimization methods require reference data, which are generally difficult and time-consuming to generate, especially for wide geographic areas such as regions and countries. The Bayesian optimization approach based on the AD metric solely depends on the image content to fine-tune the optimization process without any human intervention; hence, it can easily be used in any operational OBIA workflow to generate segmentations in near real time.

In a nutshell, our proposed metric performed better than its predecessor in identifying optimal segmentation. Identifying optimal segmentation is important for purposes of obtaining correct agricultural statistics such as the sizes of agricultural parcels. In the absence of reference data, a Bayesian optimization approach based on the AD metric can provide a means of fulfilling the aforementioned purpose in an automated and efficient manner with no human interaction. Even though we tested this optimization approach on the MRS algorithm within the thematic area of agriculture, it is easily applicable to any segmentation algorithm and different thematic areas.

Going into the future, one possible way of improving the results of the segmentation optimization process with our proposed metric will be to incorporate local variance and spatial autocorrelation in a multi-scale approach to refine under-segmented and over-segmented objects in subsequent steps as was done by Johnson et al. [37]. Different weighting schemes for different agricultural landscapes can be applied to the normalized weighted variance and spatial autocorrelation before the computation of the global score for the AD metric. The impact of this weighting scheme on the identification of the optimal segmentation result would be analyzed accordingly. The impact of the segmentation results identified by the supervised and unsupervised Bayesian optimization approaches on object classification would be assessed. The 21 tiles we used in our experimental setup had relatively flat terrains. However, our proposed metric should work fairly well in other terrains as long as there is enough spectral dissimilarity (dispersion) between adjacent parcels in any geographical area. This hypothesis will be tested in the future.

**Author Contributions:** Conceptualization, G.O.T.; methodology, G.O.T., A.G.; software, G.O.T.; formal analysis, G.O.T. and A.G.; writing—original draft preparation, G.O.T.; writing—review and editing, A.G., M.S., S.E. and C.C.; visualization, G.O.T.; supervision, A.G., M.S. and S.E. All authors have read and agreed to the published version of the manuscript.

**Funding:** This research received no external funding.

**Acknowledgments:** We are grateful to the Ministry of Food, Agriculture and Consumer Protection of Lower Saxony for providing the LPIS reference parcels. We appreciate the constructive feedbacks of Antonia Ortmann and Ann-Kathrin Holtgrave on this paper.

**Conflicts of Interest:** The authors declare no conflict of interest.

Appendix A

Table A1. Description of the test sites (tiles) used in this study.

Tile	Image Date	Agric. Land Cover	No. of Land-Use Types	No. of LPIS Parcels	Min. Area (Ha)	Max. Area (Ha)	Mean Area (Ha)
T1	20 May 2018	62.29%	12	1308	0.232	25.777	4.097
T2	5 May 2018	62.76%	8	1344	0.173	21.726	2.398
T3	8 May 2018	80.91%	4	2341	0.191	53.279	2.924
T4	7 May 2018	53.30%	14	1671	0.169	35.281	2.522
T5	5 May 2018	76.83%	14	1957	0.180	18.888	3.219
T6	5 May 2018	79.61%	11	2500	0.168	22.639	2.565
T7	5 May 2018	68.08%	16	2140	0.203	25.181	2.579
T8	8 May 2018	50.17%	12	1100	0.199	30.562	3.704
T9	5 May 2018	70.43%	11	1613	0.190	44.890	3.699
T10	5 May 2018	70.13%	12	2441	0.177	26.253	2.243
T11	5 May 2018	71.41%	15	1625	0.172	30.012	3.709
T12	5 May 2018	90.15%	12	1798	0.171	50.494	3.127
T13	5 May 2018	92.31%	12	1221	0.181	64.772	6.203
T14	5 May 2018	63.62%	15	1894	0.176	26.646	2.637
T15	5 May 2018	36.63%	15	809	0.203	23.687	3.580
T16	5 May 2018	58.45%	14	1752	0.181	29.022	2.781
T17	5 May 2018	61.10%	14	1538	0.180	28.160	2.994
T18	5 May 2018	37.26%	13	729	0.193	28.514	4.158
T19	7 May 2018	14.29%	8	420	0.217	25.855	2.471
T20	7 May 2018	33.35%	13	744	0.191	36.408	3.111
T21	7 May 2018	90.84%	11	1340	0.213	62.730	5.883

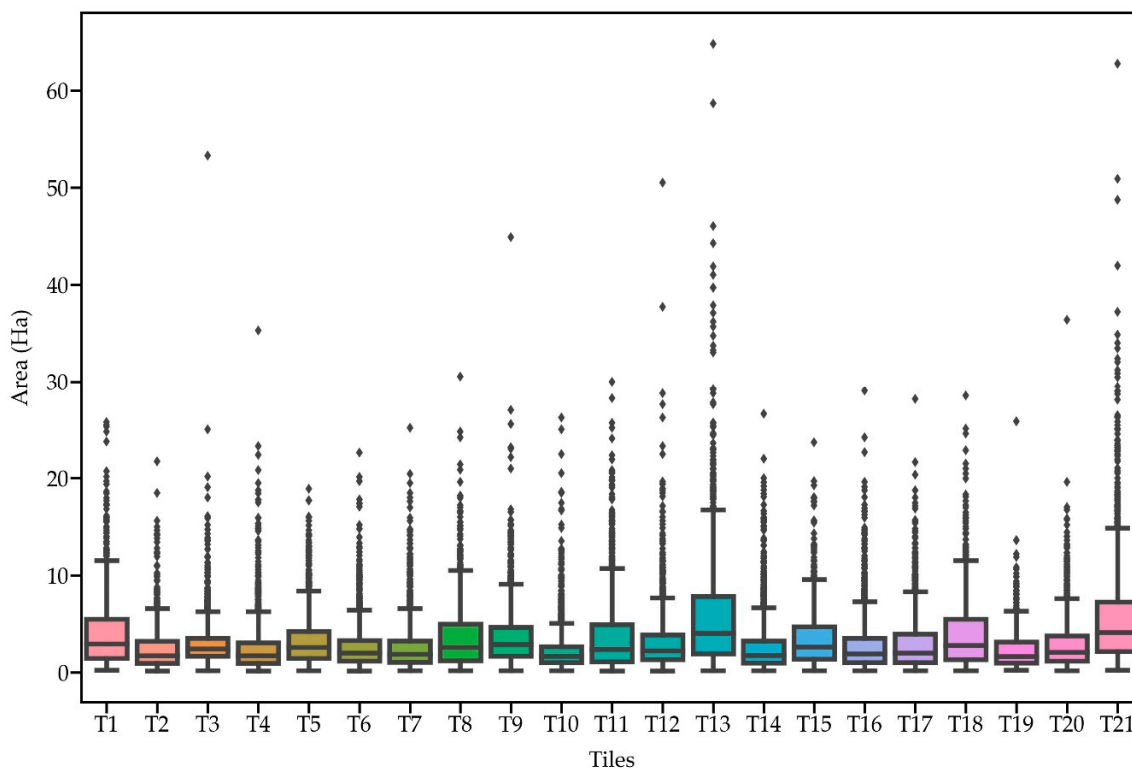


Figure A1. Boxplot of agricultural parcel sizes per tile.

**Table A2.** Empirical discrepancy measures computed for each optimal segmentation result identified by the AD and Böck metrics based on the default optimization (shape = 0.1, compactness = 0.5). The bold-faced texts within the body of the table are the optimal results.

Tile	Scale	Shape	Compactness	QR	OR	UR	RMS	Metric
T1	190	0.100	0.500	<b>55.53%</b>	0.115	<b>0.375</b>	<b>0.278</b>	<b>AD</b>
T1	300	0.100	0.500	38.42%	<b>0.057</b>	0.597	0.424	Böck
T2	80	0.100	0.500	<b>36.94%</b>	<b>0.334</b>	0.467	<b>0.406</b>	<b>AD</b>
T2	70	0.100	0.500	36.07%	0.387	<b>0.427</b>	0.407	Böck
T3	150	0.100	0.500	<b>57.91%</b>	<b>0.183</b>	0.304	0.251	<b>Böck</b>
T3	140	0.100	0.500	57.80%	0.192	<b>0.296</b>	<b>0.250</b>	AD
T4	200	0.100	0.500	<b>28.33%</b>	0.121	<b>0.685</b>	<b>0.492</b>	<b>AD</b>
T4	280	0.100	0.500	20.84%	<b>0.076</b>	0.779	0.553	Böck
T5	160	0.100	0.500	<b>44.69%</b>	0.163	<b>0.477</b>	<b>0.356</b>	<b>AD</b>
T5	200	0.100	0.500	39.00%	<b>0.122</b>	0.563	0.407	Böck
T6	170	0.100	0.500	<b>42.45%</b>	0.169	<b>0.502</b>	<b>0.375</b>	<b>AD</b>
T6	180	0.100	0.500	41.24%	<b>0.161</b>	0.520	0.385	Böck
T7	190	0.100	0.500	<b>32.84%</b>	0.128	<b>0.631</b>	<b>0.455</b>	<b>AD</b>
T7	270	0.100	0.500	25.46%	<b>0.084</b>	0.729	0.519	Böck
T8	120	0.100	0.500	<b>48.77%</b>	0.274	<b>0.339</b>	<b>0.308</b>	<b>AD</b>
T8	170	0.100	0.500	41.78%	<b>0.150</b>	0.513	0.378	Böck
T9	170	0.100	0.500	<b>44.88%</b>	0.215	<b>0.446</b>	<b>0.350</b>	<b>AD</b>
T9	300	0.100	0.500	33.86%	<b>0.101</b>	0.635	0.454	Böck
T10	180	0.100	0.500	<b>36.66%</b>	0.143	<b>0.584</b>	<b>0.425</b>	<b>AD</b>
T10	210	0.100	0.500	33.06%	<b>0.126</b>	0.631	0.455	Böck
T11	230	0.100	0.500	35.67%	0.127	0.595	0.430	AD
T11	230	0.100	0.500	35.67%	0.127	0.595	0.430	Böck
T12	150	0.100	0.500	<b>40.77%</b>	0.209	<b>0.504</b>	<b>0.386</b>	<b>AD</b>
T12	270	0.100	0.500	27.78%	<b>0.126</b>	0.697	0.501	Böck
T13	240	0.100	0.500	<b>42.42%</b>	0.177	<b>0.495</b>	<b>0.372</b>	<b>AD</b>
T13	300	0.100	0.500	35.18%	<b>0.142</b>	0.601	0.436	Böck
T14	160	0.100	0.500	<b>36.03%</b>	0.162	<b>0.574</b>	<b>0.422</b>	<b>AD</b>
T14	280	0.100	0.500	21.74%	<b>0.077</b>	0.768	0.546	Böck
T15	220	0.100	0.500	<b>32.40%</b>	0.090	<b>0.648</b>	<b>0.463</b>	<b>AD</b>
T15	300	0.100	0.500	22.41%	<b>0.062</b>	0.764	0.542	Böck
T16	180	0.100	0.500	<b>38.46%</b>	0.114	<b>0.566</b>	<b>0.408</b>	<b>AD</b>
T16	280	0.100	0.500	26.20%	<b>0.064</b>	0.723	0.513	Böck
T17	200	0.100	0.500	<b>31.89%</b>	0.137	<b>0.634</b>	<b>0.459</b>	<b>AD</b>
T17	240	0.100	0.500	27.14%	<b>0.111</b>	0.700	0.501	Böck
T18	200	0.100	0.500	<b>47.11%</b>	<b>0.167</b>	0.434	0.329	<b>Böck</b>
T18	190	0.100	0.500	47.06%	0.168	<b>0.427</b>	<b>0.325</b>	AD
T19	210	0.100	0.500	<b>37.29%</b>	<b>0.092</b>	0.595	0.426	<b>AD</b>
T19	50	0.100	0.500	36.58%	0.552	<b>0.207</b>	<b>0.417</b>	Böck
T20	220	0.100	0.500	<b>29.21%</b>	0.123	<b>0.676</b>	<b>0.486</b>	<b>AD</b>
T20	260	0.100	0.500	27.79%	<b>0.102</b>	0.698	0.499	Böck
T21	270	0.100	0.500	<b>43.91%</b>	0.133	<b>0.499</b>	<b>0.365</b>	<b>AD</b>
T21	300	0.100	0.500	40.52%	<b>0.117</b>	0.546	0.395	Böck

**Table A3.** Empirical discrepancy measures computed for the unsupervised Bayesian optimization approaches based on the Böck and AD metrics, and the supervised Bayesian optimization approach (SUP) that was used to maximize the QR measure. The bold-faced texts within the body of the table are the optimal results.

Tile	Scale	Shape	Compactness	QR	OR	UR	RMS	Metric
T1	51	0.900	0.966	<b>69.17%</b>	0.117	<b>0.224</b>	<b>0.178</b>	<b>SUP</b>
T1	160	0.300	0.500	57.47%	0.126	0.349	0.263	AD
T1	200	0.841	0.917	34.39%	<b>0.035</b>	0.648	0.459	Böck
T2	40	0.900	0.300	<b>42.04%</b>	<b>0.219</b>	0.479	<b>0.372</b>	<b>SUP</b>
T2	42	0.792	0.176	40.28%	0.309	0.429	0.374	AD
T2	56	0.415	0.192	37.40%	0.402	<b>0.395</b>	0.398	Böck
T3	77	0.842	0.906	<b>68.46%</b>	<b>0.117</b>	<b>0.235</b>	<b>0.186</b>	<b>SUP</b>
T3	117	0.420	1.000	62.79%	0.164	0.263	0.219	AD
T3	138	0.279	0.175	59.14%	0.165	0.304	0.245	Böck
T4	34	0.900	0.410	<b>50.84%</b>	0.290	<b>0.297</b>	<b>0.293</b>	<b>SUP</b>
T4	116	0.655	1.000	38.04%	0.121	0.576	0.416	AD
T4	174	0.666	0.753	24.88%	<b>0.076</b>	0.738	0.524	Böck
T5	42	0.900	0.783	<b>58.78%</b>	0.205	<b>0.273</b>	<b>0.242</b>	<b>SUP</b>
T5	132	0.468	0.701	47.21%	0.149	0.459	0.341	AD
T5	162	0.395	0.452	42.52%	<b>0.124</b>	0.524	0.381	Böck
T6	40	0.900	0.500	<b>57.67%</b>	0.225	<b>0.269</b>	<b>0.248</b>	<b>SUP</b>
T6	127	0.422	0.083	46.98%	0.172	0.442	0.335	AD
T6	144	0.377	0.000	46.05%	<b>0.161</b>	0.466	0.348	Böck
T7	40	0.900	0.500	<b>55.70%</b>	0.209	<b>0.307</b>	<b>0.263</b>	<b>SUP</b>
T7	183	0.088	0.401	35.14%	0.142	0.601	0.436	AD
T7	178	0.686	0.611	29.39%	<b>0.071</b>	0.692	0.492	Böck
T8	46	0.853	0.665	<b>56.91%</b>	0.261	<b>0.240</b>	<b>0.251</b>	<b>SUP</b>
T8	120	0.100	0.300	49.20%	0.261	0.339	0.303	AD
T8	160	0.300	0.100	43.71%	<b>0.145</b>	0.499	0.367	Böck
T9	56	0.900	0.548	<b>56.93%</b>	0.191	<b>0.310</b>	<b>0.258</b>	<b>SUP</b>
T9	129	0.398	1.000	49.61%	0.212	0.384	0.310	AD
T9	200	0.300	0.500	41.28%	<b>0.148</b>	0.532	0.390	Böck
T10	40	0.900	0.700	<b>54.15%</b>	0.196	<b>0.336</b>	<b>0.275</b>	<b>SUP</b>
T10	189	0.000	0.380	37.43%	0.152	0.573	0.419	AD
T10	184	0.587	0.633	33.58%	<b>0.084</b>	0.641	0.457	Böck
T11	50	0.900	0.699	<b>58.31%</b>	0.200	<b>0.277</b>	<b>0.241</b>	<b>SUP</b>
T11	200	0.100	0.900	40.52%	0.143	0.528	0.386	AD
T11	108	0.900	0.777	38.50%	<b>0.073</b>	0.595	0.424	Böck
T12	40	0.900	0.100	<b>49.05%</b>	0.254	<b>0.354</b>	<b>0.308</b>	<b>SUP</b>
T12	163	0.000	0.605	38.73%	0.197	0.536	0.404	AD
T12	200	0.500	0.700	33.57%	<b>0.119</b>	0.635	0.457	Böck
T13	63	0.900	0.371	<b>54.74%</b>	0.231	<b>0.293</b>	<b>0.264</b>	<b>SUP</b>
T13	151	0.643	0.272	47.92%	0.168	0.434	0.329	AD
T13	165	0.819	0.614	41.67%	<b>0.091</b>	0.551	0.395	Böck
T14	42	0.900	0.576	<b>53.68%</b>	0.204	<b>0.328</b>	<b>0.273</b>	<b>SUP</b>
T14	120	0.500	0.100	38.92%	0.156	0.539	0.397	AD
T14	200	0.700	0.100	21.35%	<b>0.059</b>	0.778	0.552	Böck
T15	40	0.900	0.300	<b>61.17%</b>	0.200	<b>0.252</b>	<b>0.228</b>	<b>SUP</b>
T15	63	0.900	0.428	52.67%	0.106	0.421	0.307	AD
T15	109	0.900	0.000	29.95%	<b>0.064</b>	0.687	0.488	Böck

Table A3. Cont.

Tile	Scale	Shape	Compactness	QR	OR	UR	RMS	Metric
T16	45	0.842	0.923	<b>59.96%</b>	0.206	<b>0.251</b>	<b>0.229</b>	<b>SUP</b>
T16	101	0.652	0.762	47.17%	0.116	0.470	0.342	AD
T16	154	0.569	0.621	35.65%	<b>0.086</b>	0.615	0.439	Böck
T17	45	0.900	0.632	<b>54.49%</b>	0.205	<b>0.320</b>	<b>0.269</b>	<b>SUP</b>
T17	200	0.104	0.192	31.68%	0.133	0.637	0.460	AD
T17	185	0.603	0.800	28.57%	<b>0.093</b>	0.691	0.493	Böck
T18	57	0.889	0.897	<b>59.15%</b>	0.199	<b>0.265</b>	<b>0.234</b>	<b>SUP</b>
T18	116	0.653	0.370	49.68%	0.172	0.398	0.307	AD
T18	160	0.700	0.300	39.16%	<b>0.094</b>	0.572	0.410	Böck
T19	54	0.730	1.000	<b>53.04%</b>	0.262	0.290	<b>0.276</b>	<b>SUP</b>
T19	40	0.900	0.700	51.35%	<b>0.221</b>	0.343	0.288	AD
T19	40	0.601	0.000	42.72%	0.460	<b>0.223</b>	0.362	Böck
T20	40	0.900	0.900	<b>53.31%</b>	0.221	<b>0.319</b>	<b>0.274</b>	<b>SUP</b>
T20	200	0.154	0.961	34.98%	0.131	0.604	0.437	AD
T20	200	0.700	0.500	24.48%	<b>0.067</b>	0.743	0.528	Böck
T21	63	0.899	0.868	<b>64.99%</b>	0.157	<b>0.231</b>	<b>0.198</b>	<b>SUP</b>
T21	170	0.627	0.582	48.55%	0.129	0.447	0.329	AD
T21	200	0.813	0.173	39.54%	<b>0.074</b>	0.579	0.412	Böck

## References

- Dudley, N.; Alexander, S. Agriculture and biodiversity: A review. *Biodiversity* **2017**, *18*, 45–49. [[CrossRef](#)]
- Foley, J.A.; Ramankutty, N.; Brauman, K.A.; Cassidy, E.S.; Gerber, J.S.; Johnston, M.; Mueller, N.D.; O'Connell, C.; Ray, D.K.; West, P.C.; et al. Solutions for a cultivated planet. *Nature* **2011**, *478*, 337–342. [[CrossRef](#)] [[PubMed](#)]
- Rey Benayas, J.M.; Bullock, J.M. Restoration of biodiversity and ecosystem services on agricultural land. *Ecosystems* **2012**, *15*, 883–899. [[CrossRef](#)]
- Beach, R.H.; DeAngelo, B.J.; Rose, S.; Li, C.; Salas, W.; DelGrosso, S.J. Mitigation potential and costs for global agricultural greenhouse gas emissions. *Agric. Econ.* **2008**, *38*, 109–115. [[CrossRef](#)]
- Adams, C.R.; Eswaran, H. Global land resources in the context of food and environmental security. In *Advances in Land Resources Management for the 20th Century*; Soil Conservation Society of India: New Delhi, India, 2000; pp. 35–50.
- Forkuor, G.; Conrad, C.; Thiel, M.; Ullmann, T.; Zoungrana, E. integration of optical and synthetic aperture radar imagery for improving crop mapping in Northwestern Benin, West Africa. *Remote Sens.* **2014**, *6*, 6472–6499. [[CrossRef](#)]
- Villa, P.; Stroppiana, D.; Fontanelli, G.; Azar, R.; Brivio, P. In-season mapping of crop type with optical and X-band SAR data: A classification tree approach using synoptic seasonal features. *Remote Sens.* **2015**, *7*, 12859–12886. [[CrossRef](#)]
- Peña-Barragán, J.M.; Ngugi, M.K.; Plant, R.E.; Six, J. Object-based crop identification using multiple vegetation indices, textural features and crop phenology. *Remote Sens. Environ.* **2011**, *115*, 1301–1316. [[CrossRef](#)]
- Blaes, X.; Vanhalle, L.; Defourny, P. Efficiency of crop identification based on optical and SAR image time series. *Remote Sens. Environ.* **2005**, *96*, 352–365. [[CrossRef](#)]
- Castillejo-González, I.L.; López-Granados, F.; García-Ferrer, A.; Peña-Barragán, J.M.; Jurado-Expósito, M.; de la Orden, M.S.; González-Audicana, M. Object- and pixel-based analysis for mapping crops and their agro-environmental associated measures using QuickBird imagery. *Comput. Electron. Agric.* **2009**, *68*, 207–215. [[CrossRef](#)]
- Atzberger, C. Advances in remote sensing of agriculture: Context description, existing operational monitoring systems and major information needs. *Remote Sens.* **2013**, *5*, 949–981. [[CrossRef](#)]

12. Blaschke, T.; Lang, S.; Lorup, E.; Strobl, J.; Zeil, P. Object-oriented image processing in an integrated GIS/remote sensing environment and perspectives for environmental applications. *Environ. Inf. Plan. Polit. Public* **2000**, *2*, 555–570.
13. Whiteside, T.G.; Boggs, G.S.; Maier, S.W. Comparing object-based and pixel-based classifications for mapping savannas. *Int. J. Appl. Earth Obs. Geoinf.* **2011**, *13*, 884–893. [[CrossRef](#)]
14. Robertson, L.D.; King, D.J. Comparison of pixel- and object-based classification in land cover change mapping. *Int. J. Remote Sens.* **2011**, *32*, 1505–1529. [[CrossRef](#)]
15. Blaschke, T. Object based image analysis for remote sensing. *ISPRS J. Photogramm. Remote Sens.* **2010**, *65*, 2–16. [[CrossRef](#)]
16. Georganos, S.; Lennert, M.; Grippa, T.; Vanhuysse, S.; Johnson, B.; Wolff, E. Normalization in unsupervised segmentation parameter optimization: A solution based on local regression trend analysis. *Remote Sens.* **2018**, *10*, 222. [[CrossRef](#)]
17. Akcay, O.; Avsar, E.O.; Inalpulat, M.; Genc, L.; Cam, A. Assessment of segmentation parameters for object-based land cover classification using color-infrared imagery. *ISPRS Int. J. Geo-Inf.* **2018**, *7*, 424. [[CrossRef](#)]
18. Gao, Y.; Mas, J.F.; Kerle, N.; Pacheco, J.A.N. Optimal region growing segmentation and its effect on classification accuracy. *Int. J. Remote Sens.* **2011**, *32*, 3747–3763. [[CrossRef](#)]
19. Georganos, S.; Grippa, T.; Lennert, M.; Vanhuysse, S.; Johnson, B.A.; Wolff, E. Scale Matters: Spatially Partitioned Unsupervised Segmentation Parameter Optimization for Large and Heterogeneous Satellite Images. *Remote Sens.* **2018**, *10*, 1440. [[CrossRef](#)]
20. Liu, D.; Xia, F. Assessing object-based classification: Advantages and limitations. *Remote Sens. Lett.* **2010**, *1*, 187–194. [[CrossRef](#)]
21. Baatz, M.; Schäpe, A. Multiresolution segmentation: An optimization approach for high quality multi-scale image segmentation. In Proceedings of the Angewandte Geographische Informations-Verarbeitung XII, Karlsruhe, Germany, 30 June 2000; Strobl, J., Blaschke, T., Griesebner, G., Eds.; Wichmann Verlag: Karlsruhe, Germany, 2000; pp. 12–23.
22. Benz, U.C.; Hofmann, P.; Willhauck, G.; Lingenfelder, I.; Heynen, M. Multi-resolution, object-oriented fuzzy analysis of remote sensing data for GIS-ready information. *ISPRS J. Photogramm. Remote Sens.* **2004**, *58*, 239–258. [[CrossRef](#)]
23. Ma, L.; Li, M.; Ma, X.; Cheng, L.; Du, P.; Liu, Y. A review of supervised object-based land-cover image classification. *ISPRS J. Photogramm. Remote Sens.* **2017**, *130*, 277–293. [[CrossRef](#)]
24. Trimble Germany GmbH. *eCognition Developer 9.5.0 Reference Book*; Trimble Germany GmbH: Munich, Germany, 2019.
25. Marpu, P.R.; Neubert, M.; Herold, H.; Niemeier, I. Enhanced evaluation of image segmentation results. *J. Spat. Sci.* **2010**, *55*, 55–68. [[CrossRef](#)]
26. Neubert, M.; Herold, H.; Meinel, G. Assessing image segmentation quality—Concepts, methods and application. In *Object-Based Image Analysis: Spatial Concepts for Knowledge-Driven Remote Sensing Applications*; Blaschke, T., Lang, S., Hay, G.J., Eds.; Lecture Notes in Geoinformation and Cartography; Springer: Berlin/Heidelberg, Germany, 2008; pp. 769–784. ISBN 978-3-540-77058-9.
27. Neubert, M.; Meinel, G. Evaluation of segmentation programs for high resolution remote sensing applications. In Proceedings of the Joint ISPRS/EARSeL Workshop “High Resolution Mapping from Space 2003”, Hannover, Germany, 8 October 2003.
28. Zhang, Y.-J. A survey on evaluation methods for image segmentation. *Pattern Recognit.* **1996**, *29*, 1335–1346. [[CrossRef](#)]
29. Zhang, H.; Fritts, J.E.; Goldman, S.A. Image segmentation evaluation: A survey of unsupervised methods. *Comput. Vis. Image Underst.* **2008**, *110*, 260–280. [[CrossRef](#)]
30. Chabrier, S.; Emile, B.; Rosenberger, C.; Laurent, H. Unsupervised Performance Evaluation of Image Segmentation. *EURASIP J. Adv. Signal Process.* **2006**, *2006*, 096306. [[CrossRef](#)]
31. Drăguț, L.; Csillik, O.; Eisank, C.; Tiede, D. Automated parameterisation for multi-scale image segmentation on multiple layers. *ISPRS J. Photogramm. Remote Sens.* **2014**, *88*, 119–127. [[CrossRef](#)]
32. Drăguț, L.; Tiede, D.; Levick, S.R. ESP: A tool to estimate scale parameter for multiresolution image segmentation of remotely sensed data. *Int. J. Geogr. Inf. Sci.* **2010**, *24*, 859–871. [[CrossRef](#)]
33. Espindola, G.M.; Camara, G.; Reis, I.A.; Bins, L.S.; Monteiro, A.M. Parameter selection for region-growing image segmentation algorithms using spatial autocorrelation. *Int. J. Remote Sens.* **2006**, *27*, 3035–3040. [[CrossRef](#)]
34. Woodcock, C.E.; Strahler, A.H. The factor of scale in remote sensing. *Remote Sens. Environ.* **1987**, *21*, 311–332. [[CrossRef](#)]

35. Moran, P.A.P. Notes on continuous stochastic phenomena. *Biometrika* **1950**, *37*, 17–23. [[CrossRef](#)]
36. Grybas, H.; Melendy, L.; Congalton, R.G. A comparison of unsupervised segmentation parameter optimization approaches using moderate- and high-resolution imagery. *GISci. Remote Sens.* **2017**, *54*, 515–533. [[CrossRef](#)]
37. Johnson, B.; Xie, Z. Unsupervised image segmentation evaluation and refinement using a multi-scale approach. *ISPRS J. Photogramm. Remote Sens.* **2011**, *66*, 473–483. [[CrossRef](#)]
38. Johnson, B.A.; Bragais, M.; Endo, I.; Magcale-Macandog, D.B.; Macandog, P.B.M. Image segmentation parameter optimization considering within- and between-segment heterogeneity at multiple scale levels: Test case for mapping residential areas using landsat imagery. *ISPRS Int. J. Geo-Inf.* **2015**, *4*, 2292–2305. [[CrossRef](#)]
39. Yang, L.; Mansaray, L.R.; Huang, J.; Wang, L. Optimal Segmentation Scale Parameter, Feature Subset and Classification Algorithm for Geographic Object-Based Crop Recognition Using Multisource Satellite Imagery. *Remote Sens.* **2019**, *11*, 514. [[CrossRef](#)]
40. Kim, M.; Madden, M.; Warner, T. Estimation of optimal image object size for the segmentation of forest stands with multispectral IKONOS imagery. In *Object-Based Image Analysis*; Blaschke, T., Lang, S., Hay, G.J., Eds.; Lecture Notes in Geoinformation and Cartography; Springer: Berlin/Heidelberg, Germany, 2008; pp. 291–307. ISBN 978-3-540-77057-2.
41. Martha, T.R.; Kerle, N.; van Westen, C.J.; Jetten, V.; Kumar, K.V. Segment optimization and data-driven thresholding for knowledge-based landslide detection by object-based image analysis. *IEEE Trans. Geosci. Remote Sens.* **2011**, *49*, 4928–4943. [[CrossRef](#)]
42. Chen, J.; Deng, M.; Mei, X.; Chen, T.; Shao, Q.; Hong, L. Optimal segmentation of a high-resolution remote-sensing image guided by area and boundary. *Int. J. Remote Sens.* **2014**, *35*, 6914–6939. [[CrossRef](#)]
43. Böck, S.; Immitzer, M.; Atzberger, C. On the objectivity of the objective function—Problems with unsupervised segmentation evaluation based on global score and a possible remedy. *Remote Sens.* **2017**, *9*, 769. [[CrossRef](#)]
44. Kim, M.; Warner, T.A.; Madden, M.; Atkinson, D.S. Multi-scale GEOBIA with very high spatial resolution digital aerial imagery: Scale, texture and image objects. *Int. J. Remote Sens.* **2011**, *32*, 2825–2850. [[CrossRef](#)]
45. Johnson, B.; Xie, Z. Classifying a high resolution image of an urban area using super-object information. *ISPRS J. Photogramm. Remote Sens.* **2013**, *83*, 40–49. [[CrossRef](#)]
46. Taşdemir, K.; Wirthardt, C. Neural network-based clustering for agriculture management. *EURASIP J. Adv. Signal Process.* **2012**, 2012. [[CrossRef](#)]
47. Tetteh, G.O.; Gocht, A.; Conrad, C. Optimal parameters for delineating agricultural parcels from satellite images based on supervised Bayesian optimization. *Comput. Electron. Agric.* **2020**, *178*, 105696. [[CrossRef](#)]
48. Main-Knorn, M.; Pflug, B.; Louis, J.; Debaecker, V.; Müller-Wilm, U.; Gascon, F. Sen2Cor for Sentinel-2. In *Proceedings of the Image and Signal Processing for Remote Sensing XXIII*, Warsaw, Poland, 11–13 September 2017; Bruzzone, L., Bovolo, F., Benediktsson, J.A., Eds.; SPIE: Warsaw, Poland, 2017; p. 3.
49. Rousseeuw, P.J. Silhouettes: A graphical aid to the interpretation and validation of cluster analysis. *J. Comput. Appl. Math.* **1987**, *20*, 53–65. [[CrossRef](#)]
50. Rasmussen, C.E.; Williams, C.K.I. *Gaussian Processes for Machine Learning*; Adaptive Computation and Machine Learning; MIT Press: Cambridge, MA, USA, 2006; ISBN 978-0-262-18253-9.
51. Jones, D.R.; Schonlau, M.; Welch, W.J. Efficient global optimization of expensive black-box functions. *J. Glob. Optim.* **1998**, *13*, 455–492. [[CrossRef](#)]
52. Dewancker, I.; McCourt, M.; Clark, S. Bayesian Optimization Primer. Available online: [https://app.sigopt.com/static/pdf/SigOpt\\_Bayesian\\_Optimization\\_Primer.pdf](https://app.sigopt.com/static/pdf/SigOpt_Bayesian_Optimization_Primer.pdf) (accessed on 4 March 2020).
53. Shahriari, B.; Swersky, K.; Wang, Z.; Adams, R.P.; de Freitas, N. Taking the human out of the loop: A review of Bayesian optimization. *Proc. IEEE* **2016**, *104*, 148–175. [[CrossRef](#)]
54. Brochu, E.; Cora, V.M.; de Freitas, N. A tutorial on Bayesian optimization of expensive cost functions, with application to active user modeling and hierarchical reinforcement learning. *arXiv* **2010**, arXiv:10122599.
55. Frazier, P.I. A tutorial on Bayesian optimization. *arXiv* **2018**, arXiv:180702811.
56. Weidner, U. Contribution to the assessment of segmentation quality for remote sensing applications. *Int. Arch. Photogramm. Remote Sens. Spat. Inf. Sci.* **2008**, *37*, 479–484.
57. Clinton, N.; Holt, A.; Scarborough, J.; Yan, L.; Gong, P. Accuracy assessment measures for object-based image segmentation goodness. *Photogramm. Eng. Remote Sens.* **2010**, *76*, 289–299. [[CrossRef](#)]

58. Liu, Y.; Bian, L.; Meng, Y.; Wang, H.; Zhang, S.; Yang, Y.; Shao, X.; Wang, B. Discrepancy measures for selecting optimal combination of parameter values in object-based image analysis. *ISPRS J. Photogramm. Remote Sens.* **2012**, *68*, 144–156. [[CrossRef](#)]
59. Belgiu, M.; Drăguț, L. Comparing supervised and unsupervised multiresolution segmentation approaches for extracting buildings from very high resolution imagery. *ISPRS J. Photogramm. Remote Sens.* **2014**, *96*, 67–75. [[CrossRef](#)]



© 2020 by the authors. Licensee MDPI, Basel, Switzerland. This article is an open access article distributed under the terms and conditions of the Creative Commons Attribution (CC BY) license (<http://creativecommons.org/licenses/by/4.0/>).

## **5 Evaluation of Sentinel-1 and Sentinel-2 feature sets for delineating agricultural fields in heterogeneous landscapes**

Full bibliographic entry of paper:

Tetteh, G.O., Gocht, A., Erasmi, S., Schwieder, M., Conrad, C., 2021. Evaluation of Sentinel-1 and Sentinel-2 Feature Sets for Delineating Agricultural Fields in Heterogeneous Landscapes. IEEE Access 9, 116702–116719. <https://doi.org/10.1109/ACCESS.2021.3105903>

Received July 12, 2021, accepted August 4, 2021, date of publication August 18, 2021, date of current version August 27, 2021.

Digital Object Identifier 10.1109/ACCESS.2021.3105903

# Evaluation of Sentinel-1 and Sentinel-2 Feature Sets for Delineating Agricultural Fields in Heterogeneous Landscapes

GIDEON OKPOTI TETTEH<sup>1</sup>, ALEXANDER GOCHT<sup>1</sup>, STEFAN ERASMI<sup>1</sup>, MARCEL SCHWIEDER<sup>1,2</sup>, AND CHRISTOPHER CONRAD<sup>3</sup>

<sup>1</sup>Thünen Institute of Farm Economics, 38116 Braunschweig, Germany

<sup>2</sup>Geography Department, Humboldt University of Berlin, 10099 Berlin, Germany

<sup>3</sup>Institute of Geosciences and Geography, Martin-Luther-University Halle-Wittenberg, 06099 Halle, Germany

Corresponding author: Gideon Okpoti Tetteh (gideon.tetteh@thuenen.de)

**ABSTRACT** The Group on Earth Observations Global Agricultural Monitoring Initiative (GEOGLAM) considers agricultural fields as one of the essential variables that can be derived from satellite data. We evaluated the accuracy at which agricultural fields can be delineated from Sentinel-1 (S1) and Sentinel-2 (S2) images in different agricultural landscapes throughout the growing season. We used supervised segmentation based on the multiresolution segmentation (MRS) algorithm to first identify the optimal feature set from S1 and S2 images for field delineation. Based on this optimal feature set, we analyzed the segmentation accuracy of the fields delineated with increasing data availability between March and October of 2018. From the S1 feature sets, the combination of the two polarizations and two radar indices attained the best segmentation results. For S2, the best results were achieved using a combination of all bands (coastal aerosol, water vapor, and cirrus bands were excluded) and six spectral indices. Combining the radar and spectral indices further improved the results. Compared to the single-period dataset in March, using the dataset covering the whole season led to a significant increase in the segmentation accuracy. For very small fields (< 0.5 ha), the segmentation accuracy obtained was 27.02%, for small fields (0.5 – 1.5 ha), the accuracy was 57.65%, for medium fields (1.5 ha – 15 ha), the accuracy was 75.71%, and for large fields (> 15 ha), the accuracy stood at 68.31%. As a use case, the segmentation result was used to aggregate and improve a pixel-based crop type map in Lower Saxony, Germany.

**INDEX TERMS** Agricultural field delineation, band indices, essential agricultural variables, feature combination, image segmentation, intersection over union, remote sensing, segmentation optimization.

## I. INTRODUCTION

As part of its activities geared towards ensuring the attainment of the United Nation's Sustainable Development Goals [1], the Group on Earth Observations Global Agricultural Monitoring Initiative (GEOGLAM<sup>1</sup>) identifies agricultural fields as one of its essential agricultural variables [2]. Additionally, agricultural fields are valuable inputs to subsequent processes such as crop type mapping [3], analysis of crop rotations [4], implementation of crop management activities [5], and the control of subsidy payments to farmers [6]. Conventionally, agricultural fields have been

generated through the manual digitization of hardcopy maps (aerial images, topographic maps, etc.) [7] or direct field measurements. The obvious problem with those approaches is that they are costly and inefficient especially as agricultural maps require continuous updates to capture the real-time or near real-time events happening on agricultural fields. The use of remote sensing (RS) is a good alternative for mapping agricultural fields given that satellite images can be acquired over wide geographical areas at a high temporal resolution [8]–[10].

The use of satellite images to delineate agricultural fields has an extensive history in the RS world. It can largely be attributed to the use of medium spatial resolution satellites like Landsat. For example, to extract agricultural fields, numerous studies [7], [11]–[14] used the Landsat

The associate editor coordinating the review of this manuscript and approving it for publication was John Xun Yang .

<sup>1</sup><https://earthobservations.org/geoglam.php> (Accessed: Jul. 9, 2021).

Thematic Mapper (TM), some [13]–[16] employed the Landsat Enhanced Thematic Mapper Plus (ETM+), and others [17]–[20] used the Landsat 8 Operational Land Imager (OLI). The common theme running through all of those studies is the use of image segmentation as a means of extracting the boundaries of the agricultural fields.

Image segmentation, which is the process of partitioning an image into homogeneous and distinct objects, is the foundation of the object-based image analysis (OBIA) paradigm [21]. The growth of the OBIA paradigm was fueled by the advent of high-resolution images and the availability of powerful computing environments [22]. It was observed in [23] that the spatial resolution of an image has a direct impact on the outcome of image segmentation. In [5], the authors established that the higher the spatial resolution, the higher the coverage of agricultural fields eligible for site-specific services like the monitoring of the Common Agricultural Policy (CAP) [24] and the application of smart farming technologies. Therefore, high or very high spatial resolution images are generally preferred for segmenting agricultural fields. For example, pan-sharpened SPOT-5 images were used by [4], RapidEye by [25], WorldView-2/3 by [26], QuickBird by [27], and digital orthophotos by [6]. However, for mapping large geographical areas, the use of high or very high spatial resolution images becomes infeasible as they become extremely expensive to acquire. Therefore, medium spatial resolution images remain the most viable option for delineating agricultural fields at regional, national, and global scales at little to no cost.

Although Landsat images have proven useful for mapping agricultural fields over large areas, the spatial resolution of 30 m is often unable to resolve individual agricultural fields thereby inhibiting field-based applications in many cropping systems around the world [28]. Building on the experiences of the Landsat and SPOT missions, Sentinel-2 (S2) was designed within the framework of the European Copernicus program for land surface and agriculture monitoring [28] at a temporal resolution of 5 days and a spatial resolution of 10 m. As opposed to optical sensors, which are inhibited by clouds, Sentinel-1 (S1), which is also part of the Copernicus program enables the continuous monitoring of the earth's surface in all weather conditions at a temporal resolution of 6 days and a spatial resolution of 20 m. Various researchers have used S1 [29], [30], and predominantly S2 [31]–[40] for segmenting agricultural fields. In using the S1 or S2 images, most of those authors used existing segmentation algorithms (e.g., [29], [30], [32]–[34], [36]–[40]), some proposed new segmentation algorithms (e.g., [31], [35]), and others proposed new segmentation parameter optimization approaches (e.g., [36], [37]). One area that is yet to be comprehensively explored is the determination of the optimal feature set from S1 and S2 images for segmenting agricultural fields given that both sensors come with different bands and additional features like band indices can be calculated as well. In an experiment based on a WorldView-2 image, the authors of [23] showed that the feature set used as the input to

the segmentation algorithm has an impact on the segmentation result. Therefore, it is worth exploring different S1 and S2 feature sets to assess their impact on the segmentation of agricultural fields.

Beyond the feature set, agricultural fields are dynamic and change throughout the growing season, thereby requiring continuous updates. Therefore, it is also relevant to analyze the accuracy at which the agricultural fields can be delineated from the S1 and S2 feature datasets at different times of the growing season. Further, it is important to assess the accuracy at which agricultural fields can be segmented from S1 and S2 at different agricultural landscapes with different field sizes. In [2], the authors categorized three different field sizes: small fields (< 1.5 ha), medium fields (1.5 ha – 15 ha), and large fields (> 15 ha). They subsequently asserted that medium spatial resolution images (here S1 and S2) are more suitable for delineating large fields. Based on their respective spatial resolutions, S1 and S2 should be capable of spatially resolving small fields. For example, a 1 ha field should be spatially resolved by S1 using 25 pixels and S2 using 100 pixels. Therefore, the validity of the assertion in [2] ought to be tested. Further, it remains to be seen what segmentation accuracy can be achieved for those three field size categories.

To fill all the aforementioned gaps, we set out in this study to execute the following objectives: (1) identify the optimal feature set from S1 and S2 images for segmenting agricultural fields, (2) analyze the evolution of the accuracy of agricultural fields segmented from the S1 and S2 feature sets throughout the growing season, and (3) assess the accuracy that can be achieved for different field sizes. To achieve our objectives, we employed the multiresolution segmentation (MRS) algorithm [41] in eCognition [42] to segment agricultural fields from different feature sets generated from S1 and S2 images acquired between March and October of 2018 in Lower Saxony, Germany.

## II. STUDY AREA & DATA

### A. STUDY AREA

The federal state of Lower Saxony in Germany was selected as the study area (Figure 1). Its total area of about 4,770,041 ha has a mostly flat terrain and is located in the temperate climate zone of Europe [36]. The majority of its landmass is covered by agricultural lands that are mostly dominated by grasslands, summer cereals, winter cereals, potatoes, winter rapeseed, and sugar beet [36]. For efficient segmentation purposes, the study area was divided into 575 tiles. Each tile is 10 km by 10 km.

To enable the smooth merger of the segmentation results from all the tiles, the geometry extent of each tile was extended or shrunk to cover the geometry of all polygons contained in the agricultural land-cover (LC) dataset (see Section II.C for the description of the dataset) whose centroids intersected that particular tile. Consequently, the extended or shrunk tiles (symbolized as blue outlines in Figure 1) have variable sizes with the average size being 11 km by 11 km. To reduce the computation time

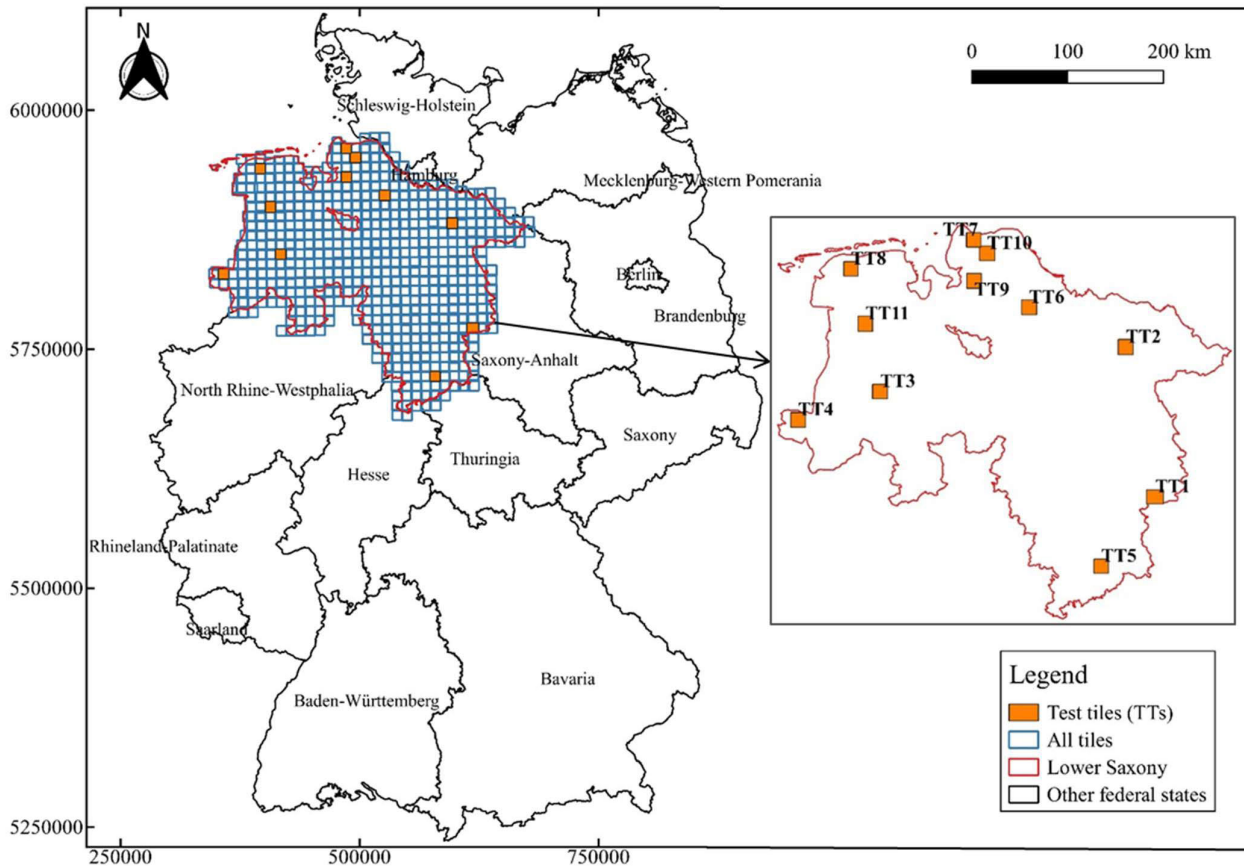


**FIGURE 1.** The study area (Lower Saxony) used in this study. A total of 575 tiles (blue outline) were created over Lower Saxony. The test tiles (TTs) used as the basis to identify the optimal feature sets are symbolized in orange color. All the coordinates in the figure are in UTM Zone 32N (EPSG:32632).

needed to identify the optimal feature set, we manually assessed and selected eleven test tiles (TTs) (symbolized as orange polygons in Figure 1) whose landscape compositions were representative of the remaining tiles in Lower Saxony. Details on how the selection was done are treated in Section III.A.

## B. SATELLITE DATA

A recent study [43] demonstrated the usability of monthly composites of S1 and S2 images for large-scale mapping of agricultural land-use (LU) types. For our study, we used monthly mean composites (MMCs) of S1 and S2 images from March to October 2018. For the MMCs of S1, we downloaded the Sentinel-1 L3 BS (Sentinel-1 Level-3 Backscatter) data from CODE-DE (Copernicus Data and Exploitation Platform – Deutschland).<sup>2</sup> CODE-DE is a cloud computing platform that provides access to the datasets of the Copernicus program covering Germany as well as virtual machines for data processing. The Sentinel-1 L3 BS images in VV and VH polarizations are created by averaging all the Sentinel-1 L2 CARD-BS (Sentinel-1 Level-2 Copernicus Analysis Ready Data – Backscatter) images over a month. The Sentinel-1 L2

CARD-BS images, which come at a resampled spatial resolution of 10 m, are generated by processing the Level-1 (L1) Ground Range Detected (GRD) images of S1 acquired in the Interferometric Wide Swath (IW) mode. The processing is done by CODE-DE with the Sentinel Application Platform (SNAP) using the standard procedure of applying an orbit file, removing GRD border noise, removing thermal noise, calibration, and terrain correction [44].

For S2, we used FORCE (Framework for Operational Radiometric Correction for Environmental monitoring) [45]. FORCE is a processing software for generating higher-level analysis-ready data (ARD) from S2 and Landsat images. Based on the top-of-atmosphere L1C images of S2, FORCE generates bottom-of-atmosphere L2 ARD images by correcting for atmospheric, geometric, and bidirectional reflectance distribution function (BRDF) effects [46]–[48]. In FORCE, clouds and cloud shadows are detected and masked using the Fmask algorithm [49]–[51]. The cloud and cloud shadow pixels were replaced using an interpolation method based on an ensemble of radial basis function (RBF) convolution filters [52]. FORCE outputs all S2 bands except the ones with a spatial resolution of 60 m, i.e., the coastal aerosol, water vapor, and cirrus bands. The bands with a spatial resolution of 20 meters are resampled to 10 m. For each band, all pixel

<sup>2</sup> <https://code-de.org/en/> (Accessed: Jul. 9, 2021).

values belonging to the same month were averaged to obtain the MMCs for S2.

### C. AGRICULTURAL LAND-COVER

From the digital landscape model of the German Official Topographic Cartographic Information System (ATKIS) of 2018, we extracted the vector layer containing polygons of the agricultural LC (arable land and grassland) present at the tiles. This layer was used to create a mask to remove non-agricultural areas from the MMC images before segmenting the agricultural fields. This approach has also been used in other studies [31], [36], [37].

### D. REFERENCE DATA

For segmentation evaluation and optimization, we used the Geospatial Aid Application (GSAA) data of 2018 covering the TTs. This data was obtained from the Lower Saxony Ministry of Food, Agriculture, and Consumer Protection. The GSAA data contains the boundaries of agricultural parcels manually digitized from very high-resolution orthoimages (spatial resolution  $\leq 1$  m) by farmers intending to access the subsidies within the CAP framework. The LU type (e.g., mowing pasture, meadow, maize, winter wheat, etc.) of each agricultural parcel is additionally declared by the farmer. The average size of an agricultural parcel over the TTs is about 3.4 ha, with the minimum size being about 0.2 ha and the maximum size being about 63 ha. The average number of agricultural parcels per tile is 2,463. For each test tile, basic descriptive information of the GSAA parcels can be found in Table 5 of Appendix A.

## III. METHODOLOGY

The workflow we used in this study is depicted in Figure 2. The components of the workflow will be explained in the next subsections.

### A. SELECTION OF TEST TILES (TTs)

The selection of the TTs was based on four criteria namely a high percentage coverage of agricultural LU, a high number of reference parcels for segmentation evaluation, the presence of both big and small agricultural fields, and a variable shape factor (SF) distribution per tile. The selected TTs are more dominated by agricultural LU as depicted in Figure 14 (Appendix A). Each selected tile contains a mixture of both big and small fields (see Table 5 of Appendix A). The authors in [36] and [53] emphasized the importance of having a sizeable number of reference objects for supervised segmentation evaluation to ensure accurate results. In our study, the minimum number of reference fields was 1,622 at TT2, which we considered as a sizeable number. The SF was used to quantify the shape characteristics of the GSAA parcels within each tile. We adopted the SF method in (1) as was proposed by [54];

$$SF = \frac{4 * \Pi * Area(X)}{(Perimeter(X))^2} \quad (1)$$

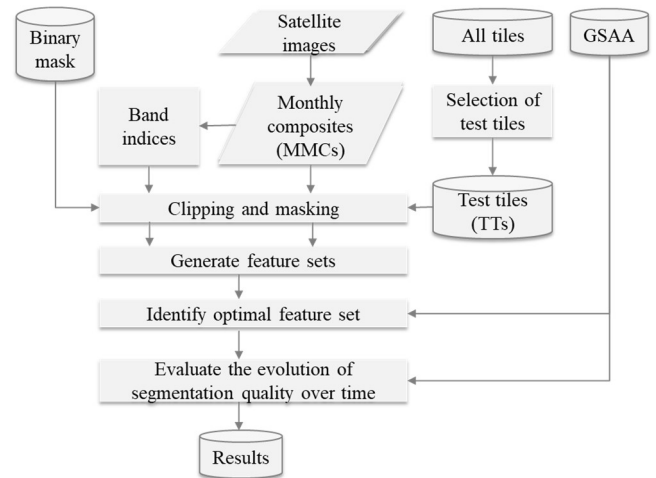


FIGURE 2. The workflow we followed in this study.

where  $X$  is a GSAA parcel. For each tile, the SF factor is calculated for all GSAA polygons. Higher SF values indicate more compact polygons, while lower values represent more elongated or irregular-shaped polygons. The selected tiles have variable SF distributions as captured by Figure 15 (Appendix A).

### B. BAND INDICES

Eight band indices (two radar and six optical) (Table 1) with extensive usage in RS for mapping agricultural lands were used in this study. The radar and optical indices were computed using the MMC images of S1 and S2, respectively. All the indices required at least two bands for computation. Given that the S2 MMC images had ten bands, the optical indices were selected to cover different parts of the electromagnetic spectrum as was previously done in [3]. The S1 MMC images come with only two bands, hence each radar index used both bands for computation.

### C. CLIPPING AND MASKING

Each MMC and band index of S1 and S2 was clipped to the boundary of a test tile. After clipping, all non-agricultural areas were removed. The agricultural vector layer extracted from ATKIS was used for this purpose. This vector layer contains cadastral polygons of all agricultural lands in Germany. We applied a negative buffer distance of 5 m to each polygon to create a separation between two adjacent polygons that share a common boundary. The reason for the negative buffer was to ensure the ease of separation between adjacent agricultural fields in the images during the segmentation process. All pixels outside the buffered polygons were masked out from each MMC and band index. These masked images were used for all subsequent processes.

### D. GENERATE FEATURE SETS

A feature set is a combination of two or more features (bands, indices). In all, nine feature sets were created (Table 2). The table shows each feature set alongside the input features that

**TABLE 1. The utilized radar and optical indices, abbreviations, formulas, and sources in the literature.**

Satellite	Index	Formula	Source
S1	Cross Ratio (CR)	$\frac{VH}{VV}$	[55]
	Radar Vegetation Index (RVI)	$\frac{4 * VH}{VV + VH}$	[56]
S2	Green Vegetation Index (GVI)	$\frac{Green - Red}{Green + Red}$	[57]
	Normalized Difference Vegetation Index (NDVI)	$\frac{NIR - Red}{NIR + Red}$	[58]
S2	Normalized Differential Senescent Vegetation Index (NDSVI)	$\frac{SWIR1 - Red}{SWIR1 + Red}$	[59]
	Normalized Difference Red Edge Index (NDRE)	$\frac{NIR - RedEdge1}{NIR + RedEdge1}$	[60]
S2	Normalized Difference Water Index (NDWI)	$\frac{NIR - SWIR1}{NIR + SWIR1}$	[61]
	Normalized Difference Tillage Index (NDTI)	$\frac{SWIR1 - SWIR2}{SWIR1 + SWIR2}$	[62]

**TABLE 2. The nine feature sets used for optimization: data sources, names, and lists of input features.**

Satellite	Feature set	Input features
S1	S1B	VH, VV
	S1I	CR, RVI
	S1BI	S1B, S1I
S2	S2B4	Blue, Green, Red, NIR
	S2B10	Blue, Green, Red, RedEdge 1, RedEdge 2, RedEdge 3, NIR, Narrow NIR, SWIR1, SWIR2
	S2I	GVI, NDVI, NDSVI, NDRE, NDWI, NDTI
	S2B4I	S2B4, S2I
	S2B10I	S2B10, S2I
S1 & S2	S2S1I	S2I, S1I

were used to create it. Three feature sets were based on S1 and five were based on S2. Those S1 and S2 feature sets were created after conducting some pretests to assess the separate impact of the bands and band indices on the segmentation accuracy. During the conduction of the pretests, we realized that a combination of the radar and optical indices led to an increase in the segmentation accuracy, hence the creation of the combined feature set named S2S1I. Based on each feature set, a feature dataset was generated for each month in the growing season using the masked images created in section III.C.

**E. IDENTIFY OPTIMAL FEATURE SET**

For each feature set in Table 2, all feature datasets from March to October were stacked together to create a seasonal

feature dataset. Nine seasonal feature datasets were created per tile. To optimize the segmentation of those nine seasonal feature datasets per tile, we used the supervised segmentation optimization (SSO) approach of [36]. That SSO approach utilizes the MRS algorithm. Given that the MRS algorithm requires three main parameters (scale, shape, and compactness), all of which take a varied range of input values, that SSO approach uses Bayesian optimization to identify the single parameter combination that yields the optimal segmentation output. The accuracy of the segmentation output of each parameter combination is measured through the overall segmentation quality (OSQ) metric, which is an area-weighted average of the Jaccard index [63]. The Jaccard index, which is widely known as Intersection over Union (IoU), is frequently used in computer vision tasks to measure the geometric similarity between a reference object and a target object extracted from an image or a video. The formula for IoU and OSQ as culled from [36] is given in (2) and (3), respectively;

$$IoU(Y) = \frac{Area(X \cap Y)}{Area(X \cup Y)} \tag{2}$$

$$OSQ = \frac{\sum_{i=1}^n Area(Y_i) * IoU(Y_i)}{\sum_{i=1}^n Area(Y_i)} \tag{3}$$

where  $X$  is a reference object,  $Y$  is its target object (segment),  $X \cap Y$  is the spatial intersection between them,  $X \cup Y$  represents their spatial union, and  $n$  is the total number of segments in a segmentation output. Given an input image and a reference dataset (GSAA in our case), the SSO approach uses 150 parameter combinations and then returns the segmentation output that best matches the reference data. It also returns the corresponding OSQ value as well as the IoU value of each segment in the optimal segmentation output. Both IoU and OSQ range from zero (lowest segmentation quality) to one (highest segmentation quality). The feature set with the highest average OSQ over the eleven tiles was adjudged as the best.

**F. EVALUATE THE EVOLUTION OF SEGMENTATION ACCURACY OVER TIME**

To assess the evolution of the segmentation accuracy of agricultural fields over time, we created incremental feature datasets covering different months of the growing season based on the optimal feature set identified in section III.E. Table 3 shows how the incremental feature datasets were created. The first incremental feature dataset (DID-1) was created using the feature dataset of March only. The one in April (DID-2) contains the feature datasets of March and April. This incremental process continued up to October (DID-8). DID-8 is the same as a seasonal feature dataset described in section III.E. The number of bands in each incremental feature dataset varied. Assuming S2B4 was established as the optimal feature set, DID-1 will have four bands, DID-2 will contain eight bands, and DID-8 will have 32 bands. For each of the eleven tiles, eight incremental feature datasets were created. Each incremental feature dataset

**TABLE 3.** The incremental feature datasets (DID-1 to DID-8) that were created in this study. The “x” symbol means that the feature dataset of that month was used in creating the incremental feature dataset.

Dataset ID	Mar	Apr	May	Jun	Jul	Aug	Sep	Oct
DID-1	x							
DID-2	x	x						
DID-3	x	x	x					
DID-4	x	x	x	x				
DID-5	x	x	x	x	x			
DID-6	x	x	x	x	x	x		
DID-7	x	x	x	x	x	x	x	
DID-8	x	x	x	x	x	x	x	x

served as an input to the SSO approach and the corresponding results were recorded.

## IV. RESULTS

### A. OPTIMAL FEATURE SET FOR SEGMENTATION

Figure 3 shows the variability of OSQs obtained at the eleven TTs for each feature set as well as the average OSQ (cyan boxes) obtained by each feature set over the test tiles. The S1 feature set based on only the radar indices (S1I) outperformed the one based on only the radar bands (S1B). The combination of the radar bands and indices (S1BI) led to an increase in OSQ. The feature set purely based on the S2 indices (S2I) outperformed those purely based on the spectral bands (S2B4, S2B10). The combination of the S2 bands and S2I to respectively create S2B4I and S2B10I improved the segmentation results as compared to separately using either S2B4 or S2B10. Among the feature sets based on only the S2 bands, S2B4 yielded better results than S2B10. The combination of the S2 and S1 indices (S2S1I) obtained the highest average OSQ. The numerical values of the average OSQs obtained by the feature sets over all the test tiles are reported in Table 6 of Appendix A.

The breakdown of the performance of each feature set per tile is shown in Figure 4. S2S1I yielded the best results at three tiles (TT3, TT4, TT10), S2B10I at three tiles (TT2, TT8, TT11), S1BI at two tiles (TT1, TT5), S1I at two tiles (TT6, TT7), and then S2B4I at one tile (TT9).

The optimal parameter combinations associated with S1BI (optimal among the S1 feature sets), S2B10I (optimal among the S2 feature sets), and S2S1I (overall optimal feature set) per tile are shown in Table 7 of Appendix A.

To understand the differences in OSQ between the feature sets, we further investigated S1BI, S2B10I, and S2S1I. We generated the area-weighted histogram in Figure 5 with ten bins using the IoU computed for each segment in the optimal segmentation results that were respectively obtained by S1BI, S2B10I, and S2S1I at all test tiles. We created an area-weighted histogram because the OSQ is also area-weighted. To create the histogram, each IoU contributed its segment area to the bin count (frequency) instead of one. As the histogram shows, the S2S1I feature set generated more

segments with better geometric matches to the GSAA parcels than the other feature sets, which resulted in it obtaining the highest average OSQ. Compared with S2B10I and S2S1I, the higher values for low-IoU bins obtained by S1BI as shown in Figure 5 explain its low accuracies in Figure 3 and Figure 4.

Based on the best feature set (S2S1I), we visually inspected the optimal segmentation results at TT1 (highest OSQ of 73.7%) and TT10 (lowest OSQ of 59.9%) to understand the reasons behind the difference in OSQ between them. Figure 6 shows the segmentation results achieved at TT1 and TT10. The false-color image of S2S1I at TT1 and TT10 are depicted in Figure 6a and Figure 6b, respectively. The GSAA parcels (black outlines) have been overlaid on the false-color images in Figure 6c and Figure 6d, respectively. The optimal segments symbolized by their respective IoU values have been overlaid on the false-color images in Figure 6e and Figure 6f, respectively. The segments that touch the boundaries of each tile are excluded in the SSO approach because they are artifacts, hence they are not displayed in Figure 6e and Figure 6f. The reason for the difference in OSQ between those two tiles is attributable to the difference in the size and shape of agricultural fields at each tile. At TT1, the tiles are bigger and more compact. The opposite can be seen at TT10, where most of the agricultural fields are smaller and less compact (more elongated).

### B. EVOLUTION OF SEGMENTATION ACCURACY OVER TIME

The average OSQ attained by each S2S1I-based incremental feature dataset over all tiles is depicted in Figure 7. The lowest OSQs were mostly obtained at the beginning of the growing season in March with DID-1. As the season progressed and more datasets were acquired and used, the segmentation accuracy increased accordingly. The highest OSQs were mostly achieved at the end of the growing season in October (DID-8). As Figure 8 shows, the optimal OSQ at eight tiles (TT1, TT4, TT5, TT6, TT7, TT8, TT9, TT11) was attained with DID-8, two tiles (TT2, TT3) with DID-7, and one tile (TT10) with DID-4. The difference in average OSQ of 5.31 percentage points between DID-1 (62.2%) and DID-8 (67.51%) was observed to be statistically significant ( $p$ -value = 0.006) based on a two-tailed t-test. In the incremental segmentation set-up, the highest improvement in OSQ of almost 2% was achieved by adding the May dataset to the incremental stack to create DID-3. This was followed by the addition of the June dataset to create DID-4, which led to an increase of about 1.2%. After June, the increase became more gradual.

We used the IoU values of the segments in the optimal segmentation results generated with the incremental feature datasets to create the area-weighted histogram shown in Figure 9, which focuses on DID-1 (start of the season), DID-3 (after the farmers submit their GSAA), and DID-8 (end of the season). The optimal segmentation results respectively obtained with DID-3 and DID-8 produced more segments that geometrically matched the GSAA parcels than DID-1 did.

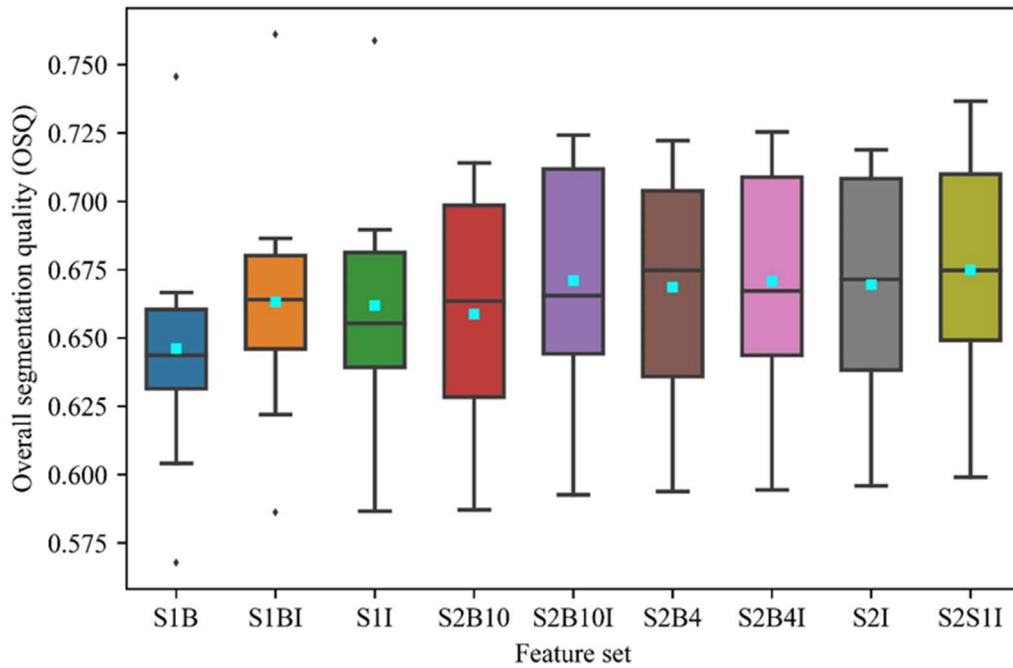


**FIGURE 3.** Boxplots showing the variability of OSQs obtained at the eleven tiles per feature set. The cyan boxes represent the average OSQs achieved by each feature set over the tiles. The within-box horizontal lines are the median OSQs. The black dots are the OSQs that are outliers.

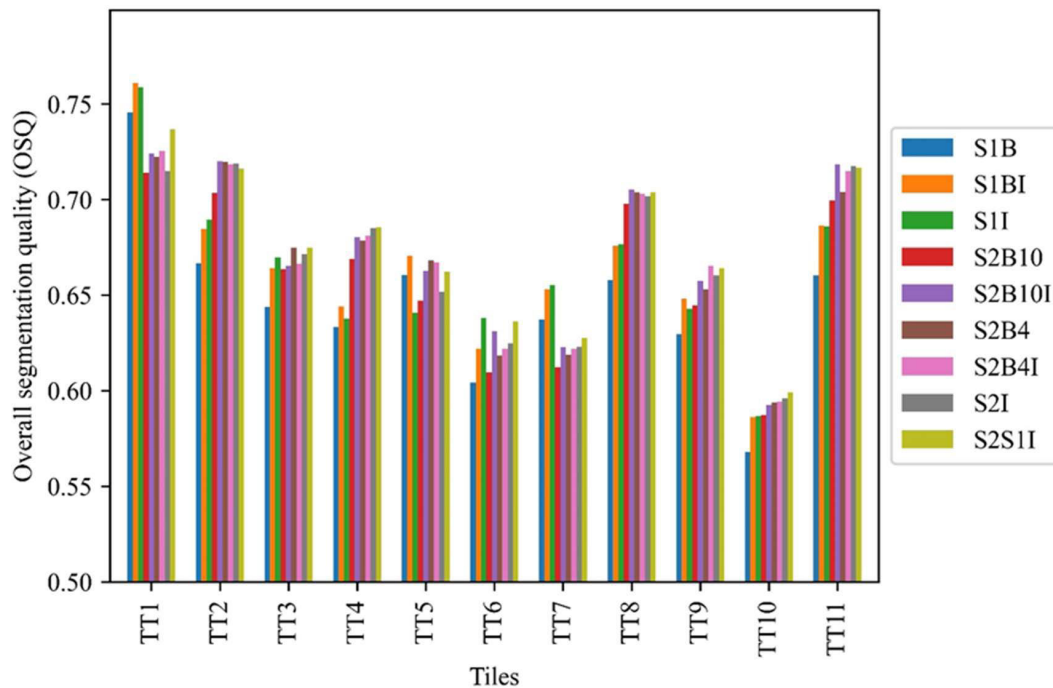


**FIGURE 4.** The OSQ obtained by each feature set per tile.

**C. PLAUSIBILITY ANALYSIS: COMPARISON OF THE SEGMENTATION RESULTS WITH THE GSAA PARCELS**

In [36], over-segmentation was identified as the main reason for the disparity between the GSAA parcels and the segmentation results. In addition to the instances of over-segmentation established in [36], we identified a new instance of over-segmentation, which was caused by the masking approach we used in this study as shown in Figure 10.

In Figure 10a, the GSAA parcel indicates the presence of a single LU (mowing pasture) but due to the inward buffer applied at the masking stage, an artificial boundary was created in the satellite image leading to the incorrect generation of two separate segments (B1, B2) as shown in Figure 10b. B1 and B2 had moderate IoU values of 51% and 35.9%, respectively. A higher IoU value could have been achieved with a single segment without any separation between them.

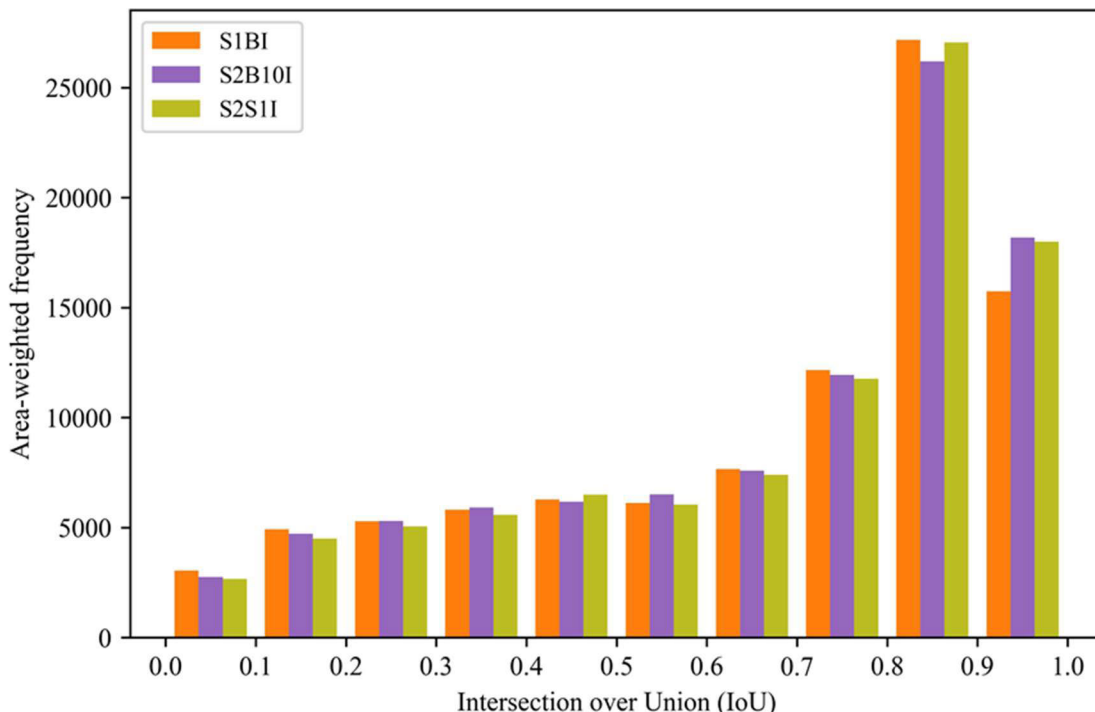


**FIGURE 5.** Area-weighted histogram of the Intersection over Union (IoU) values computed for the segments in the optimal segmentation results achieved respectively by S1B1, S2B10I, and S2S1I at all test tiles.

**TABLE 4.** Overall segmentation quality (OSQ) computed for the different field size categories.

Field size group	OSQ
Very small (< 0.5 ha)	27.03%
Small (0.5 – 1.5 ha)	57.65%
Medium (1.5 – 15 ha)	75.71%
Large (> 15 ha)	68.31%

**D. SEGMENTATION ACCURACY FOR DIFFERENT FIELD SIZES**

The segmentation optimization process was subsequently extended to the other tiles in Lower Saxony based on the DID-8 generated for S2S1I. The optimal segmentation results of the 575 tiles were then merged. The merged result can be viewed as the “original\_segmentation\_ni” layer on this web map.<sup>3</sup> Based on this merged result, we analyzed the impact of the area of the agricultural fields on the OSQ. In [5], the authors stated that a minimum of 50 pixels per field is the critical number required for site-specific smart farming. Therefore, we separated the small field size category of [2] into two sub-groups: very small fields (< 0.5 ha) and small fields (0.5 ha – 1.5 ha). The medium and large field categories were kept. Table 4 shows the OSQ computed for each category.

From Table 4, the accuracy of large fields was lower than the medium fields. A visual assessment of the results revealed some of the instances that contributed to that phenomenon

as shown in Figure 11 and Figure 12, where the size of the GSAA parcels are 19.6 ha and 15.7 ha, respectively. To receive the greening payments within CAP, farmers with arable land exceeding 15 ha have to use at least 5% of their land as an Ecological Focus Area (EFA), e.g., hedges. Due to the presence of hedges in Figure 11a, the SSO correctly created one segment containing the hedges (B1) and a second segment without hedges (B2) as captured in Figure 11b. Unfortunately, B1 had a low accuracy of 6.4%. B2 was 86.4% accurate. In Figure 12, although the image (Figure 12a) looks relatively homogenous, two separate segments (B1 and B2) with respective accuracies of 21.3% and 73.9 % were created by the SSO as shown in Figure 12b. This is an error caused by the MRS parameters not being optimal for that particular agricultural field, even though the identified parameters were optimal for the tile that contains that field.

**E. USE CASE: POST-FILTERING OF PIXEL-BASED CROP MAPS**

In [64], the authors showed that the post-filtering of pixel-based crop type maps using image segments through majority voting can improve image classification results. Therefore, as a use case, we tested if the crop type map of [65] as visualized on this webpage<sup>4</sup> could be improved using the merged segmentation result of Lower Saxony. Before proceeding with this test, we first post-processed the merged segments in GRASS GIS.<sup>5</sup> We applied “v.clean” to first

<sup>4</sup><https://ows.geo.hu-berlin.de/webviewer/croptypes/> (Accessed: Jul. 9, 2021).

<sup>5</sup><https://grass.osgeo.org/> (Accessed: Jul. 9, 2021).

<sup>3</sup><https://tisdex.thuenen.de/maps/34/view#/> (Accessed: Jul. 9, 2021).

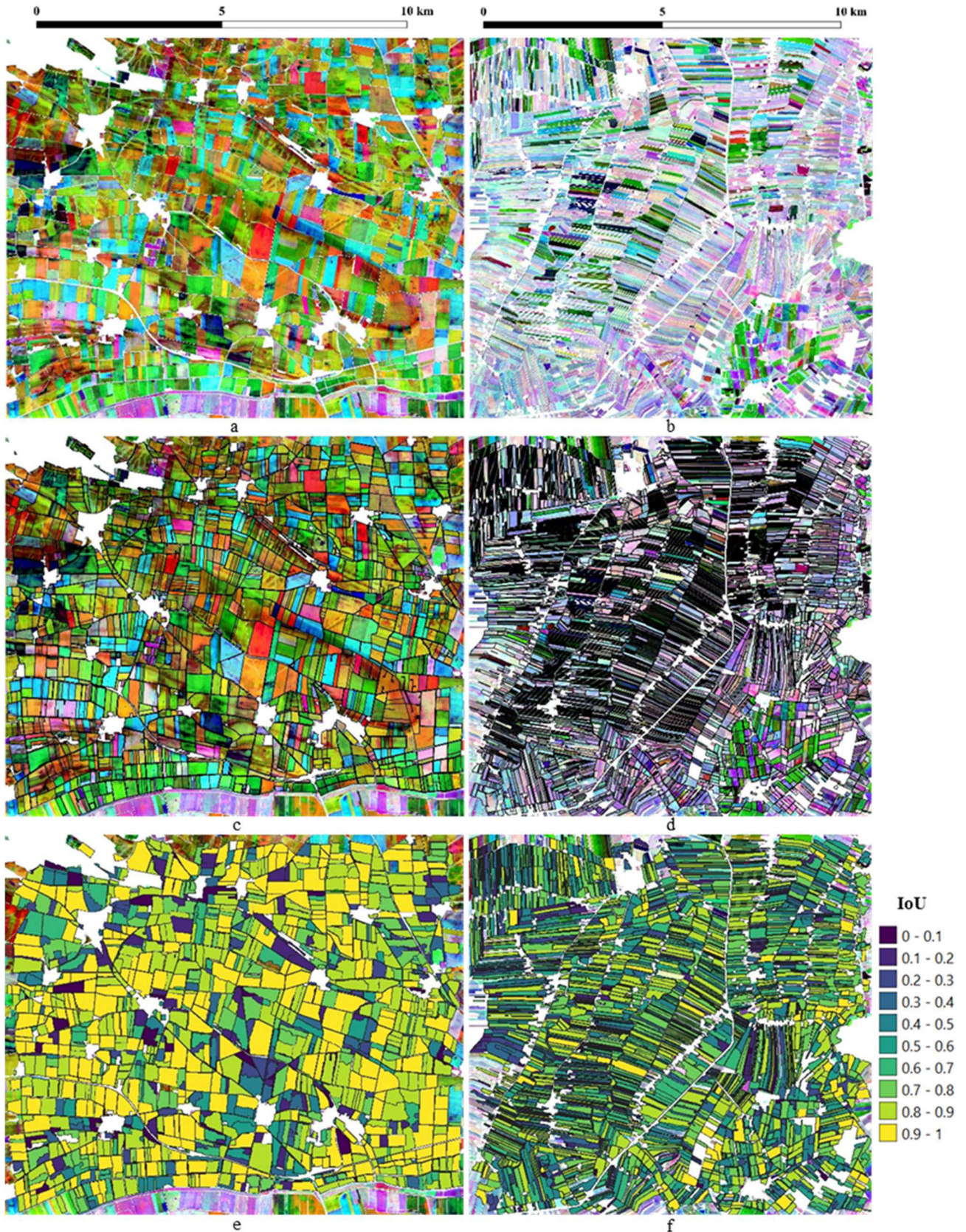


**FIGURE 6.** Optimal segmentation results obtained at TT1 (left column) and TT10 (right column) based on S2S11. (a) and (b) show the false-color composites of the NDVI MMCs of March, June, and October. The GSAA parcels (black outlines) have been overlaid on the respective images at (c) and (d). The optimal segments have been symbolized with their corresponding IoU values and subsequently draped over each image at (e) and (f), respectively. The geographical extent of TT1 is roughly 12.3 km by 10.3 km and that of TT10 is roughly 11.3 km by 10.7 km.

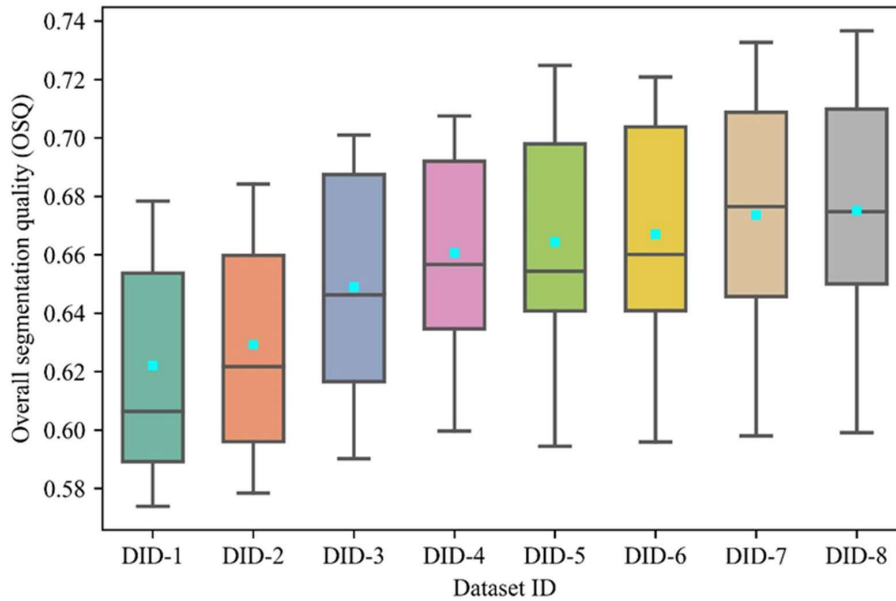


**FIGURE 7.** Boxplots showing the variability of OSQs obtained at the eleven tiles by the S2S11-based incremental feature datasets. The cyan boxes are the average OSQs over all tiles as obtained by the incremental feature datasets. The within-box horizontal lines are the median OSQs.

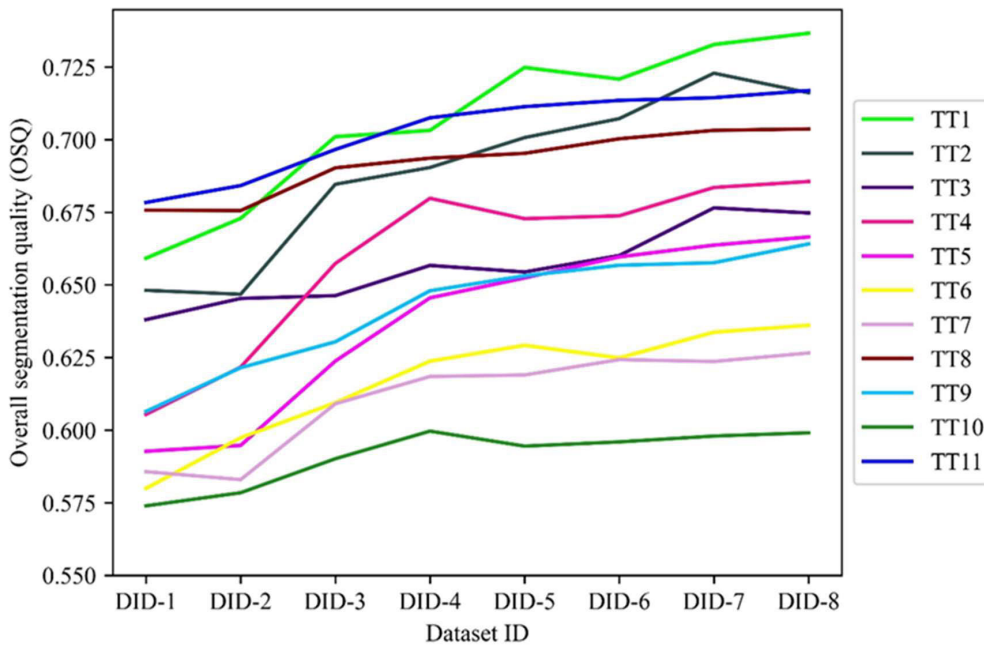


**FIGURE 8.** The OSQ obtained by each S2S11-based incremental feature dataset per tile.

remove duplicate segments created due to overlapping tiles and then applied “v.generalize” to simplify the segments. The simplified segments can be viewed as the “simplified\_segmentation\_ni” layer in this web map.<sup>6</sup> We subsequently applied a majority vote filter to determine the crop type of each segment. As an example, the pixel-based crop type map and the crop type map after the majority vote at TT7 (balanced share of arable lands and grasslands) are captured by Figure 13a and Figure 13b, respectively. The outcome of

the majority vote was a smoothed map, where most of the noise in the pixel-based map had been removed. An accuracy assessment performed using all the GSAA parcels of Lower Saxony indicated an improvement in the overall accuracy after filtering from 78% to 81.4% and the Kappa statistic from 0.705 to 0.747.

**V. DISCUSSION**

This current study builds on the previous work of [36]. In [36], the authors only focused on the development of the optimization approach. No attention was given to the

<sup>6</sup><https://tisdex.thuenen.de/maps/34/view#/> (Accessed: Jul. 9, 2021).

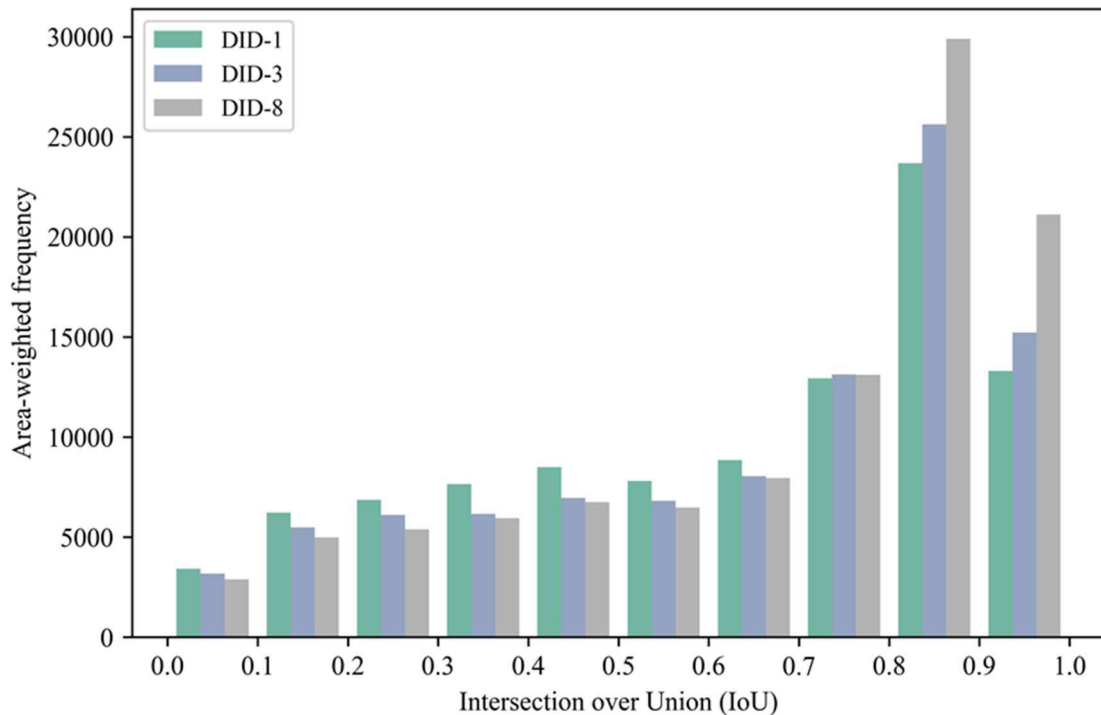


**FIGURE 9.** Area-weighted histogram of the Intersection over Union (IoU) values computed for the segments in the optimal segmentation results achieved respectively by DID-1, DID-3, and DID-8 at all test tiles.

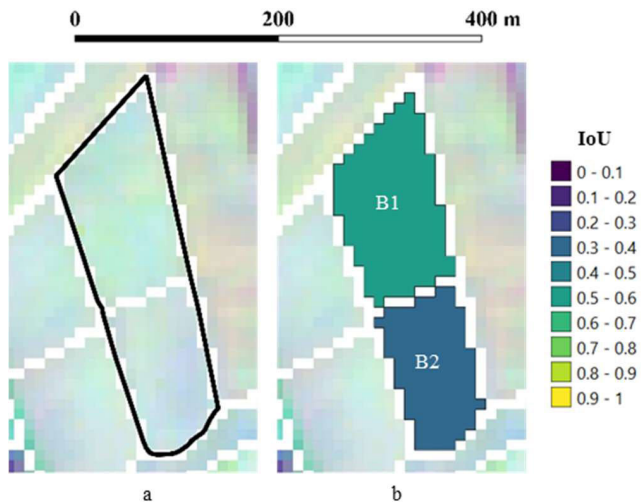


**FIGURE 10.** Over-segmentation caused by the masking approach used in this study. The background displays in (a) and (b) are based on the false-color image created for DID-8 using the NDVIs of March, June, and October. The image in (a) has been overlaid with the GSAA parcel (black outline). The corresponding segments generated are symbolized in (b) by their IoU values. Two separate segments labeled B1 and B2 were created.

identification of the optimal feature set for segmenting the agricultural fields. In [36], cloud-free S2 images were manually selected and used. In this study, an automated process based on FORCE was used to identify and replace clouds. This study also evaluated pre-processed S1 datasets as obtained from CODE-DE. For our current study, we used monthly composites of S1 and S2 unlike [36], where single-date S2 images were used. In [36], the segmentation accuracy that could be achieved for different agricultural field size

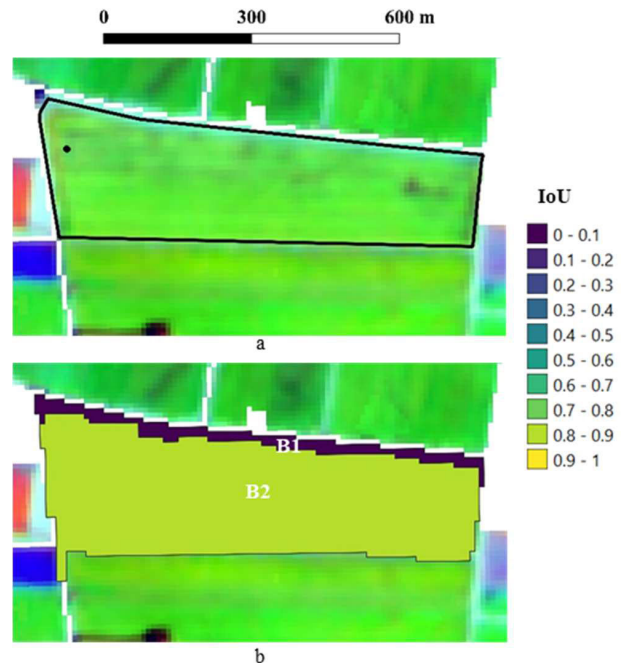


**FIGURE 11.** Over-segmentation caused by hedges. The background displays in (a) and (b) are based on the false-color image created for DID-8 using the NDVIs of March, June, and October. The image in (a) has been overlaid with the GSAA parcel (black outline). The LU of this GSAA parcel is potato. The corresponding segments generated are symbolized in (b) by their IoU values. Two separate segments labeled B1 and B2 were created.

categories was not assessed. Finally, in this study, the use of image segmentation to aggregate and improve a pixel-based crop type map was evaluated.

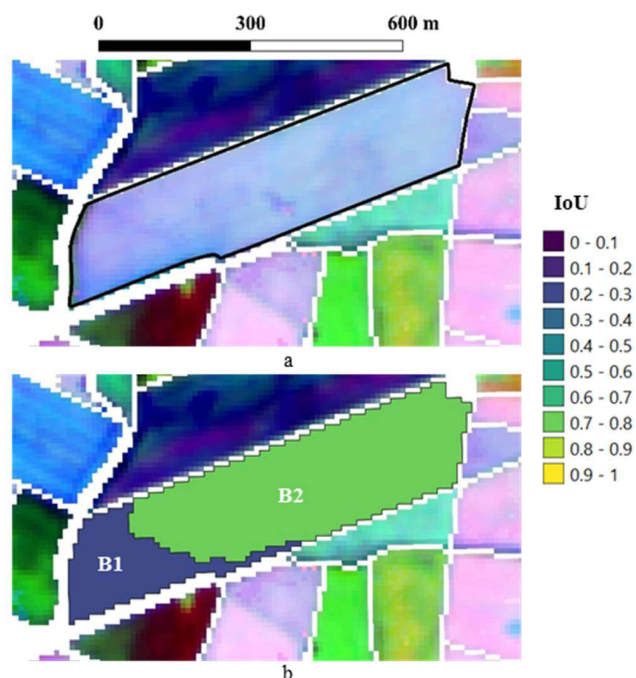


**FIGURE 12.** Over-segmentation caused by the non-optimal MRS parameters. The background displays in (a) and (b) are based on the false-color image created for DID-8 using the NDVis of March, June, and October. The image in (a) has been overlaid with the GSAA parcel (black outline). The LU of this GSAA parcel is mowing pasture. The corresponding segments generated are symbolized in (b) by their IoU values. Two separate segments labeled B1 and B2 were created.

For segmenting agricultural fields, using only the visible and near-infrared bands (S2B4) of S2 was superior to using all ten bands (S2B10) as depicted in Figure 3. A similar outcome was reported by [23], who received more accurate results using only the visible (RGB) bands of a Worldview-2 image as compared to using all the eight bands for image segmentation based on the MRS algorithm. They attributed this phenomenon to the high correlation existing between the eight bands. To deal with this problem, they applied principal component analysis (PCA) to the eight bands and used the first three components for segmentation. The result was better than using all eight bands but underperformed in comparison with the RGB bands. In using S2, most authors [33]–[40] directly used S2B4 to segment agricultural fields without testing other feature combinations. The superiority of S2B4 to S2B10 as established in this study validates the choice of S2B4 by those authors for segmenting agricultural fields.

Due to the inherently speckled nature of radar images, some researchers [66]–[68] have asserted that the segmentation of optical images is easier and more accurate. Their assertion can largely be backed by Figure 3, where most of the feature sets based on only S2 outperformed those based on only S1. However, the S1 feature sets (S1I, S1BI) containing the radar indices proved capable of segmenting agricultural fields even to the extent that they outperformed S2B10. The speckle noise in radar images often makes it difficult to visually identify the boundaries of features. Monthly compositing was particularly beneficial to S1 as it helped in reducing

the speckle noise, thereby revealing the boundaries of agricultural fields. The masking approach used in this study was potentially more beneficial to S1 in creating boundaries between adjacent fields. In situations where S2 images are not available due to clouds, monthly composites of S1 images could be used for segmenting agricultural fields. Overall, the combination of S1 and S2 resulted in the highest segmentation accuracy (Figure 3). Within the context of mapping agricultural LU types, other authors [43], [69], [70] also observed that combining S1 and S2 leads to better results than separately using each sensor.

Based on the seasonal feature dataset (DID-8) created from the combined S1 and S2 feature set, the highest OSQ occurred at TT1 (Figure 6e) and the lowest at TT10 (Figure 6f). The main driving forces behind the obtained OSQs were the area and shape of agricultural fields at the tiles. Due to the presence of big and compact agricultural fields at TT1, the segmentation process was more successful there. At TT10, most of the agricultural fields are small and elongated, and additionally, they are highly dominated by one LU (mowing pasture). Such conditions coupled with the spatial resolution of S1 and S2 make it difficult to appropriately segment agricultural fields from S1 and S2 images because clear-cut boundaries between agricultural fields cannot be distinguished in the S1 and S2 images. This observation was also made by [36] in their research as they encountered a similar problem. The use of an image with a higher spatial resolution than S2 was proposed by [36] as a likely solution.

Because agricultural fields are dynamic and change over time, to accurately map different agricultural LU types, the use of multitemporal images is considered a requirement by [71]. With multitemporal images, the different phenological behaviors of different agricultural LU types throughout the growing season can be characterized and effectively used to differentiate them [72]. Although that suggestion was made within the context of image classification, it also applies to the segmentation of agricultural fields as was highlighted by these authors [39], [73]. As Figure 7 shows, using a single-period dataset (DID-1) resulted in segments with significantly lower accuracies than those created using the dataset covering the whole growing season (DID-8). This demonstrates the importance of using multitemporal images for the effective segmentation of agricultural fields. Consecutively increasing the number of images (S2S1I in our case) led to a corresponding increase in the segmentation accuracy (Figure 7). Although these studies [74], [75] were exclusively focused on object classification, they also observed a similar phenomenon, in that, increasing the number of input images yielded an increase in the accuracy of the classified segments.

Some sources of error identified in this study included the masking approach, which led to the over-segmentation captured in Figure 10. This problem could be resolved by using an improved agricultural LC dataset. Another source of error was the presence of hedges in the images, which led to low segmentation accuracies as was highlighted in Figure 11.

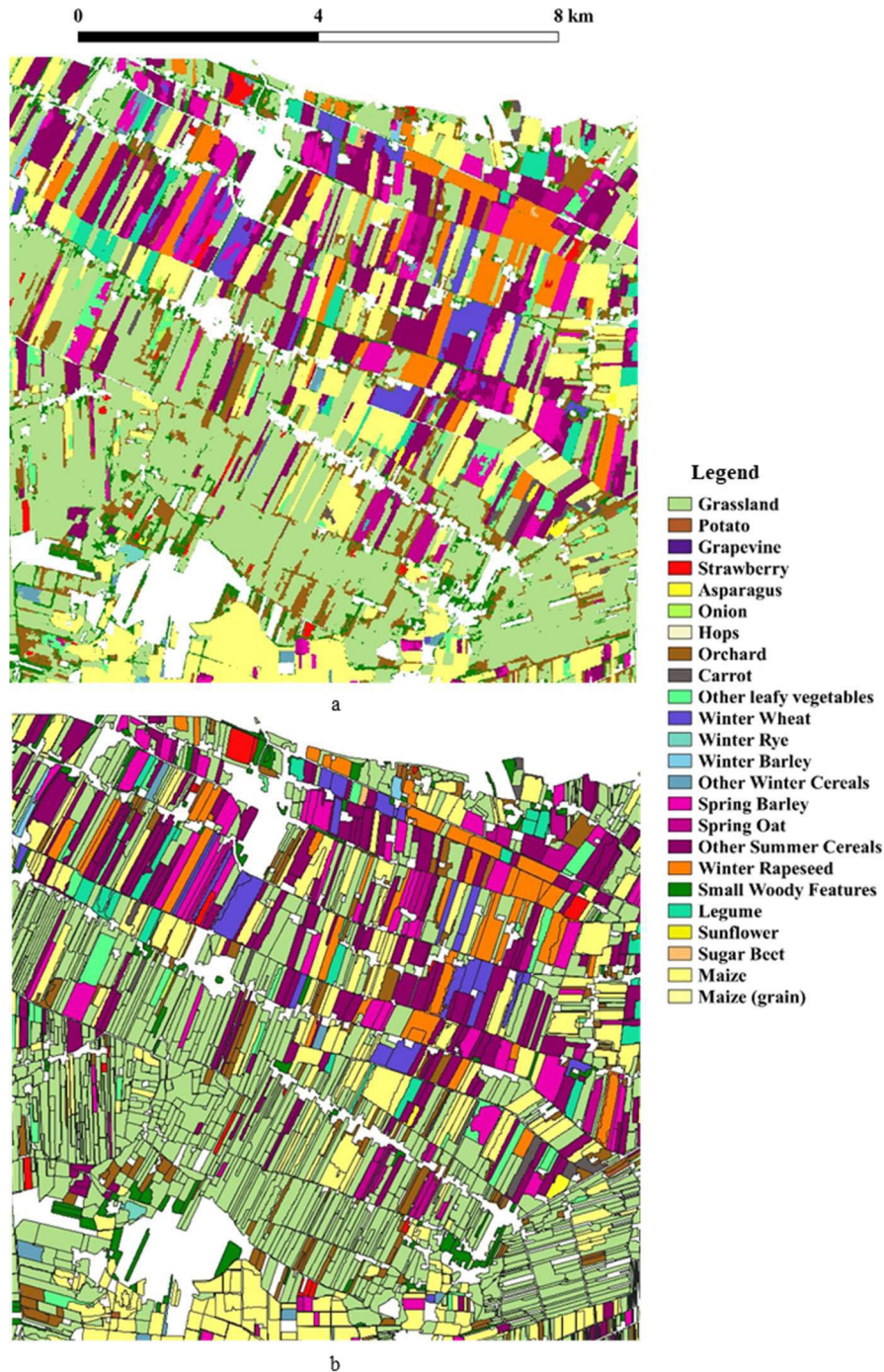


**FIGURE 13.** Usage of a majority vote to generate an object-based crop type map (b) from the pixel-based crop type map (a).

Although the presence of the hedge led to a low segmentation accuracy, such segmentation errors are acceptable especially for subsequent processes like crop type mapping meant to determine the actual LU within a field. The last source of error as highlighted in Figure 12 was caused by the non-optimal MRS parameters. The segmentation optimization in this study was applied to roughly 11 km by 11 km tiles. In tiles with predominantly smaller fields, such instances of over-segmentation as displayed in Figure 12 are unavoidable.

One solution will be to apply the segmentation optimization based on each GSAA parcel instead of using all parcels within a tile for the optimization. However, such an approach will be computationally expensive. A more efficient solution will be to merge neighboring segments with the same LU type after object classification as was proposed by [36]. After applying the majority vote filter, both segments in Figure 12b were classified as grasslands, hence they could be merged as one segment.

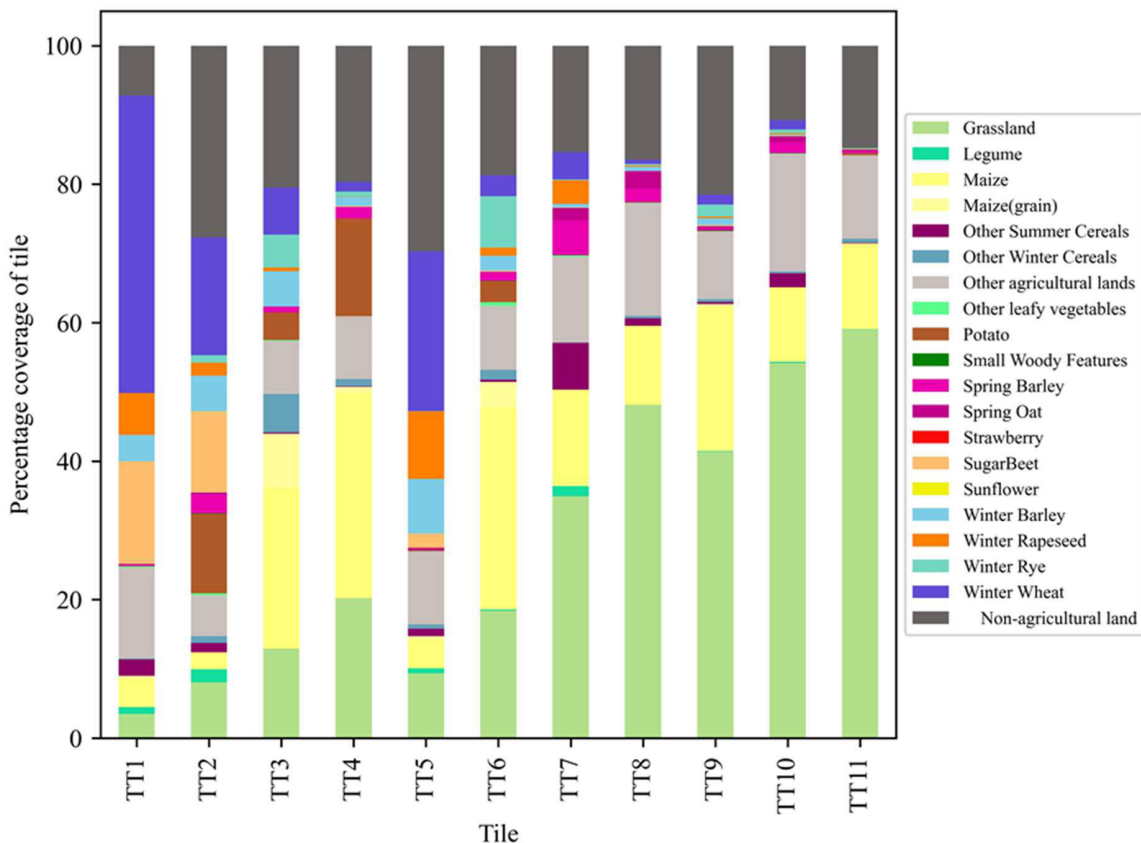


FIGURE 14. Distribution of land-use (LU) per tile.

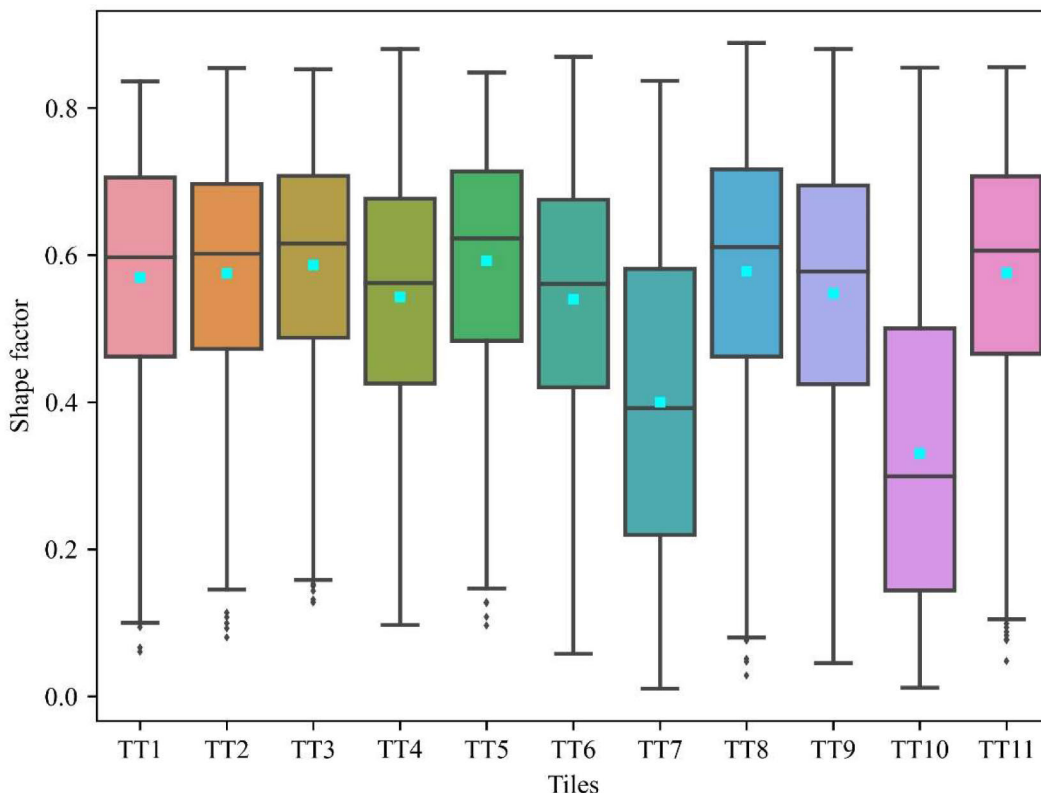


FIGURE 15. The boxplots showing the distribution of shape factors (SFs) per tile. The cyan boxes represent the average SFs. The within-box horizontal lines are the median SFs.

**TABLE 5.** Basic descriptive information of the GSAA parcels used in this study per test tile.

Tile	No. of GSAA parcels	Min. area (ha)	Max. area (ha)	Mean area (ha)
TT1	1,686	0.21	62.76	5.86
TT2	1,622	0.17	47.78	4.68
TT3	2,694	0.18	23.34	2.97
TT4	2,531	0.20	23.53	3.08
TT5	2,910	0.18	21.85	2.16
TT6	2,354	0.16	29.72	3.48
TT7	1,876	0.19	47.52	3.90
TT8	3,767	0.17	20.74	1.85
TT9	2,015	0.16	49.47	3.76
TT10	2,563	0.20	37.76	2.72
TT11	3,074	0.18	29.47	2.71

**TABLE 6.** The average OSQs obtained by each feature set over the eleven test tiles.

Feature set	Average OSQ
S1B	0.646
S1BI	0.663
S1I	0.662
S2B10	0.659
S2B10I	0.671
S2B4	0.669
S2B4I	0.671
S2I	0.670
S2S1I	0.675

The general trend discernable from Table 4 is that bigger fields lead to higher segmentation accuracies as was also established in [36]. Contrary to the suggestion of [2] that S1 and S2 are more suitable for large fields, Table 4 rather showed that the S1 and S2 images are more suitable for medium fields. The larger the fields, the higher the probability of over-segmentation as was depicted in Figure 11 and Figure 12, both of which led to lower segmentation accuracies.

The usefulness of image segmentation for post-filtering pixel-based crop type maps was briefly demonstrated in this study. The derived object-based map was more visually appealing and also increased the classification accuracy.

**VI. CONCLUSION**

In this study, we applied supervised segmentation optimization to different feature datasets generated from S1 and S2 images at eleven test tiles in Lower Saxony, Germany to identify the optimal feature set for segmenting agricultural fields. Additionally, the accuracy of agricultural fields segmented from the S1 and S2 feature datasets between March and October of 2018 was analyzed. Based on the

**TABLE 7.** The optimal parameter combinations obtained by S1BI (optimal among the S1 feature sets), S2B10I (optimal among the S2 feature sets), and S2S1I (overall optimal feature set) per tile.

Tile	Scale	Shape	Compactness	OSQ	Feature set
TT1	100	0.900	0.865	0.761	S1BI
TT1	80	0.900	0.900	0.724	S2B10I
TT1	97	0.900	0.945	0.737	S2S1I
TT2	108	0.900	1.000	0.685	S1BI
TT2	74	0.900	0.992	0.720	S2B10I
TT2	99	0.899	0.971	0.716	S2S1I
TT3	80	0.900	0.900	0.664	S1BI
TT3	97	0.734	0.757	0.665	S2B10I
TT3	80	0.900	0.700	0.675	S2S1I
TT4	93	0.900	0.918	0.644	S1BI
TT4	95	0.746	0.900	0.680	S2B10I
TT4	80	0.900	0.900	0.686	S2S1I
TT5	70	0.900	1.000	0.670	S1BI
TT5	49	0.900	0.894	0.663	S2B10I
TT5	58	0.900	1.000	0.662	S2S1I
TT6	90	0.900	1.000	0.622	S1BI
TT6	68	0.896	0.783	0.631	S2B10I
TT6	78	0.900	0.984	0.636	S2S1I
TT7	93	0.900	0.398	0.653	S1BI
TT7	90	0.900	0.381	0.623	S2B10I
TT7	103	0.900	0.933	0.628	S2S1I
TT8	66	0.900	0.813	0.676	S1BI
TT8	90	0.690	1.000	0.705	S2B10I
TT8	93	0.759	1.000	0.704	S2S1I
TT9	81	0.900	1.000	0.648	S1BI
TT9	71	0.900	0.935	0.658	S2B10I
TT9	78	0.900	0.830	0.664	S2S1I
TT10	80	0.900	0.500	0.586	S1BI
TT10	135	0.590	0.817	0.593	S2B10I
TT10	132	0.624	0.789	0.599	S2S1I
TT11	80	0.900	0.900	0.687	S1BI
TT11	92	0.810	1.000	0.719	S2B10I
TT11	72	0.900	0.811	0.717	S2S1I

results from the eleven test tiles, the segmentation optimization process was extended to every part of Lower Saxony.

The results obtained in this study allow for the following conclusions to be drawn: (1) S2 generally yields better segmentation results than S1, (2) the synergistic use of S1 and S2 can lead to an improvement in segmentation accuracy, (3) multitemporal S1 and S2 images are key to the optimal segmentation of agricultural fields, (4) S1 and S2 images are more suitable for segmenting medium-sized (1.5 – 15 ha) agricultural fields, and (5) post-filtering of pixel-based crop type maps with agricultural fields extracted via image segmentation improves classification accuracies.

The main outcome (agricultural fields) of this study can be used to produce object-based crop type maps. An object-based crop type map is useful for subsequent processes like the correct estimation of the area per crop type, crop yield modeling, crop rotation analysis, greenhouse gas (GHG) modeling, etc.

Looking ahead, we intend to extend this study to every state in Germany. The derived segmentation results will then be used as direct inputs to land-cover/land-use classification and land-use intensity mapping (mowing detection). To test the robustness of our current approach to the determination of the optimal feature set, we intend to test other segmentation algorithms particularly deep neural networks (DNN), and then compare the results to our current study. Smaller fields are more sensitive to the IoU metric than bigger fields. A small spatial misalignment between a segmented field and its corresponding reference object will have a more negative impact on the IoU value of a smaller field than a bigger field. Therefore, future studies should test other segmentation evaluation metrics that combine the percentages of the overlapped (correctly segmented) area, over-segmented area, and under-segmented area for each segmented field.

## APPENDIX A

See Figures 14 and 15, and Tables 5–7.

## ACKNOWLEDGMENT

The authors are grateful to the Lower Saxony Ministry of Food, Agriculture, and Consumer Protection for providing the GSAA data, the German Federal Agency for Cartography and Geodesy (BKG) for providing ATKIS, and CODE-DE for providing the S1 monthly mean composites. They are also grateful to Andrea Ackermann and Helge Meyer-Borstel of Thünen Institute of Rural Studies for pre-processing and validating the GSAA and ATKIS datasets. Finally, they would like to thank the reviewers of this manuscript for their constructive feedback.

## REFERENCES

- [1] United Nations, New York, NY, USA. (Sep. 2015). *Transforming Our World: The 2030 Agenda for Sustainable Development*. Accessed: Jun. 18, 2021. [Online]. Available: [https://www.un.org/ga/search/view\\_doc.asp?symbol=A/RES/70/1&Lang=E](https://www.un.org/ga/search/view_doc.asp?symbol=A/RES/70/1&Lang=E)
- [2] A. K. Whitcraft, I. Becker-Reshef, C. O. Justice, L. Gifford, A. Kavvada, and I. Jarvis, "No pixel left behind: Toward integrating earth observations for agriculture into the united nations sustainable development goals framework," *Remote Sens. Environ.*, vol. 235, Dec. 2019, Art. no. 111470, doi: 10.1016/j.rse.2019.111470.
- [3] J. M. Peña-Barragán, M. K. Ngugi, R. E. Plant, and J. Six, "Object-based crop identification using multiple vegetation indices, textural features and crop phenology," *Remote Sens. Environ.*, vol. 115, no. 6, pp. 1301–1316, Jun. 2011, doi: 10.1016/j.rse.2011.01.009.
- [4] C. Conrad, S. Fritsch, J. Zeidler, G. Rücker, and S. Dech, "Per-field irrigated crop classification in arid central Asia using SPOT and ASTER data," *Remote Sens.*, vol. 2, no. 4, pp. 1035–1056, Apr. 2010, doi: 10.3390/rs2041035.
- [5] J. Meier, W. Mauser, T. Hank, and H. Bach, "Assessments on the impact of high-resolution-sensor pixel sizes for common agricultural policy and smart farming services in European regions," *Comput. Electron. Agricult.*, vol. 169, Feb. 2020, Art. no. 105205, doi: 10.1016/j.compag.2019.105205.
- [6] A. García-Pedrero, M. Lillo-Saavedra, D. Rodríguez-Esparragón, and C. Gonzalo-Martín, "Deep learning for automatic outlining agricultural parcels: Exploiting the land parcel identification system," *IEEE Access*, vol. 7, pp. 158223–158236, 2019, doi: 10.1109/ACCESS.2019.2950371.
- [7] C. Y. Ji, "Delineating agricultural field boundaries from TM imagery using dyadic wavelet transforms," *ISPRS J. Photogramm. Remote Sens.*, vol. 51, no. 6, pp. 268–283, Dec. 1996, doi: 10.1016/0924-2716(95)00017-8.
- [8] C. Atzberger, "Advances in remote sensing of agriculture: Context description, existing operational monitoring systems and major information needs," *Remote Sens.*, vol. 5, no. 2, pp. 949–981, Feb. 2013, doi: 10.3390/rs5020949.
- [9] P. Shanmugapriya, S. Rathika, T. Ramesh, and P. Janaki, "Applications of remote sensing in agriculture—A review," *Int. J. Current Microbiol. Appl. Sci.*, vol. 8, no. 1, pp. 2270–2283, Jan. 2019, doi: 10.20546/ijcmas.2019.801.238.
- [10] M. Weiss, F. Jacob, and G. Duveiller, "Remote sensing for agricultural applications: A meta-review," *Remote Sens. Environ.*, vol. 236, Jan. 2020, Art. no. 111402, doi: 10.1016/j.rse.2019.111402.
- [11] C. Evans, R. Jones, I. Svalbe, and M. Berman, "Segmenting multispectral Landsat TM images into field units," *IEEE Trans. Geosci. Remote Sens.*, vol. 40, no. 5, pp. 1054–1064, May 2002, doi: 10.1109/TGRS.2002.1010893.
- [12] M. Möller, L. Lymburner, and M. Volk, "The comparison index: A tool for assessing the accuracy of image segmentation," *Int. J. Appl. Earth Observ. Geoinf.*, vol. 9, no. 3, pp. 311–321, Aug. 2007, doi: 10.1016/j.jag.2006.10.002.
- [13] L. Yan and D. P. Roy, "Conterminous United States crop field size quantification from multi-temporal Landsat data," *Remote Sens. Environ.*, vol. 172, pp. 67–86, Jan. 2016, doi: 10.1016/j.rse.2015.10.034.
- [14] J. Graesser and N. Ramankutty, "Detection of cropland field parcels from Landsat imagery," *Remote Sens. Environ.*, vol. 201, pp. 165–180, Nov. 2017, doi: 10.1016/j.rse.2017.08.027.
- [15] L. Yan and D. P. Roy, "Automated crop field extraction from multi-temporal web enabled Landsat data," *Remote Sens. Environ.*, vol. 144, pp. 42–64, Mar. 2014, doi: 10.1016/j.rse.2014.01.006.
- [16] J. A. Long, R. L. Lawrence, M. C. Greenwood, L. Marshall, and P. R. Miller, "Object-oriented crop classification using multitemporal ETM+SLC-off imagery and random forest," *GISci. Remote Sens.*, vol. 50, no. 4, pp. 418–436, Aug. 2013, doi: 10.1080/15481603.2013.817150.
- [17] J. K. Gilbertson, J. Kemp, and A. Van Niekerk, "Effect of pan-sharpening multi-temporal Landsat 8 imagery for crop type differentiation using different classification techniques," *Comput. Electron. Agricult.*, vol. 134, pp. 151–159, Mar. 2017, doi: 10.1016/j.compag.2016.12.006.
- [18] B. Schultz, M. Immitzer, A. Formaggio, I. Sanches, A. Luiz, and C. Atzberger, "Self-guided segmentation and classification of multi-temporal Landsat 8 images for crop type mapping in Southeastern Brazil," *Remote Sens.*, vol. 7, no. 11, pp. 14482–14508, Oct. 2015, doi: 10.3390/rs71114482.
- [19] K. Johansen, O. Lopez, Y.-H. Tu, T. Li, and M. F. McCabe, "Center pivot field delineation and mapping: A satellite-driven object-based image analysis approach for national scale accounting," *ISPRS J. Photogramm. Remote Sens.*, vol. 175, pp. 1–19, May 2021, doi: 10.1016/j.isprsjprs.2021.02.019.
- [20] H. Yang, B. Pan, W. Wu, and J. Tai, "Field-based rice classification in Wuhua county through integration of multi-temporal Sentinel-1A and Landsat-8 OLI data," *Int. J. Appl. Earth Observ. Geoinf.*, vol. 69, pp. 226–236, Jul. 2018, doi: 10.1016/j.jag.2018.02.019.
- [21] T. Blaschke, "Object based image analysis for remote sensing," *ISPRS J. Photogramm. Remote Sens.*, vol. 65, no. 1, pp. 2–16, Jan. 2010, doi: 10.1016/j.isprsjprs.2009.06.004.
- [22] T. Blaschke, S. Lang, E. Lorup, J. Strobl, and P. Zeil, "Object-oriented image processing in an integrated GIS/remote sensing environment and perspectives for environmental applications," *Environ. Inf. Planning, Politics Public*, vol. 2, pp. 555–570, Oct. 2000.
- [23] N. Mesner and K. Oštir, "Investigating the impact of spatial and spectral resolution of satellite images on segmentation quality," *J. Appl. Remote Sens.*, vol. 8, no. 1, Jan. 2014, Art. no. 083696, doi: 10.1117/1.JRS.8.083696.
- [24] European Commission. (2017). *CAP Explained: Direct Payments for Farmers 2015–2020*. LU: Publications Office. Accessed: Mar. 12, 2021. [Online]. Available: <https://data.europa.eu/doi/10.2762/572019>

- [25] G. Forkuor, C. Conrad, M. Thiel, T. Ullmann, and E. Zoungrana, "Integration of optical and synthetic aperture radar imagery for improving crop mapping in northwestern Benin, West Africa," *Remote Sens.*, vol. 6, no. 7, pp. 6472–6499, Jul. 2014, doi: [10.3390/rs6076472](https://doi.org/10.3390/rs6076472).
- [26] C. Persello, V. A. Tolpekin, J. R. Bergado, and R. A. de By, "Delineation of agricultural fields in smallholder farms from satellite images using fully convolutional networks and combinatorial grouping," *Remote Sens. Environ.*, vol. 231, Sep. 2019, Art. no. 111253, doi: [10.1016/j.rse.2019.111253](https://doi.org/10.1016/j.rse.2019.111253).
- [27] I. L. Castillejo-González, F. López-Granados, A. García-Ferrer, J. M. Peña-Barragán, M. Jurado-Expósito, M. S. de la Orden, and M. González-Audicana, "Object- and pixel-based analysis for mapping crops and their agro-environmental associated measures using QuickBird imagery," *Comput. Electron. Agricult.*, vol. 68, no. 2, pp. 207–215, Oct. 2009, doi: [10.1016/j.compag.2009.06.004](https://doi.org/10.1016/j.compag.2009.06.004).
- [28] P. Defourny et al., "Near real-time agriculture monitoring at national scale at parcel resolution: Performance assessment of the Sen2-Agri automated system in various cropping systems around the world," *Remote Sens. Environ.*, vol. 221, pp. 551–568, Feb. 2019, doi: [10.1016/j.rse.2018.11.007](https://doi.org/10.1016/j.rse.2018.11.007).
- [29] C. Luo, B. Qi, H. Liu, D. Guo, L. Lu, Q. Fu, and Y. Shao, "Using time series Sentinel-1 images for object-oriented crop classification in Google earth engine," *Remote Sens.*, vol. 13, no. 4, p. 561, Feb. 2021, doi: [10.3390/rs13040561](https://doi.org/10.3390/rs13040561).
- [30] K. Clauss, M. Ottinger, and C. Kuenzer, "Mapping rice areas with Sentinel-1 time series and superpixel segmentation," *Int. J. Remote Sens.*, vol. 39, no. 5, pp. 1399–1420, Mar. 2018, doi: [10.1080/01431161.2017.1404162](https://doi.org/10.1080/01431161.2017.1404162).
- [31] M. P. Wagner and N. Oppelt, "Extracting agricultural fields from remote sensing imagery using graph-based growing contours," *Remote Sens.*, vol. 12, no. 7, p. 1205, Apr. 2020, doi: [10.3390/rs12071205](https://doi.org/10.3390/rs12071205).
- [32] A. Nasrallah, N. Baghdadi, M. Mhawej, G. Faour, T. Darwish, H. Belhouchette, and S. Darwich, "A novel approach for mapping wheat areas using high resolution Sentinel-2 images," *Sensors*, vol. 18, no. 7, p. 2089, Jun. 2018, doi: [10.3390/rs18072089](https://doi.org/10.3390/rs18072089).
- [33] O. Csillik, M. Belgiu, G. P. Asner, and M. Kelly, "Object-based time-constrained dynamic time warping classification of crops using Sentinel-2," *Remote Sens.*, vol. 11, no. 10, p. 1257, May 2019, doi: [10.3390/rs11101257](https://doi.org/10.3390/rs11101257).
- [34] B. Watkins and A. Van Niekerk, "Automating field boundary delineation with multi-temporal Sentinel-2 imagery," *Comput. Electron. Agricult.*, vol. 167, Dec. 2019, Art. no. 105078, doi: [10.1016/j.compag.2019.105078](https://doi.org/10.1016/j.compag.2019.105078).
- [35] F. Waldner and F. I. Diakogiannis, "Deep learning on edge: Extracting field boundaries from satellite images with a convolutional neural network," *Remote Sens. Environ.*, vol. 245, Aug. 2020, Art. no. 111741, doi: [10.1016/j.rse.2020.111741](https://doi.org/10.1016/j.rse.2020.111741).
- [36] G. O. Tetteh, A. Gocht, and C. Conrad, "Optimal parameters for delineating agricultural parcels from satellite images based on supervised Bayesian optimization," *Comput. Electron. Agricult.*, vol. 178, Nov. 2020, Art. no. 105696, doi: [10.1016/j.compag.2020.105696](https://doi.org/10.1016/j.compag.2020.105696).
- [37] G. O. Tetteh, A. Gocht, M. Schwieder, S. Erasmí, and C. Conrad, "Unsupervised parameterization for optimal segmentation of agricultural parcels from satellite images in different agricultural landscapes," *Remote Sens.*, vol. 12, no. 18, p. 3096, Sep. 2020, doi: [10.3390/rs12183096](https://doi.org/10.3390/rs12183096).
- [38] M. Vogels, S. de Jong, G. Sterk, H. Douma, and E. Addink, "Spatio-temporal patterns of smallholder irrigated agriculture in the horn of Africa using GEOBIA and Sentinel-2 imagery," *Remote Sens.*, vol. 11, no. 2, p. 143, Jan. 2019, doi: [10.3390/rs11020143](https://doi.org/10.3390/rs11020143).
- [39] B. Watkins and A. van Niekerk, "A comparison of object-based image analysis approaches for field boundary delineation using multi-temporal Sentinel-2 imagery," *Comput. Electron. Agricult.*, vol. 158, pp. 294–302, Mar. 2019, doi: [10.1016/j.compag.2019.02.009](https://doi.org/10.1016/j.compag.2019.02.009).
- [40] M. Belgiu and O. Csillik, "Sentinel-2 cropland mapping using pixel-based and object-based time-weighted dynamic time warping analysis," *Remote Sens. Environ.*, vol. 204, pp. 509–523, Jan. 2018, doi: [10.1016/j.rse.2017.10.005](https://doi.org/10.1016/j.rse.2017.10.005).
- [41] M. Baatz and A. Schäpe, "Multiresolution segmentation: An optimization approach for high quality multi-scale image segmentation," in *Angewandte Geographische Informations-Verarbeitung XII*, J. Strobl, T. Blaschke, and G. Griesebner, Eds. Karlsruhe, Germany: Wichmann Verlag, 2000, pp. 12–23.
- [42] *eCognition Developer 9.5.0 Reference Book*, Trimble Germany GmbH, Munich, Germany, 2019.
- [43] C. Luo, H.-J. Liu, L.-P. Lu, Z.-R. Liu, F.-C. Kong, and X.-L. Zhang, "Monthly composites from Sentinel-1 and Sentinel-2 images for regional major crop mapping with Google earth engine," *J. Integrative Agricult.*, vol. 19, pp. 2–15, Jul. 2020.
- [44] U. Benz, I. Banovsky, A. Cesarz, and M. Schmidt. (2020). *CODE-DE Portal Handbook, Version 2.0. Germany: DLR*. Accessed: Mar. 23, 2021. [Online]. Available: [https://code-de.cdn.prismic.io/code-de/ff151913-16e0-4dc3-8005-696bf25bf65d\\_User+Manual\\_v2.0.2\\_ENG.pdf](https://code-de.cdn.prismic.io/code-de/ff151913-16e0-4dc3-8005-696bf25bf65d_User+Manual_v2.0.2_ENG.pdf)
- [45] D. Frantz, "FORCE—Landsat + Sentinel-2 analysis ready data and beyond," *Remote Sens.*, vol. 11, no. 9, p. 1124, May 2019, doi: [10.3390/rs11091124](https://doi.org/10.3390/rs11091124).
- [46] J. Buchner, H. Yin, D. Frantz, T. Kuemmerle, E. Askerov, T. Bakuradze, B. Bleyhl, N. Elizbarashvili, A. Komarova, K. E. Lewińska, A. Rizayeva, H. Sayadyan, B. Tan, G. Tepanosyan, N. Zazanashvili, and V. C. Radeloff, "Land-cover change in the caucasus mountains since 1987 based on the topographic correction of multi-temporal Landsat composites," *Remote Sens. Environ.*, vol. 248, Oct. 2020, Art. no. 111967, doi: [10.1016/j.rse.2020.111967](https://doi.org/10.1016/j.rse.2020.111967).
- [47] D. Frantz, A. Roder, M. Stellmes, and J. Hill, "An operational radiometric Landsat preprocessing framework for large-area time series applications," *IEEE Trans. Geosci. Remote Sens.*, vol. 54, no. 7, pp. 3928–3943, Jul. 2016, doi: [10.1109/TGRS.2016.2530856](https://doi.org/10.1109/TGRS.2016.2530856).
- [48] D. Roy, Z. Li, and H. Zhang, "Adjustment of Sentinel-2 multi-spectral instrument (MSI) red-edge band reflectance to nadir BRDF adjusted reflectance (NBAR) and quantification of red-edge band BRDF effects," *Remote Sens.*, vol. 9, no. 12, p. 1325, Dec. 2017, doi: [10.3390/rs9121325](https://doi.org/10.3390/rs9121325).
- [49] D. Frantz, E. Haß, A. Uhl, J. Stoffels, and J. Hill, "Improvement of the Fmask algorithm for Sentinel-2 images: Separating clouds from bright surfaces based on parallax effects," *Remote Sens. Environ.*, vol. 215, pp. 471–481, Sep. 2018, doi: [10.1016/j.rse.2018.04.046](https://doi.org/10.1016/j.rse.2018.04.046).
- [50] Z. Zhu, S. Wang, and C. E. Woodcock, "Improvement and expansion of the Fmask algorithm: Cloud, cloud shadow, and snow detection for Landsats 4–7, 8, and Sentinel 2 images," *Remote Sens. Environ.*, vol. 159, pp. 269–277, Mar. 2015, doi: [10.1016/j.rse.2014.12.014](https://doi.org/10.1016/j.rse.2014.12.014).
- [51] Z. Zhu and C. E. Woodcock, "Object-based cloud and cloud shadow detection in Landsat imagery," *Remote Sens. Environ.*, vol. 118, pp. 83–94, Mar. 2012, doi: [10.1016/j.rse.2011.10.028](https://doi.org/10.1016/j.rse.2011.10.028).
- [52] M. Schwieder, P. J. Leitão, M. M. da Cunha Bustamante, L. G. Ferreira, A. Rabe, and P. Hostert, "Mapping Brazilian savanna vegetation gradients with Landsat time series," *Int. J. Appl. Earth Observ. Geoinf.*, vol. 52, pp. 361–370, Oct. 2016, doi: [10.1016/j.jag.2016.06.019](https://doi.org/10.1016/j.jag.2016.06.019).
- [53] A. Novelli, M. Aguilar, F. Aguilar, A. Nemmaoui, and E. Tarantino, "AssesSeg—A command line tool to quantify image segmentation quality: A test carried out in southern Spain from satellite imagery," *Remote Sens.*, vol. 9, no. 1, p. 40, Jan. 2017, doi: [10.3390/rs9010040](https://doi.org/10.3390/rs9010040).
- [54] D. D. Polsby and R. Popper, "The third criterion: Compactness as a procedural safeguard against partisan gerrymandering," *Social Sci. Res. Netw.*, Rochester, NY, USA, Tech. Rep. 2936284, Mar. 1991, doi: [10.2139/ssrn.2936284](https://doi.org/10.2139/ssrn.2936284).
- [55] X. Blaes, P. Defourny, U. Wegmuller, A. D. Vecchia, L. Guerriero, and P. Ferrazzoli, "C-band polarimetric indexes for maize monitoring based on a validated radiative transfer model," *IEEE Trans. Geosci. Remote Sens.*, vol. 44, no. 4, pp. 791–800, Apr. 2006, doi: [10.1109/TGRS.2005.860969](https://doi.org/10.1109/TGRS.2005.860969).
- [56] R. Nasirzadehdizaji, F. B. Sanli, S. Abdikan, Z. Cakir, A. Sekertekin, and M. Ustuner, "Sensitivity analysis of multi-temporal Sentinel-1 SAR parameters to crop height and canopy coverage," *Appl. Sci.*, vol. 9, no. 4, p. 655, Feb. 2019, doi: [10.3390/app9040655](https://doi.org/10.3390/app9040655).
- [57] A. A. Gitelson, Y. J. Kaufman, R. Stark, and D. Rundquist, "Novel algorithms for remote estimation of vegetation fraction," *Remote Sens. Environ.*, vol. 80, pp. 76–87, Apr. 2002, doi: [10.1016/S0034-4257\(01\)00289-9](https://doi.org/10.1016/S0034-4257(01)00289-9).
- [58] W. Rouse and R. H. Haas, "Monitoring vegetation systems in the great plains with ERTS," in *Proc. Earth Resour. Technol. Satell. Symp.*, Washington, DC, USA, vol. 1, 1973, pp. 309–317.
- [59] J. Qi, R. Marsett, P. Heilman, S. Bieden-Bender, S. Moran, D. Goodrich, and M. Weltz, "RANGES improves satellite-based information and land cover assessments in southwest United States," *Eos Trans. Amer. Geophys. Union*, vol. 83, no. 51, pp. 601–606, 2002, doi: [10.1029/2002EO000411](https://doi.org/10.1029/2002EO000411).
- [60] E. M. Barnes, T. R. Clarke, S. E. Richards, P. D. Colaizzi, J. Haberland, M. Kostrowski, P. Waller, C. Choi, E. Riley, T. Thompson, R. J. Lascano, H. Li, and M. S. Moran, "Coincident detection of crop water stress, nitrogen status and canopy density using ground based multispectral data," in *Proc. 5th Int. Conf. Precis. Agricult.*, Bloomington, MN, USA, vol. 1619, 2000, p. 15.
- [61] B.-C. Gao, "NDWI—A normalized difference water index for remote sensing of vegetation liquid water from space," *Remote Sens. Environ.*, vol. 58, no. 3, pp. 257–266, Dec. 1996, doi: [10.1016/S0034-4257\(96\)00067-3](https://doi.org/10.1016/S0034-4257(96)00067-3).

- [62] A. P. van Deventer, A. D. Ward, P. H. Gowda, and J. G. Lyon, "Using thematic mapper data to identify contrasting soil plains and tillage practices," *Photogramm. Eng. Remote Sens.*, vol. 63, no. 1, pp. 87–93, 1997.
- [63] P. Jaccard, "Etude de la distribution florale dans une portion des Alpes et du Jura," *Bull. de la Societe Vaudoise des Sciences Naturelles*, vol. 37, pp. 547–579, Jan. 1901, doi: 10.5169/seals-266450.
- [64] S. Valero, D. Morin, J. Inglada, G. Sepulcre, M. Arias, O. Hagolle, G. Dedieu, S. Bontemps, P. Defourny, and B. Koetz, "Production of a dynamic cropland mask by processing remote sensing image series at high temporal and spatial resolutions," *Remote Sens.*, vol. 8, no. 1, p. 55, Jan. 2016, doi: 10.3390/rs8010055.
- [65] L. Blickensdörfer, M. Schwieder, D. Pflugmacher, S. Erasmí, C. Nendel, and P. Hostert, "Multi-year national-scale crop type mapping with combined time series of Sentinel-1, Sentinel-2 and Landsat 8 data," *Remote Sens. Environ.*, to be published.
- [66] Y. Cai, X. Li, M. Zhang, and H. Lin, "Mapping wetland using the object-based stacked generalization method based on multi-temporal optical and SAR data," *Int. J. Appl. Earth Observ. Geoinf.*, vol. 92, Oct. 2020, Art. no. 102164, doi: 10.1016/j.jag.2020.102164.
- [67] S. Mahdavi, B. Salehi, M. Amani, J. E. Granger, B. Brisco, W. Huang, and A. Hanson, "Object-based classification of wetlands in Newfoundland and Labrador using multi-temporal PolSAR data," *Can. J. Remote Sens.*, vol. 43, no. 5, pp. 432–450, Sep. 2017, doi: 10.1080/07038992.2017.1342206.
- [68] G. Shuai, J. Zhang, B. Basso, Y. Pan, X. Zhu, S. Zhu, and H. Liu, "Multi-temporal RADARSAT-2 polarimetric SAR for maize mapping supported by segmentations from high-resolution optical image," *Int. J. Appl. Earth Observ. Geoinf.*, vol. 74, pp. 1–15, Feb. 2019, doi: 10.1016/j.jag.2018.08.021.
- [69] M. Campos-Taberner, F. J. García-Haro, B. Martínez, S. Sánchez-Ruiz, and M. A. Gilabert, "A Copernicus Sentinel-1 and Sentinel-2 classification framework for the 2020+European common agricultural policy: A case study in València (Spain)," *Agronomy*, vol. 9, no. 9, p. 556, Sep. 2019, doi: 10.3390/agronomy9090556.
- [70] K. Van Tricht, A. Gobin, S. Gilliams, and I. Piccard, "Synergistic use of radar Sentinel-1 and optical Sentinel-2 imagery for crop mapping: A case study for Belgium," *Remote Sens.*, vol. 10, no. 10, p. 1642, Oct. 2018, doi: 10.3390/rs10101642.
- [71] G. Waldhoff, C. Curdt, D. Hoffmeister, and G. Bareth, "Analysis of multi-temporal and multisensor remote sensing data for crop rotation mapping," *ISPRS Ann. Photogramm., Remote Sens. Spatial Inf. Sci.*, vol. 1, no. 7, pp. 177–182, Jul. 2012.
- [72] J. Inglada, J.-F. Dejoux, O. Hagolle, and G. Dedieu, "Multi-temporal remote sensing image segmentation of croplands constrained by a topographical database," in *Proc. IEEE Int. Geosci. Remote Sens. Symp.*, Munich, Germany, Jul. 2012, pp. 6781–6784, doi: 10.1109/IGARSS.2012.6352607.
- [73] H. C. North, D. Pairman, and S. E. Belliss, "Boundary delineation of agricultural fields in multitemporal satellite imagery," *IEEE J. Sel. Topics Appl. Earth Observ. Remote Sens.*, vol. 12, no. 1, pp. 237–251, Jan. 2019, doi: 10.1109/JSTARS.2018.2884513.
- [74] C. Conrad, S. Dech, O. Dubovyk, S. Fritsch, D. Klein, F. Löw, G. Schorch, and J. Zeidler, "Derivation of temporal windows for accurate crop discrimination in heterogeneous croplands of uzbekistan using multitemporal RapidEye images," *Comput. Electron. Agricult.*, vol. 103, pp. 63–74, Apr. 2014, doi: 10.1016/j.compag.2014.02.003.
- [75] Q. Song, Q. Hu, Q. Zhou, C. Hovis, M. Xiang, H. Tang, and W. Wu, "In-season crop mapping with GF-1/WFV data by combining object-based image analysis and random forest," *Remote Sens.*, vol. 9, no. 11, p. 1184, Nov. 2017, doi: 10.3390/rs9111184.

**GIDEON OKPOTI TETTEH** was born in Accra, Ghana. He received the M.Sc. degree in photogrammetry and geoinformatics from Stuttgart University of Applied Sciences, in 2012. He is currently pursuing the Ph.D. degree with Martin-Luther-University Halle-Wittenberg, Halle (Saale), Germany.

From October 2012 to July 2017, he worked as a Remote Sensing Application Developer with Planet Labs Germany GmbH, Berlin. Since August 2017, he has been working as a Scientific Researcher with Thünen Institute of Farm Economics, Braunschweig.

**ALEXANDER GOCHT** received the degree in agricultural studies from the Imperial College of London, and the Ph.D. degree from the University of Bonn, Germany, in 2009, with a focus on methods of economic farm modeling.

Since 2004, he has been a Senior Research Fellow with Thünen Institute of Farm Economics, Braunschweig, and works in close cooperation with the CAPRI Modeling Group. He is one of the CAPRI Core Developers. From 2017 to 2020, he coordinated the working group for remote sensing (RS) at Thünen Institute and since then, he has been closely involved in the methodological development of remote sensing applications for modeling purposes. He has contributed to various studies to the development models aiming to assess the impacts of the Common Agricultural Policy (CAP) on farm economics and environmental effects. He has also undertaken various quantitative analyses of agricultural and environmental policies. He continuously researches farm typology particularly on developing methods for consistent aggregation.

**STEFAN ERASMI** was born in Bremen, Germany, in 1969. He received the Diploma and Ph.D. degrees in geography from the University of Göttingen, in 1997 and 2002, respectively.

From 2002 to 2019, he worked in research and education at the Institute of Geography, University of Göttingen. Since 2019, he has been a Senior Research Scientist with Thünen Institute of Farm Economics, Braunschweig. He has long experience in monitoring agricultural land-use and land-cover, agricultural practices, landscape patterns, and forest parameters from multi-source satellite data for applications in ecology and socio-economics. At Thünen Institute, he is leading the Thünen Earth Observation (ThEO) Working Group that provides EO-based area-wide solutions and objective information for policymakers in terms of the impact assessment of political decisions as well as societal and environmental trends. He is an Editor of the *Journal of Photogrammetry, Remote Sensing and Geoinformation Science* (PFG).

**MARCEL SCHWIEDER** received the M.Sc. degree in physical geography and the Ph.D. degree with a focus on the phenological analysis of Cerrado vegetation using Landsat time series from Humboldt University, Berlin, in 2013 and 2018, respectively.

From 2013 to 2017, he was a Research Assistant with the Geomatics Laboratory, Humboldt University. From 2018 to 2021, he was a Postdoctoral Researcher with the Geomatics Laboratory, Humboldt University. Since March 2021, he has been working as a Scientific Researcher with Thünen Institute of Farm Economics, Braunschweig. He is also a Guest Scientist with the Earth Observation Laboratory, Humboldt University.

**CHRISTOPHER CONRAD** was born in Alzenau, Germany, in 1974. He received the Diploma degree in geography from the University of Mainz, Germany, in 2002, and the Ph.D. degree in geography from the University of Würzburg, Germany, in 2006.

From 2006 to 2011, he was a Research Assistant and a Lecturer in the framework of the Bavarian Elite Network at the Universities of Bayreuth and Würzburg, Germany. From 2011 to 2017, he was a Junior Professor of geographical remote sensing with the University of Würzburg. Since 2017, he has been representing the professorship of geocology with the University of Halle-Wittenberg, Germany, as a Substitute Professor, and took over the full professorship, in 2019. He is an author of over 70 peer-reviewed articles in the field of remote sensing for sustainable land and water management, in particular of agricultural landscapes, with a regional focus on Central Asia and Central Europe. He is an Editor of the *Journal of Photogrammetry, Remote Sensing, and Geoinformation Science* (PFG).

• • •

## 6 Discussion

In this thesis, an automated framework for optimally delineating agricultural fields from Sentinel-1 (S1) and Sentinel-2 (S2) images was presented. Unlike the other studies that only used existing segmentation algorithms or proposed new algorithms for segmenting agricultural fields from the S1 and/or S2 images, this thesis presented a more complete approach that encompassed the optimization of the segmentation algorithm and the optimization of the input data passed to the segmentation algorithm. For segmenting the agricultural fields from the S1 and S2 datasets, the multiresolution segmentation (MRS) algorithm as implemented in eCognition was used. A supervised and unsupervised approach was proposed to optimize the three main parameters (scale, shape, and compactness) of the MRS algorithm.

### 6.1 Optimization of the data preparation

In Chapters 3 and 4, the S2 images as downloaded from the European Space Agency (ESA) data repository were locally processed to obtain the Bottom-Of-Atmosphere (BOA) images. Those BOA images were visually inspected to identify the cloud-free images that were used for segmentation. This process is time-consuming and inhibits the full automation of the processing chain. To focus more attention on the segmentation process itself and its automation, analysis-ready data (ARD) of S1 and S2 were used in Chapter 5. For S1, the ARD was downloaded from CODE-DE. For S2, the Framework for Operational Radiometric Correction for Environmental monitoring (FORCE) software was used to create the ARD. Additionally, FORCE was used to automatically identify and mask out clouds. In this thesis, FORCE was employed in a local computing environment to generate the S2 ARD. There are ongoing discussions on the full integration of FORCE into the CODE-DE platform. This will further help in the automation process as the S2 ARD will readily become available on CODE-DE for download. Having the ARD of both S1 and S2 available on CODE-DE would open up the possibility of using the powerful cloud computing platform provided by CODE-DE for segmentation optimization without downloading the ARD.

In Chapters 3 and 4, the same masking approach was employed to remove non-agricultural areas. To do the masking, linear features (tracks, cycleways, paths, etc.) were buffered and combined with the agricultural vector layer extracted from the Digital Landscape Model (DLM) of the German Official Topographic Cartographic Information System (ATKIS). The reason for using those linear features was to help create clear boundaries between adjacent agricultural land-cover (LC) polygons. However, it was later observed that this approach was not entirely effective because all linear features bounding the agricultural LC polygons were either not mapped in the Open Street Map (OSM) data or they did not geometrically align with the OSM linear features. Therefore, in Chapter 5, only ATKIS was used. To create clear boundaries, a 10 m inward

buffer was applied to each agricultural LC polygon. This was more effective as it already pre-segmented the images before the segmentation optimization was applied to delineate the individual parcels.

The same tile grid system was used in Chapters 3 and 4. Each tile was 10 km by 10 km. Neighboring tiles had an overlap of 1 km. Due to the introduction of FORCE in Chapter 5, a new tile grid system was generated that aligned with the non-overlapping 30 km by 30 km tiles used by FORCE as the basis for data processing. Further, the boundary of each tile in this new tile grid system was automatically adjusted to accommodate the centroids of the agricultural LC polygons that intersected each tile. Consequently, the tiles had variable sizes with the average size being 11 km by 11 km. Neighboring tiles had variable degrees of spatial overlap. The creation of this new tile grid system made it easier to spatially merge all the optimal segmentation results to obtain a single vector layer for Lower Saxony.

## 6.2 Optimization of the MRS algorithm

In using the MRS algorithm, the focus is mostly placed on optimizing the scale parameter. Often, the shape and compactness parameters are kept constant while the scale is varied within a certain range to identify the optimal scale value. This approach has been used by numerous researchers (Anders et al., 2011; Böck et al., 2017; Drăguț et al., 2014; Drăguț et al., 2010; Johnson and Xie, 2013, 2011; Johnson et al., 2015; Kim et al., 2011; Liu and Xia, 2010; Yang et al., 2019). However, the results of Chapter 3 revealed that to obtain optimal segmentation, all three parameters ought to be optimized. This was also observed in Chapter 4, where the unsupervised Bayesian optimization that was used in optimizing all three MRS parameters generally yielded better results than using it to optimize only the scale parameter while holding the other parameters constant. For optimizing the segmentation of agricultural fields with the MRS algorithm, grid search has been tested to optimize all three parameters by some authors (Conrad et al., 2010; Forkuor et al., 2014; Watkins and van Niekerk, 2019b). The computationally expensive nature of grid search prevents the evaluation of all possible parameter combinations before determining the optimal one. In the above-cited studies that used the grid search, the authors only tested a set of some parameter combinations based upon which the optimal combination was identified. This approach is not the most effective as one could miss out on the actual optimal combination if the tested parameter set does not contain the actual optimal combination. Bayesian optimization as was proposed in this thesis is a more effective approach for efficiently approximating the actual optimal combination. The supervised optimization approach presented in Chapter 3 and the unsupervised approach in Chapter 4 are complementary methods for optimizing the three MRS parameters. Although the supervised approach outperformed the unsupervised approach as was highlighted in Chapter 4, in areas where reference data is not available, the unsupervised approach becomes inevitable. For example, in Germany, the Geospatial Aid Application (GSAA) or Land Parcel Identification System (LPIS) are presently not publicly

available for all federal states. Therefore, the supervised optimization approach cannot be applied in federal states without reference data. The unsupervised approach would have to be evaluated in those states.

### 6.3 Optimization of the input data

After drawing experiences from some published studies (Belgiu and Csillik, 2018; Csillik et al., 2019; Watkins and van Niekerk, 2019a, 2019b), only the visible and near-infrared (VNIR) bands of S2 were selected and used in Chapter 3 to delineate the agricultural fields. The reason often given in the literature for this choice is the relatively higher spatial resolution (10 m) of the VNIR bands compared to the other S2 bands. This reason is justifiable as the paper of Mesner and Oštir (2014) showed that the higher the spatial resolution, the higher the segmentation quality. In that same paper, the authors also observed that the spectral resolution of the input image also influences the segmentation outcome. Therefore, in Chapter 5, different feature sets were generated and used for segmentation optimization to evaluate their impact on the segmentation results. To segment agricultural fields, S2 is preferred to S1 due to the higher spatial resolution of S2 and the ease at which it can be visually interpreted. While the preference for S2 can largely be justified by the results of Chapter 5, S1 does add some value to the accurate segmentation of agricultural fields. This was demonstrated in Chapter 5, where the best segmentation accuracy was achieved through the synergistic use of S1 and S2. The use of VNIR in Chapters 3 and 4 was justified by its better performance in comparison with the ten bands of S2 as was observed in Chapter 5. However, Chapter 5 also indicated that using only the band indices of S1 or S2 produces better segmentation results than using only the bands of S1 or S2.

To accurately map different agricultural land-use (LU) types, the use of a time series of images is often recommended in the literature as a means of accurately characterizing the phenological behaviors of the different LU types and using that as the basis to differentiate them (Griffiths et al., 2019; Inglada et al., 2012; Waldhoff et al., 2012). As was revealed in Chapter 5, the worst segmentation results were mostly achieved with the single-period datasets at the beginning of the growing season in March and the best segmentation results were mostly achieved when the multi-period datasets were used at the end of the season in October. In March, most summer crops are yet to be sown. Therefore, among the summer crops, visible boundaries between the different agricultural parcels cannot be seen, hence the poor segmentation results. As the season progresses, the subdivisions among the different parcels become more visible, thereby enabling their effective segmentation. The bane of using a time series of images to map large geographical areas often lies in the amount of time and storage capacity needed to process them. Therefore, in this thesis, monthly mean composites (MMCs) were used as the basis for generating the image time series. Without any significant loss in segmentation accuracy, it was faster to apply the supervised optimization approach to the time series based on the MMCs than a time series generated from single image dates. Moreover, the MMCs of S1 are readily available as standard products on CODE-DE, with S2 being in the works.

## 6.4 Spatial distribution of the optimal parameters

The optimal scale, shape, and compactness parameters obtained in Chapters 3 and 5 are respectively depicted in Figure 6-1, Figure 6-2, and Figure 6-3. The overall segmentation quality (OSQ) corresponding to each optimal scale, shape, and compactness combination can be seen in Figure 6-4. Here, the focus was placed on only the results of Chapters 3 and 5 because the supervised approach outperformed the unsupervised approach as was revealed in Chapter 4. Moreover, in Chapter 4, the segmentation optimization was limited to only 21 tiles. It is worth noting here that the symbology levels used in Figure 6-1, Figure 6-2, and Figure 6-3, and Figure 6-4 are different from the ones used in Fig. 14 and Fig. 7 of Chapter 3. The modification of the symbology levels was done to enable the comparison of the results between Chapters 3 and 5.

The mean scale value in Chapter 3 was 47 with a standard deviation of 13. The modal value was 40. In Chapter 5, the optimal scale values were higher. The mean scale value in Chapter 5 was 86 with a standard deviation of 23. The modal value was 80. Regarding the optimal shape values, similar patterns were observed in both chapters. Most of the shape values were between 0.8 and 0.9, and in the majority of the cases, the maximum value of 0.9 was obtained. When it comes to compactness, the mean value obtained in Chapter 3 was 0.686 with a standard deviation of 0.183. The compactness values in Chapter 5 were higher and they often reached the maximum value of 1.0. The mean compactness value stood at 0.848 and the standard deviation was 0.214. The OSQs obtained in Chapter 5 were generally higher than those of Chapter 3. This can largely be attributed to the use of multitemporal images in Chapter 5. The mean OSQ obtained in Chapter 3 was 0.573 and the standard deviation was 0.043. In Chapter 5, the mean OSQ was 0.691 with a standard deviation of 0.061.

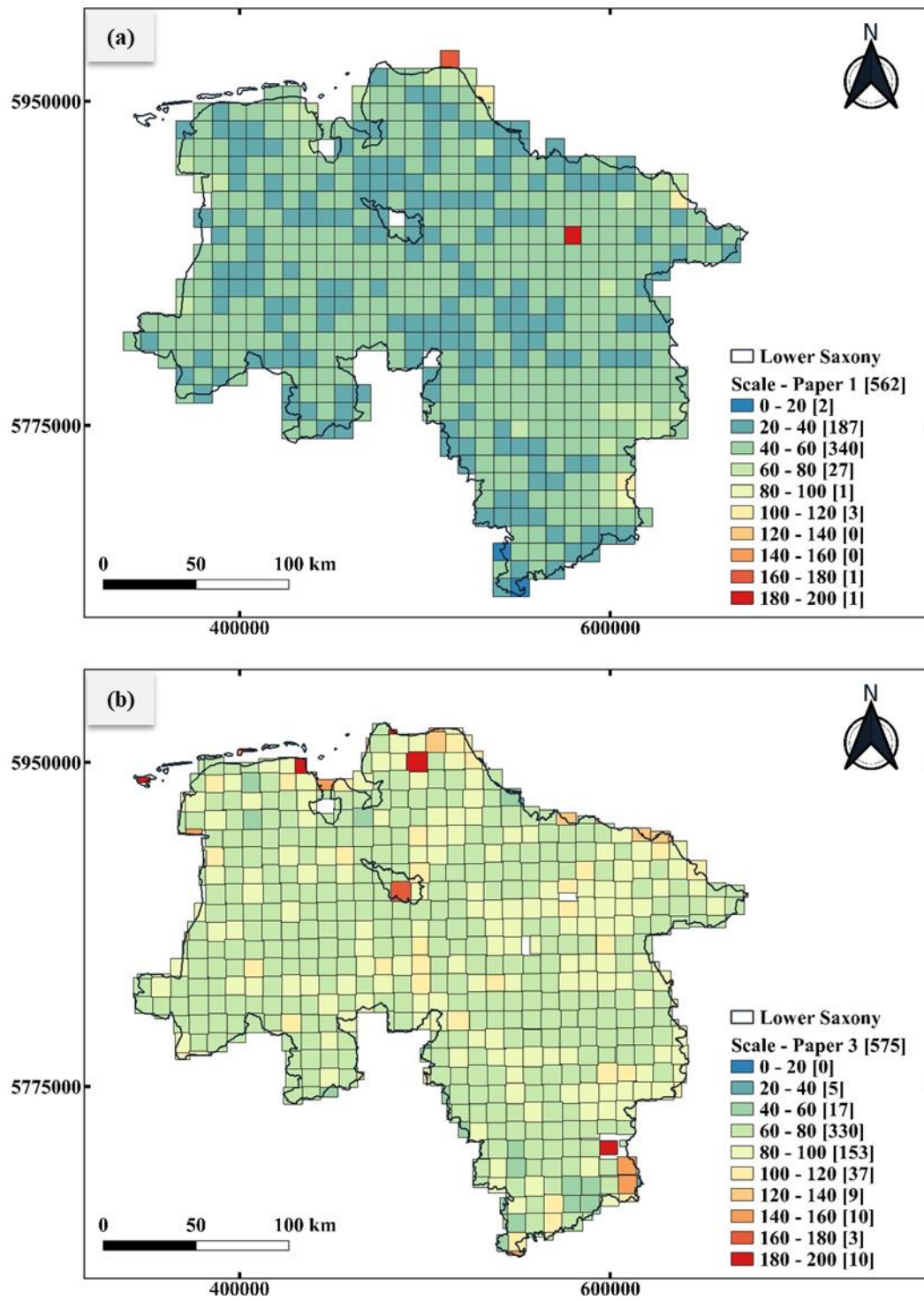


Figure 6-1. The optimal scale of each tile in Chapter 3 (a) and Chapter 5 (b). The numbers in the square brackets represent the number of tiles.

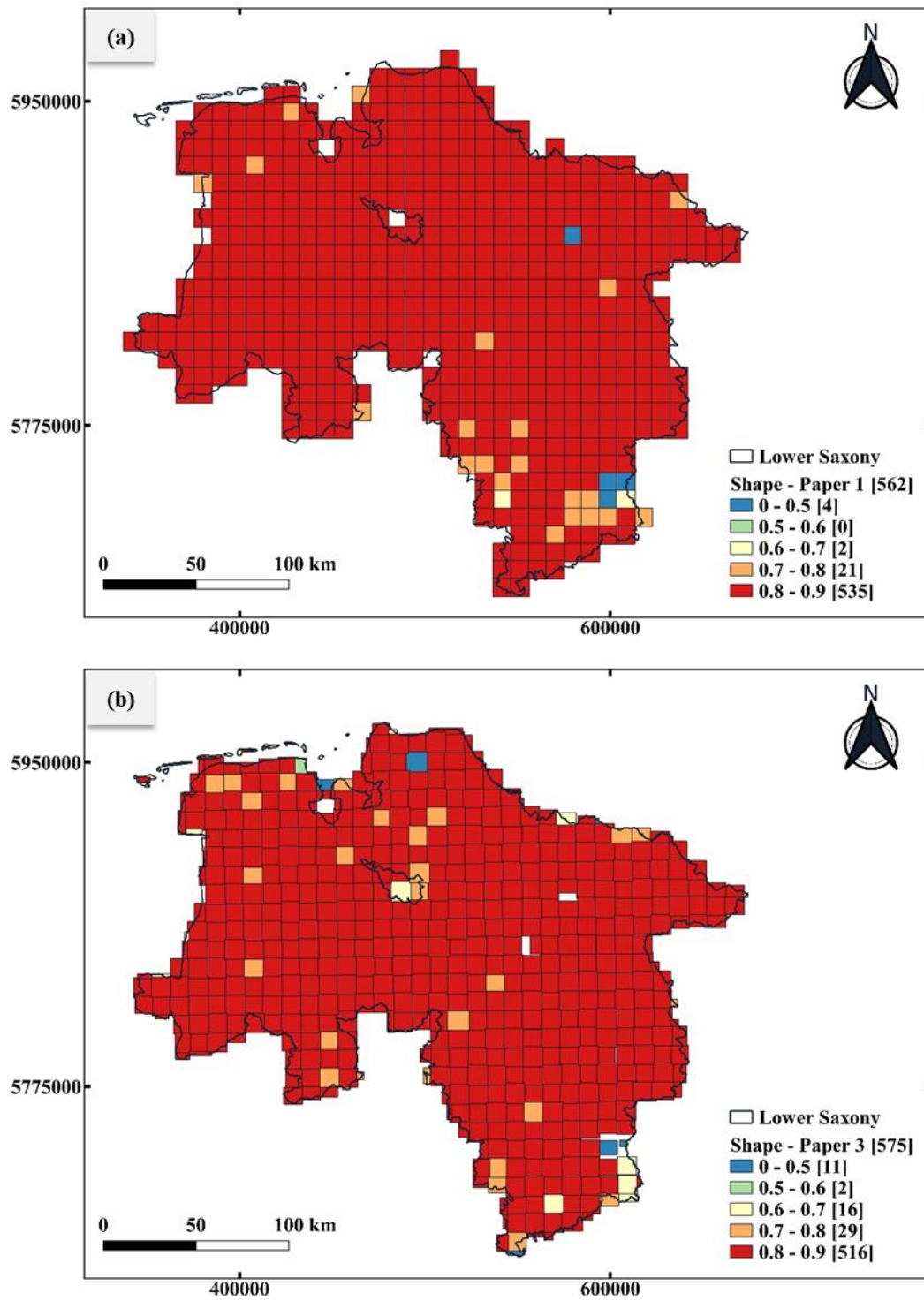


Figure 6-2. The optimal shape of each tile in Chapter 3 (a) and Chapter 5 (b). The numbers in the square brackets represent the number of tiles.

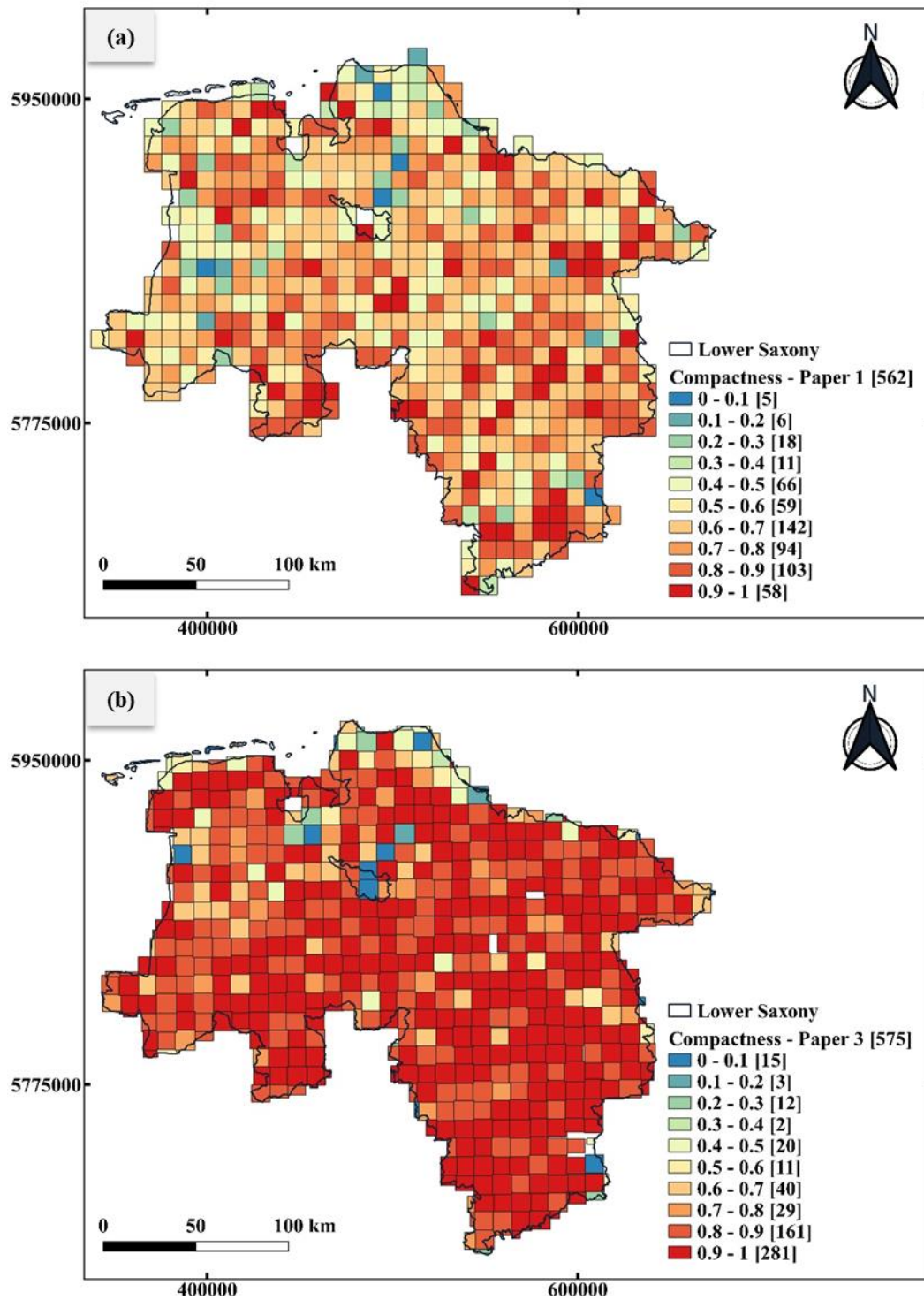


Figure 6-3. The optimal compactness of each tile in Chapter 3 (a) and Chapter 5 (b). The numbers in the square brackets represent the number of tiles.

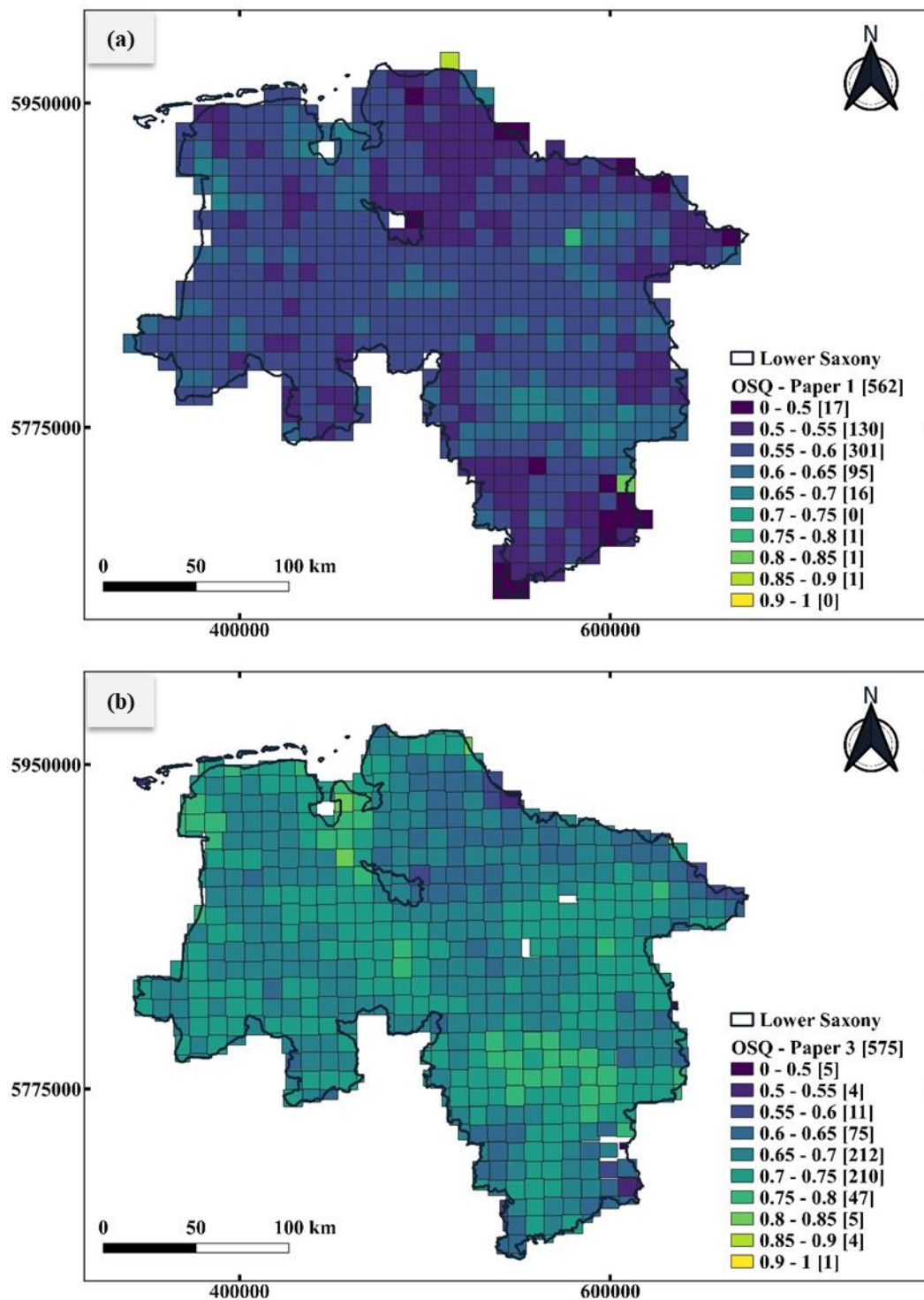


Figure 6-4. The overall segmentation quality (OSQ) corresponding to the optimal scale, shape, and compactness combination identified for each tile in Chapter 3 (a) and Chapter 5 (b). The numbers in the square brackets represent the number of tiles.

## 6.5 Application of identified optimal parameters

While the segmentation of the agricultural fields is the ultimate goal of this thesis, the identification of the optimal MRS parameters is a very important step. The optimal parameters identified with the supervised approach generate better segmentation results than those of the unsupervised approach. As aforementioned, the main drawback of the supervised approach is the need for the GSAA or LPIS for optimization. Given that the landscape structure (size, shape) of agricultural parcels in Germany does not drastically change between years, the supervised optimal parameters identified for a particular year (2018 in this thesis) could be used to directly segment images acquired for different years without the need for the GSAA or LPIS. This was tested and highlighted in the conclusion of Chapter 3 where the optimal parameters of 2018 were applied to segment S2 images acquired in 2019 and the loss of segmentation accuracy was less than 2%. The supervised optimal parameters obtained in Chapter 5 were based on the optimal feature set (combination of the S1 and S2 indices) covering the whole season (DID-8). In another test, those established parameters were used to directly segment the incremental dataset up to May (DID-3) and the loss of segmentation accuracy was less than 1%. Therefore, without waiting till the end of the season, the established parameters of 2018 could be used to segment in-season images acquired in a different year. The outcome of those two tests shows that the optimal MRS parameters established at one point in time could be transferred to segment images acquired at different points in time without a substantial loss in segmentation accuracy.

In RS, the main challenge regarding the temporal transferability of models is that different spectral responses (reflectances) are recorded for the same object at different points in time due to the different atmospheric conditions under which the images are acquired as well as changes in land-use or land-cover. This is particularly true when it comes to the temporal transferability of image classification models because such models are built on the statistical distribution of the reflectances of objects at some point in time. Therefore, any changes in reflectance at a different point in time will largely render the application of that classification model ineffective. Unlike image classification, the MRS algorithm does not build a statistical model from the reflectances but simply clusters the pixels in any given image. To do the clustering, it takes both the reflectance (color) and shape of the pixels into account (see Eq. 1). As Figure 6-2 shows, the MRS algorithm placed more weight on shape than color. In addition to shape and color, the average size of the fields as manifested through the scale parameter is also taken into account by the MRS algorithm. Therefore, the main condition that can inhibit the temporal transfer of the optimal MRS parameters of 2018 to other times of interest is a drastic change in the shape and size of the agricultural fields at that particular time of interest. Where drastic changes in the landscape structure are envisaged, the segmentation optimization process ought to be repeated using images acquired at the time of interest to establish new optimal parameters. Otherwise, the already established optimal parameters can be used to segment images in different years without repeating the whole segmentation optimization process.

## 6.6 Potential usage of the segmentation results

### 6.6.1 Object-based crop-type mapping

Increasing crop yields to match the increasing world population comes with attendant environmental problems such as the increase in GHG emissions and the destruction of biodiversity. To formulate policies targeted at ensuring sustainable agriculture, accurate spatial information about agricultural lands is needed. In Chapter 5, the merged segmentation result of Lower Saxony was used to post-filter a pixel-based crop-type map to generate an object-based crop-type map, which resulted in a 3.4 percentage points increase in the classification accuracy. The difference between the pixel-based map and the object-based map was found to be statistically significant ( $p$ -value  $< 0.01$ ) after performing McNemar's test. The precision (user's accuracy), recall (producer's accuracy), and F-score per class (land-use type) can be seen in Table 6-1. The F-score (Eq. 5), which is the harmonic mean of the precision and recall, represents the accuracy per class.

$$F - score = 2 * \frac{precision * recall}{precision + recall} \quad (5)$$

The object-based map had higher accuracies for all classes except winter barley, winter rapeseed, sugar beet, and potato. The most noticeable improvements of 4.85 and 3.41 percentage points in accuracy respectively occurred in the strawberry and grassland classes. With the improved overall accuracy, the object-based map can be used for a more accurate estimation of the acreage per crop type, GHG modeling, crop yield forecasting, and the computation of landscape metrics for assessing the biodiversity on agricultural lands.

Table 6-1. The computed precision, recall, and F-score for the land-use types in the pixel-based and object-based crop-type maps.

Land-use type	Precision (%)		Recall (%)		F-Score (%)	
	Pixel-based	Object-based	Pixel-based	Object-based	Pixel-based	Object-based
Grassland	96.76	97.05	78.55	84.11	86.71	90.12
Winter Wheat	93.95	92.47	80.68	82.6	86.81	87.26
Winter Rye	76.98	77.64	80.72	82.73	78.8	80.11
Winter Barley	89.58	88.24	82.52	83.17	85.91	85.63
Other Winter Cereals	50.49	51.98	65.77	69.19	57.13	59.37
Spring Barley	82.89	82.73	63.48	65.9	71.9	73.36
Spring Oat	31.88	32.53	39.4	41.24	35.24	36.37
Other Summer Cereals	32.49	33.12	68.22	69.96	44.02	44.96
Winter Rapeseed	93.37	92.13	92.35	91.41	92.86	91.77
Legume	55.01	56.49	52.59	54.45	53.77	55.45
Sunflower	4.93	5.15	34.05	34.33	8.61	8.95
SugarBeet	93.67	93	93.56	94.17	93.61	93.58
Maize	90.22	89.51	74.5	77.76	81.61	83.22
Maize(grain)	28.54	28.92	50.51	51.64	36.47	37.07
Potato	91.02	89.23	89.23	89.38	90.12	89.3
Strawberry	20.45	24.25	88.07	88.28	33.2	38.05
Other leafy vegetables	27.59	28.51	22.61	23.36	24.85	25.68

### 6.6.2 Verification of the GSAA parcels

The segmentation results could be used within the framework of the EU's Common Agricultural Policy (CAP) for checks by monitoring (CbM). With CbM, all the declared GSAA parcels must be verified instead of the currently used approach of randomly sampling 5 % of the declarations for on-the-spot checks (OTSCs). Therefore, for CbM to be efficient and effective, a smart sampling plan must be used to identify the declared parcels that show a high level of disparity compared to the information retrieved from the S1 and/or S2 images. The IoU computed for each segment enables one to set a reliability threshold value to identify the GSAA parcels that might need the attention of an operator at a National Control and Paying Agency (NCPA). The segments whose IoU values are smaller than the threshold value could then be visually examined alongside their corresponding GSAA parcels. This targeted approach of checking the GSAA parcels will be more efficient than inspecting all the declared GSAA parcels as required by the CbM. Reducing the visual inspection to a subset of GSAA parcels can help to quickly identify those parcels whose geometries are inconsistent with the real-world situation like the one captured in Fig. 8a of Chapter 3. While image segmentation can help in flagging such inconsistent GSAA parcels, to be conclusive on the compliance or otherwise of the GSAA parcels to the CAP rules, the next steps of verifying the agricultural LU types and activities existing on those GSAA parcels must be done.

The object-based crop-type map produced in Chapter 5 could also be used for CbM. One important component of CAP is the greening payment (European Commission, 2021b), which aims at ensuring the sustainable use of agricultural lands. To access the greening payments, farmers have to comply with the greening rules. The greening rules cover three aspects namely crop diversification, maintenance of permanent grassland, and ecological focus areas (EFAs) (European Commission, 2021b). Under crop diversification, arable lands exceeding 10 ha must have at least two crop types, and those greater than 30 ha must have at least three crop types. To maintain permanent grassland, each EU country has to dedicate a certain percentage of its total agricultural area to permanent grasslands. Under the EFAs, for arable lands exceeding 15 ha, 5% of the land must be dedicated to EFAs (hedges, trees, or fallow land). To check the compliance of the farmers to those greening rules, a crop-type map like the object-based crop-type map that was produced in Chapter 5 can be used. Based on that object-based crop-type map, a smart sampling plan can be used here as well so that the NCPA operator will only focus on the GSAA parcels whose declarations are in disagreement with what has been observed in the object-based crop-type map.

### 6.6.3 Essential agricultural variables

The concept of essential variables (EVs) emerged through different scientific communities as a means of adequately characterizing the various sub-systems (e.g., atmosphere, biosphere, geosphere, hydrosphere) of the Earth system (Lehmann et al., 2020; Reyers et al., 2017). EVs are a set of variables that are critical for monitoring the aforementioned sub-systems (Earth Science Data Systems Program, 2021). Over the years, various scientific communities have established different EVs for different thematic areas such as the essential climate variables (<https://gcos.wmo.int/en/essential-climate-variables>) of the Global Climate Observing System (GCOS) and the essential biodiversity variables (<https://geobon.org/ebvs/what-are-ebvs/>) of the Group on Earth Observations Biodiversity Observation Network (GEO BON).

Within the framework of supporting the attainment of the United Nation’s Sustainable Development Goals (SDGs) especially the second goal (“End hunger, achieve food security and improved nutrition and promote sustainable agriculture”), the Group on Earth Observations Global Agricultural Monitoring Initiative (GEO-GLAM) has identified some essential agricultural variables (EAVs) including “cropland and rangeland masks, crop-type map and planted area, cropland and rangeland condition, crop yield forecast, water use and productivity, field delineation, crop phenology/stage, crop biophysical variables, and environmental variables” (Whitcraft et al., 2019). This thesis showed that at a regional level, S1 and S2 images could be used to extract agricultural fields, which is one of those EAVs. Further, the agricultural fields were used to produce a crop-type map, which is another EAV. To achieve food security, accurate crop-type maps are required (See et al., 2015). An accurate crop-type map like the object-based crop-type map produced in Chapter 5 could serve as the basis for yield forecasting. Indeed, in-season object-based crop-type maps could be generated and subsequently used for near real-time yield forecasting. Through yield forecasting, production shortfalls

could be identified and then appropriate measures could be devised to boost the agricultural output (See et al., 2015). Based on the object-based crop-type map, the agricultural practices used on agricultural lands and their corresponding impact on the environment could be assessed. This will enable policy-makers to stipulate policies that will ensure the use of sustainable agricultural practices by farmers.

## 6.7 Limitations of this thesis

There are two main limitations associated with this thesis. The first limitation is imposed by the methodologies proposed for optimizing the MRS algorithm. The supervised Bayesian optimization approach, which proved to be more accurate than the unsupervised approach, requires reference data. In this thesis, the freely available GSAA data of Lower Saxony was used. The other federal state in Germany that has made the GSAA data publicly available is Brandenburg. This can inhibit the application of the supervised approach to those federal states where the GSAA data is not publicly available.

The second limitation is associated with the input data. While a direct comparison between the results of Chapters 3 and 4 and Chapter 5 cannot be done due to the use of different tiles, the use of the multitemporal S1 and S2 images in Chapter 5 generally improved the segmentation accuracy as can be seen in Figure 6-4. The lowest segmentation accuracy of 42.04% was obtained at T2 in Chapter 3. The segmentation accuracy for T2 in Chapter 4 was 40.28%. After averaging the results of the tiles in Chapter 5 that intersected T2, the segmentation accuracy came up to 56.21%. Regardless of this improvement, the problem posed by very small fields to the effective segmentation of the agricultural fields persisted in all three papers. The use of multitemporal data in Chapter 5 could not resolve this problem. Therefore, any geographical area within the EU with very small agricultural fields will pose a problem to the use of the S1 and S2 images for effective monitoring of those fields. Within the context of CbM, this problem has been recognized by the Joint Research Centre (JRC) of the European Commission (EC) in their technical report (Devos et al., 2017). As was shown in Chapter 5, the highest overall segmentation quality (OSQ) was achieved by the medium field-size category. However, at the field level, the highest Intersection over Union (IoU) value of 0.984 was achieved by a large field with an area of 21.72 ha and a shape factor (SF) of 0.678.

## 7 Conclusions

This thesis presented a comprehensive framework for optimizing the segmentation of agricultural fields from S1 and S2 images using the MRS algorithm as implemented in eCognition. This framework enables the optimized delineation of agricultural fields from S1 and S2 images in a fully automated way. In this thesis, a Bayesian optimization approach based on supervised and unsupervised segmentation evaluation metrics was proposed. Further, the optimal feature set from S1 and S2 for segmenting agricultural fields was identified.

The outcome of this thesis showed that to optimally segment agricultural fields, all three MRS parameters (scale, shape, and compactness) must be optimized, whether a supervised or unsupervised optimization method is used. To optimize the MRS algorithm, unsupervised optimization is preferred due to the difficulty and cost that come with obtaining reference data over large geographical areas. This thesis, however, showed that to optimally segment agricultural fields, supervised optimization outperforms unsupervised optimization. Therefore, where reference data is available, supervised optimization ought to be used. Although the optimization approaches proposed in this thesis were applied to the MRS algorithm, they can be used to optimize the parameters of any segmentation algorithm. The proposed optimization approaches can also be applied to other satellite images and other thematic areas outside agriculture. Beyond the optimization approaches, this thesis also highlighted the importance of optimizing the input data given to the segmentation algorithm. To achieve optimal segmentation, the synergistic use of multitemporal S1 and S2 band indices is recommended. It was observed in this thesis that through image segmentation, the classification accuracy of pixel-based crop-type maps can be improved. The optimal segmentation layer of Lower Saxony and the corresponding object-based crop-type map produced in this thesis are essential agricultural variables that can be used for CAP monitoring, crop yield forecasting, GHG modeling, and biodiversity monitoring.

For future research, it should be tested if the optimal parameters of Lower Saxony can be spatially transferred to the other states of Germany where the GSAA data is not publicly available. One way of doing this is by building a regression model between the optimal parameters of Lower Saxony and agricultural statistics computed from ATKIS per tile. This model can then be used to predict new parameters for tiles in the other federal states. The segmentation result from this exercise can then be compared with the unsupervised optimization approach. To deal with the limitations imposed by very small field sizes, higher spatial resolution images like SPOT, PlanetScope, or WorldView could be tested. Instead of post-filtering the pixel-based crop-type map with the segmentation results to obtain the object-based map, the segmentation results can be directly used for object-based classification and the outcome can then be compared to the results after post-filtering and the pixel-based map. Instead of using eCognition, which is proprietary, open-source software (OSS) could be tested. Some OSS includes the region growing and merging algorithm in GRASS GIS (Momsen and Metz, 2015) and the foremost DNN for instance segmentation called Mask R-CNN.

## References

- Achanta, R., Shaji, A., Smith, K., Lucchi, A., Fua, P., Süsstrunk, S., 2012. SLIC Superpixels Compared to State-of-the-Art Superpixel Methods. *IEEE Transactions on Pattern Analysis and Machine Intelligence* 34, 2274–2282. <https://doi.org/10.1109/TPAMI.2012.120>
- Achanta, R., Süsstrunk, S., 2017. Superpixels and Polygons Using Simple Non-iterative Clustering, in: 2017 IEEE Conference on Computer Vision and Pattern Recognition (CVPR). Presented at the 2017 IEEE Conference on Computer Vision and Pattern Recognition (CVPR), IEEE, Honolulu, HI, pp. 4895–4904. <https://doi.org/10.1109/CVPR.2017.520>
- Adams, C.R., Eswaran, H., 2000. Global land resources in the context of food and environmental security. *Advances in Land Resources Management for the 20th Century* 35–50.
- Adams, R., Bischof, L., 1994. Seeded region growing. *IEEE Transactions on Pattern Analysis and Machine Intelligence* 16, 641–647. <https://doi.org/10.1109/34.295913>
- Akçay, O., Avsar, E.O., Inalpulat, M., Genc, L., Cam, A., 2018. Assessment of Segmentation Parameters for Object-Based Land Cover Classification Using Color-Infrared Imagery. *ISPRS International Journal of Geo-Information* 7, 424. <https://doi.org/10.3390/ijgi7110424>
- Anders, N.S., Seijmonsbergen, A.C., Bouten, W., 2011. Segmentation optimization and stratified object-based analysis for semi-automated geomorphological mapping. *Remote Sensing of Environment* 115, 2976–2985. <https://doi.org/10.1016/j.rse.2011.05.007>
- Arbeláez, P., Maire, M., Fowlkes, C., Malik, J., 2011. Contour Detection and Hierarchical Image Segmentation. *IEEE Transactions on Pattern Analysis and Machine Intelligence* 33, 898–916. <https://doi.org/10.1109/TPAMI.2010.161>
- Baatz, M., Schäpe, A., 2000. Multiresolution Segmentation: an optimization approach for high quality multi-scale image segmentation, in: Strobl, J., Blaschke, T., Griesebner, G. (Eds.), *Angewandte Geographische Informations-Verarbeitung XII*. Wichmann Verlag, Karlsruhe, pp. 12–23.
- Badrinarayanan, V., Kendall, A., Cipolla, R., 2017. SegNet: A Deep Convolutional Encoder-Decoder Architecture for Image Segmentation. *IEEE Transactions on Pattern Analysis and Machine Intelligence* 39, 2481–2495. <https://doi.org/10.1109/TPAMI.2016.2644615>
- Ball, G.H., Hall, D.J., 1965. *Isodata, a Novel Method of Data Analysis and Pattern Classification*. Stanford Research Institute.
- Belgiu, M., Csillik, O., 2018. Sentinel-2 cropland mapping using pixel-based and object-based time-weighted dynamic time warping analysis. *Remote Sensing of Environment* 204, 509–523. <https://doi.org/10.1016/j.rse.2017.10.005>
- Benz, U.C., Hofmann, P., Willhauck, G., Lingenfelder, I., Heynen, M., 2004. Multi-resolution, object-oriented fuzzy analysis of remote sensing data for GIS-ready information. *ISPRS Journal of Photogrammetry and Remote Sensing* 58, 239–258. <https://doi.org/10.1016/j.isprsjprs.2003.10.002>
- Bergstra, J., Bengio, Y., 2012. Random Search for Hyper-Parameter Optimization. *Journal of Machine Learning Research* 13, 280–305.
- Bergstra, J.S., Bardenet, R., Bengio, Y., Kégl, B., 2011. Algorithms for Hyper-Parameter Optimization, in: Shawe-Taylor, J., Zemel, R.S., Bartlett, P.L., Pereira, F., Weinberger, K.Q. (Eds.), *Advances in Neural Information Processing Systems* 24. Curran Associates, Inc., pp. 2546–2554.
- Blaschke, T., 2010. Object based image analysis for remote sensing. *ISPRS Journal of Photogrammetry and Remote Sensing* 65, 2–16. <https://doi.org/10.1016/j.isprsjprs.2009.06.004>
- Böck, S., Immitzer, M., Atzberger, C., 2017. On the Objectivity of the Objective Function—Problems with Unsupervised Segmentation Evaluation Based on Global Score and a Possible Remedy. *Remote Sensing* 9, 769. <https://doi.org/10.3390/rs9080769>

- Campos-Taberner, García-Haro, Martínez, Sánchez-Ruiz, Gilabert, 2019. A Copernicus Sentinel-1 and Sentinel-2 Classification Framework for the 2020+ European Common Agricultural Policy: A Case Study in València (Spain). *Agronomy* 9, 556. <https://doi.org/10.3390/agronomy9090556>
- Canny, J., 1987. A Computational Approach to Edge Detection, in: Fischler, M.A., Firschein, O. (Eds.), *Readings in Computer Vision*. Morgan Kaufmann, San Francisco (CA), pp. 184–203. <https://doi.org/10.1016/B978-0-08-051581-6.50024-6>
- Chabrier, S., Emile, B., Rosenberger, C., Laurent, H., 2006. Unsupervised Performance Evaluation of Image Segmentation. *EURASIP J. Adv. Signal Process.* 2006, 096306. <https://doi.org/10.1155/ASP/2006/96306>
- Chan, T.F., Vese, L.A., 2001. Active contours without edges. *IEEE Transactions on Image Processing* 10, 266–277. <https://doi.org/10.1109/83.902291>
- Chen, J., Deng, M., Mei, X., Chen, T., Shao, Q., Hong, L., 2014. Optimal segmentation of a high-resolution remote-sensing image guided by area and boundary. *International Journal of Remote Sensing* 35, 6914–6939. <https://doi.org/10.1080/01431161.2014.960617>
- Clauss, K., Ottinger, M., Kuenzer, C., 2018. Mapping rice areas with Sentinel-1 time series and superpixel segmentation. *International Journal of Remote Sensing* 39, 1399–1420. <https://doi.org/10.1080/01431161.2017.1404162>
- Clinton, N., Holt, A., Scarborough, J., Yan, L., Gong, P., 2010. Accuracy Assessment Measures for Object-based Image Segmentation Goodness. *Photogrammetric Engineering & Remote Sensing* 76, 289–299. <https://doi.org/10.14358/PERS.76.3.289>
- Conrad, C., Fritsch, S., Zeidler, J., Rücker, G., Dech, S., 2010. Per-Field Irrigated Crop Classification in Arid Central Asia Using SPOT and ASTER Data. *Remote Sensing* 2, 1035–1056. <https://doi.org/10.3390/rs2041035>
- Csillik, O., Belgiu, M., Asner, G.P., Kelly, M., 2019. Object-Based Time-Constrained Dynamic Time Warping Classification of Crops Using Sentinel-2. *Remote Sensing* 11, 1257. <https://doi.org/10.3390/rs11101257>
- d’Andrimont, R., Lemoine, G., van der Velde, M., 2018. Targeted Grassland Monitoring at Parcel Level Using Sentinels, Street-Level Images and Field Observations. *Remote Sensing* 10, 1300. <https://doi.org/10.3390/rs10081300>
- Devos, W., Fasbender, D., Lemoine, G., Loudjani, P., Milenov, P., Wirthardt, C., 2017. Discussion document on the introduction of monitoring to substitute OTSC: supporting non paper DS/CDP/2017/03 revising R2014/809. Publications Office, LU.
- Diakogiannis, F.I., Waldner, F., Caccetta, P., Wu, C., 2020. ResUNet-a: A deep learning framework for semantic segmentation of remotely sensed data. *ISPRS Journal of Photogrammetry and Remote Sensing* 162, 94–114. <https://doi.org/10.1016/j.isprsjprs.2020.01.013>
- Drăguț, L., Csillik, O., Eisank, C., Tiede, D., 2014. Automated parameterisation for multi-scale image segmentation on multiple layers. *ISPRS Journal of Photogrammetry and Remote Sensing* 88, 119–127. <https://doi.org/10.1016/j.isprsjprs.2013.11.018>
- Drăguț, L., Tiede, D., Levick, S.R., 2010. ESP: a tool to estimate scale parameter for multiresolution image segmentation of remotely sensed data. *International Journal of Geographical Information Science* 24, 859–871. <https://doi.org/10.1080/13658810903174803>
- Dudley, N., Alexander, S., 2017. Agriculture and biodiversity: a review. *Biodiversity* 18, 45–49. <https://doi.org/10.1080/14888386.2017.1351892>
- Earth Science Data Systems Program, 2021. Essential Variables [WWW Document]. URL <https://earthdata.nasa.gov/learn/backgrounders/essential-variables/> (accessed 8.29.21).

- Espindola, G.M., Camara, G., Reis, I.A., Bins, L.S., Monteiro, A.M., 2006. Parameter selection for region-growing image segmentation algorithms using spatial autocorrelation. *International Journal of Remote Sensing* 27, 3035–3040. <https://doi.org/10.1080/01431160600617194>
- European Commission, 2021a. The common agricultural policy at a glance [WWW Document]. European Commission - European Commission. URL [https://ec.europa.eu/info/food-farming-fisheries/key-policies/common-agricultural-policy\\_en](https://ec.europa.eu/info/food-farming-fisheries/key-policies/common-agricultural-policy_en) (accessed 3.11.21).
- European Commission, 2021b. Sustainable land use (greening) [WWW Document]. European Commission - European Commission. URL [https://ec.europa.eu/info/food-farming-fisheries/key-policies/common-agricultural-policy/income-support/greening\\_en](https://ec.europa.eu/info/food-farming-fisheries/key-policies/common-agricultural-policy/income-support/greening_en) (accessed 7.24.21).
- European Commission, 2013. Regulation (EU) No 1306/2013 of the European Parliament and of the Council of 17 December 2013 on the financing, management and monitoring of the common agricultural policy and repealing Council Regulations (EEC) No 352/78, (EC) No 165/94, (EC) No 2799/98, (EC) No 814/2000, (EC) No 1290/2005 and (EC) No 485/2008. *Official Journal of the European Union* 59.
- European Union, 2018. Commission Implementing Regulation (EU) 2018/746 of 18 May 2018 amending Implementing Regulation (EU) No 809/2014 as regards modification of single applications and payment claims and checks. *Official Journal of the European Union* 61, L125/1.
- Evans, C., Jones, R., Svalbe, I., Berman, M., 2002. Segmenting multispectral Landsat TM images into field units. *IEEE Trans. Geosci. Remote Sensing* 40, 1054–1064. <https://doi.org/10.1109/TGRS.2002.1010893>
- Foley, J.A., Ramankutty, N., Brauman, K.A., Cassidy, E.S., Gerber, J.S., Johnston, M., Mueller, N.D., O’Connell, C., Ray, D.K., West, P.C., Balzer, C., Bennett, E.M., Carpenter, S.R., Hill, J., Monfreda, C., Polasky, S., Rockström, J., Sheehan, J., Siebert, S., Tilman, D., Zaks, D.P.M., 2011. Solutions for a cultivated planet. *Nature* 478, 337–342. <https://doi.org/10.1038/nature10452>
- Forkuor, G., Conrad, C., Thiel, M., Ullmann, T., Zoungrana, E., 2014. Integration of Optical and Synthetic Aperture Radar Imagery for Improving Crop Mapping in Northwestern Benin, West Africa. *Remote Sensing* 6, 6472–6499. <https://doi.org/10.3390/rs6076472>
- Frazier, P.I., 2018. A Tutorial on Bayesian Optimization. arXiv:1807.02811 [cs, math, stat].
- Fukunaga, K., Hostetler, L., 1975. The estimation of the gradient of a density function, with applications in pattern recognition. *IEEE Transactions on Information Theory* 21, 32–40. <https://doi.org/10.1109/TIT.1975.1055330>
- Gao, Y., Mas, J.F., Kerle, N., Pacheco, J.A.N., 2011. Optimal region growing segmentation and its effect on classification accuracy. *International Journal of Remote Sensing* 32, 3747–3763. <https://doi.org/10.1080/01431161003777189>
- García-Pedrero, A., Gonzalo-Martín, C., Lillo-Saavedra, M., 2017. A machine learning approach for agricultural parcel delineation through agglomerative segmentation. *International Journal of Remote Sensing* 38, 1809–1819. <https://doi.org/10.1080/01431161.2016.1278312>
- García-Pedrero, A., Lillo-Saavedra, M., Rodríguez-Esparragón, D., Gonzalo-Martín, C., 2019. Deep Learning for Automatic Outlining Agricultural Parcels: Exploiting the Land Parcel Identification System. *IEEE Access* 7, 158223–158236. <https://doi.org/10.1109/ACCESS.2019.2950371>
- Georganos, S., Grippa, T., Lennert, M., Vanhuyse, S., Johnson, B.A., Wolff, E., 2018a. Scale Matters: Spatially Partitioned Unsupervised Segmentation Parameter Optimization for Large and Heterogeneous Satellite Images. *Remote Sensing* 10, 1440. <https://doi.org/10.3390/rs10091440>
- Georganos, S., Lennert, M., Grippa, T., Vanhuyse, S., Johnson, B., Wolff, E., 2018b. Normalization in Unsupervised Segmentation Parameter Optimization: A Solution Based on Local Regression Trend Analysis. *Remote Sensing* 10, 222. <https://doi.org/10.3390/rs10020222>

- Graesser, J., Ramankutty, N., 2017. Detection of cropland field parcels from Landsat imagery. *Remote Sensing of Environment* 201, 165–180. <https://doi.org/10.1016/j.rse.2017.08.027>
- Griffiths, P., Nendel, C., Hostert, P., 2019. Intra-annual reflectance composites from Sentinel-2 and Landsat for national-scale crop and land cover mapping. *Remote Sensing of Environment* 220, 135–151. <https://doi.org/10.1016/j.rse.2018.10.031>
- Grybas, H., Melendy, L., Congalton, R.G., 2017. A comparison of unsupervised segmentation parameter optimization approaches using moderate- and high-resolution imagery. *GIScience & Remote Sensing* 54, 515–533. <https://doi.org/10.1080/15481603.2017.1287238>
- He, K., Gkioxari, G., Dollár, P., Girshick, R., 2017. Mask R-CNN, in: 2017 IEEE International Conference on Computer Vision (ICCV). Presented at the 2017 IEEE International Conference on Computer Vision (ICCV), pp. 2980–2988. <https://doi.org/10.1109/ICCV.2017.322>
- Hossain, M.D., Chen, D., 2019. Segmentation for Object-Based Image Analysis (OBIA): A review of algorithms and challenges from remote sensing perspective. *ISPRS Journal of Photogrammetry and Remote Sensing* 150, 115–134. <https://doi.org/10.1016/j.isprsjprs.2019.02.009>
- Huang, G., Liu, Z., Van Der Maaten, L., Weinberger, K.Q., 2017. Densely Connected Convolutional Networks, in: 2017 IEEE Conference on Computer Vision and Pattern Recognition (CVPR). Presented at the 2017 IEEE Conference on Computer Vision and Pattern Recognition (CVPR), pp. 2261–2269. <https://doi.org/10.1109/CVPR.2017.243>
- Huang, H., Lan, Y., Yang, A., Zhang, Y., Wen, S., Deng, J., 2020. Deep learning versus Object-based Image Analysis (OBIA) in weed mapping of UAV imagery. *International Journal of Remote Sensing* 41, 3446–3479. <https://doi.org/10.1080/01431161.2019.1706112>
- Inglada, J., Dejoux, J.-F., Hagolle, O., Dedieu, G., 2012. Multi-temporal remote sensing image segmentation of croplands constrained by a topographical database, in: 2012 IEEE International Geoscience and Remote Sensing Symposium. Presented at the IGARSS 2012 - 2012 IEEE International Geoscience and Remote Sensing Symposium, IEEE, Munich, Germany, pp. 6781–6784. <https://doi.org/10.1109/IGARSS.2012.6352607>
- InterImage, 2014. InterImage User Guide - Version 1.41 [WWW Document]. URL <http://www.lvc.ele.puc-rio.br/projects/interimage/documentation/files/InterImage%201.41%20-%20User%20Guide.pdf> (accessed 9.14.21).
- Jaccard, P., 1901. Etude de la distribution florale dans une portion des Alpes et du Jura. *Bulletin de la Societe Vaudoise des Sciences Naturelles* 37, 547–579. <https://doi.org/10.5169/seals-266450>
- Ji, C.Y., 1996. Delineating agricultural field boundaries from TM imagery using dyadic wavelet transforms. *ISPRS Journal of Photogrammetry and Remote Sensing* 51, 268–283. [https://doi.org/10.1016/0924-2716\(95\)00017-8](https://doi.org/10.1016/0924-2716(95)00017-8)
- Johnson, B., Xie, Z., 2013. Classifying a high resolution image of an urban area using super-object information. *ISPRS Journal of Photogrammetry and Remote Sensing* 83, 40–49. <https://doi.org/10.1016/j.isprsjprs.2013.05.008>
- Johnson, B., Xie, Z., 2011. Unsupervised image segmentation evaluation and refinement using a multi-scale approach. *ISPRS Journal of Photogrammetry and Remote Sensing* 66, 473–483. <https://doi.org/10.1016/j.isprsjprs.2011.02.006>
- Johnson, B.A., Bragais, M., Endo, I., Magcale-Macandog, D.B., Macandog, P.B.M., 2015. Image Segmentation Parameter Optimization Considering Within- and Between-Segment Heterogeneity at Multiple Scale Levels: Test Case for Mapping Residential Areas Using Landsat Imagery. *ISPRS International Journal of Geo-Information* 4, 2292–2305. <https://doi.org/10.3390/ijgi4042292>
- Kass, M., Witkin, A., Terzopoulos, D., 1988. Snakes: Active contour models. *Int J Comput Vision* 1, 321–331. <https://doi.org/10.1007/BF00133570>

- Kavzoglu, T., Tonbul, H., 2018. An experimental comparison of multi-resolution segmentation, SLIC and K-means clustering for object-based classification of VHR imagery. *International Journal of Remote Sensing* 39, 6020–6036. <https://doi.org/10.1080/01431161.2018.1506592>
- Kavzoglu, T., Tonbul, H., 2017. A Comparative Study of Segmentation Quality for Multi-resolution Segmentation and Watershed Transform. *IEE Proceedings-International Conference on Recent Advances in Space Technologies*.
- Kim, M., Madden, M., Warner, T., 2008. Estimation of optimal image object size for the segmentation of forest stands with multispectral IKONOS imagery, in: Blaschke, T., Lang, S., Hay, G.J. (Eds.), *Object-Based Image Analysis, Lecture Notes in Geoinformation and Cartography*. Springer Berlin Heidelberg, Berlin, Heidelberg, pp. 291–307. [https://doi.org/10.1007/978-3-540-77058-9\\_16](https://doi.org/10.1007/978-3-540-77058-9_16)
- Kim, M., Warner, T.A., Madden, M., Atkinson, D.S., 2011. Multi-scale GEOBIA with very high spatial resolution digital aerial imagery: scale, texture and image objects. *International Journal of Remote Sensing* 32, 2825–2850. <https://doi.org/10.1080/01431161003745608>
- Kotaridis, I., Lazaridou, M., 2021. Remote sensing image segmentation advances: A meta-analysis. *ISPRS Journal of Photogrammetry and Remote Sensing* 173, 309–322. <https://doi.org/10.1016/j.isprsjprs.2021.01.020>
- Lehmann, A., Masò, J., Nativi, S., Giuliani, G., 2020. Towards integrated essential variables for sustainability. *International Journal of Digital Earth* 13, 158–165. <https://doi.org/10.1080/17538947.2019.1636490>
- Li, P., Xiao, X., 2007. Multispectral image segmentation by a multichannel watershed-based approach. *International Journal of Remote Sensing* 28, 4429–4452. <https://doi.org/10.1080/01431160601034910>
- Li, Y., Qi, H., Dai, J., Ji, X., Wei, Y., 2016. Fully Convolutional Instance-aware Semantic Segmentation. *arXiv:1611.07709 [cs]*.
- Liu, D., Xia, F., 2010. Assessing object-based classification: advantages and limitations. *Remote Sensing Letters* 1, 187–194. <https://doi.org/10.1080/01431161003743173>
- Long, J., Shelhamer, E., Darrell, T., 2015. Fully Convolutional Networks for Semantic Segmentation. *arXiv:1411.4038 [cs]*.
- López-Andreu, F.J., Erena, M., Dominguez-Gómez, J.A., López-Morales, J.A., 2021. Sentinel-2 Images and Machine Learning as Tool for Monitoring of the Common Agricultural Policy: Calasparra Rice as a Case Study. *Agronomy* 11, 621. <https://doi.org/10.3390/agronomy11040621>
- Lozano-Tello, A., Fernández-Sellers, M., Quirós, E., Frago-Campón, L., García-Martín, A., Gallego, J.A.G., Mateos, C., Trenado, R., Muñoz, P., 2021. Crop identification by massive processing of multiannual satellite imagery for EU common agriculture policy subsidy control. *European Journal of Remote Sensing* 54, 1–12. <https://doi.org/10.1080/22797254.2020.1858723>
- Lucieer, A., Stein, A., 2002. Existential uncertainty of spatial objects segmented from satellite sensor imagery. *IEEE Transactions on Geoscience and Remote Sensing* 40, 2518–2521. <https://doi.org/10.1109/TGRS.2002.805072>
- Luo, C., Qi, B., Liu, H., Guo, D., Lu, L., Fu, Q., Shao, Y., 2021. Using Time Series Sentinel-1 Images for Object-Oriented Crop Classification in Google Earth Engine. *Remote Sensing* 13, 561. <https://doi.org/10.3390/rs13040561>
- Lv, Y., Zhang, C., Yun, W., Gao, L., Wang, H., Ma, J., Li, H., Zhu, D., 2020. The Delineation and Grading of Actual Crop Production Units in Modern Smallholder Areas Using RS Data and Mask R-CNN. *Remote Sensing* 12, 1074. <https://doi.org/10.3390/rs12071074>
- Ma, L., Li, M., Ma, X., Cheng, L., Du, P., Liu, Y., 2017. A review of supervised object-based land-cover image classification. *ISPRS Journal of Photogrammetry and Remote Sensing* 130, 277–293. <https://doi.org/10.1016/j.isprsjprs.2017.06.001>

- Mallat, S., Zhong, S., 1992. Characterization of signals from multiscale edges. *IEEE Transactions on Pattern Analysis and Machine Intelligence* 14, 710–732. <https://doi.org/10.1109/34.142909>
- Marpu, P.R., Neubert, M., Herold, H., Niemeyer, I., 2010. Enhanced evaluation of image segmentation results. *Journal of Spatial Science* 55, 55–68. <https://doi.org/10.1080/14498596.2010.487850>
- Martha, T.R., Kerle, N., van Westen, C.J., Jetten, V., Kumar, K.V., 2011. Segment Optimization and Data-Driven Thresholding for Knowledge-Based Landslide Detection by Object-Based Image Analysis. *IEEE Trans. Geosci. Remote Sensing* 49, 4928–4943. <https://doi.org/10.1109/TGRS.2011.2151866>
- Martin, D.R., Fowlkes, C.C., Malik, J., 2004. Learning to detect natural image boundaries using local brightness, color, and texture cues. *IEEE Transactions on Pattern Analysis and Machine Intelligence* 26, 530–549. <https://doi.org/10.1109/TPAMI.2004.1273918>
- Mesner, N., Oštir, K., 2014. Investigating the impact of spatial and spectral resolution of satellite images on segmentation quality. *J. Appl. Remote Sens* 8, 083696. <https://doi.org/10.1117/1.JRS.8.083696>
- Momsen, E., Metz, M., 2015. i.segment [WWW Document]. URL <https://grass.osgeo.org/grass79/manuals/i.segment.html> (accessed 7.26.21).
- Moran, P.A.P., 1950. Notes on Continuous Stochastic Phenomena. *Biometrika* 37, 17–23. <https://doi.org/10.2307/2332142>
- Nasrallah, A., Baghdadi, N., Mhawej, M., Faour, G., Darwish, T., Belhouchette, H., Darwich, S., 2018. A Novel Approach for Mapping Wheat Areas Using High Resolution Sentinel-2 Images. *Sensors* 18, 2089. <https://doi.org/10.3390/s18072089>
- Neubert, M., Herold, H., Meinel, G., 2008. Assessing image segmentation quality – concepts, methods and application, in: Blaschke, T., Lang, S., Hay, G.J. (Eds.), *Object-Based Image Analysis: Spatial Concepts for Knowledge-Driven Remote Sensing Applications*, Lecture Notes in Geoinformation and Cartography. Springer, Berlin, Heidelberg, pp. 769–784. [https://doi.org/10.1007/978-3-540-77058-9\\_42](https://doi.org/10.1007/978-3-540-77058-9_42)
- North, H.C., Pairman, D., Belliss, S.E., 2019. Boundary Delineation of Agricultural Fields in Multitemporal Satellite Imagery. *IEEE J. Sel. Top. Appl. Earth Observations Remote Sensing* 12, 237–251. <https://doi.org/10.1109/JSTARS.2018.2884513>
- Persello, C., Tolpekin, V.A., Bergado, J.R., de By, R.A., 2019. Delineation of agricultural fields in smallholder farms from satellite images using fully convolutional networks and combinatorial grouping. *Remote Sensing of Environment* 231, 111253. <https://doi.org/10.1016/j.rse.2019.111253>
- Plaza, A., Martinez, P., Perez, R., Plaza, J., 2002. Spatial/spectral endmember extraction by multidimensional morphological operations. *IEEE Transactions on Geoscience and Remote Sensing* 40, 2025–2041. <https://doi.org/10.1109/TGRS.2002.802494>
- Pont-Tuset, J., Arbeláez, P., T. Barron, J., Marques, F., Malik, J., 2017. Multiscale Combinatorial Grouping for Image Segmentation and Object Proposal Generation. *IEEE Transactions on Pattern Analysis and Machine Intelligence* 39, 128–140. <https://doi.org/10.1109/TPAMI.2016.2537320>
- Reis, M.S., Falcão de Oliveira, M.A., Körting, T.S., Pantaleão, E., Siqueira Sant’Anna, S.J., Dutra, L.V., Lu, D., 2015. Image segmentation algorithms comparison, in: 2015 IEEE International Geoscience and Remote Sensing Symposium (IGARSS). Presented at the 2015 IEEE International Geoscience and Remote Sensing Symposium (IGARSS), pp. 4340–4343. <https://doi.org/10.1109/IGARSS.2015.7326787>
- Reyers, B., Stafford-Smith, M., Erb, K.-H., Scholes, R.J., Selomane, O., 2017. Essential Variables help to focus Sustainable Development Goals monitoring. *Current Opinion in Environmental Sustainability*, Open issue, part II 26–27, 97–105. <https://doi.org/10.1016/j.cosust.2017.05.003>
- Rieke, C., 2017. Deep Learning for Instance Segmentation of Agricultural Fields (Master’s thesis dissertation). Friedrich-Schiller-University Jena, Thuringia, Germany.

- Ronneberger, O., Fischer, P., Brox, T., 2015. U-Net: Convolutional Networks for Biomedical Image Segmentation, in: Navab, N., Hornegger, J., Wells, W.M., Frangi, A.F. (Eds.), *Medical Image Computing and Computer-Assisted Intervention – MICCAI 2015*, Lecture Notes in Computer Science. Springer International Publishing, Cham, pp. 234–241. [https://doi.org/10.1007/978-3-319-24574-4\\_28](https://doi.org/10.1007/978-3-319-24574-4_28)
- Rousi, M., Sitokonstantinou, V., Meditskos, G., Papoutsis, I., Gialampoukidis, I., Koukos, A., Karathanassi, V., Drivas, T., Vrochidis, S., Kontoes, C., Kompatsiaris, I., 2021. Semantically Enriched Crop Type Classification and Linked Earth Observation Data to Support the Common Agricultural Policy Monitoring. *IEEE J. Sel. Top. Appl. Earth Observations Remote Sensing* 14, 529–552. <https://doi.org/10.1109/JSTARS.2020.3038152>
- Rydberg, A., Borgefors, G., 2001. Integrated Method for Boundary Delineation of Agricultural Fields in Multispectral Satellite Images. *IEEE TRANSACTIONS ON GEOSCIENCE AND REMOTE SENSING* 39, 7.
- Sarvia, F., Xausa, E., Petris, S.D., Cantamessa, G., Borgogno-Mondino, E., 2021. A Possible Role of Copernicus Sentinel-2 Data to Support Common Agricultural Policy Controls in Agriculture. *Agronomy* 11, 110. <https://doi.org/10.3390/agronomy11010110>
- See, L., Fritz, S., You, L., Ramankutty, N., Herrero, M., Justice, C., Becker-Reshef, I., Thornton, P., Erb, K., Gong, P., Tang, H., van der Velde, M., Ericksen, P., McCallum, I., Kraxner, F., Obersteiner, M., 2015. Improved global cropland data as an essential ingredient for food security. *Global Food Security* 4, 37–45. <https://doi.org/10.1016/j.gfs.2014.10.004>
- Seiffert, C., Khoshgoftaar, T.M., Van Hulse, J., Napolitano, A., 2010. RUSBoost: A Hybrid Approach to Alleviating Class Imbalance. *IEEE Transactions on Systems, Man, and Cybernetics - Part A: Systems and Humans* 40, 185–197. <https://doi.org/10.1109/TSMCA.2009.2029559>
- Sitokonstantinou, V., Papoutsis, I., Kontoes, C., Lafarga Arnal, A., Armesto Andrés, A.P., Garraza Zurbano, J.A., 2018. Scalable Parcel-Based Crop Identification Scheme Using Sentinel-2 Data Time-Series for the Monitoring of the Common Agricultural Policy. *Remote Sensing* 10, 911. <https://doi.org/10.3390/rs10060911>
- Snoek, J., Larochelle, H., Adams, R.P., 2012. Practical Bayesian Optimization of Machine Learning Algorithms, in: Pereira, F., Burges, C.J.C., Bottou, L., Weinberger, K.Q. (Eds.), *Advances in Neural Information Processing Systems* 25. Curran Associates, Inc., pp. 2951–2959.
- Trimble Germany GmbH, 2019. eCognition Developer 9.5.0 Reference Book. Trimble Germany GmbH, Germany.
- Turker, M., Kok, E.H., 2013. Field-based sub-boundary extraction from remote sensing imagery using perceptual grouping. *ISPRS Journal of Photogrammetry and Remote Sensing* 79, 106–121. <https://doi.org/10.1016/j.isprsjprs.2013.02.009>
- Vogels, M.F.A., de Jong, S.M., Sterk, G., Douma, H., Addink, E.A., 2019. Spatio-Temporal Patterns of Smallholder Irrigated Agriculture in the Horn of Africa Using GEOBIA and Sentinel-2 Imagery. *Remote Sensing* 11, 143. <https://doi.org/10.3390/rs11020143>
- Wagner, M.P., Oppelt, N., 2020. Extracting Agricultural Fields from Remote Sensing Imagery Using Graph-Based Growing Contours. *Remote Sensing* 12, 1205. <https://doi.org/10.3390/rs12071205>
- Waldhoff, G., Curdt, C., Hoffmeister, D., Bareth, G., 2012. Analysis of multitemporal and multisensor remote sensing data for crop rotation mapping. *ISPRS Ann. Photogramm. Remote Sens. Spatial Inf. Sci* 1, 7.
- Waldner, F., Diakogiannis, F.I., 2020. Deep learning on edge: Extracting field boundaries from satellite images with a convolutional neural network. *Remote Sensing of Environment* 245, 111741. <https://doi.org/10.1016/j.rse.2020.111741>

## References

- Watkins, B., van Niekerk, A., 2019a. Automating field boundary delineation with multi-temporal Sentinel-2 imagery. *Computers and Electronics in Agriculture* 167, 105078. <https://doi.org/10.1016/j.compag.2019.105078>
- Watkins, B., van Niekerk, A., 2019b. A comparison of object-based image analysis approaches for field boundary delineation using multi-temporal Sentinel-2 imagery. *Computers and Electronics in Agriculture* 158, 294–302. <https://doi.org/10.1016/j.compag.2019.02.009>
- Weidner, U., 2008. Contribution to the assessment of segmentation quality for remote sensing applications. *International Archives of Photogrammetry, Remote Sensing and Spatial Information Sciences* 37, 479–484.
- Whitcraft, A.K., Becker-Reshef, I., Justice, C.O., Gifford, L., Kavvada, A., Jarvis, I., 2019. No pixel left behind: Toward integrating Earth Observations for agriculture into the United Nations Sustainable Development Goals framework. *Remote Sensing of Environment* 235, 111470. <https://doi.org/10.1016/j.rse.2019.111470>
- Woodcock, C.E., Strahler, A.H., 1987. The factor of scale in remote sensing. *Remote Sensing of Environment* 21, 311–332. [https://doi.org/10.1016/0034-4257\(87\)90015-0](https://doi.org/10.1016/0034-4257(87)90015-0)
- Yan, L., Roy, D.P., 2014. Automated crop field extraction from multi-temporal Web Enabled Landsat Data. *Remote Sensing of Environment* 144, 42–64. <https://doi.org/10.1016/j.rse.2014.01.006>
- Yang, L., Mansaray, L.R., Huang, J., Wang, L., 2019. Optimal Segmentation Scale Parameter, Feature Subset and Classification Algorithm for Geographic Object-Based Crop Recognition Using Multi-source Satellite Imagery. *Remote Sensing* 11, 514. <https://doi.org/10.3390/rs11050514>
- Yang, R., Ahmed, Z.U., Schulthess, U.C., Kamal, M., Rai, R., 2020. Detecting functional field units from satellite images in smallholder farming systems using a deep learning based computer vision approach: A case study from Bangladesh. *Remote Sensing Applications: Society and Environment* 20, 100413. <https://doi.org/10.1016/j.rsase.2020.100413>
- Zhang, H., Fritts, J.E., Goldman, S.A., 2008. Image segmentation evaluation: A survey of unsupervised methods. *Computer Vision and Image Understanding* 110, 260–280. <https://doi.org/10.1016/j.cviu.2007.08.003>

## **Curriculum vitae**

### **Personal Information**

- Name: Gideon Okpoti Tetteh
- Date of birth: 19 November 1984
- Place of birth: Accra, Ghana
- Nationality: Ghanaian

### **Education**

- Since September 2019: Doctoral student, Martin Luther University of Halle-Wittenberg, Halle (Saale), Saxony-Anhalt.
- October 2010 – March 2012: M.Sc. in Photogrammetry and Geoinformatics, University of Applied Sciences, Stuttgart, Germany.
- August 2003 – May 2007: B.Sc. in Geodetic Engineering, Kwame Nkrumah University of Science and Technology, Kumasi, Ghana.
- September 2000 – August 2002: Senior High School, Adisadel College, Cape Coast, Ghana.

### **Work Experience**

- Since August 2017: Scientific researcher, Thünen Institute of Farm Economics, Braunschweig, Germany.
- October 2012 – July 2017: Remote Sensing Application Developer, Planet Labs Germany GmbH, Berlin, Germany.
- April 2012 – September 2012: Intern, World Meteorological Organization (WMO), Geneva, Switzerland.
- June 2007 – July 2010: Assistant Geodetic Engineer, Daov Tech Design Group, Accra, Ghana.

### **Honors and awards**

- German Academic Exchange Service (DAAD) scholarship holder from 2010 to 2012.
- Award for outstanding academic achievements in the M.Sc. program in Photogrammetry and Geoinformatics at the University of Applied Sciences, Stuttgart, Germany.

## List of publications

### Publications used in this thesis

Tetteh, G.O., Gocht, A., Erasmi, S., Schwieder, M., Conrad, C., 2021. Evaluation of Sentinel-1 and Sentinel-2 Feature Sets for Delineating Agricultural Fields in Heterogeneous Landscapes. *IEEE Access* 9, 116702–116719. <https://doi.org/10.1109/ACCESS.2021.3105903>

Tetteh, G.O., Gocht, A., Schwieder, M., Erasmi, S., Conrad, C., 2020. Unsupervised Parameterization for Optimal Segmentation of Agricultural Parcels from Satellite Images in Different Agricultural Landscapes. *Remote Sensing* 12, 3096. <https://doi.org/10.3390/rs12183096>

Tetteh, G.O., Gocht, A., Conrad, C., 2020. Optimal parameters for delineating agricultural parcels from satellite images based on supervised Bayesian optimization. *Computers and Electronics in Agriculture* 178, 105696. <https://doi.org/10.1016/j.compag.2020.105696>

### Other publications

Marx, A., Tetteh, G.O., 2017. A Forest Vitality and Change Monitoring Tool Based on RapidEye Imagery. *IEEE Geoscience and Remote Sensing Letters* 14, 801–805. <https://doi.org/10.1109/LGRS.2017.2675164>

Tetteh, G.O., Schönert, M., 2015. Automatic Generation of Water Masks from RapidEye Images. *Journal of Geoscience and Environment Protection* 3, 17–23. <https://doi.org/10.4236/gep.2015.310003>

## **Eidesstattliche Erklärung / Declaration under Oath**

Ich erkläre an Eides statt, dass ich die Arbeit selbstständig und ohne fremde Hilfe verfasst, keine anderen als die von mir angegebenen Quellen und Hilfsmittel benutzt und die den benutzten Werken wörtlich oder inhaltlich entnommenen Stellen als solche kenntlich gemacht habe.

*I declare under penalty of perjury that this thesis is my own work entirely and has been written without any help from other people. I used only the sources mentioned and included all the citations correctly both in word or content.*

---

Datum / Date

---

Unterschrift des Antragstellers / Signature of the applicant